seit 1558

Friedrich-Schiller-Universität Jena

Characteristics of salt flow and syn-kinematic sedimentary structures in extensional basins

Dissertation

(kumulativ)

zur Erlangung des akademischen Grades doctor rerum naturalium
(Dr. rer. nat.)

---

vorgelegt dem Rat der Chemisch-Geowissenschaftlichen Fakultät der
Friedrich-Schiller-Universität Jena

von Dipl.-Geol. Michael Warsitzka
geboren am 16.11.1984 in Gera

Gutachter/-in:

1. Prof. Dr. Nina Kukowski
   Friedrich-Schiller-Universität Jena

2. Prof. Dr. Jonas Kley
   Georg-August-Universität Göttingen

3. Prof. Dr. Magdalena Scheck-Wenderoth
   Helmholtz-Zentrum Potsdam –
   Deutsches GeoForschungsZentrum GFZ

Tag der Verteidigung: 04.10.2017

Summary

Salt tectonics can significantly affect structure and depositional patterns of evaporite-bearing sedimentary basins, because rock salt deformation behaviour corresponds to that of a viscous fluid. Consequently, salt is able to flow according to an internal hydraulic-head gradient and produce local subsidence centres in regions of salt expulsion and topographic uplifts (e.g. salt diapirs, salt pillows) in regions of salt influx. In many world-wide salt-bearing sedimentary basins, e.g. the Southern Permian Basin in central Europe, a hydraulic-head gradient and consequent salt flow is induced by phases of regional tectonic extension. In such a tectonic setting, differential basement subsidence, e.g. due to normal faulting of sub-salt basement, may result in gravitationally driven flow towards the basin centre, and differential loading between basin lows and their flanks potentially squeezes salt away from imposed loads and causes upward directed salt flow. In order to investigate effects of syn- and post-extensional salt flow on structure and subsidence pattern of a basin, analogue experiments as well as analytical and numerical modelling are frequently applied. Existing analogue modelling studies dealing with processes of extensionally driven salt tectonics mostly examined brittle deformation and sedimentary structures in the supra-salt overburden, but rarely investigated flow pattern in the viscous substratum. Numerous analytical and numerical modelling studies, in contrast, addressed dynamics of flow in the salt, but only a few included sub-salt normal faulting as a trigger for salt flow.

This thesis aims to gain a better comprehension of first-order salt flow kinematics and dynamics induced by sub-salt extensional faulting and supra-salt sedimentary differential loading. To unravel structural geometries, flow patterns and driving mechanisms resulting from the interaction between sub-salt faulting, syn-kinematic sedimentation and salt flow, the following methods were applied: (1) A literature review was undertaken compiling a database of salt structures of the Southern Permian Basin, which is a prime natural example for studying extensionally driven salt tectonics. This literature study intends to visualise periods in which salt structures were initiated and periods in which salt structures grew fastest. Furthermore, geological scenarios and boundary conditions typically occurring during the onset and the subsequent growth of extensionally driven salt structures were determined and used in the following studies. (2) 2D retro-deformation of one geological cross section of a prominent extensional basin (Glückstadt Graben, Northern Germany) was performed to examine sedimentary structures in the overburden, which formed due to tectonic stretching and syn- and post-extensional salt flow. The retro-deformation sequentially restored the initial thickness of overburden layers by applying decompaction and vertical shear unfolding. (3) An experimental analogue modelling study was conducted to examine strain patterns in the viscous layer above an extensional basement fault. The experimental set-up consisted of a rigid base dissected by two normal faults, a ductile layer made of viscous silicone elastomer which represents the salt layer, and sand

layers with a higher bulk density representing brittle overburden sediments. The experiments were analysed using particle imaging velocimetry at the frontal glass wall illustrating flow patterns in the viscous layer. (4) Analytical computations were used to determine direction and velocities of salt flow taking place above a sub-salt fault in dependence on the fault displacement and the amount of differential loading between hanging wall and footwall side. The idealised model set-up consisted of a basement displaced by a normal fault, a layer with Newtonian viscous rheology of salt and an overburden, whose density increased with depth. The flow velocity was calculated according to the prevailing hydraulic-head gradient for various different geological parameter, e.g. thicknesses of the salt and the cover, inclination of the basement fault, compaction behaviour of the overburden or salt density.

On the basis of the results of this thesis, a comprehensive concept of early-stage salt flow in extensional basins can be developed including the temporal development of the syn-kinematic peripheral sinks and the salt flow patterns as well as the dynamics driving the salt flow. First of all, dating of salt structures (Chapter 2) emphasised that in many parts of the Southern Permian Basin, movement of the Upper Permian salt started in the period from middle Early Triassic to the Middle Triassic and, therefore, in the first 15 Myrs after salt deposition. This can be inferred from thickness and stratigraphic patterns in depocentres (peripheral sinks) between the present-day salt structures. The initiation was localised in extension-related sub-basins and fault zones implying that sub-salt extensional faulting was the main trigger for salt movements. Coinciding with additional phases of basin-wide extensional movement at the beginning of the Late Triassic and during the Jurassic to Early Cretaceous, many of the salt structures in the previously formed sub-basins passed a phase of intense, syn-sedimentary growth. This is indicated by thickening of sedimentary strata in subsidence centres adjacent to salt structures.

The restoration of syn-kinemtic sedimentary structures of the Glückstadt Graben (Chapter 3) revealed original structural geometries of the syn-kinematic peripheral sinks that typically develop in such an extensional sub-basin. Initial sub-salt normal faulting during the Early Triassic caused the formation of a relatively narrow, up to 3500 m deep minibasin in the basin centre bounded by two highly elevated salt structures. Additionally, extension in the cover triggered the development of salt structures and minor, bowl-shaped peripheral sinks above the graben flanks. The subsidence of these sinks lasted until the Middle Keuper time, when additional normal faulting in the sub-salt basement induced rapid diapiric growth of the previously initiated salt structures. Consequently, depocentres in the peripheral sinks moved closer towards the diapirs due to progressive salt expulsion underneath. In the following period from Late Triassic throughout the Cenozoic, the deepest depocentres adjacent to the diapirs sequentially shifted away from the basin centre, whereby additional diapirs and pillows were initiated at the margins of the Glückstadt Graben.

The analogue modelling study (Chapter 4) aimed to contribute insights into the structural evolution of early-stage peripheral sinks in extensional basins and into the temporal and spatial distribution of viscous material flow occurring in such a setting. Due to an initial phase of normal faulting in the base of the viscous layer and a subsequent phase of syn-kinematic sand accumulation, a *"central peripheral sink"* and pillow-like structures next to the basement fault as well as further pillow structures

with additional minor peripheral sinks at large distance from the basement fault developed. During initial basement extension, combined Couette shear flow and Poiseuille channel flow was detected in the regions above the basal faults. Poiseuille flow was directed towards the downthrown hanging wall block and counteracted the Couette flow induced by laterally moving footwall blocks. Due to post-extensional sand accumulation in the peripheral sink above the hanging wall block, Poiseuille flow reversed and the viscous material was squeezed upwards driven by differential loading on top of the sand layer. Material inflation above the footwall blocks close to the normal faults led to uplifts of pillow-like structures ("primary pillows"). During later phases of sand accumulation, additional peripheral sinks developed at the outer side of the pillow structures. Consequently, the primary pillows were inflated from both sides and the viscous material was squeezed into a second generation of pillows ("secondary pillows") further away from the basal normal faults.

The analytical models (Chapter 5) examined the driving forces of salt flow beneath a central hanging wall peripheral sink in order to translate observed flow patterns to natural geological conditions, i.e. to test the dependency of flow patterns on the thickness and the depth-related density of the overburden. The models revealed that in most geological scenarios, a minimum displacement of the basement fault in the range of $700 - 2600$ m is required that salt flow above the normal fault turns from downward to upward flow assuming that the central peripheral sink is always filled up with sediments. The concrete fault displacement at which flow reversal occurs is smaller if the depth-related density of the overburden increases faster, the cover thickness in the central peripheral sink is higher, or the average salt density is smaller.

In summary, the results of these studies help to understand how salt flow patterns and syn-kinematic sedimentary structures in an extensionally induced basin evolve in time. Especially in the early phase of a such basin, when most of the salt structures are established, the interference between pressure-induced Poiseuille flow and shear-induced Couette flow were analysed, and the interplay between early downward flow and subsequent upward flow were comprehended. Overall, these findings can be applied to various types of extensional basins in order to reconstruct the structural evolution of overburden minibasins in relation to the salt flow underneath.

Kurzfassung

In Sedimentbecken mit einer genügend mächtigen salinaren Abfolge kann Salztektonik großen Einfluss auf die strukturgeologische und sedimentäre Beckenentwicklung nehmen. Da Salzgestein über geologische Zeiträume ein viskoses Deformationsverhalten aufweist, kann es entlang eines hydraulischen Druckgradienten fließen. Dadurch entstehen lokale Subsidenzzentren oberhalb von Regionen mit Salzabwanderung und Strukturen mit erhöhter Salzmächtigkeit (z.B. Salzkissen, Salzdiapire) in Regionen von Salzakkumulation. In vielen Sedimentbecken, in denen Salztektonik stattfand (z.B. dem Südlichen Permbecken in Zentraleuropa), haben vorrangig tektonische Extensionsbewegungen den hydraulischen Druckgradienten und damit eine Salzfließbewegung ausgelöst. Folgende Mechanismen können in solchen extensionalen Becken wirken: (1) Differentielle Absenkung der Salinarbasis, z.B. durch Abschiebungen, kann zu einem gravitativ getriebenen Abwärtsfließen des Salzes führen. (2) Syn-tektonische, sedimentäre Auflastunterschiede zwischen den Absenkungszentren und deren Flanken können das Salz von Regionen mit höherer Auflast verdrängen und zu einem aufwärtsgerichteten Salzfluss führen. Um den Einfluss von syn- und posttektonischen Salzbewegungen auf die Deformations- und Sedimentstrukturen im Deckgebirge nachvollziehen zu können, werden häufig analoge Sandkastenexperimente oder analytische und numerische Modelle angewendet. Bisherige Analogexperimente zur Untersuchung von Prozessen der Salztektonik befassten sich zumeist nur mit tektonischen Strukturen im Deckgebirge der Salzschicht, jedoch nur selten mit dem Salzfluss an sich. Es existieren zahlreiche numerische und analytische Modelle, die verschiedene Szenarien des Salzflusses untersuchen, aber nur wenige bezogen tektonische Extension als Auslöser der Salzbewegung ein.

In dieser Dissertation soll ein besseres Verständnis von der Kinematik und Dynamik der Salzfließbewegung erlangt werden, welche durch Auflastunterschiede und Störungsversatz in der Salinarbasis ausgelöst werden. Um die dynamische Wechselwirkung zwischen tektonischen Störungen, synkinematischer Sedimentation und Salzfluss zu untersuchen, wurden folgende Methoden angewendet: (1) In einer Literaturrecherche wurde eine Datenbank aller Salzstrukturen des Südlichen Permbeckens zusammengestellt. Basierend auf den geologischen Daten der Salzstrukturen wurden die Phasen, in denen jede Salzstruktur initialisiert wurde, und die Phasen, in denen jede Salzstruktur ihr schnellstes Wachstum erlebte, in geologischen Karten visualisiert. Des Weiteren wurden für die nachfolgenden Studien die geologischen Randbedingungen ermittelt, unter denen die Initiierung und das folgende Wachstum der Salzstrukturen stattfand. (2) Anhand eines geologischen Profils durch eine bedeutende Grabenstruktur des Südlichen Permbeckens, dem Glückstadt Graben, wurde eine strukturelle 2D-Rekonstruktuion durchgeführt. Mit dieser Rekonstruktion wurde die Strukturentwicklung synkinematischer Depozentren untersucht, die durch Grabenbildung und Salzfluss entstanden sind.

Die Rekonstruktionsmethode umfasste die Dekompaktion und „vertical shear unfolding“ der Deckgebirgssedimente. (3) In einer Studie mit analogen Sandkastenexperimenten sind die Fließmuster in einer viskosen Schicht und die Sedimentstrukturen in deren Deckschicht oberhalb einer basalen Grabenstruktur erforscht worden. Der experimentelle Aufbau bestand aus einer festen Basis, die durch zwei Abschiebungen geteilt wurde, einer viskosen Schicht aus einem Silikonpolymer, welche die Salzgesteinsschicht repräsentierte, und Sandschichten, die das Deckgebirge simulieren sollten und eine höhere Gesamtdichte als die Silikonschicht besaßen. (4) Analytische Berechnungen wurden durchgeführt, um die Richtung und Geschwindigkeit der Salzfließbewegung über einer subsalinaren Störung in Abhängigkeit vom Versatz der Störung und vom Auflastunterschied im Deckgebirge zu ermitteln. Die idealisierten Modelle bestanden wiederum aus einem starren Basement, welches von einer Abschiebung durchzogen war. Darüber befanden sich eine Schicht mit dem linear-viskosen (Newtonischen) Deformationsverhalten von Salzgestein sowie eine Deckschicht, dessen Dichte mit zunehmender Tiefe stieg. In den Modellen wurde das Geschwindigkeitsfeld gemäß des vorherrschenden hydraulischen Gradienten berechnet und verschiedene geologische Parameter variiert, wie z.B. die Mächtigkeit der Salzschicht und des Deckgebirges, das Einfallen der Basementstörung, das Kompaktionsverhaltens des Deckgebirges sowie die Dichte der Salzschicht.

Die Resultate dieser Studien bilden die Grundlage, um ein konzeptionelles Modell des Salzflusses in Extensionsbecken zu entwickeln, angefangen von der zeitlichen Entwicklung der synkinematischen Randsenken und der Salzfließmuster bis hin zu den dominierenden Prozessen, die den Salzfluss antreiben. Die Analyse der Initiierungsalter der Salzstrukturen im Südlichen Permbecken (Kapitel 2) ergab zunächst, dass die Mobilisierung des Permischen Salzes in vielen Beckenteilen bereits in der frühen und mittleren Trias begann und damit in dem Zeitraum von rund 15 Mio. Jahren nach Ende der Salzablagerung. Dies kann anhand von Mächtigkeitsschwankungen in lokalen Depozentren (peripheren Senken) zwischen den heutigen Salzstrukturen abgeleitet werden. Die ersten Salzstrukturen wurden vor allem in Gräben und Störungszonen mobilisiert, was darauf hinweist, dass Dehnungstektonik der Hauptauslöser für den Salzfluss war. Während nachfolgender Dehnungsphasen im Becken in der späten Trias und in der Periode vom Jura bis in die frühe Kreide durchliefen viele der Salzstrukturen in den zuvor gebildeten Gräben eine Phase verstärkten Wachstums. Dies wird anhand von mächtigen Randsenken deutlich, die sich direkt neben den aufsteigenden Salzstrukturen bildeten.

Die Rekonstruktion der synkinematischen Sedimentstrukturen im Glückstadt Graben (Kapitel 3) verdeutlichte die initialen Geometrien der salz-beeinflussten Randsenken, die typischerweise in salzbeeinflussten Gräben entstehen. Während der frühen Trias führten initiale Abschiebungen zunächst zur Bildung eines relativ schmalen, ca. 3500 m tiefen Sedimenttroges im Grabenzentrum (*„zentrale Randsenke“*), der seitlich von zwei schnell wachsenden Salzstrukturen begrenzt wurde. Weiterhin löste die Grabenbildung die Entstehung flacherer Salzstrukturen sowie schüsselförmiger Randsenken auf den Hochlagen des Grabens aus. Eine Phase schnellen Wachstums der Salzstrukturen wurde durch erneute Dehnungsbewegungen in der späten Trias initiiert. In Folge der schnellen Salzabwanderung unterhalb der Randsenken bewegten sich die Depozentren zunehmend näher zu den Rändern der Salzstrukturen. Die folgenden Phasen waren geprägt vom kontinuierlichen diapirischen Aufstieg in verschiedenen Regionen des Grabens. In der Zeitspanne von der späten Trias bis ins Känozoikum

verlagerten sich die Depozentren dabei graduell zu den Beckenrändern. Diese Verlagerung wurde vermutlich durch eine mehr oder weniger kontinuierliche Salzmigration in die wachsenden Diapire bewirkt.

Die analogen Sandkastenexperimente (Kapitel 4) dienten zur Untersuchung der Fließbewegungen in einer viskosen Schicht und der synchron entstehenden synsedimentären Randsenken, die durch Grabenbildung angetrieben werden. Ausgelöst durch eine initiale Dehnungsphase und anschließender synkinematischer Sandakkumulation wurden eine zentrale Randsenke über dem Zentrum sowie kissenähnliche Strukturen an den Rändern des simulierten Grabens erzeugt. Über den vom Graben entfernten Hochlagen entstanden später weitere Kissenstrukturen und flachere Randsenken. Während der Dehnungsphase war in der viskosen Silikonschicht direkt über der Abschiebung eine Überlagerung von Scherströmung (Couette-Strömung) und laminarer Strömung mit einerm parabolischen Geschwindigkeitsprofil (Poiseuille-Strömung) zu beobachten. Die Poiseuille-Strömung war zum Grabenzentrum gerichtet und damit entgegengesetzt zur Scherbewegung der Couette-Strömung. Sobald zusätzliches Granulat in die zentrale Randsenke gefüllt wurde, kehrte sich die Bewegungsrichtung der Poiseuille-Strömung um und das viskose Material wurde, bedingt durch die Auflastunterschiede an der Oberfläche, aufwärts zu den Grabenflanken gepresst. Dort akkumulierte es in kissenähnlichen Strukturen (*„Primärkissen“*). Nach weiteren Phasen der Sandeinfüllung bildeten sich zusätzliche Randsenken an den vom Graben abgewandten Seiten der Kissenstrukturen. Ab diesem Stadium floss das viskose Material von beiden Seiten in die Primärkissen und zusätzlich nach außen in nachfolgende Kissenstrukturen (*„Sekundärkissen“*).

Anhand von analytischen Modellrechnungen (Kapitel 5) wurden die Mechanismen untersucht, die den Salzfluss oberhalb einer subsalinaren Abschiebung antreiben. Es sollte getestet werden, wie sich die in den Analogexperimenten beobachteten Fließmuster in Abhängigkeit von der Kompaktion und der Mächtigkeit des Deckgebirges entwickeln. Die Modelle konnten zeigen, dass es in den meisten geologisch realistischen Szenarien zunächst zu einer Abwärtsfließbewegung des Salzes über einer subsalinaren Abschiebung kommt. Erst ab einem Störungsversatz von 700 – 2600 m sind die Auflastunterschiede bedingt durch die zentrale Randsenke groß genug, um das Salz auf die Hochlage der Abschiebung zu verdrängen (unter der Annahme, dass die zentrale Randsenke stets mit Sediment gefüllt ist). Der erforderliche Versatzbetrag, ab dem das Aufwärtsfließen einsetzt, ist geringer, wenn die kompaktionsabhängige Dichte des Deckgebirges höher, die Mächtigkeit in der zentralen Randsenke höher oder die durchschnittliche Dichte des Salzes niedriger ist.

Die Resultate dieser Studien geben ein besseres Prozessverständnis über die Salzfließmuster und die Entwicklung synkinematischer Randsenken in extensionalen Becken. Speziell in der Frühphase solcher Becken, in der die meisten Salzstrukturen angelegt werden, konnte die Überlagerung von Couette- und Poiseuille-Strömung sowie die Wechselwirkung zwischen abwärts- und aufwärtsgerichtetem Salzfluss nachvollzogen werden. Diese Ergebnisse können auf verschiedenste Extensionsbecken angewendet werden, um die strukturelle Entwicklung von Randsenken in Abhängigkeit vom darunter stattfindenden Salzfluss zu rekonstruieren.

Contents

List of Manuscripts

Manuscript #1/ Chapter 3:
Warsitzka, M., Kley, J., Jähne-Klingberg, F., and Kukowski, N., 2017. Dynamics of prolonged salt movement in the Glückstadt Graben (NW Germany) driven by tectonic and sedimentary processes. *Int J Earth Sci (Geol Rundsch)*, 106: 131-151, doi:10.1007/s00531-016-1306-3.
http://link.springer.com/article/10.1007/s00531-016-1306-3

Manuscript #2/ Chapter 4:
Warsitzka, M., Kley, J., and Kukowski, N., 2015. Analogue experiments of salt flow and pillow growth due to basement faulting and differential loading, *Solid Earth*, 6: 9-31, doi:10.5194/se-6-9-2015.
http://www.solid-earth.net/6/9/2015/

Manuscript #3/ Chapter 5:
Warsitzka, M., Kukowski, N., Kley, J. Salt flow direction and velocity during sub-salt normal faulting and syn-kinematic sedimentation – implications from analytical calculations. submitted to *Geophysical Journal International*, Oxford University Press. Date of submission: 11.02.2017.

List of Figures

List of Tables

List of Abbreviations

BGFZ	Braunschweig-Gifhorn fault zone
BFB	Broad Fourteens Basin
C	Cenozoic
CCD	Charge-coupled device
CBH	Cleaver Bank High
CEBS	Central European Basin System
CG	Central Graben
CNB	Central Netherlands Basin
CPS	Central peripheral sink
Cr	Cretaceous
DC	Dislocation creep
DFZ	Dowsing fault zone
EAH	Eichsfeld-Altmark High
EH	Elevation head
EHG	Elevation-head gradient
EHMB	East Holstein-Mecklenburg Block
EHT	East Holstein Trough
ET	Ems Trough
Fm.	Formation
FPS	Footwall peripheral sink
GG	Glückstadt Graben
GroH	Groningen High
HG	Horn Graben
HHG	Hydraulic-head gradient
HPS	Hanging wall peripheral sink
LJ	Lower Jurassic
LP	Lower Permian
LSB	Lower Saxony Basin
LT	Lower Triassic
LTG	Leinetal Graben
MPT	Mid-Polish Trough
MJ	Middle Jurassic
MT	Middle Triassic
NDFZ	North Dogger fault zone
NEGB	North-East German Basin
NeS	Netherland swell
PDI	Point of density inversion
PDMS	Polydimethylsiloxane
PH	Pressure head
PHG	Pressure-head gradient
PIV	Particle Image Velocimetry
POM	Point of maximum
POR	Point of reversal
PSP	Primary peripheral sink
PVC	Polyvinylchlorid
RBT	Rheinsberg Trough
RFH	Ringkøbing-Fyn High
SGH	Schillgrund High
SHB	Subhercynian Basin
SiPB	Silver Pit Basin
SoPT	Sole Pit Trough
SPB	Southern Permian Basin
SPC	Solution - precipitation creep
SPS	Secondary peripheral sink
ST	Solling Trough
SWH	Szczecin-Wolsztyn High
TB	Terschelling Basin
TS	Thuringian Syncline
UJ	Upper Jurassic
UP	Upper Permian
UT	Upper Triassic
WT	Weser Trough
WHT	West Holstein Trough
WNB	West Netherlands Basin
WSB	West Schleswig Block

List of Symbols

Symbol	Name	Dimension
α	Dip of the cover monocline (Chapter 5)	[°]
β	Dip of the basement fault (Chapter 5)	[°]
c	Porosity depth coefficient/ Compaction coefficient	[km^{-1}]
C	Cohesion	[Pa]
d	Displacement or vertical offset	[m]
e	Displacement rate at the basement fault (Chapter 4)	[m s^{-1}]
ε	strain	-
$\dot{\varepsilon}$	strain rate	[s^{-1}]
η	Viscosity	[Pa s]
g	Gravitational acceleration	[m s^{-2}]
h_b	Thickness of the brittle cover layer (Chapter 4)	[m]
h_B	Thickness of the basin filling (Chapter 5)	[m]
h_{Bcoeff}	Basin fill coefficient (Chapter 5)	-
h_C	Thickness of cover layer (Chapter 5)	[m]
h_d	Thickness of ductile layer (salt) (Chapter 4)	[m]
h_S	Thickness of salt layer (Chapter 5)	[m]
l^*	Geometric scaling factor	-
μ	Coefficient of internal friction	-
φ	Angle of internal friction	[°]
ϕ	Porosity	-
ϕ_0	Initial porosity	-
ρ_b	Density of the brittle cover layer (Chapter 4)	[kg m^{-3}]
ρ_C	Density of the cover (Chapter 5)	[kg m^{-3}]
ρ_{Cavg}	Average density of the cover	[kg m^{-3}]
$\rho_{Cavgeff}$	Average effective density of the cover	[kg m^{-3}]
ρ_{Cmax}	Maximum density of the cover	[kg m^{-3}]
ρ_d	Density of ductile layer (salt)	[kg m^{-3}]
ρ_G	Grain density	[kg m^{-3}]
ρ_W	Water density	[kg m^{-3}]
S	Solidity fraction	-
S_b	Strength of brittle layer (cover)	[Pa]
S_d	Strength of ductile layer (salt)	[Pa]
S_{sa}	Subsidence driven by salt expulsion	[m]
S_{tec}	Tectonic subsidence	[m]
S_{tot}	Total subsidence	[m]
t	Time	[s]
τ	Shear stress	[Pa]
u	Extension rate, Flow velocity	[m s^{-1}]
w_{coeff}	Width coefficient (Chapter 5)	-
z	Depth	[m]

1. Introduction

1.1 General remarks and aims

Tectonic processes related to the movement of mechanically weak salt (termed *"salt tectonics"*) strongly affect the tectono-stratigraphic evolution of salt-bearing sedimentary basins. The basic requirement for salt tectonic to occur is a sufficiently thick layer of ductile evaporites (*"salt layer"*; larger than ∼300 m) (Ten Veen et al., 2012). Deformation in the underlying rocks (*"sub-salt basement"*) as well as sedimentary processes or tectonic deformation of overlying sedimentary strata (*"supra-salt cover"* or *"salt overburden"*) can trigger flowage in the salt layer (Hudec and Jackson, 2007), which then causes the formation of local topographic uplifts (*"salt structures"*, e.g. salt pillows, salt diapirs) and sinks (*"minibasin"* or *"peripheral sinks"*). To unravel the development of sedimentary and tectonic structures in supra-salt cover (e.g. Maystrenko et al., 2005a), to reconstruct the local effect of salt structures on broad-scale tectonic strain patterns (e.g. Lohr et al., 2007), or to derive present-day geomechanical information of the stress field in and around salt bodies (e.g. Nikolinakou et al., 2014), intra-salt deformation processes have to be fundamentally understood.

Salt (as used in "salt tectonics") is a general term describing evaporitic rocks mainly consisting of halite with varying amounts of intercalated anhydrite, gypsum, carbonates, bittern salt minerals or clastic clay. The strong influence of salt on various geological processes results from the exceptional physical properties of halite, which are:

- A visco-elastic rheology resulting in the ability to flow in response to gravitational body forces and internal pressure gradients and to decouple strain between sub-salt basement and the supra-salt overburden (Waltham, 1997; Hudec and Jackson, 2007). Owing to this property, the basin structure can be significantly modified by post-depositional salt flow and detached deformation (e.g. Maystrenko et al., 2013), and it also causes viscous drag forces risking, for instance, well bore stability during drilling campaigns (Weijermars et al., 2014).
- A depth-independent density (∼2040 – 2160 kg m^{-3}), which is lower than that of most moderately to fully compacted clastic or carbonatic sediments (e.g. Urai et al., 2008; Hudec et al., 2009). Under certain geological circumstances, this property causes salt to rise buoyantly next to minibasins filled with denser sediments (Hudec and Jackson, 2007).
- A low permeability of ∼10^{-21} m^2 resulting in a barrier function for fluid transport (e.g. Urai et al., 2008). Because of this property, salt creates traps for hydrocarbons (e.g. McBride et al., 1998; Peel, 2014) and is suggested to be a suitable host rocks for storage of radioactive waste (e.g. Hunsche and Hampel, 1999) or gas resources (e.g. Zander-Schiebenhöfer et al., 2015).
- A high thermal conductivity of 3.5 – 4.8 W m^{-1} K^{-1} (Bayer et al., 1997; Norden and Förster, 2006)

influencing the regional geothermal field (e.g. Scheck-Wenderoth et al., 2014) and, consequently, the maturation history of hydrocarbons in host rocks close to salt formations (Magri et al., 2008).

Investigations on the dynamics driving salt deformation and salt structure growth generally follow two different approaches (Van Gent et al., 2011): (1) the external approach, usually related to hydrocarbon exploration, focuses on supra- or sub-salt structures and takes salt as a homogeneous, structureless body without caring about intra-salt strain patterns; (2) the internal approach, mostly related to geomechanical issues during salt mining or storage sites, studies detailed intra-salt structures including the complex lithological and rheological stratification of evaporite successions and the strain patterns provoked by internal and external stresses. Sub- and supra-salt rocks usually deform by brittle-plastic behaviour, whereas deformation structures are well preserved in outcrops and well imaged in seismic data. Thus, sequential deformation phases can be reconstructed by backward restoration techniques (Roberts et al., 1990; Mohr et al., 2005; Scheck et al., 2003a; Maystrenko et al., 2005a; Rowan and Ratliff, 2012; Vackiner et al., 2013), or simulated by forward experimental modelling (e.g. Koyi et al., 1993; Nalpas and Brun, 1993; Jackson et al., 1994; Vendeville et al., 1995; Withjack and Callaway, 2000; Dooley et al., 2005). In contrary, internal salt deformation is characterised by mirco- or macro-scale ductile deformation usually leading to enigmatic internal deformation structures in salt bodies (folds, boudins, competent "stringers"). These structures are commonly difficult to reconstruct (e.g. Van Gent et al., 2011; Strozyk et al., 2012; Dooley et al., 2015). Hence, forward modelling techniques (analogue, analytical or numerical modelling) are often the only methods to understand the evolution of internal salt deformation (e.g. Chemia et al., 2008; Peel, 2014).

In recent years, a growing number of modelling studies have addressed the interplay between external and internal structural dynamics of salt deformation. Many geological processes, however, have not yet been modelled, e.g. salt flow in response to extensionally induced peripheral sinks. In numerous salt-bearing sedimentary basins worldwide, the primary trigger for salt tectonics is regional extension resulting in faulting and displacement of the base and the overburden of the salt layer (Jackson and Vendeville, 1994). Analogue modelling studies simulating salt tectonics triggered by sub-salt faulting mostly investigated overburden deformation structures (e.g. Jackson and Vendeville, 1994; Vendeville et al., 1995; Ge et al., 1997; Withjack and Callaway, 2000; Dooley et al., 2003; Soto et al., 2007; Ferrer et al., 2014), but only a few were concerned with strain patterns within the salt layer itself (Richard, 1991; Nalpas and Brun, 1993; Koyi et al., 1993; Burliga et al., 2012). Numerical or analytical modelling of salt tectonics often address strain patterns of salt flow and salt-related minibasins, e.g. driven by contraction (Ings and Beaumont, 2010), uneven sedimentation (e.g. Massimi et al., 2007; Allen and Beaumont, 2012; Goteti et al., 2012; Peel, 2014) or downbuilding (e.g. Chemia et al., 2008; Burchardt et al., 2011; Fuchs et al., 2014). However, studies concerning salt flow triggered by extensional deformation of the cover or the basement are rare (Daudré and Cloetingh, 1994; Schultz-Ela and Jackson, 1996; Waltham, 1997; Schultz-Ela and Walsh, 2002; Perić and Crook, 2004).

The lack of investigations of salt flow in an extensional tectonic setting is the primary motivation for this thesis. The principal aim is to comprehend the overall effect of sub-salt normal faulting

and syn-kinematic sediment accumulation on strain patterns within salt layers. Therefore, geological restoration, analogue sandbox experiments and analytical computations are applied to investigate following subjects:

1. the temporal and spatial evolution of salt flow and supra-salt, syn-kinematic overburden structures affected by basement faulting,
2. the flow patterns in a viscous layer affected by basement extension and syn-kinematic sedimentation,
3. the dynamics driving salt flow in extensional basins, and
4. the dependence of salt flow kinematics and dynamics on external processes and boundary conditions, e.g. sedimentary loading, cover thicknesses, extension rate etc.

Before guiding through the general thesis outline, fundamental theories of salt rheology and salt flow dynamics are explained in the following sections. This should provide an understanding of methods and assumptions applied in the studies presented in this thesis.

1.2 Fundamental principles of salt tectonics

A salt layer is composed of multiple evaporitic successions of different evaporite minerals and minor clastic sediments. In basins affected by salt tectonics, e.g. the North German Basin (central Southern Permian Basin) or the Gulf of Mexico Basin, the volumetrically most relevant component is polycrystalline halite (70 – 90 %), also termed *rock salt* (NaCl) (Hunsche, 1978; Hudec et al., 2009). Thus, the macro scale rheology of an impure salt layer is commonly characterised by the rheology and deformation behaviour of rock salt.

1.2.1 Creep processes in rock salt

Microstructural processes in rock salt are manifold and depend on temperature, deviatoric stresses, confining pressure, grain size, impurities, second phase content and the presence of water at grain boundaries (Urai et al., 2008). At low effective confining pressures (a few MPa) and high differential stresses ($>15-20$ MPa), rock salt is prone to fail by cataclastic deformation due to inter- and intragranular microcracking, grain rotation and intergranular slip (Urai et al., 2008). At higher confining pressures ($>\sim$10 MPa), rock salt deforms by crystal-plastic creep and recrystallisation processes, more precisely by a combination of dislocation creep (DC) and solution-precipitation creep (SPC) (e.g. van Keken et al., 1993; Schoenherr et al., 2007). The relative dominance of each creep process can be highly variable (Urai et al., 2008). Laboratory experiments on natural and synthetic rock salt reveal that DC is the dominant creep process at strain rates below 10^{-6} s^{-1}, confining pressures below 10 MPa, and differential stresses larger than 10 MPa (Carter et al., 1993; Hunsche and Hampel, 1999; Pennock et al., 2005). In natural evaporite sequences, water containing minerals (e.g. gypsum) or sediments (e.g. clays) are intercalated and small amounts of water are enclosed in halite minerals (10 – 20 ppm) (Urai et al., 2008). Laboratory examinations of slightly wet halite (average grain size of D = 10 mm) suggest that SPC dominates in rock salt with water contents of higher than 0.05 wt%,

when strain rates are lower than 10^{-12} s^{-1}, confining pressures larger than 10 – 20 MPa and differential stresses ranging between 2 and 10 MPa (Urai et al., 1986; Spiers et al., 1990). The strain rate – stress dependence during steady-state creep is suggested to be linear (power-law exponent n = 1) and grain size sensitive for SPC and exponential (power-law exponent n = 3 – 6) and grain size insensitive for DC (Spiers et al., 1990; Carter et al., 1993; Schoenherr et al., 2007; Urai et al., 2008).

Natural deformation of rock salt takes place at much lower strain rates and for longer periods of time than under laboratory conditions. Hence, experimentally-derived data has to be extrapolated to natural conditions. Nevertheless, microstructural studies confirmed that DC processes accompanied by water-assisted grain boundary migration due to SPC operate in naturally deformed rock salt (Urai et al., 2008). Thereby, DC is suggested to be the best representation for deformation behaviour of salt in the early stage of deformation (Urai et al., 2008). An increasing importance of fluid-assisted SPC arises during an advanced stage of salt deformation because of the enhanced formation of sub-grains including more fluid inclusion (van Keken et al., 1993; Urai et al., 2008; Li and Urai, 2016).

1.2.2 Viscosity and density of salt

Related to the prevailing creep mechanism, the viscosity of rock salt depends on grain size, differential stress and temperature (van Keken et al., 1993), but also on the amount of impurities or intercalations (e.g. carbonates, anhydrites or bittern salts) in a salt layer (Wagner and Jackson, 2011). Estimates based on laboratory experiments infer that the viscosity of rock salt ranges from 10^{12} to 10^{20} Pa s (van Keken et al., 1993; Ter Heege et al., 2005; Mukherjee et al., 2010). The combination of Newtonian SPC and power-law DC during steady-state creep leads to a power-law relationship between shear stress τ and strain rate $\dot{\varepsilon}$ expressed in terms of the effective viscosity η_{eff} (e.g. Urai et al., 1986; Carter et al., 1993; van Keken et al., 1993; Ter Heege et al., 2005):

$$\eta_{eff} = \frac{\tau^n}{2\dot{\varepsilon}} \tag{1.1}$$

The power-law exponent n of natural rock salt is >1 (Weijermars and Jackson, 2014) meaning that viscosity decreases with increasing strain rate.

The bulk viscosity of large salt masses can also be obtained by field observations e.g. the shape and surface slope of emergent salt diapir crests and glaciers (e.g. Mukherjee et al., 2010, and reference therein), numerical modelling of internal salt deformation (Li et al., 2012a), well hole closure velocities or the amount of uplift rates of diapirs (Weinberger et al., 2006). Viscosity estimates based on these methods range between 10^{17} Pa s and 10^{21} Pa s.

Viscosities of other typical evaporite minerals are, for instance, in the order of 10^9 Pas for carnallite or 10^{19} Pas for anhydrite (Wagner and Jackson, 2011). Besides viscous rock salt and bitter salts, an evaporitic sequence may also contain more competent intercalations, e.g. siliciclastics, carbonates and anhydrites, or igneous intrusions (e.g. Jackson et al., 1990; Van Gent et al., 2011). The strength and the position of these low-viscous or competent interlayers within an evaporite succession affect the large-scale mean viscosity of the salt layer (Wagner and Jackson, 2011; Weijermars and Jackson,

2014).

The density of pure rock salt varies between 2040 and 2160 $\mathrm{kg\,m^{-3}}$ (e.g. Urai et al., 2008; Hudec et al., 2009). Salt is nearly incompressible and only slightly compacts with depth by roughly 3 % from the surface to a depth of 5000 m. This compaction is usually compensated by the volumetric thermal expansion of the halite mineral with increasing temperature ($1.3 \times 10^{-4}\,\mathrm{K^{-1}}$ for a geothermal gradient of $20\,\mathrm{K\,km^{-1}}$) (Walker et al., 2004).

The entire salt layer usually has a higher bulk density than that of pure halite. On the basis of the average composition of an evaporitic succession (Bornemann, 1979), salt density is commonly suggested to be $2200\,\mathrm{kg\,m^{-3}}$, which is the average for e.g. 96 % halite and 4 % anhydrite (Hudec et al., 2009). The density of compacted siliciclastic or carbonate sediments typically overlying a salt layer exceeds the salt density at depths between 600 and 1500 m (e.g. Dickinson, 1953; Jackson and Talbot, 1986; Hudec et al., 2009). The resulting density inversion can cause buoyant upwelling of salt from beneath the denser overburden (Jackson, 1995).

1.2.3 Dynamics of salt flow

Because salt behaves like a fluid over geological time scales, the concept of hydraulic gradient derived from fluid dynamics can be used to characterise the main driving forces of salt flow (Kehle, 1988; Waltham, 1997; Hudec and Jackson, 2007). This concept involves effects of gravitational loading termed pressure head and elevation head. The pressure head is created by the weight of the overburden and acts at the upper boundary of a fluid layer. Elevation head is produced by gravitational body forces of the fluid itself. Spatial differences of both heads define the pressure gradient and the elevation gradient (Kehle, 1988; Hudec and Jackson, 2007).

A pressure gradient is caused by lateral differences of the thickness or the density of the overburden (Fig. 1.1A), which can be caused by sedimentary or tectonic differential loading. Sedimentary differential loading include: (1) uneven sedimentation on a planar salt layer top, e.g. due to deltaic wedges (e.g. Ge et al., 1997; Gemmer et al., 2004), coral reefs (Jackson and Talbot, 1986), clastic fans (Goteti et al., 2012), or ice sheets (Sirocko et al., 2008); (2) sediment accumulation into depocentres formed either by differential basement subsidence (Geil, 1991; Remmelts, 1995), folding of the overburden (Coward and Stewart, 1995; Ings and Beaumont, 2010), salt expulsion into neighbouring regions (Warsitzka et al., 2013; Peel, 2014) or salt dissolution (Cartwright et al., 2001); (3) erosion of supra-salt sediments e.g. due to river incision (Schultz-Ela and Walsh, 2002); or (4) lateral facies changes (Waltham, 1997), e.g. sub-marine channel sandstones and inter-channel mudstones. Tectonic differential loading is provoked by: (1) local extension and thinning of the supra-salt cover ("unloading") (e.g. Vendeville and Jackson, 1992b; Penge et al., 1993; Jackson and Vendeville, 1994; Mohr et al., 2005), or (2) thrusting of the cover (e.g. Waltham, 1997; Costa and Vendeville, 2002).

An elevation gradient occurs as soon as the top of a salt layer is vertically displaced. This can be induced by: (1) tilting of the salt layer e.g. due to thermal subsidence or flexure (Fig. 1.1B) (Dooley et al., 2007; Brun and Fort, 2011) or (2) differential vertical displacement of the salt base e.g. due to normal (Fig. 1.1B) or thrust faulting (Koyi et al., 1993; Coward and Stewart, 1995; Ge et al., 1997).

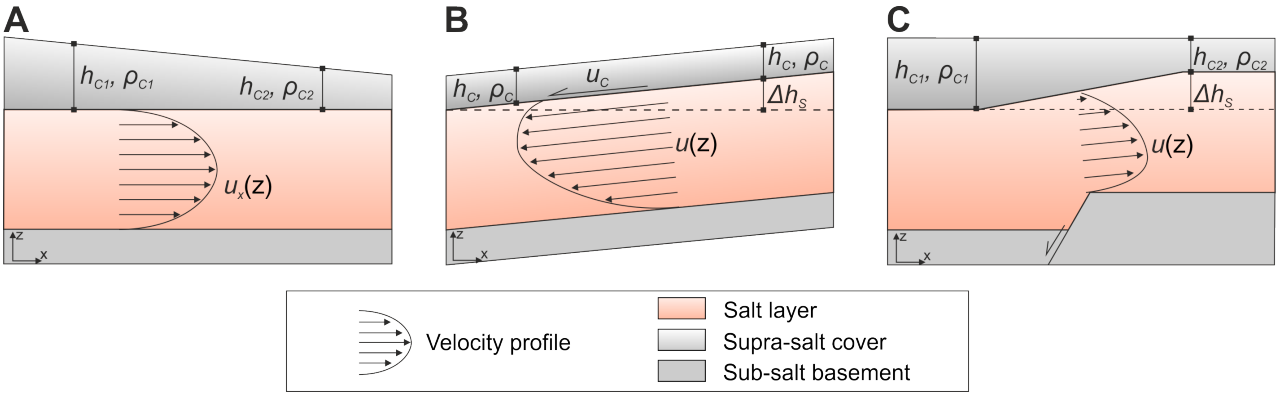

Figure 1.1: Sketches illustrating the effect of **A** pressure gradient, **B** elevation gradient and **C** the combined hydraulic gradient on flow patterns in a salt layer (modified from Hudec and Jackson, 2007). h_C – thickness of the cover, ρ_C – density of the cover, $\Delta\ h_S$ – height difference of the salt layer, u – flow velocity, u_C – velocity of the cover, u_x – horizontal flow velocity.

Besides salt flow driven by a hydraulic gradient, shear flow can be established by lateral movement at the sub- or supra-salt boundaries (Waltham, 1997). Particularly during rapid tectonic stretching or shortening and during down-slope gliding of the overburden (Fig. 1.1B), shear flow dominates intra-salt strain patterns (Gemmer et al., 2004; Weijermars et al., 2014).

Resisting forces opposing salt flow are: (1) the strength of mostly brittlely deforming overburden sediments and (2) the friction at the boundaries of a salt layer (Hudec and Jackson, 2007). The overburden strength is due to a combination of the elastic flexural rigidity, the plastic yield strength, the frictional resistance and the cohesion (Schultz-Ela et al., 1993). The strength increases when the overburden becomes thicker, because confining pressures and consolidation of sediments increase. The boundary friction within a salt layer is more significant, when the salt layer is thinner. Both factors, a thick overburden layer or a thin salt layer can prevent or hinder salt flow (Hudec and Jackson, 2007). Tectonic extension can effectively reduce the overburden strength by thinning and fracturing and, therefore, trigger salt flow, albeit a thick overburden (Jackson and Vendeville, 1994).

1.2.4 Flow patterns in salt layers

In viscous material, two types of flow occur depending on stresses at the external boundaries and internal pressure gradients: (1) *Poiseuille flow* describes a channel flow parallel to horizontally stable boundaries (Fig. 1.2A) (White, 2011; Turcotte and Schubert, 2014). The vertical velocity profile ideally has a parabolic shape with a maximum velocity in the middle of the channel and zero velocity at the boundaries. Regarding salt tectonics, Poiseuille flow typically occurs when differential loading on top of the salt layer induces a pressure gradient within the salt (e.g. Davison et al., 1996; Gemmer et al., 2004). (2) *Couette flow* is characterised by a linear velocity gradient across the salt layer caused by shearing at the boundaries moving parallel to each other (Fig. 1.2B) (Turcotte and Schubert, 2014). During salt deformation, both flow types can superimpose in various ways (Davison et al., 1996; Weijermars and Jackson, 2014). In cases where a sedimentary wedge becomes unstable and fails, gravitational collapse causes a horizontal movement of the wedge (Fig. 1.2C) (Gemmer et al., 2004). Hence, Poiseuille flow and Couette flow act in the same direction. Such behaviour typically

occurs in passive margin basins, e.g. the Gulf of Mexico basin (Peel et al., 1995) or the West African continental margin (Fort et al., 2004), where basement inclination and sediment progradation are both seaward directed. In cases of differential subsidence of the sub-salt basement but a more or less even sedimentary surface, Poiseuille and Couette flow can act oppositely (Fig. 1.2D), because downward directed stresses induced by differential basement subsidence are opposed by the pressure gradient due to sediment accumulation in the basin centre. This scenario is rather characteristic of intra-continental and extensional basins, e.g. the North Sea Central Graben (Penge et al., 1999) or the Mid-Polish Trough (Burliga et al., 2012).

As mentioned above, an evaporitic sequence contains various interlayers with different competences. The flow regime in such a multi-layered sequence is suggested to be characterised by multiple flow channels in less viscous members (halite, bitter salts, etc.) (Fig. 1.2E) (e.g. Talbot et al., 1982; Davison et al., 1996; Weijermars et al., 2014). Competent interlayers remain rather undeformed at the beginning of deformation. During advanced stages of deformation, competent layers are folded or dismembered into boudins (e.g. Bornemann, 1979; Talbot and Jackson, 1987; Clark et al., 1998; Zulauf et al., 2009; Van Gent et al., 2011) and then dragged by less viscous evaporites (Wagner and Jackson, 2011).

Assuming a non-Newtonian power-law rheology for salt, the effective viscosity decreases with increasing shear rate. Consequently, the Poiseuille flow velocity profile of Non-Newtonian fluids becomes damped in the centre of the flow channel (Fig. 1.2F), whereas the shear zones at the boundaries of the fluid are narrower than for Newtonian fluids (Hudec and Jackson, 2007).

1.2.5 Implications for modelling salt tectonics

The internal variability of the rheology and composition in a salt layer is responsible for highly varying strain rates occurring in salt tectonics ($10^{-9} - 10^{-16}\,s^{-1}$) and complex internal structures as observed in salt mines, outcrops or seismic data (e.g. Bornemann, 1979; Richter-Bernburg, 1980; Talbot and Jackson, 1987; Bornemann, 1991; Behlau and Mingerzahn, 2001; Schléder et al., 2008; Van Gent et al., 2011; Strozyk et al., 2012). Nevertheless, for the purpose of analogue or numerical modelling, it is convenient to assume that the properties of multi-layered evaporite sequences can be averaged for a mean "salt layer" characterised by a mean density of $2200\,kg\,m^{-3}$, a mean viscosity of 10^{18} Pa s in case of Newtonian behaviour or a stress-dependent effective viscosity in case of Power-law behaviour (e.g. Schultz-Ela et al., 1993; Gemmer et al., 2004; Chemia et al., 2008; Burchardt et al., 2011; Li and Urai, 2016). Simulations of detailed structures and deformation processes within salt layers, however, demand that rheologically stratified evaporite sequences have to be considered as simulated e.g. by Koyi (2001); Chemia et al. (2008); Wagner and Jackson (2011); Li et al. (2012b); Fuchs et al. (2014); Weijermars and Jackson (2014) and Dooley et al. (2015). In analogue sandbox experiments (e.g. Chapter 4), salt is usually modelled by silicone elastomer (polymethylsiloxane polymer PDMS), which deforms in a nearly Newtonian viscous behaviour at low strain rates ($<10^{-2}\,s^{-1}$) and power-law behaviour at higher strain rates (Rudolf et al., 2016). This might be a similar shear thinning behaviour as shown by natural rock salt.

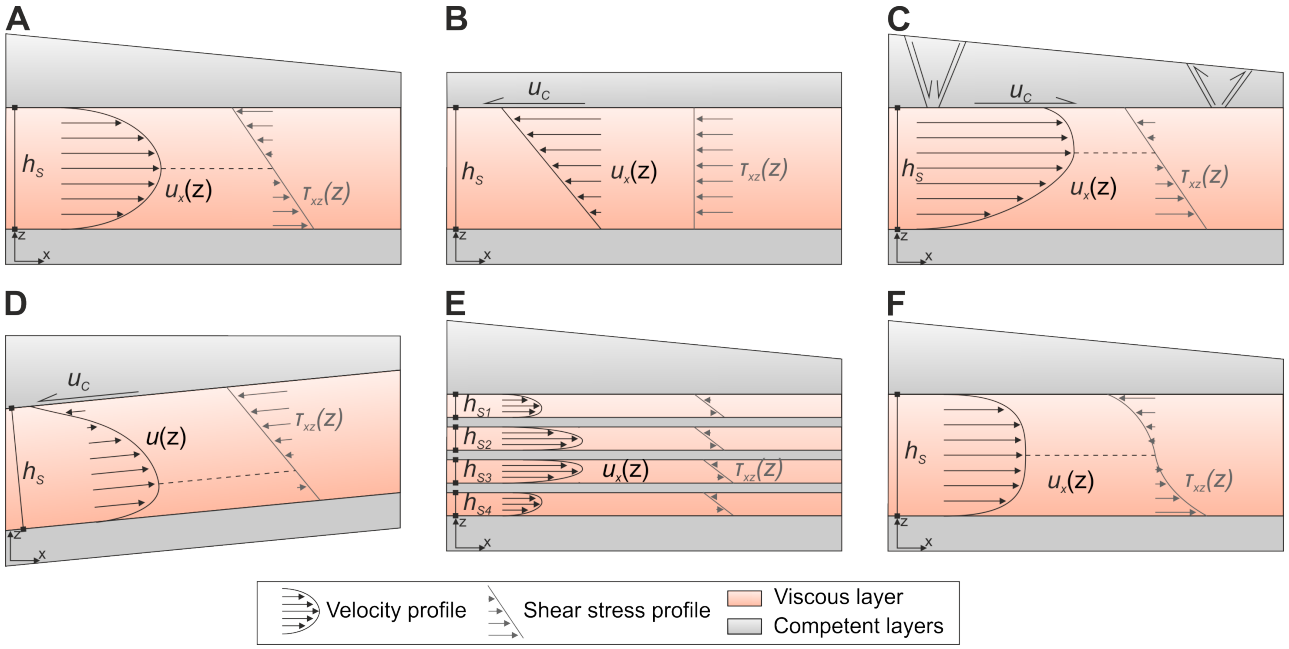

Figure 1.2: Salt flow patterns for simplified geological settings. **A** Poiseuille flow in Newtonian fluids is characterised by a parabolic shape of the velocity field and a linear shear stress profile. Poiseuille flow is caused by a homogeneous pressure gradient in the fluid. **B** Couette flow results from shearing at the fluid boundary causing a linear velocity profile and a homogeneous shear stress profile in Newtonian fluids. **C** and **D** display superposition of Poiseuille and Couette flow patterns acting either in the same direction or oppositely. **E** demonstrates the flow pattern in case the fluid layer (evaporitic succession) is interbedded by competent rocks (e.g. carbonates, anhydrites). Flow is restricted to less viscous layers, whereas competent layers remain stable or become fractured or folded (modified from Weijermars et al. (2014)). **F** The Poiseuille flow for a Non-Newtonian (power-law) fluid is characterised by damped velocities in the centre and increased shearing at the boundaries of the fluid layer. h_C – thickness of the cover, h_S – thickness of the salt layer, ρ_C – density of the cover, τ_{xy} – shear stress, u – flow velocity, u_C – velocity of the cover, u_x – horizontal flow velocity.

This thesis deals with large-scale processes during the initiation of salt movement. To understand the first-order dynamics, e.g. the direction of salt flow driven by gravitational forces (Chapter 4, Chapter 5), the rheology of the salt layer should be described as simple as possible. Hence, the conventional simplification assuming a homogeneously viscous and dense salt layer with Newtonian viscosity enclosed between rigid or brittlely deforming basement and cover layer is appropriate.

1.3 Thesis outline

The following outline of the studies included in this thesis explains their link to the objectives mentioned above, provides brief summaries of scientific findings and acknowledges researchers and institutions that contributed to the conducted research.

After this introductory chapter, **Chapter 2** compiles results of existing literature to create an overview of salt structures of the Southern Permian Basin (central Europe) and periods of geological history when they were initiated and grew fastest. It is discussed, in which parts of the basin, salt structures were triggered first as well as which processes and geological conditions can be expected during salt structure initiation in extensional basins. Based on this literature survey, geological boundary conditions and parameters used for the following modelling studies have been derived.

The literature review and data analysis outlined in this chapter was mostly conducted at the Helmholtz Centre Potsdam – GFZ German Research Centre for Geosciences, at the Friedrich Schiller University Jena, and at the Federal Institute for Geosciences and Natural Resources (BGR) Hannover. The analysis benefited from discussions with researchers from the Federal Institute for Geosciences and Natural Resources (BGR) Hannover and co-authors of the other chapters of this thesis. The outcomes of Chapter 2 are presently prepared for publication in an international scientific journal.

Chapter 3 (Manuscript #1) deals with the restoration of supra-salt sedimentary structures in the Glückstadt Graben (central Southern Permian Basin) using a key 2D geological cross section. The post-salt (post-Permian) strata are sequentially decompacted and restored. This procedure provides the geometrical evolution of syn-kinematic peripheral sinks affected by graben formation and salt movement, temporal changes of the subsidence patterns in the peripheral sinks and estimations of growth rates of the salt structures.

The research for geological restorations presented in this chapter was conducted at the Helmholtz Centre Potsdam – GFZ German Research Centre for Geosciences, the University of Texas at Austin (USA) and the Friedrich Schiller University Jena. This study profited from contributions by the co-authors and discussions with resident researchers of the mentioned institutions. This chapter is published by Springer in *International Journal of Earth Sciences (Geologische Rundschau)*:

> Warsitzka, M., Kley, J., Jähne-Klingberg, F., and Kukowski, N., 2017. Dynamics of prolonged salt movement in the Glückstadt Graben (NW Germany) driven by tectonic and sedimentary processes. *Int J Earth Sci (Geol Rundsch)*, 106: 131–151, doi:10.1007/s00531-016-1306-3.

Chapter 4 (Manuscript #2) addresses flow patterns in a ductile layer deformed by an underlying normal fault and affected by syn-kinematic sedimentation on the surface. In order to examine the kinematics of these flow patterns, analogue modelling using scaled physical sandbox experiments has been applied. The experiments consist of viscous silicone elastomer to simulate the salt layer and a dry granular mixture to simulate the brittle cover sediments. This study revealed crucial insights into the evolution of flow in the viscous material and syn-kinematic depositional structures in the brittle cover layers. Furthermore, the variability of flow patterns and overburden structures is demonstrated for various thicknesses of the cover and the viscous layer, and for variable displacement rates at the basement normal faults.

Laboratory work and data analyses of the analogue sandbox experiments were undertaken at the Helmholtz Centre Potsdam – GFZ German Research Centre for Geosciences with support by resident researcher and technicians. Furthermore, this study benefited from contributions by the co-authors. This chapter is published by Copernicus Publications on behalf of the European Geosciences Union (EGU) in *Solid Earth*:

> Warsitzka, M., Kley, J., and Kukowski, N., 2015. Analogue experiments of salt flow and pillow growth due to basement faulting and differential loading, *Solid Earth*, 6: 9–31, doi:10.5194/se-6-9-2015.

It comprises separate appendices (**Appendix A, B**), which are not provided at the end of this thesis. Additional experimental data (photos, cross sections, tables) of the experiments can be found in the digital **Appendix C.2**.

Chapter 5 (Manuscript #3) focuses on dynamics of salt flow above a sub-salt normal fault. Analytical computations were carried out to calculate the depth-dependent density of the supra-salt overburden, the resulting hydraulic gradient and the steady-state velocity field in a homogeneous salt layer. By varying geometrical and lithological parameters in the model set-up, the relative dominance between pressure gradient and elevation gradient on driving salt flow was examined.

The scripting for the analytical computations and the data analyses were mainly conducted at the Friedrich Schiller University Jena with contributions by the co-authors and resident researchers. This chapter has been accepted for publication in Geophysical Journal International published by Oxford University Press on behalf of the Royal Astronomical Society:

> Warsitzka, M., Kukowski, N., Kley, J. Salt flow direction and velocity during sub-salt normal faulting and syn-kinematic sedimentation – implications from analytical calculations. Submitted to *Geophysical Journal International*, Oxford University Press. Date of submission: 11.02.2017.

Chapter 6 summarizes the major findings of the entire research, discusses and compares the methods applied in this thesis, exemplarily describes scenarios of salt flow evolution in various extensional basins, and gives a brief outlook for potential future investigations.

Appendix C.1 provides additional methodical descriptions for Chapter 2. **Appendix C.2** provides a content list of files included in the digital appendix. The digital supplementary material can be found on the attached CD.

The work undertaken for this thesis received financial support by the German Research Foundation (DFG, KL 495/14-1), the Federal Ministry of Education and Research (BMBF) (grant Nr. 03IS2091A INFLUINS) and the German Academic Exchange Service (DAAD).

2. Age analysis of salt structures in the Southern Permian Basin

Authors
Michael Warsitzka[1]

Affiliation
[1] Institute of Geosciences, Friedrich Schiller University Jena, Burgweg 11, 07749 Jena, Germany

This chapter is in preparation for publication. References cited in this chapter can be found in the final reference list at the end of this thesis. Detailed descriptions of methodical aspects, the data quality found in literature and uncertainties of the data analysis are attached in Appendix C.1. A database of salt structures of the Southern Permian Basin is attached in the electronic supplement of this thesis (Appendix C.2).

2. Age analysis of salt structures in the Southern Permian Basin

2.1 Introduction

The Southern Permian Basin (SPB) is characterised by numerous salt structures with diversified shapes and growth histories (Kukla et al., 2008; Scheck-Wenderoth et al., 2008b). Post-Permian sedimentary thickness and facies patterns in the SPB were significantly influenced by halotectonic movements and subrosion of the Upper Permian salt and by contemporaneous subsidence of characteristic minibasins (e.g. Maystrenko et al., 2008). The subsidence patterns in these minibasins allow to reconstruct the evolution of salt structures. This relationship is used to date (1) the age of first initiation and (2) the age of the main activity of each salt structure in the SPB and to relate these ages to specific tectonic structures and events. The initiation of a salt structure is here defined as the first post-salt occurrence of deformation in the supra-salt cover or any lateral thickness variations adjacent to the present-day salt structure. The age of main activity is defined as the period in which the growth of a salt structure was fastest, which is assumed to coincide with the fastest subsidence of adjacent minibasins.

In the sections that follow, mechanisms driving salt tectonics in the SPB are explained and then a geological overview of the SPB is given. In the results, geological maps displaying salt structure ages for each period are described and discussed in the framework of major tectonic events in the SPB. More detailed information, definitions of theses ages, the method applied and the literature used for dating can be found in Appendix C.1. A database of all dated salt structures is attached in the digital Appendix (Appendix C.2).

2.2 Geological overview of the Southern Permian Basin

The Southern Permian Basin, roughly defined by the maximum extent of Permian sediment accumulations in Central Europe, reaches from Central Poland to Western Britain and from Northern Denmark to Southern Germany. It is separated from the Northern Permian Basin by the Mid-North Sea–Ringkøbing-Fyn High (Fig. C.1) (Ziegler, 1990; Scheck-Wenderoth et al., 2008a). Both basins belong to the larger Central European Basin System, which lies between lithospheric boundaries of the Baltic and East European Precambrian Craton in the East marked by the Sorgenfrei-Tornquist zone and Teisseyre-Tornquist zone and the West European Palaeozoic Platform in the West (Maystrenko et al., 2008; Doornenbal and Stevenson, 2010). The SPB contains numerous, more or less connected epicontinental sub-basins of different origin, some of them active as depocentres since the

Carboniferous or the Late Permian (Ziegler, 1990; Scheck-Wenderoth et al., 2008a; Doornenbal and Stevenson, 2010). The elongation of these sub-basins reveal that two structural trends dominate in the SPB (Kley et al., 2008): (1) one group of sub-basins strike roughly NW/WNW–SE/ESE and are mostly located in the north-eastern or south-western marginal parts of the SPB (e.g. Broad Fourteens Basin, Lower Saxony Basin, Mid Polish Trough, Sole Pit Trough, Subhercynian Basin, Teisseyre Basin). (2) A second group of sub-basins are elongated in NNE/NNW–SSW/SSE direction and dominantly located along the central axis of the SPB (e.g. southern Central Graben, Glückstadt Graben, Horn Graben, Ems Trough, Rheinsberg Trough). The most characteristic feature of the SPB is the occurrence of salt structures (pillows, diapir, walls, etc.) in most parts of the basin (Kukla et al., 2008).

2.2.1 Evaporitic successions in the Southern Permian Basin

The most important evaporitic succession in terms of salt tectonics is the Upper Permian salt layer built up by a sequence of Rotliegend clay-rich salt and thick Zechstein salts (Maystrenko et al., 2005a). The Rotliegend salt was deposited in sabkha and playa lake facies and contains multiple rock salt layers of highly variable thickness interbedded with mudstone and carbonates (Reinhold and Hammer, 2016). The Zechstein salt accumulated under marine conditions. Repeated phases of evaporation interrupted by marine incursions led to 5 to 7 more or less complete evaporitic cycles, which began with clastic clays followed by evaporitic carbonate, anhydrite, halite and potassium salt minerals (Geluk, 2005; Stollhofen et al., 2008; Reinhold and Hammer, 2016). Overall, approximately 70 % of the entire Zechstein succession consists of rock salt with largest volumes occurring in the second and third succession (Staßfurt and Leine Formation) (Warren, 2008).

Due to strong post-Permian diapirism and salt expulsion, the initial thickness of the Permian salt layer is difficult to ascertain in most parts of the SPB. Three-dimensional restoration and backstripping analyses suggest an original thickness of at least 3000 m in the basin centre (Glückstadt Graben), roughly 1000 to 1500 m in platform regions (e.g. Northeast German Basin, central Northwest German Basin, offshore Netherlands) and several hundreds of metres in marginal areas of the SPB (e.g. Thuringian Syncline) (Scheck et al., 2003a; Ten Veen et al., 2012; Maystrenko et al., 2013).

Minor evaporite layers occur in the continentally dominated Upper Buntsandstein (Röt) and the marine Middle Muschelkalk achieving thicknesses from 200 to 300 m and containing anhydrites, carbonates and halite (Warren, 2008; Reinhold and Hammer, 2016). Locally important evaporites (thicknesses of up to 1700 m) were deposited in peripheral sinks of salt diapirs located in the centre of the SPB during Middle Keuper time ("Gipskeuper"). These evaporites consists of alternations of claystones, carbonates and evaporite series deposited under mixed marine to continental conditions (Warren, 2008). Similarly, Upper Jurassic (Upper Malm) evaporites occur next to diapirs abundantly located in the area of the Lower Saxony Basin (Stollhofen et al., 2008; Reinhold and Hammer, 2016) with thicknesses of up to 1000 m. Both, Keuper and Jurassic evaporites are suggested to be redeposited Permian salt dissolved from extruded diapirs (Trusheim, 1960; Warren, 2008). Locally large thicknesses of both evaporite layers are explained by deeply subsided peripheral sinks and forma-

tion of autonomous salt pillows (see Fig. C.1 for locations) within these peripheral sinks (Frisch and Kockel, 1999).

2.2.2 Salt tectonics in the Southern Permian Basin

Despite early works suggesting autonomous buoyancy driven salt diapirism (e.g. Lachmann, 1911; Arrhenius and Lachmann, 1912; Meinhold, 1956; Trusheim, 1960; Sannemann, 1968), it is now generally accepted that salt movement in the SPB was dominantly provoked and intensified by multiple post-Permian tectonic events (e.g. Vejbæk, 1990; Kockel, 2002; Kossow et al., 2000; Scheck et al., 2003a; Krzywiec, 2004a; Maystrenko et al., 2005a; Mohr et al., 2005; Kukla et al., 2008). Various mechanisms are proposed to trigger the initial stage of salt structures. Salt pillows and anticlines are suggested to have been formed as buckle folds due to detached shortening e.g. in the North German Basin (Mohr et al., 2005) or the Sole Pit Trough (Stewart, 2007) or due to sub-salt normal faulting, e.g. in the Southern North Sea (Remmelts, 1995). Early stage reactive diapirs were induced by sub-salt faulting, e.g. associated with extensional sub-basins (e.g. Best et al., 1983; Krzywiec, 2004a; Duffy et al., 2013), by thin-skinned supra-salt faulting, e.g. in the Rheinsberg Trough (Maystrenko et al., 2008) or by gravity driven raft tectonics of the detached cover layer, e.g. in the Northwestern and Southern North Sea (Thieme and Rockenbauch, 2001; Karlo et al., 2014) or in the Ems Trough (Mohr et al., 2005).

Generally, mature stage salt tectonics characterised by diapiric breakthrough are usually also originated from tectonic movements (Jackson and Vendeville, 1994). Tectonic extension can effectively thin and weaken the cover providing space for salt uprise and form reactive diapirs (e.g. Vendeville and Jackson, 1992b; Koyi et al., 1993; Nalpas and Brun, 1993). Since multiple phases of extension affected large parts of the SPB (particularly during Late Triassic, Mid – Late Jurassic and Mid – Late Tertiary), it is generally assumed that normal faulting in the sub-salt basement, stretching of the supra-salt cover and regional tilting of the basin floor were prevalent triggers for salt diapirism in the SPB (Kockel, 1998; Mohr et al., 2005; Kukla et al., 2008).

Once diapirs pierced the overburden, they continue to rise with respect to the adjacent sedimentary surface, a process called downbuilding or passive diapirism (Barton, 1933; Vendeville and Jackson, 1992b; Jackson et al., 1994). If salt supply from the source layer is faster than the accumulation rate of overburden sediments, salt can extrude at the sedimentary surface causing the formation of salt glaciers or so called “namakiers“. Buried salt extrusions are documented e.g. adjacent to diapirs in the Ems Trough (Mohr et al., 2007; Warren, 2008).

If tectonic deformation once again affects mature or buried (dormant) diapirs, their growth can be intensified or reactivated. Lateral stretching usually causes collapse and burial of diapirs (Vendeville and Jackson, 1992a). Such collapsed salt structures are not reported in the SPB. Shortening laterally squeezes diapirs causing crestal uplift or lateral intrusion of salt at the border of diapirs (Vendeville and Nilsen, 1995; Dooley et al., 2009). Such structures are well known from the Lower Saxony Basin and the Subhercynian Basin (Fig. C.4C) (Baldschuhn et al., 1991, 1998; Kockel, 2003).

Many modern studies addressing passive margin salt basins emphasize the importance of sedimentary

differential loading in triggering salt tectonics. Due to lateral differences sediment thickness and density, e.g. by progradation of sedimentary wedges, basin wide gravity spreading takes place. Such mechanisms were also suggested for some regions in the SPB (e.g. Ge et al., 1997), but seem to be of minor importance as a basin scale trigger for salt tectonics.

Coincidently to each stage of a salt structure (initial, mature, dormant/reactivation), specific syn-kinematic sedimentary structures develop next to it. During rise of early-stage salt structures (pillows, cover grabens) roughly symmetric minibasins develop, which are called "primary peripheral sinks" (PPS; Fig. C.2A-B). During the diapiric downbuilding stage (mature stage), usually largest flow rates arise in the salt layer (e.g. Seni and Jackson, 1983; Sørensen, 1998; Zirngast, 1996) leading to a shift of depocentres further towards the border of the diapir (Chapter 3). Consequently, asymmetric minibasins are formed, called "Secondary peripheral sinks" (SPS; Fig. C.2C). During reactivation of mature or dormant diapirs, minibasins form next to the culmination point of the uplifted diapir crest. Originally, these troughs were called "Tertiary peripheral sinks" (Trusheim, 1960), but this name is generally avoided now, because of confusion with the time period Tertiary.

2.2.3 Evolution of the Southern Permian Basin

Carboniferous to Permian: The evolution of the SPB has begun in the period from the Latest Carboniferous (Stephanian) to Early Permian (Early Rotliegend). Igneous activity and mostly WNW–ESE directed extension and transtension affected parts of the collapsing Variscan orogen, its foreland basin and parts north of it (Glennie, 1986; Brink et al., 1992; Ziegler, 1990; Scheck-Wenderoth et al., 2008a; Maystrenko et al., 2008). This phase of basin initiation was followed by thermal subsidence and crustal relaxation from Late Rotliegend (Early Permian) to the beginning of the Triassic (Ziegler, 1990; Scheck-Wenderoth et al., 2008a; Van Wees et al., 2000).

With beginning of the Late Permian, the SPB was flooded owing to continuing thermal subsidence, a global eustatic sea level highstand and an opening connection to the Arctic ocean by the Norwegian-Greenland rift (Scheck-Wenderoth et al., 2008a). Repeated cycles of evaporation and transgression lead to the deposition of thick evaporites (Upper Rotliegend – Zechstein salt layer).

Triassic: During the Triassic, Central Europe was affected by the beginning of the break-up of Pangea, rifting in the Neotethys area and in the Arctic-North Atlantic area (Ziegler, 1990; Scheck-Wenderoth et al., 2008a). Thermal subsidence in the SPB was accelerated by repeated phases of more or less E–W directed extension. This started already during Late Zechstein time (Late Permian), culminated during Late Triassic Keuper time and continued until the Early Jurassic (Scheck-Wenderoth et al., 2008a). Extension led to formation of sub-basins, which first became evident during the Early Triassic or some of them already in the Late Permian (e.g. Glückstadt Graben, Horn Graben, Mid Polish Trough) (Scheck-Wenderoth et al., 2008a; Maystrenko et al., 2013). The initiation of these extensional basins was associated with first movements of the Permian salt during Early and Middle Triassic times. Additional phases of extension during the Late Triassic caused strong salt diapirism (Maystrenko et al., 2013) and the accumulation of up to 5800 m of sediments in locally diversified depocentres (e.g. Glückstadt Graben, Horn Graben, Rheinsberg Trough) (McCann et al., 2006;

Scheck-Wenderoth et al., 2008a). Contemporaneous to Late Triassic extension, far field intra-plate stresses due to collision of Cimmerian terranes at the southern border of Central Europe ("Early Cimmerian" phase) led to reduced subsidence or moderate inversion of parts of the SPB, e.g. the Mid-Polish Trough (Scheck-Wenderoth et al., 2008a).

During Early to Middle Buntsandstein time, continental facies with the deposition of terrigenous clastics at high accommodation rates dominated in the entire SPB (Scheck-Wenderoth et al., 2008a). From Late Buntsandstein to Muschelkalk time, eustatic sea level rise led to marine transgression into the SPB in favour of carbonate and evaporite deposition. The Late Triassic period was again characterised by continental facies dominated by fine-grain siliciclastics. Occasional marine transgression and playa lake facies resulted in deposition of evaporitic successions in the centre of the SPB.

Jurassic to Early Cretaceous: During the Early Jurassic, the geodynamic realm from Late Triassic prevailed. The Mid-Jurassic marked a geodynamic change related to the onset of oceanic spreading of the Central Atlantic and the Alpine Tethys. This led to increased extension in the central North Sea rift system. At the same time, widespread doming occurred in the central North Sea because of a deep seated thermal anomaly (Scheck-Wenderoth et al., 2008a). The doming caused uplift and erosion first in the central North Sea during the Middle Jurassic marked by the "Mid-Cimmerian" unconformity. Later, uplift spread across Central Europe and affected northwestern Germany (e.g. Glückstadt Graben) at the end of the Middle Jurassic (Baldschuhn et al., 1996) and the Northeast German Basin during the Late Jurassic (Kossow and Krawczyk, 2002). Coeval to the North Sea doming, NW–SE trending extensional basins (e.g. Broad Fourteens Basin, Lower Saxony Basin, Mid-Polish Trough, Sole Pit Trough) (Scheck-Wenderoth et al., 2008a) formed in southern and central parts of the SPB probably related to northward propagation of the Atlantic oceanic rift and the opening of the Bay of Biscay rift (Scheck-Wenderoth et al., 2008a; Stollhofen et al., 2008).

During the Early Jurassic, regional marine transgression is recorded all over the SPB, which caused the deposition of marine shales and carbonates with intercalating coastal sands. Sedimentation during Middle and Late Jurassic times was locally restricted to the extensionally driven depocentres and peripheral sinks of salt structures (Scheck-Wenderoth et al., 2008a; Maystrenko et al., 2005a). The base of the Lower Cretaceous is marked by the regional "Late Cimmerian" unconformity (Stollhofen et al., 2008). Afterwards, terrestrial to shallow marine deposition of siliciclastic sediments prevailed in wide parts of the SPB, before fully marine conditions with sedimentation of clays and marls returned during the late Early Cretaceous.

Late Cretaceous to present-day: From the Late Cretaceous (late Turonian) to the Early Tertiary ($\sim$early Miocene), Iberia collision, closure of the Alpine Tethys, and collision of Africa-Arabia and Eurasia induced multiple phases of N–S to NE–SW shortening in the SPB. This led to inversion of former NW–SE trending extensional faults, basement uplifts (e.g. Flechtingen uplift, Harz mountains, Thuringian Forest) (Scheck et al., 2003a; Ziegler, 1987; Kley and Voigt, 2008) and thin-skinned folding of Mesozoic strata detached by the Permian and post-Permian salt layers (e.g. Kossow et al., 2000). Inversion mostly affected the southern (e.g. Lower Saxony Basin, Subhercynian Basin) and northeastern marginal parts of the SPB (Teisseyre-Tornquist zone, Grimmen High), whereas shorten-

ing in the central parts was minor or absent (Maystrenko et al., 2008). The inverted basins are often surrounded by marginal basins containing thick Cretaceous to Lower Tertiary sediments (Voigt et al., 2008). From Eocene to Oligocene, E–W to NW–SE directed extension started causing the development of the European Cenozoic Rift System (Dèzes et al., 2004; Kley et al., 2008). In the period from Late Eocene to Middle Miocene, major horizontal contraction changed to NW–SE direction coeval to the E–W trending extension established during the Eocene (Kley et al., 2008). This tectonic regime persisted throughout the Neogene.

Sea level highstand during the Late Cretaceous led to widespread sedimentation of limestones in the SPB dominated by carbonates in the northern and clastics in the southern part. Marine conditions characterised by clastic deposits widely prevailed until the Middle Pliocene. Afterwards, continental sedimentation with limnic and fluival deposits returned (Voigt et al., 2008).

2.3 Results of the age analysis

2.3.1 First initiation

In Fig. 2.1, geological maps illustrate the periods of initiation for each salt structure. The background displays the present-day thickness of the specific unit.

Early to Middle Buntsandstein time: At first, salt structures developed in regions of NNE–SSW trending sub-basins and fault zones in the North German Basin (NGB) e.g. in the Glückstadt Graben (e.g. Kockel, 1995; Maystrenko et al., 2005a)), the northern Ems Trough (e.g. Kockel, 1995; Mohr et al., 2005), the Horn Graben (e.g. Kockel, 1995), the Braunschweig-Gifhorn fault zone/ Weser Trough (Jaritz, 1973; Kockel, 1991; Baldschuhn et al., 2001; Köthe et al., 2007) (Fig. 2.1A). In these regions, salt structures are aligned in multiple rows of highly-elongated walls oriented parallel to the graben axes. Additionally, salt structures were initiated in the NW-SE trending striking Mid Polish Trough (Dadlez et al., 1995; Dadlez, 2003; Krzywiec, 2004a,b, 2006, 2012; Wagner et al., 2002). Some salt structures in the northwestern part of the North German Basin (here referred to as Northwest German Basin, NWGB) reflect NW–SE striking structural trends not related to prominent sub-basins (red lines; Fig. 2.1A) (Röhling, 1991; Franke and Hoffmann, 1999; Best and Zirngast, 2000; Scheck et al., 2002).

Late Buntsandstein to Muschelkalk time: Salt walls related to sub-salt faults in the NNE–SSW striking Central Graben (e.g. Kockel, 1995; Remmelts, 1995; Wong et al., 2007) and salt diapirs and walls in the NW–SE striking Sole Pit Trough (van Hoorn, 1987; Allen et al., 1994; Hughes and Davison, 1993; Coward and Stewart, 1995; Griffiths et al., 1995; Stewart, 2007) became active in this period (Fig. 2.1B). Nevertheless, dating of most of these salt structures is uncertain, especially in the Sole Pit Trough, because of the small number of geological cross-sections published. Thus, dating is predominantly based on descriptions as cited above.

Additional salt walls and diapirs were mobilised at the borders of the Glückstadt Graben, the Horn Graben and the Braunschweig-Gifhorn fault zone. Besides, several individual salt diapirs became

evident in the eastern part of the North German Basin (here referred to as Northeast German Basin, NEGB) and in the central NWGB (Scheck and Bayer, 1999).

Keuper time: During Keuper time, salt structures in almost all parts in between the priorly formed sub-basins as well as in newly formed sub-basins were initiated (Fig. 2.1C). In the Silver Pit Basin, salt walls developed in the basin centre contemporaneous to reactive diapirs at the basin edges (van Hoorn, 1987; Allen et al., 1994; Hughes and Davison, 1993; Coward and Stewart, 1995; Griffiths et al., 1995; Stewart et al., 1996; Stewart, 2007). Salt structures in the Broad Fourteens Basin were likely activated during Keuper time (Duin et al., 2006; Wong et al., 2007). At the flanks of the Glückstadt Graben, the Braunschweig-Gifhorn fault zone and the Mid Polish Trough elongated pillows and salt walls were mobilised during Keuper time. Coincidently, the NNE–SSW trending Rheinsberg Trough first occurred as a sub-basins associated with the formation of slightly elongated diapirs (Benox et al., 1997; Scheck et al., 2003a; Beutler et al., 2012). Salt structures in the Rheinsberg Trough were possibly triggered by thin-skinned extension decoupled from graben structures and fault zone to the West (Glückstadt Graben, Braunschweig-Gifhorn fault zone) (Scheck et al., 2003a). In the southern and northern parts of the NEGB, NW–SE trending salt structures probably evolved due to the activity of fault zones in the sub-salt basement (Meinhold and Reinhardt, 1967; Beutler and Schüler, 1978; Reinhardt, 1993; Kossow, 2001; Beutler et al., 2012). Rather circular diapirs were initiated in regions between the Rheinsberg Trough and the Braunschweig-Gifhorn fault zone (Benox et al., 1997; Köthe et al., 2007) and in the south of the Glückstadt Graben (Jaritz, 1973; Kockel and Krull, 1995; Frisch and Kockel, 1999, 2004). On the West Schleswig Block, several salt pillows evolved at this time (Kockel, 1995). Some of them are marked as uncertain, because lateral thickness variations of the Keuper units are little and partly caused by erosion instead of syn-sedimentary subsidence of peripheral sinks. Similarly, salt pillows on the Northern East Holstein-Mecklenburg Block (Bay of Kiel) are inferred only from slight thickness variations of the Upper Triassic (Hansen et al., 2005, 2007; Zöllner et al., 2008; Hübscher et al., 2010) and, therefore, classified as uncertain.

Generally, thickness distribution of Triassic sediments (Fig. 2.1A-C) reflects dominating subsidence of NNE–SSW trending depocentres (e.g. Central Graben, Horn Graben, Glückstadt Graben). Likewise, aligned salt structures or elongation of salt walls and anticlines trace NW–SE trending sub-basins, e.g. the Mid Polish Trough or the Sole Pit Trough and additional structural trends (red lines; Fig. 2.1C) (Kossow et al., 2000; Scheck et al., 2003a; Krauss and Mayer, 2004).

Early to Middle Jurassic: Lower and Middle Jurassic units have increased thickness in or adjacent to extensional sub-basins (e.g. Broad Fourteens Basin, Central Graben, Mid Polish Trough, Sole Pit Trough) indicating locally increased subsidence (Fig. 2.1D). However, almost no new salt structures were initiated close to the Triassic sub-basins. A few singular salt pillows and diapirs occurred in the NEGB and the central NWGB.

Late Jurassic to Early Cretaceous: Similar to the previous period, only a few salt structures were initiated during the Late Jurassic to the Early Cretaceous (Fig. 2.1E). In the Lower Saxony Basins, large, NW–SE trending salt walls were likely induced (Jaritz, 1973; Kockel and Krull, 1995), although minor salt pillows probably grew in this region since the Late Triassic (Maystrenko et al.,

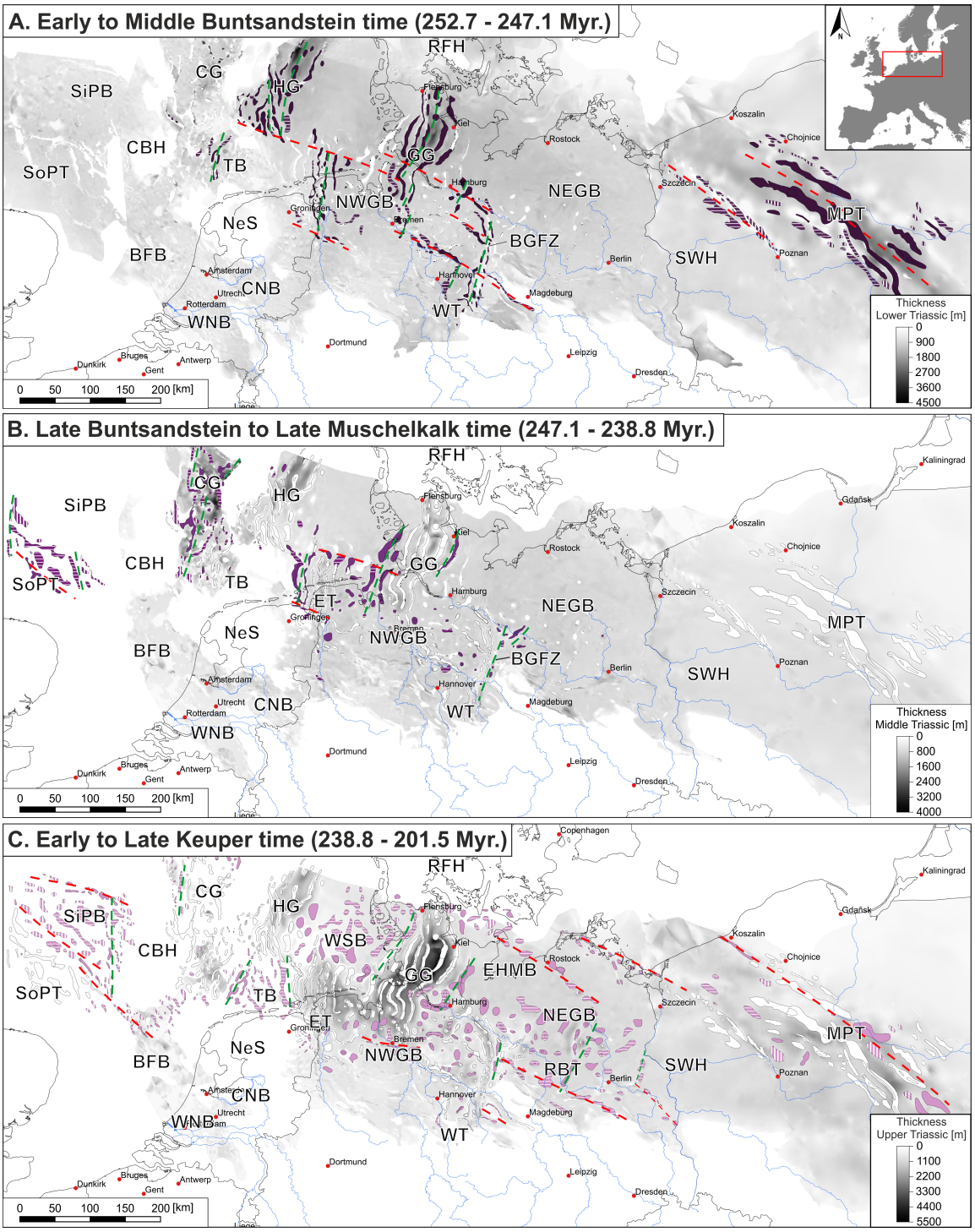

Figure 2.1: Sequence of maps highlighting periods of the initiation of each salt structure and the present-day thickness pattern of the specific unit. **A** Mainly salt walls in extensional sub-basins and along sub-salt fault zones in the central and the eastern parts of the SPB were initiated. **B** Additional salt structures in the NWGB and in the western sub-basins began to rise. **C** Most of salt structures in the NWGB and in the NEGB as well as in the Silver Pit Basin were initiated. Note that thickness data of Middle and Upper Triassic from the UK North Sea sector is not included in Doornenbal and Stevenson (2010). *(see next page)*

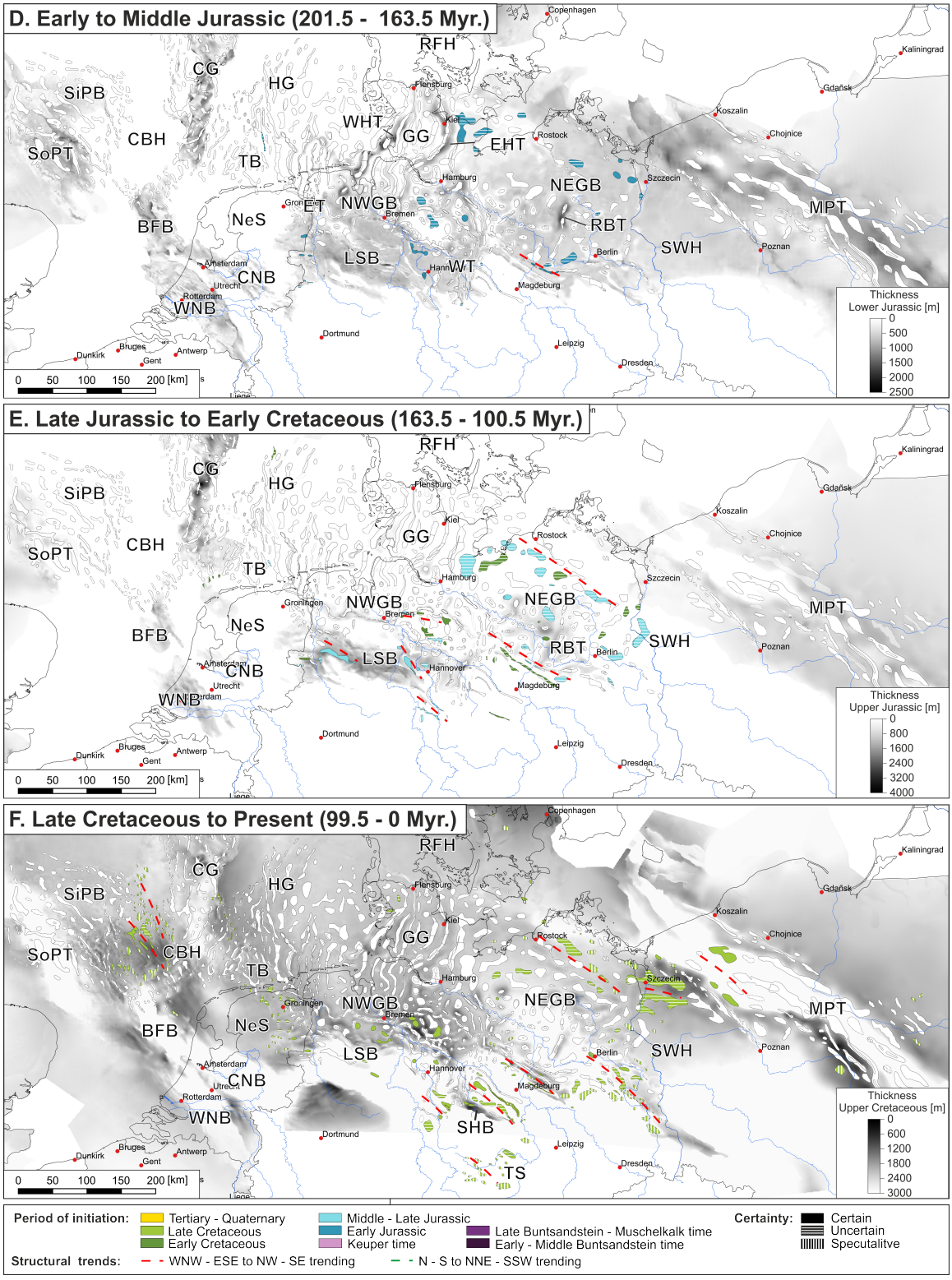

Figure 2.1: *(continued)* **D** and **E** Isolated salt structures predominately in the NEGB were initiated. **F** Eventually, salt movement in the southern part and the transition from the NEGB and the MPT commenced. The shapes of the salt structures are modified from Doornenbal and Stevenson (2010). For definition of the certainty of dating see Appendix C.1. BGFZ – Braunschweig-Gifhorn fault zone, BFB – Broad Fourteens Basin, CBH – Cleaver Bank High, CG – Central Graben, CNB – Central Netherlands Basin, EHMB – East Holstein-Mecklenburg Block, ET – Ems Trough, HG – Horn Graben, GG – Glückstadt Graben, LSB – Lower Saxony Basin, MPT – Mid Polish Trough, NEGB – Northeast German Basin, NWGB – Northwest German Basin, RFH – Ringkøbing-Fyn High, SHB – Subhercynian Basin, SiPB – Silver Pit Basin, SoPT – Sole Pit Trough, SWH – Szczecin-Wolsztyn High, TB – Terschelling Basin, TS – Thuringian Syncline, WNB – West Netherland Basin, WSB – West Schleswig Block, WT – Weser Trough.

2013). However, owing to the strong Late Jurassic – Early Cretaceous extension and subsequent inversion, Triassic pillow structures are difficult to prove in this region.

In the central and southern NEGB, several elongated salt pillows occurred, which can possibly assigned to NW–SE striking structural trends (e.g. Jubitz, 1964). Nevertheless, most of these pillows were dated by means of the subcrop map of the Lower Cretaceous (Beutler et al., 2012) and thickness maps (Noack et al., 2010). Additionally, partial erosion of Jurassic sediments complicates the exact dating of these salt structures leaving high uncertainties in these regions.

Late Cretaceous to Present: During Late Cretaceous to Early Tertiary times, a NNE/NE–SSW/SW trending compressional stress regime affected large parts of the SPB. Many existing salt structures were inverted or reactivated (Baldschuhn et al., 1985, 1991, 1998; Kockel, 2003; Otto, 2003; Mazur et al., 2005). Additionally, new salt-cored anticlines were formed in particular at the southern and the northwestern margin of the SPB (Fig. 2.1F). A few salt pillows in the central NWGB were initiated. In the region between the Sole Pit Trough and the Central Graben, many small pillows were mobilised, which are marked as uncertain. In this region as well as in other regions at the southern margin, e.g. the Subhercynian Basin (Patzelt, 2003; Brandes, 2012; Brandes et al., 2013) or the Thuringian Syncline (Franzke et al., 1986; Stackebrandt and Franzke, 1989; Malz and Kley, 2012), parts of Triassic and most of Jurassic sediments were eroded. Except in the Thuringian Syncline, Lower Cretaceous unconformably overlies these eroded regions. Here, subcrop maps locally indicate a topographic relief of the present-day salt structures. Hence, these salt structures were initiated not later than Early Cretaceous, but an earlier activation cannot be excluded.

On the Cleaver Bank High and the Netherlands swell, Late Cretaceous uplift and erosion incised until the Zechstein level. Hence, no salt structures are preserved here at all.

2.3.2 Main activity

The period characterised by fastest growth of a salt structure and deepest subsidence of adjacent peripheral sinks is defined as phase of main activity (Appendix C.1). A sequence of geological maps displays the main activity for all salt structures in the SPB (Fig. 2.2).

Buntsandstein to Keuper time: Until end of Muschelkalk time, only a few salt walls in the Horn Graben and in the Glückstadt Graben passed their stage of main activity (Fig. 2.2A). Much of the salt walls and diapirs in the extensional sub-basins and fault zones achieved the phase of main activity during Keuper time (Fig. 2.2A). These salt structures are often surrounded by deep secondary peripheral sinks, in which Upper Triassic sediments can reach thicknesses of up to 6000 m (Frisch and Kockel, 1999).

Some extensional fault zones first occurred in the Late Triassic, e.g. close to the Grimmen High at the northern edge of the NEGB (Krauss and Mayer, 2004) or in the North Dogger fault zone at the northern edge of the Silver Pit Basin (Griffiths et al., 1995). Salt structure growth in these regions already reached its maximum during Keuper time.

Early to Middle Jurassic: Similar to the previous period, salt walls and diapirs in or close to sub-basins and fault zones passed their phase of fastest growth, especially in the Braunschweig-Gifhorn fault zone, at the western margin of the Glückstadt Graben, in the western Mid Polish Trough and in the central Rheinsberg Trough (Fig. 2.2B). In addition, some salt structures in the Sole Pit Trough, in the Broad Fourteens Basins and in the central NWGB reached the phase of main activity.

Late Jurassic to Early Cretaceous: During the Late Jurassic, salt walls in the Central Graben reached the phase of fastest growth, which was accompanied by accumulation of up to 4000 m Upper Jurassic sediments (Fig. 2.2C) (e.g. Jähne-Klingberg et al., 2014). In the Sole Pit Trough, the Lower Saxony Basin and the central NWGB, dominantly NW–SE striking salt walls rapidly grew during Late Jurassic to Early Cretaceous. Some diapirs in the central NEGB passed their phase of main activity, which was apparently not related to any grabens or fault zones.

Late Cretaceous: During the Late Cretaceous, many salt structures particularly north of the Lower Saxony Basin, in the marginal parts of the Mid Polish Trough and in the NEGB reached their phase of main activity (Fig. 2.2D). Most of the salt structures in these regions are clearly oriented at NW–SE striking structural trends (red lines). Many salt-cored anticlines, which were initiated during Late Cretaceous, e.g. in the Subhercynian Basin and in the southern NEGB, reached the phase of main activity at the same time. It has to be mentioned that it is not distinguished between salt structure uplift due to halokinesis (e.g. downbuilding) or due to tectonic contraction.

In regions of the SPB affected by widespread erosion of Mesozoic sediments (e.g. west of the Lower Saxony Basin, the eastern Sole Pit Trough, the eastern Silver Pit Trough, the Thuringian Syncline), the Late Cretaceous is assumed to be the phase of main activity although no or minor Upper Cretaceous sediments are preserved. These basin parts, however, were uplifted or inverted during the Late Cretaceous. Insofar there are no indications for a strong pre-Late Cretaceous salt structure uplift, it is suggested that lateral contraction significantly enhanced the growth of these salt structures.

Cenozoic: In the Cenozoic, the region in which many salt structures passed their phase of main activity switched back to the central part of the SPB, whereas N–S to NE–SSW structural trends predominate (Fig. 2.2E). Deeply subsided NNE–SSW trending marginal troughs of the Glückstadt Graben (East Holstein Trough, West Holstein Trough) developed comprising up to 4500 m thick sediments (Maystrenko et al., 2005a). Salt walls and diapirs encompassing these troughs achieved the phase of main activity at this time (Fig. 2.2E). Likewise, primary peripheral sinks of Cenozoic age indicate the activity of low amplitude salt pillows in the neighbouring areas West Schleswig Block and East Holstein-Mecklenburg Block. NNE–SSW striking salt structures at the eastern and western flank of the Rheinsberg Trough as well as in the northern continuation of the Ems Trough achieved the phase of fastest growth. Rapidly rising NW–SE trending salt structures occurred in the Silver Pit Basin and the northern NEGB. A further Cenozoic depocentre is the central North Sea Basin with sedimentary thicknesses of up to 3000 m. Most of the salt structures in this region already became dormant during Jurassic or Cretaceous time and were buried under thick Cenozoic sediments without reactivation.

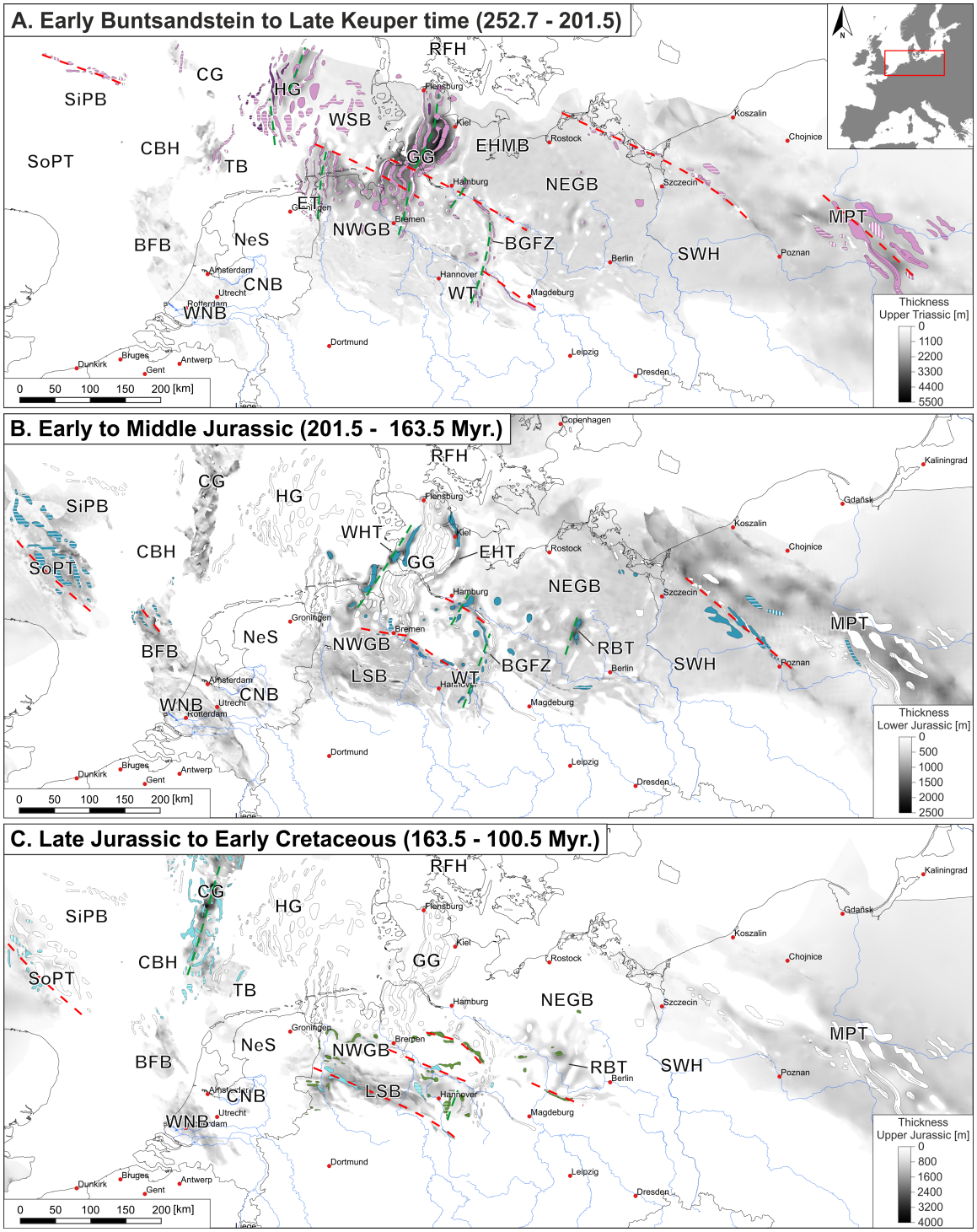

Figure 2.2: Sequence of maps highlighting periods of the main activity of each salt structure in the SPB and the present-day thickness pattern for each unit. **A** Only a few diapirs achieved their stage of main activity during Early or Middle Triassic in the northern GG and the HG. Many salt walls in the earliest extensional basins (GG, HG, MPT) reached their main activity already during Late Triassic Keuper time. **B** Salt walls in the Sole Pit Trough and at the basin edge of the GG, the MPT and the BGFZ reached their maximum growth. **C** Salt walls in the CG, in the SoPT and the LSB showed strong activity. *(see next page)*

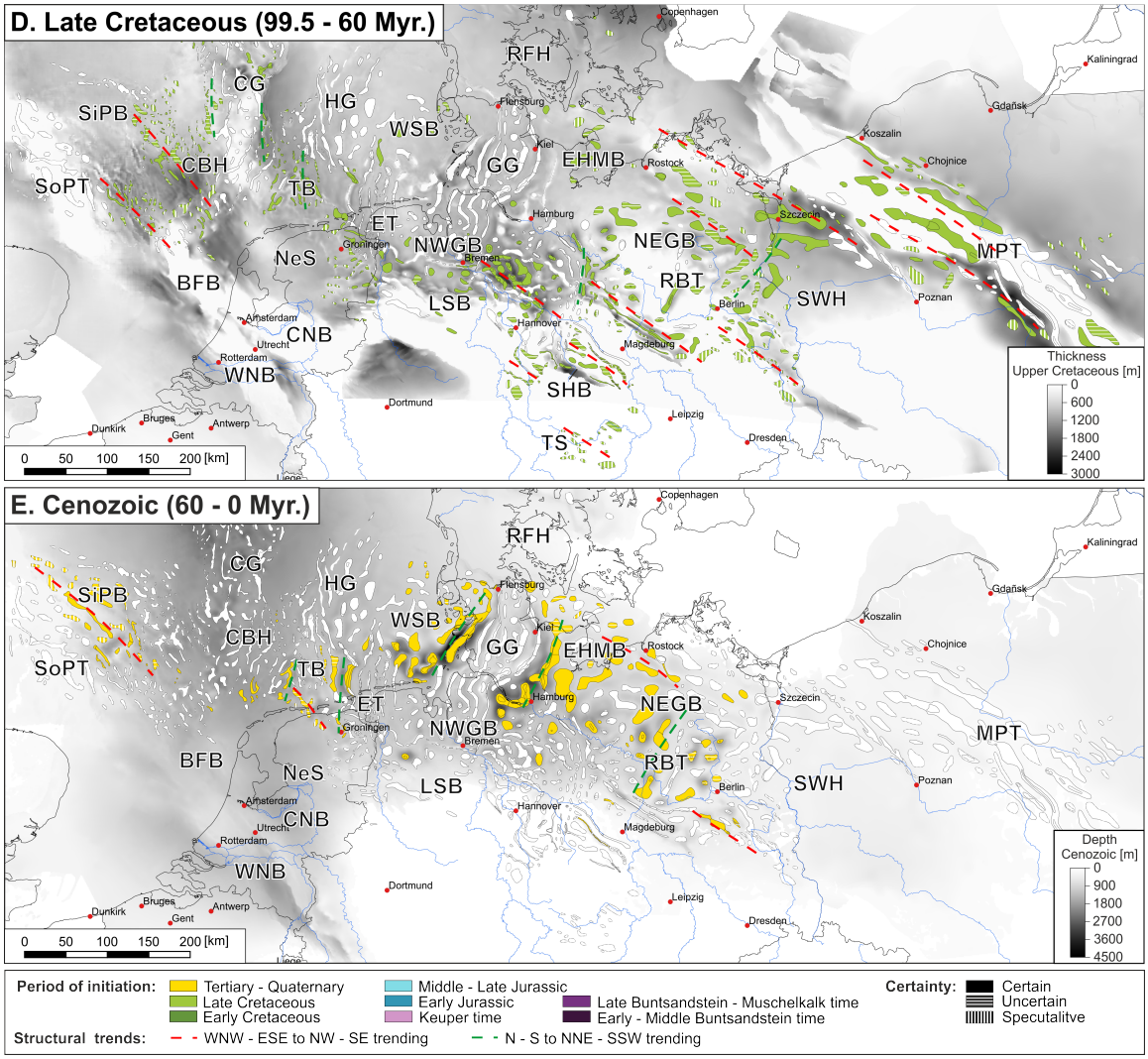

Figure 2.2: *(continued)* **D** Salt structures in the entire SPB, in particular in the southern parts, in the NEGB, the MPT and the SiPB achieved their phase of main activity. **E** Salt diapirs in the marginal basins of the GG and in the SiPB as well as salt pillows in the NEGB were mainly active. The shapes of the salt structures are modified from Doornenbal and Stevenson (2010). For definition of the certainty of dating see Appendix C.1. BGFZ – Braunschweig-Gifhorn fault zone, BFB – Broad Fourteens Basin, CBH – Cleaver Bank High, CG – Central Graben, CNB – Central Netherlands Basin, EHMB – East Holstein-Mecklenburg Block, ET – Ems Trough, HG – Horn Graben, GG – Glückstadt Graben, LSB – Lower Saxony Basin, MPT – Mid Polish Trough, NEGB – Northeast German Basin, NWGB – Northwest German Basin, NeS – Netherland Swell, RFH – Ringkøbing-Fyn High, SHB – Subhercynian Basin, SiPB – Silver Pit Basin, SoPT – Sole Pit Trough, SWH – Szczecin-Wolsztyn High, TB – Terschelling Basin, TS – Thuringian Syncline, WNB – West Netherland Basin, WSB – West Schleswig Block.

2.4 Summary and discussion

Fig. 2.3 illustrates the frequency of dated ages of structures related to each period. Additionally, the maps in Fig. 2.4 summarise periods of initiation and main activity for all salt structures in the SPB. A first peak of initiation already occurred in the Late Early Triassic, whereas salt tectonic activity predominantly concentrated in the major N–S to NNE–SSW trending sub-basins and NW–SE directed fault zones. A second culmination of salt structure initiation is revealed for the Late Triassic Keuper time (Fig. 2.3A). In this period, many salt structures in platform areas and minorly subsided basin parts (e.g. West Schleswig Block, NEGB) were activated (Fig. 2.4A). Thus, salt movement

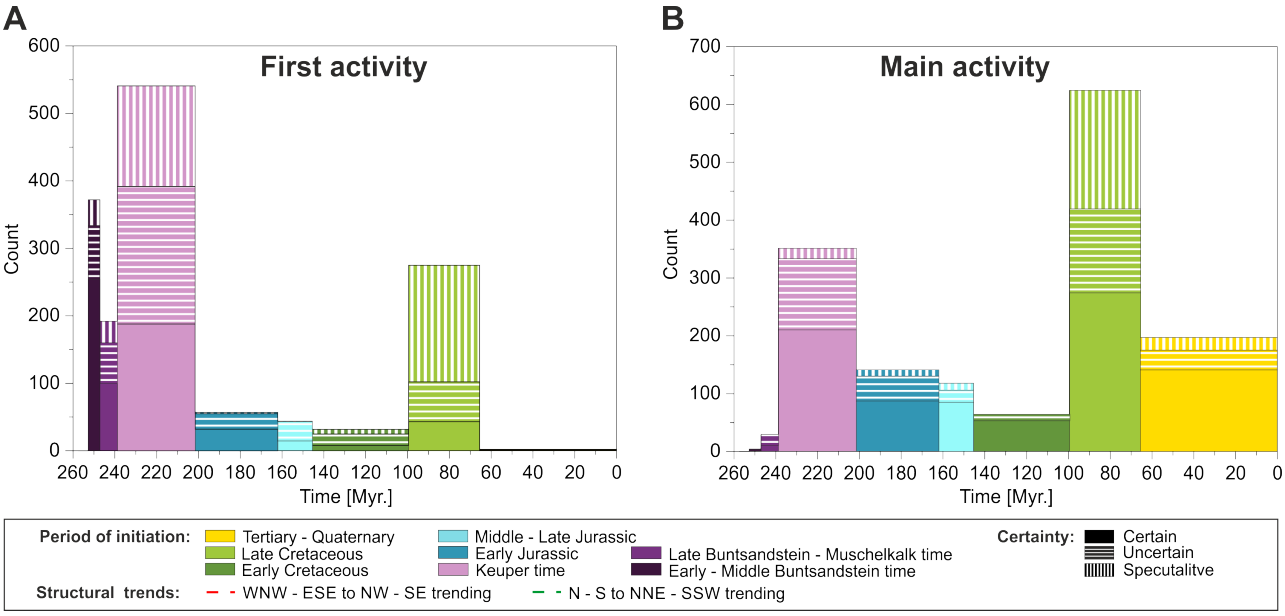

Figure 2.3: Frequency of dated ages for each period. **A** Most salt structures were initiated during Buntsandstein time, Keuper time and the Late Cretaceous. **B** A first peak in main salt structure activity can be observed for Keuper time. Most salt structures reached their main phase during the Late Cretaceous and the Cenozoic.

extended to regions in between the sub-basins. From the Jurassic to Early Cretaceous, fewer new salt structures were formed (Fig. 2.3), partly because salt movement had already affected most parts of the SPB. Nevertheless, a third peak in the initiation of salt structures can be denoted for the Late Cretaceous (Fig. 2.3), during which shortening affected large parts of the SPB. Salt structures dated for the Late Cretaceous are mostly marked as uncertain or speculative, because they are often located on uplifted parts of the SPB, where much of the post-Permian sediments were eroded (e.g. Cleaver Bank High, Thuringian Syncline, western edge of the Mid Polish Trough). Therefore, there was no other possibility than to assign these salt structures to be initiated during the Late Cretaceous.

The dating of the main activity clearly reveals three peaks: in the Late Triassic, the Late Cretaceous and the Cenozoic Fig. 2.3B. Salt structures reaching their main activity during Late Triassic are dominantly located in the sub-basins and fault zones initiated during the Early to Middle Triassic (e.g. Horn Graben, Glückstadt Graben, Braunschweig-Gifhorn fault zone, Mid Polish Trough; Fig. 2.4B). During the Late Cretaceous, many NW–SE trending salt structures at the southern edge of the SPB as well as in the NEGB and the northern Mid Polish Trough achieved their main phase. The Cenozoic phase of main activity again affected salt structures in the centre of the SPB surrounding the Glückstadt Graben as well as in the southern and western North Sea region, and, therefore, in regions, where many salt structures were already in their main phase during the Late Triassic. The structural trends dominated during this phase are roughly NNE–SSW directed, but minorly also NW–SE directed.

The temporal relationship between phases of salt movement to phases of main tectonic movements in major sub-basins of the SPB is displayed in Fig. 2.5 . In all sub-basins (except the Lower Saxony Basin) salt movement started during the Early or the Middle Triassic (Buntsandstein to Muschelkalk

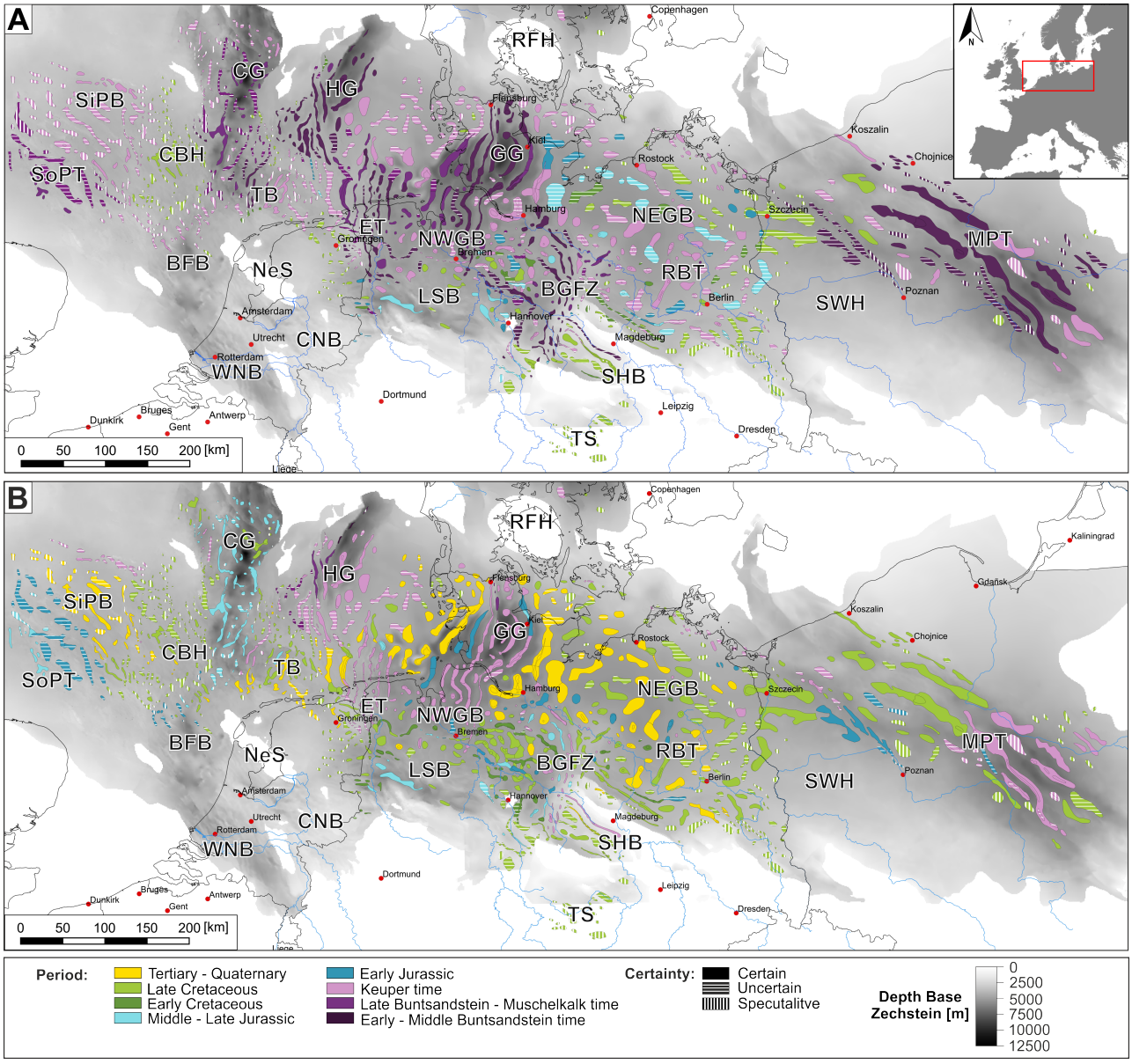

Figure 2.4: Maps summarizing **A** periods of first initiation and **B** main activity of each salt structure in the SPB. BGFZ – Braunschweig-Gifhorn fault zone, BFB – Broad Fourteens Basin, CBH – Cleaver Bank High, CG – Central Graben, CNB – Central Netherlands Basin, DFZ – Dowsing fault zone, EHMB – East Holstein-Mecklenburg Block, ET – Ems Trough, HG – Horn Graben, GG – Glückstadt Graben, LSB – Lower Saxony Basin, MPT – Mid Polish Trough, NEGB – Northeast German Basin, NWGB – Northwest German Basin, NeS – Netherland Swell, RBT – Rheinsberg Trough, RFH – Ringkøbing-Fyn High, SHB – Subhercynian Basin, SiPB – Silver Pit Basin, SoPT – Sole Pit Trough, SWH – Szczecin-Wolsztyn High, TB – Terschelling Basin, TS – Thuringian Syncline, WNB – West Netherlands Basin, WSB – West Schleswig Block.

times) and, therefore, in the first 15 Myr after deposition of the Permian evaporites. This clearly coincided with the first phase of regional extension of the mostly N-S to NNE-SSW oriented sub-basins (e.g. Maystrenko et al., 2013). However, many salt structures were also initiated along E-W to WNW-ESE striking lineaments in the sub-salt basement indicating the activity of these basement faults. This interference of two major structural trends indicates either overlapping multi-directional regional extension (Stollhofen et al., 2008) or dominantly E-W directed extension with strain partitioning between multi-directional (possibly pre-existing) faults in the sub-Permian basement.

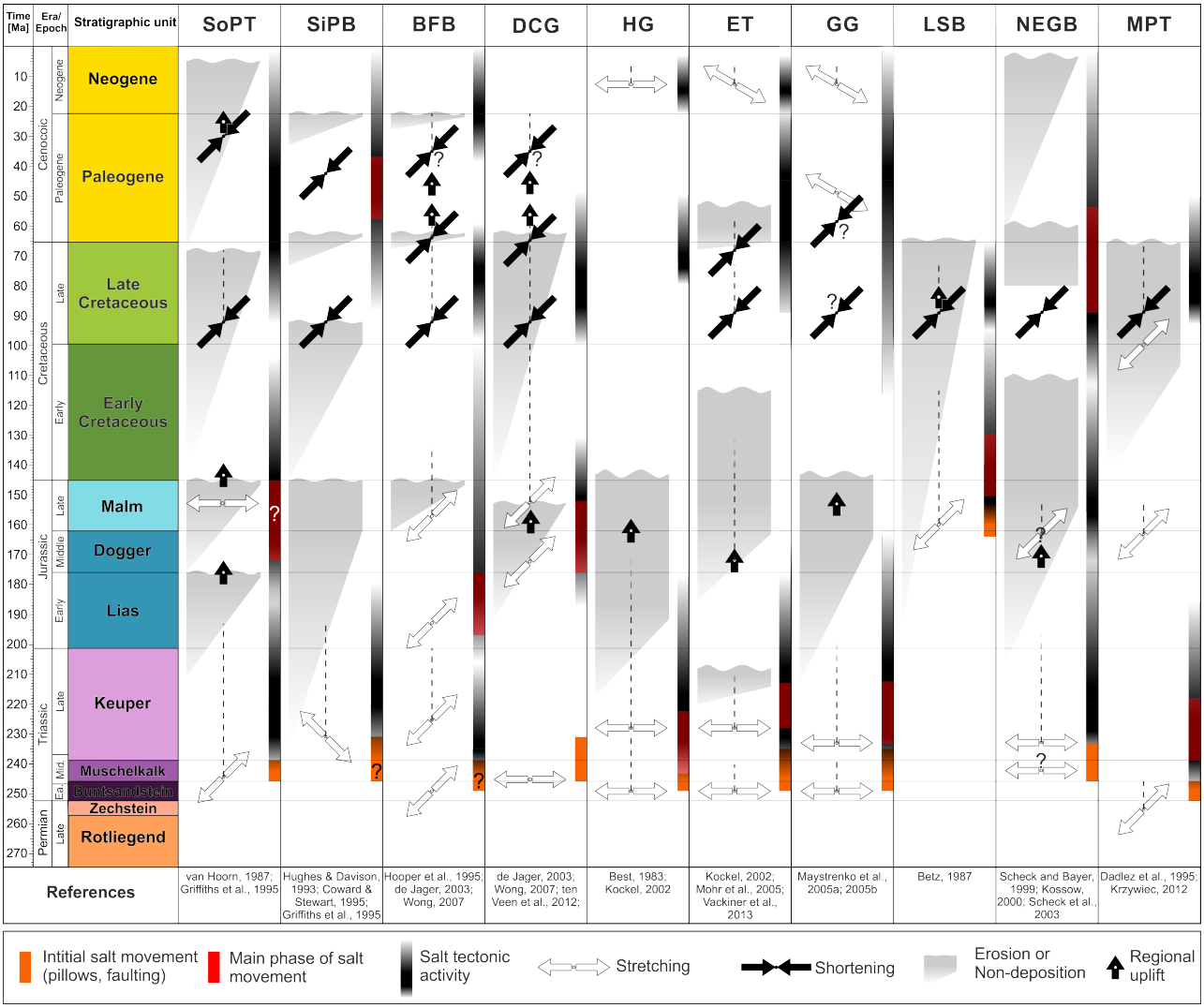

Figure 2.5: Time chart comparing phases of tectonic movements and salt tectonics in major sub-basins of the SPB aligned from West to East. Tectonic movements (derived from references listed in the figure) are denoted by arrows. Salt tectonic activity is denoted by shaded bars. Markings of the initial salt movement (orange) and the main phase (red) are based on the age analysis presented above. BFB – Broad Fourteens Basin, DCG – Dutch Central Graben, ET – Ems Trough, HG – Horn Graben, GG – Glückstadt Graben, LSB – Lower Saxony Basin, MPT – Mid Polish Trough, NEGB – Northeast German Basin, SiPB – Silver Pit Basin, SoPT – Sole Pit Trough

In most of the sub-basins formed during Early to Middle Triassic (except the Central Graben), initial salt movement was followed by a long-lasting phase of salt structure rise from the Late Triassic throughout the Early Jurassic (Fig. 2.5). This was enhanced by additional events of basin extension. In the Ems Trough, the Glückstadt Graben, the Horn Graben and the Mid Polish Trough, the phase of strongest salt structure growth occurred during the Middle or Late Triassic and, thus, approximately $\sim$10 Myr after initiation of salt movements. In the Broad Fourteens Basin and the Central Graben, extensional movements and the phase of main activity was delayed and took place during the Early Jurassic or the Middle to Late Jurassic, respectively. The Lower Saxony Basin represents a special case, where salt tectonics was probably first initiated during the Late Jurassic and reached its maximum during the Early Cretaceous.

A basin-wide attenuation of salt movements can be observed for the late Early Cretaceous – early Late Cretaceous period. This is related to a phase of tectonic quiescence and non-deposition or erosion in many parts of the SPB (Maystrenko et al., 2013).

In all sub-basins, salt flow and the rise of already dormant diapirs was reanimated or intensified by regional shortening during Late Cretaceous – Paleogene times (Fig. 2.5), albeit these salt structures were buried under a thick overburden. Many sub-basins were inverted during this period (e.g. Broad Fourteens Basin, Lower Saxony Basin, Mid-Polish Trough) clearly resulting in contractional overprinting of existing salt structures. However, in some sub-basins (e.g. Glückstadt Graben, Horn Graben), the specific influence of lateral contraction on salt structure rise is difficult to ascertain, since these basins show no clear evidence for basin inversion. Another mechanism probably explaining salt structure reactivation here, is that a general tilting of the basin floor or detached shortening from the southern regions of the SPB caused thin-skinned contraction affecting only supra-salt layers.

In the time chart (Fig. 2.5), many platform areas or highs are excluded (e.g. northern NEGB, Cleaver Bank High, West Schleswig Block). In such platform areas, the periods of salt structure initiation and main activity predominantly occur later than in adjacent extensional sub-basins. Mostly, salt movement was initiated during Late Triassic to Jurassic time or even the Late Cretaceous. The main activity of salt structures in platform regions mainly took place during the Late Cretaceous triggered by basin contraction and inversion or during the Cenozoic triggered by contraction and regional extension.

2.5 Outlook

In order to provide further insights into the relationship between tectonic movements and salt tectonics, additional literature research and data analysis should be undertaken. More studies (dissertations, theses) focussing on local basin structures should be incorporated. If available, primary data (well data, seismic data) has to be analysed in regions where dating of salt structures is uncertain. Eventually, the salt structure database should include the following additional information:

- timing of diapiric piercing, if a suitable criterion for defining the translation into diapiric stage can be defined (see Appendix C.1)
- a more detailed uncertainty relationship
- periods in which diapirs or pillows became inactive, i.e. buried by sediments on the crests or cessation of peripheral sink subsidence.
- possible trigger mechanisms of each salt structure e.g. extension due to basement normal fault, detached thin-skinned extension, rafting, folding due to regional shortening, etc.
- indications for compressional overprinting of salt structures (salt intrusions, uplifted diapir crests, overthrusting) to identify basin parts affected by Late Cretaceous – Early Tertiary shortening
- indications for recently active uplift of salt structure crests, e.g. determined by GPS-measurements

Furthermore, the area of interest should be extended to the Northern Permian Basin including large sub-basins, e.g. the Northern Central Graben and the Norwegian Danish Basin.

2.6 Implications for modelling early-stage salt tectonics

Most of the first appearing salt structures in the SPB are located in extensional sub-basins or along discrete fault zones. Hence, normal faulting in the sub-salt basement is most likely the prime trigger for early stage salt movements. First extensional tectonics in the SPB during the Early and Middle Triassic are characterised by multiple rifting pulses separated by phases of thermal subsidence (Stollhofen et al., 2008). Fault offsets might vary between a few hundreds of meters in fault zones (e.g. Braunschweig-Gifhorn fault zone) to several thousand meters in deeply subsided grabens (e.g. Glückstadt Graben, Horn Graben). Sub-salt faulting is usually accompanied by syn-kinematic accumulation of siliciclastics during Early and Middle Buntsandstein time as well as carbonates and evaporites during Late Buntsandstein to Muschelkalk time. These observations were considered in the studies presented in the following chapters when carrying out restoration of peripheral sinks and planning experimental model set-up and procedure. It is assumed that multiple pulses of fault displacement take place during onset of salt movement. Coevally, syn-kinematic sediment is accumulated at different rates and also after fault movement has stopped. Overburden sediments have to be considered as less dense than salt at the beginning, but compacting and exceeding salt density during continued sediment accumulation.

3. Dynamics of prolonged salt movement in the Glückstadt Graben (NW Germany) driven by tectonic and sedimentary processes

Manuscript #1

Authors
Michael Warsitzka[1], Jonas Kley[2], Fabian Jähne-Klingberg[3], Nina Kukowski[1]

Affiliations
[1] Institute of Geosciences, Friedrich Schiller University Jena, Burgweg 11, 07749 Jena, Germany
[2] Geoscience Centre, Structural Geology and Geodynamics, Georg-August-University Göttingen, Goldschmidtstr. 3, 37077 Göttingen, Germany
[3] Federal Institute for Geosciences and Natural Resources, Stilleweg 2, 30655 Hannover, Germany

This chapter is published by Springer in the journal *International Journal of Earth Sciences*:

Warsitzka, M., Kley, J., Jähne-Klingberg, F., and Kukowski, N., 2017. Dynamics of prolonged salt movement in the Glückstadt Graben (NW Germany) driven by tectonic and sedimentary processes. *Int J Earth Sci (Geol Rundsch)*, 106: 131–151, doi:10.1007/s00531-016-1306-3.

Int J Earth Sci (Geol Rundsch) (2017) 106:131–155
DOI 10.1007/s00531-016-1306-3

ORIGINAL PAPER

Dynamics of prolonged salt movement in the Glückstadt Graben (NW Germany) driven by tectonic and sedimentary processes

Michael Warsitzka[1] · Jonas Kley[2] · Fabian Jähne-Klingberg[3] · Nina Kukowski[1]

Received: 9 September 2015 / Accepted: 4 February 2016 / Published online: 26 February 2016

Abstract The formation of salt structures exerted a major influence on the evolution of subsidence and sedimentation patterns in the Glückstadt Graben, which is part of the Central European Basin System and comprises a post-Permian sediment thickness of up to 11 km. Driven by regional tectonics and differential loading, large salt diapirs, salt walls and salt pillows developed. The resulting salt flow significantly influenced sediment distribution in the peripheral sinks adjacent to the salt structures and overprinted the regional subsidence patterns. In this study, we investigate the geometric and temporal evolution of salt structures and subsidence patterns in the central Glückstadt Graben. Along a key geological cross section, the post-Permian strata were sequentially decompacted and restored in order to reconstruct the subsidence history of minibasins between the salt structures. The structural restoration reveals that subsidence of peripheral sinks and salt structure growth were initiated in Early to Middle Triassic time. From the Late Triassic to the Middle Jurassic, salt movement and salt structure growth never ceased, but were faster during periods of crustal extension. Following a phase from Late Jurassic to the end of the early Late Cretaceous, in which minor salt flow occurred, salt movement was renewed, particularly in the marginal parts of the Glückstadt Graben. Subsidence rates and tectonic subsidence derived from backstripping of 1D profiles reveal that especially the Early Triassic and Middle Keuper times were periods of regional extension. Three specific types of salt structures and adjacent peripheral sinks could be identified: (1) Graben centre salt walls possessing deep secondary peripheral sinks on the sides facing away from the basin centre, (2) platform salt walls, whose main peripheral sinks switched multiple times from one side of the salt wall to the other, and (3) Graben edge pillows, which show only one peripheral sink facing the basin centre.

Keywords Salt tectonics · Glückstadt Graben · Extensional basin · Structural restoration

Introduction

In salt basins affected by tectonic stresses, horizontal strain effectively triggers the formation of salt structures. Overburden deformation is usually decoupled from the subsalt basement due to the mechanical weakness of the salt (Jackson and Vendeville 1994). Once the salt layer has been vertically displaced by basement faulting, lateral thickness changes in post-salt sediments (differential loading) can act as the main driving mechanism for further salt flow and growth of down-built salt structures (Hudec and Jackson 2007). Large accommodation space can be created due to the subsidence of characteristic minibasins in the suprasalt succession, namely primary peripheral sinks (PSP) and secondary peripheral sinks (SPS) (sensu Trusheim 1960; Hudec and Jackson 2007). The first type of minibasins is a diagnostic structure for deposition next to salt pillows or salt diapirs in an early stage of development. The second

✉ Michael Warsitzka
Michael.Warsitzka@uni-jena.de

[1] Institute of Geosciences, Friedrich Schiller University Jena, Burgweg 11, 07749 Jena, Germany

[2] Geoscience Centre, Structural Geology and Geodynamics, Georg-August-University Götingen, Goldschmidtstr. 3, 37077 Göttingen, Germany

[3] Federal Institute for Geosciences and Natural Resources, Stilleweg 2, 30655 Hannover, Germany

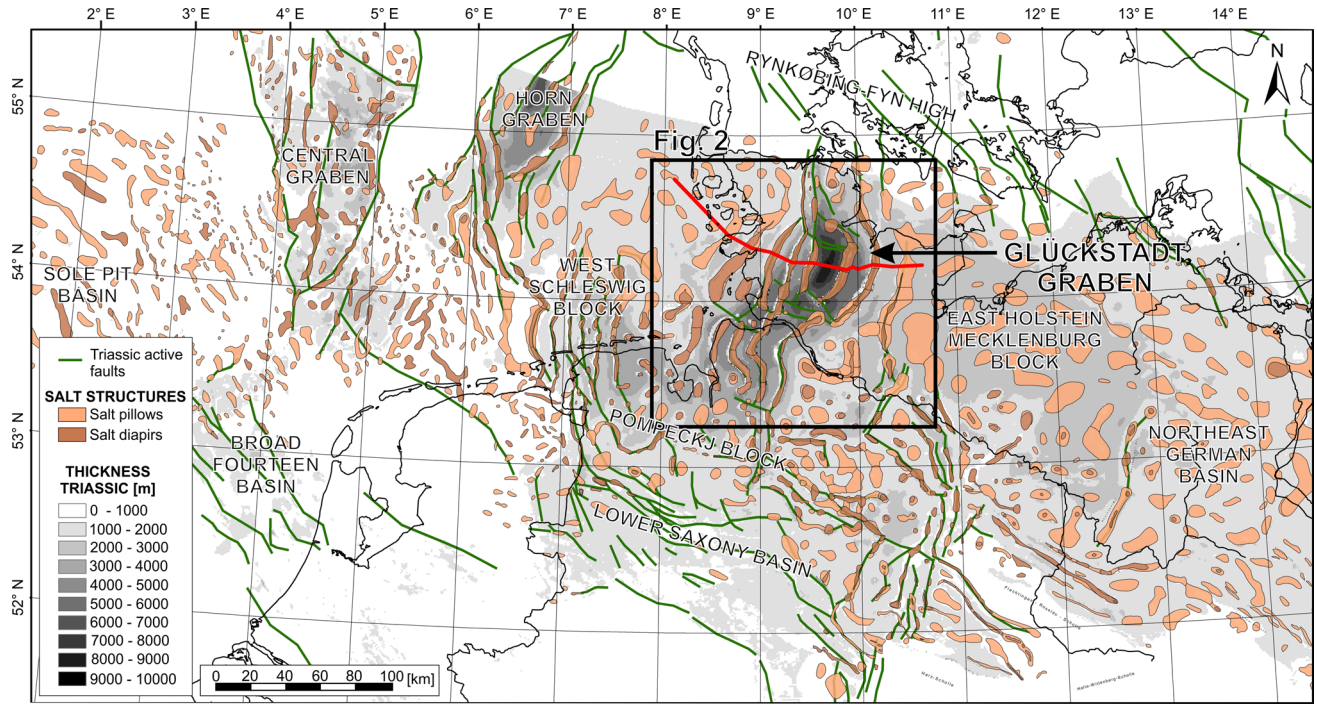

Fig. 1 Map of the Central European Basin System showing the distribution of salt structures and main faults active during Triassic. Salt structures and thickness data are modified from Doornenbal and Stevenson (2010)

type is characteristic for forming next to passively growing salt diapirs (Sørensen 1998; Hudec and Jackson 2011).

The Glückstadt Graben in north-west Germany (Fig. 1) is an excellent example for studying the evolution of salt structures and peripheral sinks in an extensional setting, since it contains some of the deepest peripheral sinks and largest salt walls found in the Central European Basin System (CEBS). First investigations of salt structure evolution in the Glückstadt Graben by Trusheim (1960) and Sannemann (1968) using seismic reflection data found that the ages of salt structures and of the sediments in the peripheral sinks progressively decreases from the basin centre towards the graben flanks. On the basis of this observation, the concept of salt stock families was proposed, which holds that daughter diapirs develop as a consequence of buoyancy forces exerted by a neighbouring mother diapir (Sannemann 1968). Later, new seismic profiles, gravity surveys and drill hole data enabled to study the deep structure and basin evolution over large areas of north-west Germany (e.g. Best et al. 1983; Bachmann and Grosse 1989; Brink et al. 1992). It became evident that regional extension was the dominant trigger for salt tectonics and diapirism (Best et al. 1983). Based on seismic lines as well as structural thickness and depth maps provided in the Tectonic Atlas of NW Germany (Baldschuhn 1996; Baldschuhn et al. 2001), regional scale 3D geological models were reconstructed (Maystrenko et al. 2005a; Hese 2012) and backstripping restorations (Frisch and Kockel 1999; Maystrenko et al. 2005b, 2006) were performed. These studies led to substantial advances in the understanding of the original distribution of the Upper Permian salt layer, the timing of tectonic phases and the salt motion. The Early and Late Triassic, the Early to Middle Jurassic and the Paleogene were identified as periods of major salt movements in the Glückstadt Graben (Frisch and Kockel 1999; Kockel 2002; Maystrenko et al. 2005b). These phases correlate with events of regional extension found in areas surrounding the Glückstadt Graben. Eventually, salt flowage resulted in the development of large salt walls and salt pillows (e.g. Maystrenko et al. 2005b). The associated expulsion of the originally up to 3000-m-thick salt succession crucially affected subsidence patterns and overprinted regional tectonic strain patterns from the Triassic to the present (Maystrenko et al. 2005b).

However, a comprehensive reconstruction of salt structure evolution in the Central Glückstadt Graben in particular for the Triassic has not yet been undertaken. In the present study, we aim to reconstruct the temporal and spatial evolution of salt structures and subsidence patterns in the Glückstadt Graben by means of sequential decompaction and restoration of the peripheral sinks. Furthermore, we provide subsidence curves and subsidence rates of the sedimentary succession in the peripheral sinks. Although salt flowage is usually three dimensional (Rowan and Ratliff 2012), up to 100-km-long salt walls and elongated

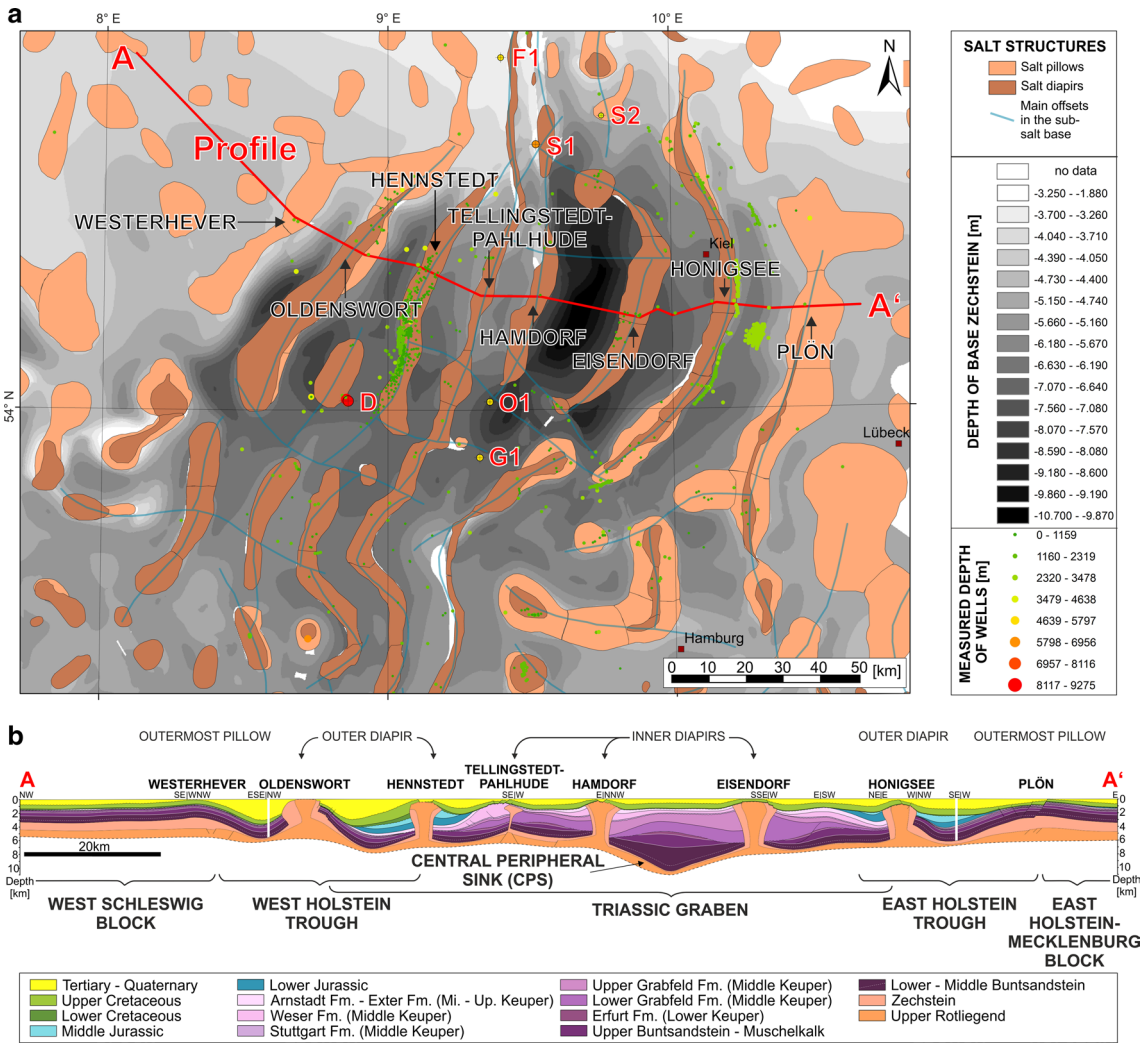

Fig. 2 **a** Map of the Glückstadt Graben area displaying the base of Zechstein (Late Permian), outlines of present-day salt structures (after Reinhold et al. 2008), locations of wells with maximum depths colour-coded and the trace of the cross section (*red*). Deep wells are labelled: D Dieksand, F1 Flensburg Z1, G1 Glückstadt T1, O1 Oldenbuettel T1, S1 Schleswig Z1, S2 Steinfeld Z1. Note that due to horizontal deviation of the well path, the measured depth of the wells is usually higher than the true vertical depth. **b** Cross section of the Central Glückstadt Graben displaying salt walls and sedimentary patterns of the post-Permian strata (modified from Baldschuhn 1996). The depth of the Top Lower Buntsandstein (*white dashed line*) was inferred from regional thickness maps (Doornenbal and Stevenson 2010)

depocentres striking mostly parallel to the graben axis of the Glückstadt Graben suggest that salt flowed mainly perpendicular to the graben axis. Therefore, this study focuses on a representative geological cross section that is based on a seismic interpretation (Baldschuhn 1996) and crosses the entire central Glückstadt Graben (Fig. 2).

Geological and structural setting

The NNE-SSW to NE-SW striking Glückstadt Graben is part of an assembly of scattered Permo-Triassic extensional basins within the larger Central European Basin System (CEBS) (Maystrenko et al. 2006; Littke et al. 2008; Scheck-Wenderoth et al. 2008a) (Fig. 1). The Glückstadt Graben is framed by the Rynkøbing-Fyn High to the north and the Pompeckj Block to the south. To the east and west, the Glückstadt Graben is surrounded by platforms of almost undeformed sediments (West Schleswig Block, East Holstein-Mecklenburg Block).

In the basin centre, numerous more than 6000-m-high salt walls coincide with offsets in the sub-salt basement (Fig. 2). The mobile layer building the salt structures contains Upper Rotliegend and Zechstein (Upper Permian) evaporites. Three-dimensional forward modelling predicts an original salt layer (Upper Rotliegend and Zechstein)

thickness of as much as 3000 m in the basin centre, approximately 1500 m on the eastern flank and 1700 m on the western flank of the graben (Maystrenko et al. 2005a). Information on the nature and the configuration of the subsalt basement in the basin centre is sparse due to the lack of deep boreholes and because seismic imaging is heavily impaired by the strong attenuation of seismic energy at the boundaries of the salt layer (Baykulov et al. 2009; Maystrenko et al. 2005b).

The Glückstadt Graben contains the thickest Meso-Cenozoic succession of the entire CEBS (~11 km). Triassic strata exhibit their maximum thickness in a ~20-km-wide trough in the central part of the Glückstadt Graben, which extends roughly 100 km in north–south direction. In particular, Middle to Upper Keuper (Upper Triassic) sediments fill up to 6000-m-deep asymmetric peripheral sinks adjacent to the inner salt walls (Tellingstedt-Pahlhude, Hamdorf and Eisendorf). According to Maystrenko et al. (2005a), the region of increased Triassic thickness is here referred to as the Triassic Graben (Fig. 2b). Lower to Middle Jurassic sediments are only preserved in secondary peripheral sinks of the outer, Hennstedt and Honigsee salt walls. Lower to Upper Cretaceous strata cover the innermost salt walls and are only slightly thickened in the peripheral sinks of the Hennstedt and Honigsee structures. Cenozoic sediments display again increased thicknesses adjacent to all salt walls in two marginal troughs, the West Holstein Trough and the East Holstein Trough (Maystrenko et al. 2005a). In the outer part of the basin, the Glückstadt Graben is bounded by undeformed areas of the West Schleswig Block and the East Holstein-Mecklenburg Block. The basic structural pattern of main depocentres and salt walls continues northward of the cross section for roughly 50 km and southward for roughly 100 km (Fig. 2a) (Baldschuhn et al. 2001; Maystrenko et al. 2005a).

Tectonic evolution

The early tectonic history of the region of the Glückstadt Graben supposedly started with transtensional tectonics during the Late Carboniferous to Early Permian, which was associated with faulting and igneous activity (Ziegler 1982, 1990; Gast and Gundlach 2006; Kley et al. 2008). The Permian transtension was followed by a long-lasting period of thermal subsidence in the entire Permian Basin from the Late Permian to the beginning of the Early Triassic (e.g. Bachmann and Grosse 1989; Van Wees et al. 2000; Littke et al. 2008). During the Triassic, thermal subsidence was interrupted by numerous episodes of regional extension indicated by variations in sedimentary onlap patterns (e.g. Maystrenko et al. 2006) and locally increased subsidence rates (e.g. Littke et al. 2008; Rodon and Littke 2005). This extension led to segmentation of the larger Southern Permian Basin (Doornenbal and Stevenson 2010) into separated grabens or troughs, e.g. the Glückstadt Graben, the Horn Graben or the Central Graben (Kley et al. 2008; Van Wees et al. 2000). Early phases of post-Permian extension in the Glückstadt Graben are postulated for the Early Triassic (Middle Buntsandstein time: mainly Detfurth and Hardegsen Formations) and for the Middle Triassic (Upper Buntsandstein–Middle Muschelkalk) (Röhling and Gast 1991; Brink et al. 1992; Kockel 2002). During these events, a relatively narrow graben formed in the centre of the Glückstadt Graben (Brink et al. 1992). In Late Triassic times (Grabfeld Formation and Weser Formation time), E-W-directed extension occurred in the area of the Glückstadt Graben ("Early Kimmerian phase") (Frisch and Kockel 1999; Jaritz 1987; Kockel 2002; Maystrenko et al. 2006; Ziegler 1982). This caused a widening of the graben and intense salt movements including diapirism (Brink et al. 1992; Maystrenko et al. 2005a). In Middle to Late Jurassic times, regional NE-SW extension prevailed ("Middle Cimmerian phase") in some parts of the CEBS (Kockel 2002; Kley et al. 2008). This event probably affected the marginal parts of the Glückstadt Graben (Maystrenko et al. 2005a), but far less than the neighbouring areas, in particular Lower Saxony Basin to the south. A major interruption of sedimentation and regional erosion in the area around the Glückstadt Graben can be recognised from the Kimmeridgian to the Valanginian (Late Jurassic–Early Cretaceous (Maystrenko et al. 2005a). The depth of erosion is estimated to be roughly 800 m in the central area of the Glückstadt Graben (Maystrenko et al. 2005a; Littke et al. 2008). The Late Cretaceous is a phase of enhanced subsidence in the Glückstadt Graben. From Coniacian to Campanian, a NW-SE-directed shortening regime prevailed in Central Europe (Kley et al. 2008; Ziegler 1990), which significantly affected regions adjacent to the Glückstadt Graben (e.g. Lower Saxony Basin). In the Glückstadt Graben, roofs of the diapirs were slightly uplifted at the end of Cretaceous, which is probably a result of this regional compression (Maystrenko et al. 2006). During Eocene to Miocene time, ESE-WNW to E-W extension and contemporary NE-SW compression prevailed in Central Europe (Kley et al. 2008; Scheck-Wenderoth et al. 2008b). In this period, subsidence rates in the West Holstein Trough and in the East Holstein Trough attained its maximum (Maystrenko et al. 2005a).

Sedimentary history

The lack of deep wells prevents exact identification of sedimentary facies in the centre of the Glückstadt Graben. However, information about the stratigraphic succession in the central Glückstadt Graben was obtained from wells located on structural highs in the Glückstadt Graben (see Fig. 2a for location) and correlated with the centre of the

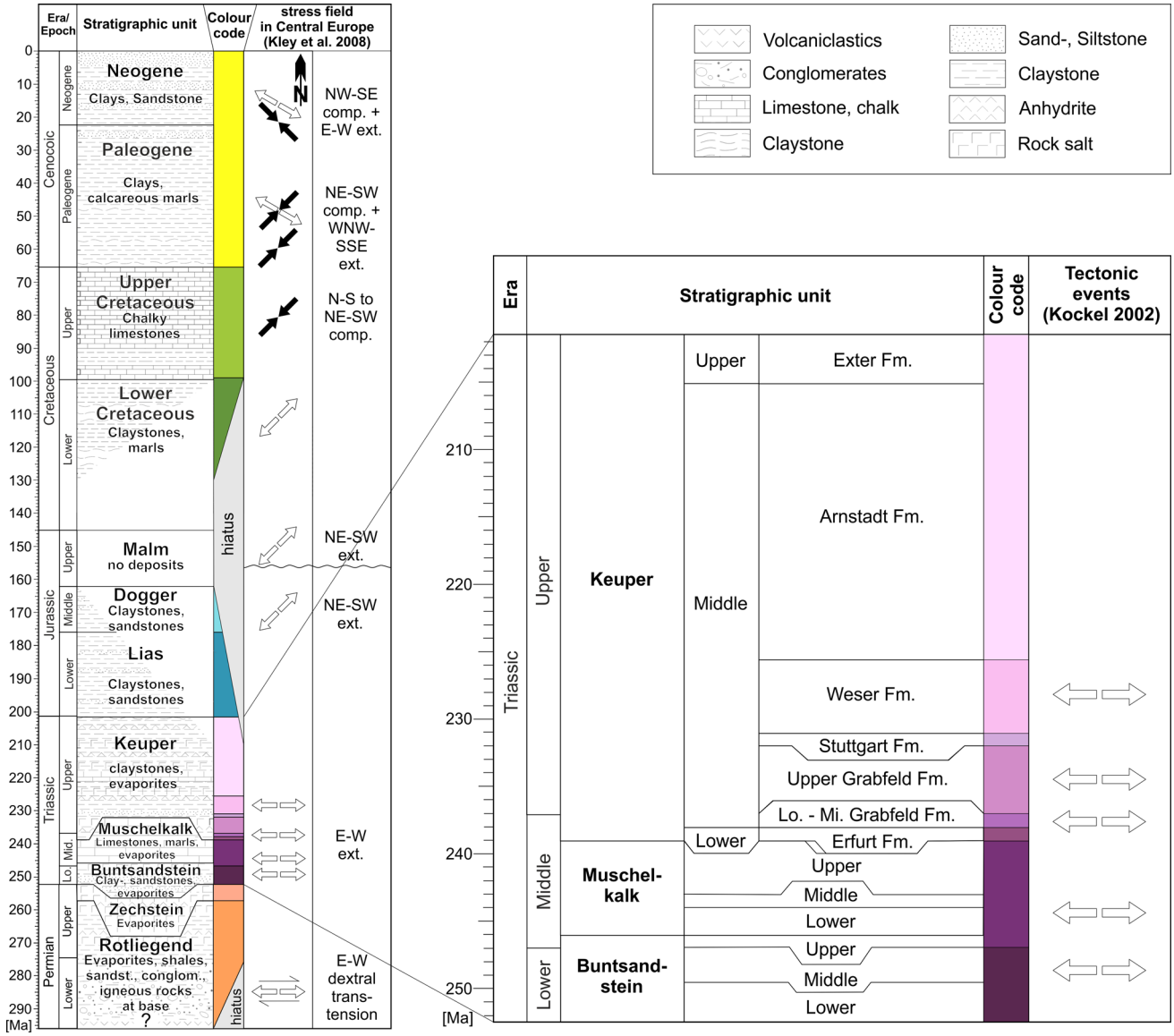

Fig. 3 Stratigraphy of the Glückstadt Graben (modified from Maystrenko et al. 2005a; Rodon and Littke 2005; Barnasch 2010). Colour coding of stratigraphic units as in the geological cross section

basin (Maystrenko et al. 2005b). The stratigraphic succession in the area of the Glückstadt Graben can be divided into three main parts (Maystrenko et al. 2005b): (1) the basement beneath the main salt layer consisting of clastic sediments, which are likely of Late Devonian to Early Permian age, (2) Lower to Upper Permian evaporites building the salt structures and (3) the Mesozoic to Cenozoic post-salt succession (Fig. 3).

The basement beneath the Permian salt is characterised by conglomerates and volcaniclastics, which grade upwards into clays and evaporites (Maystrenko et al. 2005b). The Permian Rotliegend evaporite succession consists mostly of rock salt (~55 % of the Rotliegend succession) with intercalated carbonates and clastics deposited in sabkha and desert lake environments (Maystrenko et al. 2005a). The Zechstein consists of seven more or less complete evaporation cycles (dominantly rock salt, carbonates, anhydrites and potassium salts) deposited under marine conditions (Stollhofen et al. 2008). The sedimentary succession of the Triassic starts with continental deposits of the Lower to Middle Buntsandstein (Lower Triassic) mainly consisting of fluvio-lacustrine siliciclastics and minor evaporites (Lepper et al. 2013). Marine conditions from Late Buntsandstein until the end of Muschelkalk (Middle Triassic) time lead to the sedimentation of shallow marine limestones and marlstones with significant intercalations of evaporites in the Upper Buntsandstein (Roet) and the Middle Muschelkalk (Stollhofen et al. 2008). During Keuper time (Late

Middle Triassic–Late Triassic), depositional environments in the CEBS changed back to continental facies (Barnasch 2010). The Erfurt Fm. (Lower Keuper) mainly contains siliciclastics deposited in a continental and partly marine environment (Beutler 2005; Stollhofen et al. 2008). The Middle Keuper Grabfeld and Weser Fms. are dominated by sabkha and playa facies represented by claystones and siltstones and widespread intercalations of evaporites (mainly anhydrites and rock salt). Both formations are separated by the Stuttgart Fm. consisting of fluvio-deltaic sandstones (Stollhofen et al. 2008). The Arnstadt Fm. (Middle Keuper) contains mudstones of playa lake origin. The Exter Fm. (Upper Keuper) is characterised by a transition of continental environments to marine conditions dominated during Jurassic (Stollhofen et al. 2008). Sediments of Early to Middle Jurassic age are composed of shallow marine carbonates and marine clastics (Stollhofen et al. 2008). After a major hiatus from Late Jurassic time to the beginning of the Early Cretaceous, fluvio-deltaic claystones and subordinate sandstones were deposited unconformably over Triassic and Jurassic strata (Maystrenko et al. 2005a). The global eustatic sea level highstand led to deposition of chalky limestones during the Late Cretaceous. An additional erosional unconformity separates Mesozoic and Cenozoic sediments. Since the Early Tertiary, fluvial and lacustrine clastics prevailed (Stollhofen et al. 2008).

Data base and method

The available data consist of a geological cross section (Fig. 2b) provided in the Geotectonic Atlas of Northern Germany (GTA) (Baldschuhn 1996; Baldschuhn et al. 2001). The cross section is based on interpreted 2D seismic data. Depth migration of the interpreted seismic line is based on Jaritz et al. (1991). In order to show the structures on the platforms bounding the Glückstadt Graben, we used two additional cross sections from Baldschuhn et al. (2001), which have been attached to the east and west of the original cross section (Baldschuhn et al. 2001). This cross section is similar to other seismic sections trending parallel to it (Baldschuhn et al. 2001; Baykulov et al. 2009; Maystrenko et al. 2005a) and is therefore taken to be representative of the general structural framework of the Glückstadt Graben. The post-Permian sedimentary succession is subdivided into 13 units (Table 1). The geological cross sections of the Geotectonic Atlas of Northern Germany are based on depth-migrated seismic interpretations, which were correlated with borehole data (Baldschuhn et al. 2001; Hese 2012). Nevertheless, there are ongoing debates concerning the accuracy of the interpretation in particular for the base of the Lower Triassic, the base of the Permian salt layer and the pre-Permian layers (e.g. Bayer et al. 2003; Maystrenko et al. 2005b).

Decompaction and restoration

Compaction and subsidence were sequentially restored using simple shear along vertical planes (Bishop et al. 1995; Buchanan et al. 1996; Rowan 1993). The work procedure included decompaction and vertical simple shear restoration of all post-Permian layers employing the 2DMOVE™ software package (Midland Valley) to obtain the sequential evolution of sediment accumulation for each unit. As is common usage, the decompaction tool available in 2DMOVE™ assumes that porosity is mostly lost due to mechanical compaction, while chemical compaction is not included. Thus, porosity gradually decreases according to an equation first presented by Athy (1930):

$$\phi(z) = \phi_0 e^{-cz} \tag{1}$$

where Φ is the porosity, Φ_0 the initial porosity, c the compaction factor and z the burial depth. Lithological and petrophysical data (density, initial porosity) used for the decompaction calculation (Table 1) were taken from published data from the Glückstadt T1 (Rodon and Littke 2005), Schleswig Z1, Flensburg Z1, and Oldenbuettel T1 wells (Schöner 2006) (see Fig. 2 for location) as well as from stratigraphic studies (Barnasch 2010; Lepper et al. 2013). Using this information, the average lithological composition was estimated for each stratigraphic unit considered here (Table 1). For the compaction factor c, default values implemented in the MOVE™ software package (Midland Valley), Yegorova et al. (2008) and Allen and Allen (2013) were used. Initial porosities and porosity–depth coefficients applied here (see used values in Table 1) represent average values with regard to the lithological composition. A reduced depth coefficient of 0.1 was assigned for the Lower Triassic sandstones instead of using a standard porosity–depth factor $c = 0.27$ for sandstone. It has been shown that sandstones of the Lower Triassic Buntsandstein in the North German Basin and the Netherlands possess high porosities (25–35 %, including cements) due to early cementation even at greater depth (1500–4000 m) (e.g. Purvis and Okkerman 1996; Wolfgramm et al. 2008). However, Lower Triassic clays were assumed to compact with a standard coefficient of $c = 0.51$, which results in an average compaction coefficient of $c = 0.305$ for the Lower to Middle Buntsandstein unit (Table 1).

In order to estimate errors on decompacted layer thicknesses of all units, a sensitivity study was carried out applying maximum and minimum values for initial porosity and compaction coefficients (Table 1).

Table 1 Lithologies and petrophysical parameters used for decompaction procedure and sensitivity analysis

Unit/ formation	Age of top (Myr)	Lithology	% Sandstone	% Claystone	% Chalk	% Limestone	% Evaporites	c (min) [km^{-1}]	c (max) [km^{-1}]	c (used) [km^{-1}]	ϕ_0 (min)	ϕ_0 (max)	ϕ_0 (used)	ρ_G[kg m^{-3}]
Tertiary + Quatenary	0	SHALE, SHALEsand, SANDshale[1, 2]	0.4	0.6	0	0	0	0.27	0.51	0.414	0.48	0.57	0.558	2680
Upper Cretaceous	65.5	CHALK, Limeshaly[1, 2]	0	0.1	0.7	0.2	0	0.68	0.71	0.69	0.57	0.65	0.568	2709
Lower Cretaceous	99.5	SHALEcarb[1, 2]	0	0.8	0.2	0	0	0.4	0.71	0.55	0.52	0.52	0.65	2702
Upper Jurassic	145.5	No sediments	–	–	–	–	–	–	–	–	–	–	–	–
Middle Jurassic	162	SHALEsand[1, 2]	0.3	0.7	0	0	0	0.33	0.51	0.438	0.63	0.63	0.581	2685
Lower Jurassic	176	SHALE, SHALEsand, SHALEcalcsand[1, 2]	0.1	0.8	0.1	0	0	0.33	0.71	0.506	0.55	0.57	0.627	2696
Arnstadt–Exter Fm. (Middle–Upper Keuper)	201.5	SHALEcarb, SHALEevap, SHALEsand[1, 2, 4]	0.1	0.5	0.3	0	0.1	0.39	0.71	0.478	0.48	0.62	0.563	2688
Weser Fm. Middle Keuper	226	SHALEcarb, SALT[1, 2, 4]	0	0.4	0.1	0	0.5	0	0.51	0.275	0.52	0.62	0.33	2651
Stuttgart Fm. (Middle Keuper)	231	SAND&SHALE, SHALEsand[1, 2, 4]	0.2	0.8	0	0	0	0.27	0.51	0.428	0.49	0.52	0.604	2690
Upper Grabfeld Fm. (Middle Keuper)	234	SHALEcarb, SHALEevap, SALT[1, 2, 4]	0	0.6	0	0	0.4	0	0.51	0.306	0.47	0.62	0.394	2660
Lower–Middle Grabfeld Fm. (Middle Keuper)	237	SHALEcarb, SHALEevap, SALT[1,2, 4]	0	0.6	0	0	0.4	0	0.51	0.306	0.47	0.62	0.394	2660
Erfurt Fm. (Lower Keuper)	238	SHALEcarb, SHALE[1,2, 4]	0	0.8	0.2	0	0	0.51	0.71	0.55	0.62	0.65	0.65	2702

Table 1 continued

Unit/ formation	Age of top (Myr)	Lithology	% Sandstone	% Claystone	% Chalk	% Limestone	% Evaporites	c (min) [km^{-1}]	c (max) [km^{-1}]	c (used) [km^{-1}]	ϕ_0 (min)	ϕ_0 (max)	ϕ_0 (used)	ρ_G[kg m^{-3}]
Upper Buntsandstein–Muschelkalk	238.8	LIME, SHALEevap, MARLcarb[1,2]	0	0.3	0.1	0.3	0.3	0	0.71	0.344	0.39	0.47	0.335	2674
Lower–Middle Buntsandstein	247.1	SAND&SHALE, SHALEsand, SHALE-calcsand[1, 2, 3]	0.4	0.6	0	0	0	0.27	0.51	0.346	0.52	0.57	0.558	2680
Zechstein	252.7	EVAPORITES[1, 2]	0	0	0	0	1	–	–	–	0	0	0	2685
Upper Rotliegend	260.5	EVAPshaly, SHALEsilt[1, 2]	0	0.5	0	0	0.5	–	–	–	–	–	–	2600

Capital letters in the description of the lithologies denote the main lithologic component. Chronostratigraphic ages of layer boundaries came from Kozur and Bachmann (2008) and Littke et al. (2008). Default values for c according to each lithology came from Schöner (2006). ρ_G is the average grain density. References for lithology: (1) Rodon and Littke (2005), (2) Schöner (2006), (3) Barnasch (2010), (4) Lepper et al. (2013). Reference for ϕ_0: Schöner (2006). Default values for c are (Sclater and Christie 1980), 2DMOVE™ software package): shale: 0.51, sand: 0.27, chalk: 0.71, limestone: 0.4, evaporites: 0.0

In the reconstruction procedure presented here, the load effect of the uppermost layer is removed, whereupon all underlying layers decompact. All decompacted horizons are then restored applying vertical shear restoration. The top of the uppermost layer is made horizontal, and all deeper layers are passively uplifted with equal vertical displacement vectors. The vertical shear restoration preserves the thickness of each layer, but distorts horizon lengths. We assume that three-dimensional salt flow is balanced by vertical movement of the post-salt peripheral sinks. Therefore, two-dimensional restoration of the subsidence of post-salt layers can be applied, if the cross section is chosen to strike perpendicular to main trend of the elongated salt structures and the tectonic fault pattern in the sub-salt basement (Hossack 1995).

The structural restoration was limited to the post-salt layers, since neither the salt layer nor the sub-salt basement could be restored directly. This is because the present-day geometry of the top basement is difficult to identify in seismic data (see model limitation). However, for subsidence curves and interpretive sketches, the configuration of the basement was drawn by assuming a maximum original salt layer (Zechstein and Upper Rotliegend) thickness of 1500 m above the eastern graben flank and 3000 m in the basin centre (Maystrenko et al. 2005a) and by adopting the basement faults shown on the structural map of Northern Germany provided by the GTA (Baldschuhn et al. 2001). For the sake of simplicity, both Permian evaporite successions (Upper Rotliegend and Zechstein) are considered as a single mobile layer named "salt layer" throughout this paper. The basement beneath the salt layer thus corresponds to the base of the salt-rich Rotliegend. Furthermore, the term "pre-kinematic" is used for sediments deposited before salt structure growth, "syn-pillow" for sediments accumulated in primary peripheral sinks (sensu Hudec and Jackson 2011) during the salt pillow stage and "syn-diapiric" for sediments accumulated in secondary peripheral sinks (sensu Hudec and Jackson 2011) attributable to a specific salt diapir. Furthermore, salt structures in the transitional stage from pillow to diapir are called "immature", salt structures in a downbuilding stage are called "mature", and diapirs which ceased to grow are named "dormant diapirs". The side of a salt structure is called "inner side" if it faces the centre of the graben and "outer side" if it faces the graben flanks.

Subsidence curves, subsidence rates and salt structure growth

Decompacted layer thicknesses were measured across 102 1D profiles along the restored cross section for each time step. This enables us to quantify (1) magnitudes of salt structure growth, (2) the total subsidence, and (3)

subsidence rates averaged for each time interval considered here.

1. The amount of growth of each salt structure was determined from the thickness changes in the neighbouring peripheral sinks assuming that growth can be calculated by the relative difference between the thickness of neighbouring sediments and the crest of the salt structure. Furthermore, we assumed that salt structures pass through the pillow stage as long as they are surrounded by primary peripheral sinks and that they enter the diapiric stage as soon as they are encompassed by secondary peripheral sinks. During the pillow stage, amounts of growth h_P are defined as half the maximum thickness of the adjacent primary peripheral sinks minus the thickness above the pillow crest (Fig. 4) (Seni and Jackson 1983). For the diapir stage, the amount of growth h_D equals the average maximum thickness of the secondary peripheral sink on both sides of the diapir (Fig. 4). Values determined by this method have to be considered as first-order estimates. This is because, near-surface salt dissolution and erosion of sediments from the peripheral sinks cannot be quantified, but may enhance or reduce the actual amount of growth (see model limitations).
2. Following the backstripping procedure of Allen and Allen (2013), 1D tectonic subsidence curves were calculated from total subsidence. The tectonic subsidence S_{tec}—this contains fault-induced subsidence, thermal subsidence and subsidence induced by salt expulsion—was calculated by subtracting the Airy isostatic subsidence induced by the sediment load from the total subsidence and by correcting it for paleo-water depth S_{PW} and eustatic sea level change ΔS_{SL} (Allen and Allen 2013):

$$S_{tec} = H\left(\frac{\rho_M - \overline{\rho_S}}{\rho_M - \rho_W}\right) - \Delta S_{SL}\left(\frac{\rho_W}{\rho_M - \rho_W}\right) + (S_{PW} - \Delta S_{SL}) \quad (2)$$

Here, H is the total decompacted sedimentary thickness, ρ_M the density of the mantle (3300 kg/m^3), ρ_W the density of sea water (1050 kg/m^3), and $\overline{\rho_S}$ the average bulk density of the entire sedimentary column. Information about paleo-water depths came from well data (Schöner 2006 and references therein), and values of the eustatic sea level change were taken from Haq et al. (1987).

Since the basement of the salt layer was excluded from the restoration procedure, we refrained from reconstructing the amount of basement extension and the exact backstripping of the basement of the salt layer. However, we attempted to distinguish the effect of subsidence induced by salt expulsion S_{sa} from tectonic subsidence. We assumed a specific initial thickness of the Upper Permian salt layer (as explained above) at the end of Permian. This thickness decreases beneath peripheral sinks and increases in regions of salt structure uplift (e.g. growing salt pillows) through time. Hence, we defined an amount of thickness change in the salt layer for each time step, which was either added to or subtracted from the original salt layer thickness, respectively. The magnitude of these thickness changes in each time interval was estimated by the depth of the crestal erosion or the depth of the peripheral sink in relation to the regional thickness of each layer. Based on estimations of subsidence induced by salt flowage, the Upper Permian salt layer can be added to the total subsidence of the base Buntsandstein and, therefore, incorporated into the backstripping procedure (Eq. 2). Eventually, that gives the tectonic subsidence for the base of the salt layer.
3. Subsidence rates were calculated by dividing the incremental total subsidence of the base of the Buntsandstein by duration of the considered time interval. This calculation provides subsidence rates without including subsidence due to sediment compaction. Furthermore, it underestimates subsidence rates in periods of low temporal resolution of the layering, e.g. the Cretaceous or the Tertiary.

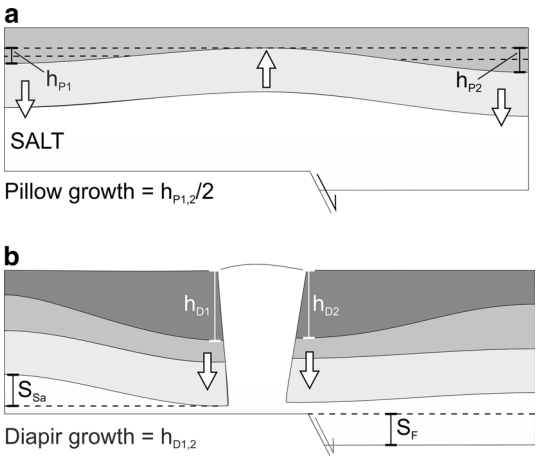

Fig. 4 Sketch showing the method for calculating net growth of a salt structure. **a** Growth of a salt pillow equals half of the layer thinning above the pillow crest assuming that layer thinning is syn-depositional. The other half of $h_{P1/2}$ is accounted for the subsidence of the peripheral sink. **b** Growth of a diapir is calculated by the depth of the surrounding secondary peripheral sink assuming that the top of the diapir remains at or close to the surface. Additionally, the amounts of fault-induced subsidence S_F and subsidence induced by salt expulsion S_{Sa} are indicated

Results

Evolution obtained from 2D-retro deformation

Figure 5 shows the sequentially restored cross sections in a chronological sequence. This illustration summarises the evolution of peripheral sinks in the Glückstadt Graben.

First phase: Buntsandstein to Early Keuper time

The post-Permian evolution of the Glückstadt Graben started with the formation of a deep approximately 15-km-wide basin-centred synclinal depocentre, here referred to as central peripheral sink (CPS) (Fig. 5a). In the CPS, the decompacted thickness of Lower to Middle Buntsandstein layers reaches 4500 m and decreases to roughly 1500 adjacent to the innermost salt structures. The thickness of the Lower–Middle Buntsandstein averages 1000–1200 m above the West Schleswig Block. In the western part of the Glückstadt Graben, the thickness of the Lower to Middle Buntsandstein varies adjacent to some salt structures (Tellingstedt-Pahlhude, Hennstedt). These thickness variations indicate development of normal faults and local, 5- to 10-km-wide uplifts. Above the East Holstein-Mecklenburg Block, the Lower to Middle Buntsandstein is nearly isopachous. Here, differences in thickness probably began to develop adjacent to the Honigsee salt diapir first in the period from Late Buntsandstein to Muschelkalk time.

Upper Buntsandstein to Lower Keuper strata taper towards the boundaries of the salt walls and are thickest in the centres between the salt structures. This led to the formation of symmetric bowl-shaped primary peripheral sinks (PPS) (Fig. 5b). Furthermore, erosional unconformities of Buntsandstein to Lower Keuper units are spatially associated with salt structures (Fig. 2). This indicates that part of the thickness decrease close to the salt structures is due to post-depositional erosion on top of rising salt structures. The pattern of increased subsidence in the centres of the PPSs continued until the end of Early Keuper time without significant lateral migration of the main depocentres.

Second phase: Middle Keuper to Middle Jurassic time

With the beginning of the Grabfeld Fm. (Middle Keuper) time, increased layer thickness is found over an approximately 70-km-wide region (Triassic Graben) (Fig. 5c, d). In this region, thicknesses of Middle to Upper Keuper strata range from 1000 to 6000 m. The depocentres in the peripheral sinks moved from the centres of the PPSs towards their flanks. This shift caused the formation of asymmetric wedge-like deposits (secondary peripheral sinks) adjacent to the salt wall boundaries and of double-wedge-like turtle-back structures (sensu Hudec and Jackson 2011), e.g. between the innermost salt structures.

Fig. 5 2D restoration of the supra-salt (post-Permian) strata. **a**, **b** ▶ Phase 1: The central peripheral sink subsides. Additional thickness variations occur above the graben flanks. **c**, **f** Phase 2: Adjacent to the innermost salt structures deep secondary peripheral sinks develop. Until the Middle Jurassic, locations of main depocentres migrate towards the graben flanks. **g**, **h** Phase 3: Most salt structures become buried by Lower Cretaceous sediments and are partly reactivated during the Tertiary. The outermost salt structures are most active during this phase. The geological cross section (**h**) was modified from Baldschuhn (1996). Note that horizontal strain (mostly extensional) is not considered. Locations of the present-day diapirs are covered with transparent areas in the reconstructed cross section, which does not imply whether each salt structure is in a diapir stage or still covered by overburden in the specific period. The depth of the Top Lower Buntsandstein (white dashed line) was inferred from regional thickness maps (Doornenbal and Stevenson 2010). Black triangles denote locations of main depocentres. CPS—Central peripheral sink, PPS—Primary peripheral sink, SPS—Secondary peripheral sink

During deposition of the Lower to Middle Grabfeld Fm., SPSs first developed close to the salt structures of Tellingstedt–Pahlhude, Hamdorf and Eisendorf. During this short period (~1 Myr), subsidence peaked at ~4500 m in the eastern SPS of the Eisendorf salt wall. The main depocentres (areas of strongest subsidence) are located adjacent to the innermost salt structures, but opposite the CPS. During Upper Grabfeld Fm. time, the main depocentres switched back to the inner side of the innermost diapirs (Fig. 5d). In this period, maximum decompacted layer thicknesses ranged from 2500 to 3500 m. No significant SPSs formed adjacent to the outer salt structures of Oldenswort, Hennstedt and Honigsee. However, layer thinning and erosional unconformities close to these salt structures (Fig. 2) indicate continued uplift since phase 1.

During deposition of the Stuttgart and Weser Fms. (Late Middle Keuper time), the deepest SPS developed next to the salt structure of Tellingstedt–Pahlhude, where these formations are as thick as 2200 m (Fig. 5e). During Arnstadt and Exter Fm. time, SPSs occurred next to the outer salt structures Hennstedt and Honigsee. Subsidence close to the innermost diapirs (Eisendorf, Hamdorf) continued. However, thicknesses of the Arnstadt and Exter Fms. next to these salt structures are smaller than those of the Grabfeld Fm.

In the latest stage of phase 2, from Early to Middle Jurassic time, SPSs of the outer diapirs of Hennstedt and Honigsee continued to subside. Here, a maximum of 1300 m of Early Jurassic and 1100 m of Middle Jurassic sediments accumulated (Fig. 5f). Thinning of Keuper and Lower to Middle Jurassic strata over the Plön salt pillow denotes the occurrence of an uplifted pillow crest until the beginning of the Early Cretaceous. Different from the innermost salt structures, SPSs of the outer salt structures (Hennstedt, Tellingstedt–Pahlhude, Honigsee) are first deeper on their inner sides. Later, the main depocentres in the SPSs switch to the outer sides of these salt structures.

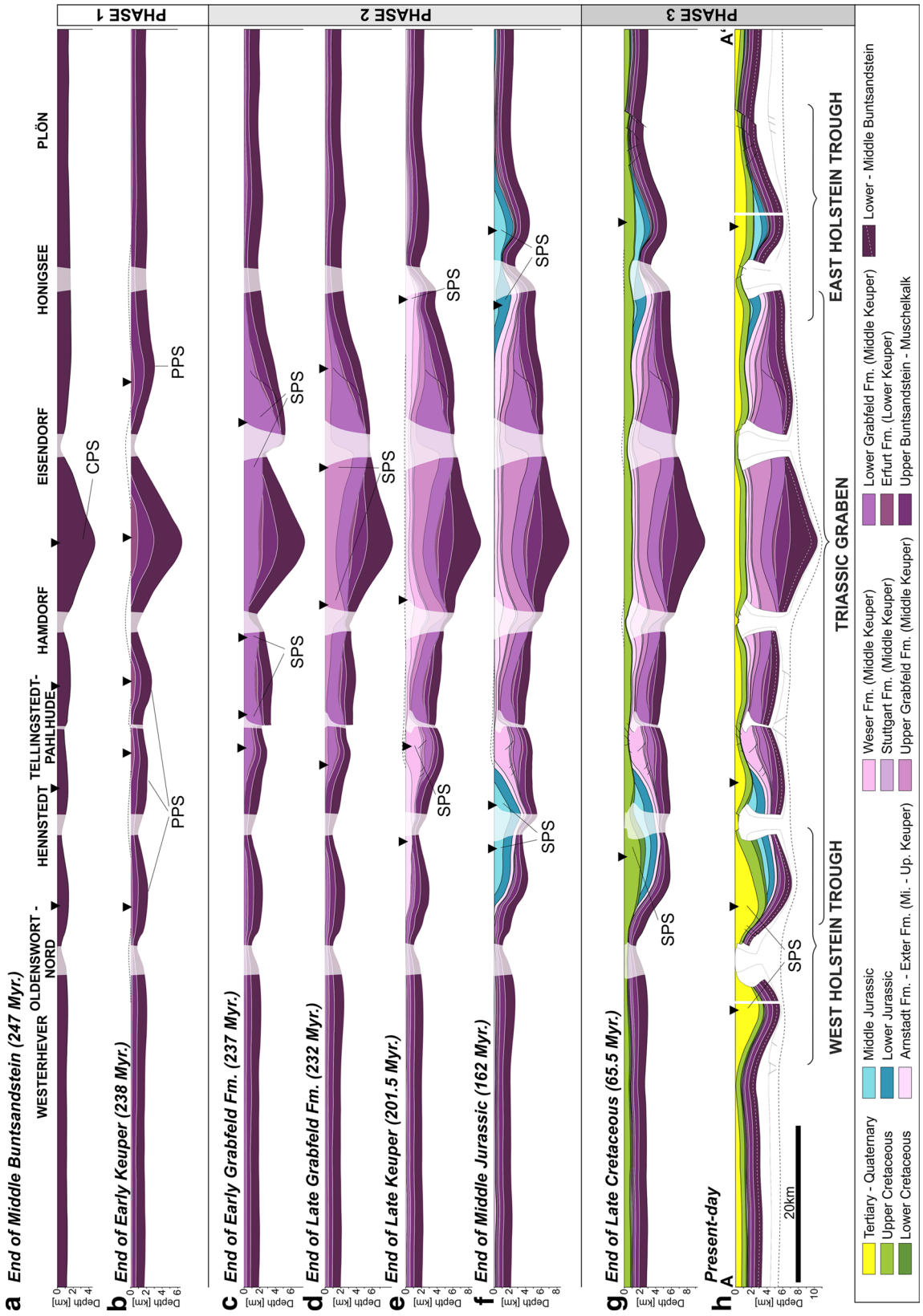
PHASE 1
PHASE 2
PHASE 3
WESTERHEVER
OLDENSWORT - NORD
HENNSTEDT
TELLINGSTEDT-PAHLHUDE
HAMDORF
EISENDORF
HONIGSEE
PLÖN
a End of Middle Buntsandstein (247 Myr.)
b End of Early Keuper (238 Myr.)
c End of Early Grabfeld Fm. (237 Myr.)
d End of Late Grabfeld Fm. (232 Myr.)
e End of Late Keuper (201.5 Myr.)
f End of Middle Jurassic (162 Myr.)
g End of Late Cretaceous (65.5 Myr.)
h Present-day
CPS
PPS
SPS
A
A'
WEST HOLSTEIN TROUGH
TRIASSIC GRABEN
EAST HOLSTEIN TROUGH
20km
Depth [km]
Tertiary - Quaternary
Upper Cretaceous
Lower Cretaceous
Middle Jurassic
Lower Jurassic
Arnstadt Fm. - Exter Fm. (Mi. - Up. Keuper)
Weser Fm. (Middle Keuper)
Stuttgart Fm. (Middle Keuper)
Upper Grabfeld Fm. (Middle Keuper)
Lower Grabfeld Fm. (Middle Keuper)
Erfurt Fm. (Lower Keuper)
Upper Buntsandstein - Muschelkalk
Lower - Middle Buntsandstein

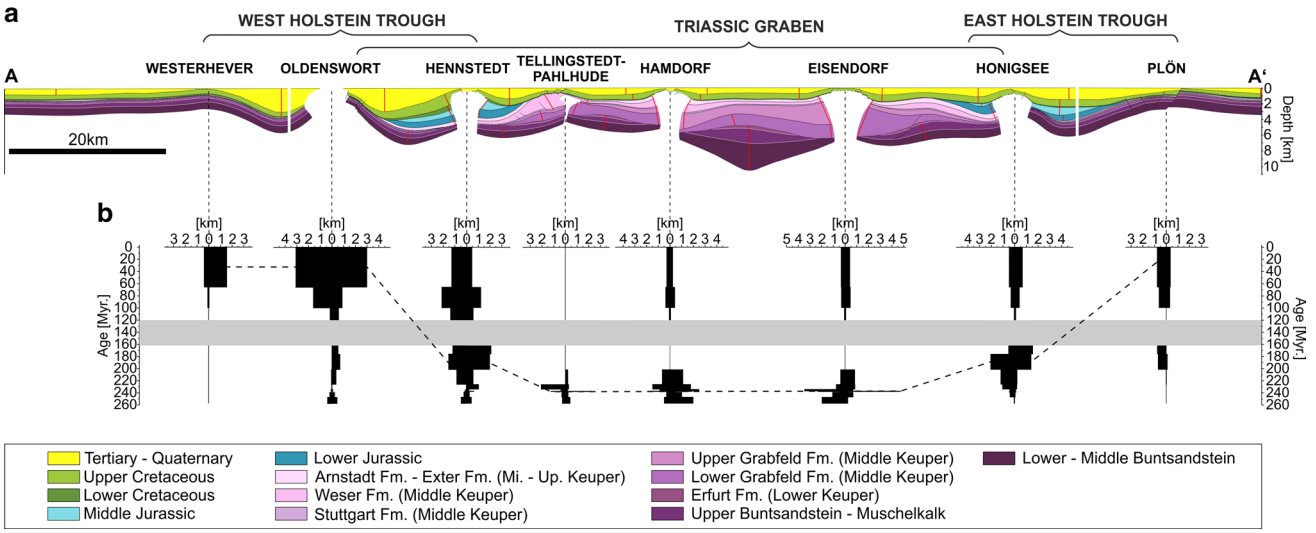

Fig. 6 Timing and amounts of growth of the salt structures in the Glückstadt Graben related to the geological cross section. **a** Geological cross section through the Glückstadt Graben. **b** Diagrams displaying amounts of salt structure growth (*black bars*) calculated from the depth of peripheral sinks on both sides (*red lines* in **a**). The *grey shaded interval* marks the hiatus during the Late Jurassic–Early Cretaceous. The *dashed line* connects phases of maximum growth of each salt structure through time

Third phase: Early Cretaceous to present

After a hiatus from the Late Jurassic to the beginning of the Early Cretaceous, Lower Cretaceous strata (mainly Barremian-Hauterivian) with an almost constant thickness of 80–90 m were deposited across the crests of the inner diapirs (Fig. 5g). Only in the vicinity of the Hennstedt diapir, Lower Cretaceous layers onlap the diapir flanks and form minor SPSs. During the Late Cretaceous, regional sedimentary thickness is 700–1000 m on average. Increased layer thicknesses (~2200 m) were found in the SPS of the Hennstedt diapir. Furthermore, Upper Cretaceous strata are slightly thinned and truncated above the crests of the other diapirs. This indicates uplift of the tops of the diapirs at the end of the Late Cretaceous.

During the Cenozoic, SPSs only formed next to the outer salt wall Oldenswort (West Holstein Trough) with a max. depth of 3100 m. The outer SPS is at the same time the PPS of the outermost salt pillow Westerhever, which began to form in Cenozoic times. Besides the deeply subsided West Holstein Trough, Cenozoic sediments are also slightly thickened between the inner and the eastern salt structures and symmetrically thinned towards the diapirs' crests. Similar to earlier PPSs, this indicates uplift of the diapir roofs (Fig. 5h).

Growth of salt structures

Lateral thickness variations indicate that all salt structures in the Glückstadt Graben except the outermost salt pillows were initiated during Phase 1 (Fig. 6). The innermost salt structures Tellingstedt-Pahlhude, Hamdorf and Eisendorf show their strongest growth during the beginning of Grabfeld Fm. time. The growth of these structures then gradually slowed until the end of the Triassic. In contrast, uplift of the westernmost salt structures of Oldenswort and Hennstedt slowed down after its initiation in Early–Middle Triassic time. The uplift of the Hennstedt diapir was reanimated during Weser Fm. time and reached its maximum during the Early Jurassic, contemporaneous with the strongest uplift of the easternmost diapir Honigsee. This stage was accompanied by the initiation of the easternmost salt pillow of Plön. For the Late Jurassic, amounts of growth are indeterminable owing to the lack of sediments of this age. The Hennstedt and Oldenswort diapirs reveal growth during Early Cretaceous time, possibly indicating continuous rise since the Late Triassic. The uplift of the Oldenswort salt structure reached its maximum during the Cenozoic, accompanied by the initiation of the westernmost salt pillow Westerhever.

Overall, the main phases of salt structure growth became younger with increasing distance from the centre of the Glückstadt Graben (dashed line, Fig. 6). On average, the diapirs spent between 50 and 100 million years in a passive downbuilding stage.

Subsidence curves

Subsidence curves are presented for several characteristic peripheral sinks (Fig. 7). Generally, the total subsidence S_{tot} was strongest during Late Permian and Buntsandstein time. During Late Buntsandstein to Muschelkalk time,

subsidence slightly decelerated. An additional peak of subsidence occurred in the period from the Erfurt Fm. (Early Keuper) to the Grabfeld Fm. time. Thereafter and until the beginning of the Cretaceous, S_{tot} increased only slightly. Subsidence accelerated again in the entire basin during the Late Cretaceous.

By incorporating subsidence due to salt expulsion into the backstripping procedure, the tectonic subsidence of the base of salt layer S_{tecS} represents the actual tectonic subsidence of the basin. It can be shown that in periods of strong salt expulsion, tectonic subsidence of the base of Buntsandstein S_{tecB} is seemingly higher than S_{tecS}. In contrast, in the period before strong salt expulsion, S_{tecB} is seemingly lower than S_{tecS}. Curves of S_{tecS} reveal two phases of rapid tectonic subsidence: during Buntsandstein time and in the period from Early Keuper to Grabfeld Fm. time. In contrast, S_{tecS} nearly levels off during later phases, in which S_{tecB} is high, i.e. during the Jurassic (profiles 3, 4; Fig. 7), the Late Cretaceous (profile 4) and the Cenozoic (profile 2; Fig. 7).

The ratio between final tectonic subsidence and the final total subsidence S_{tecS}/S_{totS} ranges between ~0.5 on the graben flanks (profile 1; Fig. 7), ~0.4 in profiles in the Triassic graben (profiles 2 and 7; Fig. 7) and ~0.35 in the basin centre (profile 8; Fig. 7). Hence, the percentage of the isostatic component of the total subsidence is lower in the basin centre than at the plateaus. Since there is no evidence for fault activity at the graben plateau, it can be assumed that tectonic subsidence is completely composed of thermal subsidence (50 % of S_{totS}). In contrast, in the basin centre much of the tectonic subsidence is caused by fault-induced subsidence.

Note that Late Jurassic uplift and resulting removal of sediments were not included in the backstripping procedure. The apparent uplift observed in the curve of S_{tec} during the Late Jurassic is caused by sea level fluctuations.

Subsidence rates

Subsidence rates measured in the 1D profiles were projected onto the 2D cross section according to the position of each 1D subsidence profile on the horizontal axis (Fig. 8). During Early to Middle Buntsandstein time, maximum subsidence rates (~850 m/Myr) occurred in the CPS, while subsidence rates were ~250 m/Myr on average above the West Schleswig Block and the East Holstein-Mecklenburg Block. From Late Buntsandstein to Muschelkalk time, subsidence rates decreased. Enhanced subsidence rates can be observed during Early Keuper time with maximum amounts of 550 m/Myr in the CPS. At the beginning of phase 2 (Early to Middle Grabfeld time), highest subsidence rates can be observed for the entire geological history of the Glückstadt Graben with ~2000 m/Myr on average. The eastern SPS of the Eisendorf diapir subsided fastest at a maximum rate of 4600 m/Myr. By contrast, subsidence rates of the outer platforms of the Glückstadt Graben are approximately 200 m/Myr on average. In Late Grabfeld Fm. time, subsidence rates elevated in the CPS and in SPSs of the innermost diapirs (max. 500 m/Myr). Subsidence rates during the deposition of the Weser and Arnstadt Fms. decreased significantly to 100–200 m/Myr on average and maximum 300 m/Myr within the SPS of the Triassic Graben. Lower Jurassic sediments—preserved in the SPS of the outer diapirs—accumulated at maximum rates of 50 m/Myr. Maximal subsidence rates during the Middle Jurassic are slightly higher (max. 80 m/Myr). Including Late Jurassic erosion and the removal of ~800 m (e.g. Littke et al. 2008) of sediments, average subsidence rates can be as high as ~130 m/Myr.

After the Late Jurassic hiatus, subsidence rates remain generally low compared to those of the Triassic. Although deep depocentres formed in the East Holstein and the West Holstein Trough, maximum subsidence rates in these troughs are ~40 m/Myr averaged over the Late Cretaceous and ~35 m/Myr averaged over the Cenozoic. Even if we assume that the main Cenozoic sediment accumulation took place in Paleogene time with a maximum thickness of 3200 m in the West Holstein trough (Maystrenko et al. 2005a), subsidence rates remained lower than ~100 m/Myr.

Discussion

Salt structure evolution

First phase: Early Buntsandstein to Early Keuper time

Phase 1 is characterised by subsidence of primary peripheral sinks and initiation of most salt structures in the Glückstadt Graben. To explain the subsidence of the Central peripheral sink (CPS), Brink et al. (1992) suggested fault-controlled formation of a relatively narrow graben in the basement below the Permian salt layer. We suggest that the normal faults ("cover grabens") in the Buntsandstein and Muschelkalk layers above the graben flanks are decoupled from the basement faults by the thick salt layer (thin-skinned extension, e.g. Jackson and Vendeville 1994; Nalpas and Brun 1993; Stewart 2007) (Fig. 9a).

Layer thinning, erosional unconformities and sedimentary onlap patterns in the vicinity of the present-day salt diapirs (Baldschuhn 1996; Maystrenko et al. 2005a) implicate either the growth of salt pillows assuming that the salt layer was still covered by post-salt sediments, or of immature salt diapirs assuming that the salt structures were in the stage of pillow to diapir transition (Sørensen 1998). We suggest that the formation of cover grabens during phase

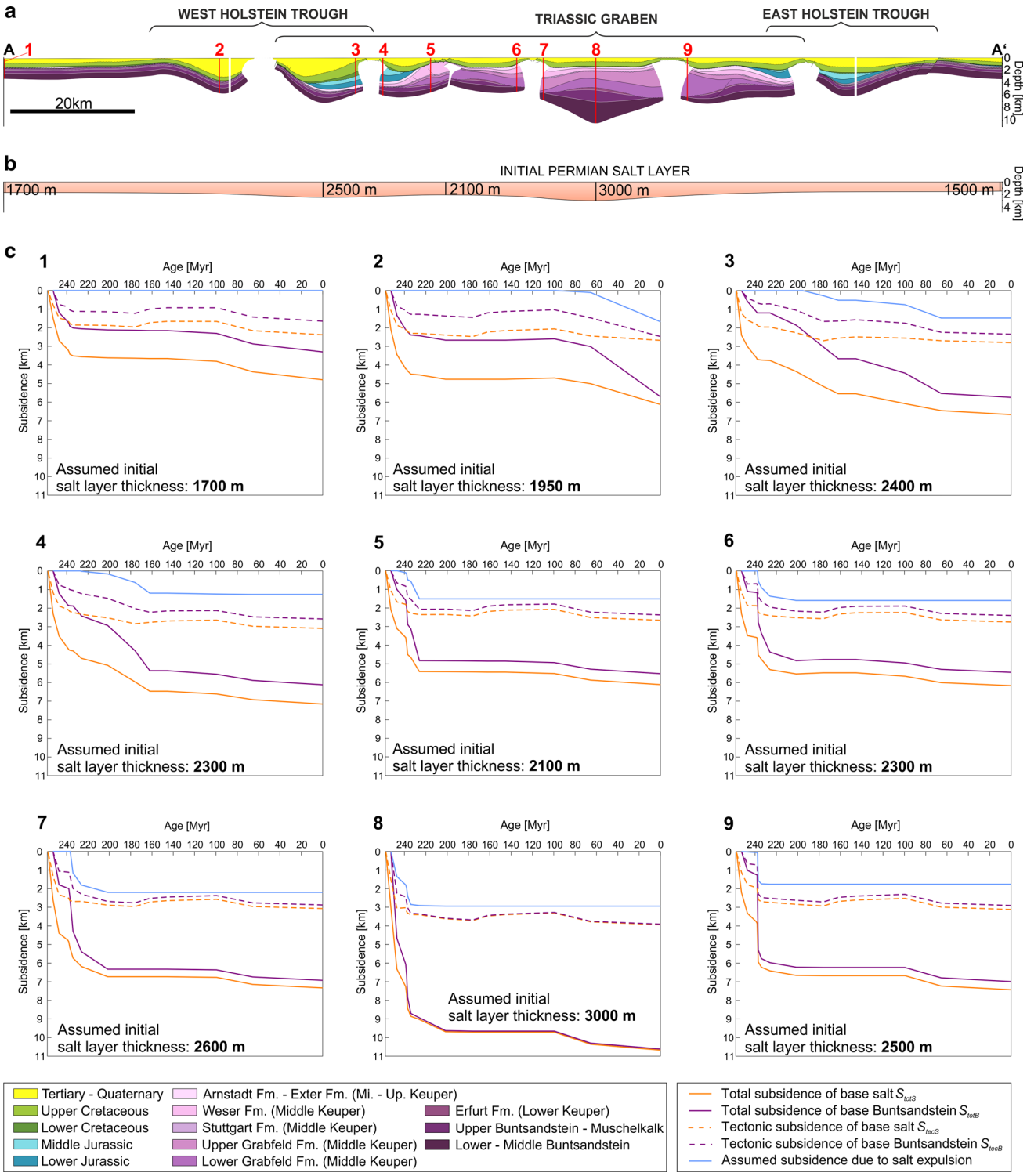

Fig. 7 Subsidence curves for some characteristic peripheral sinks of the Glückstadt Graben. **a** Geological cross section showing locations of the presented subsidence curves. **b** Cross section showing the initial thickness of the Upper Permian salt layer assumed for the 1D backstripping. *Thickness* estimates are according to reconstructions by Maystrenko et al. (2005a). **c** Subsidence profiles showing total subsidence and tectonic subsidence, both for the base of the Buntsandstein layer and the base of the salt layer. The latter was obtained by incorporating the initial salt layer thickness and the temporal reduction of this thickness (*blue curve*) into the backstripping procedure

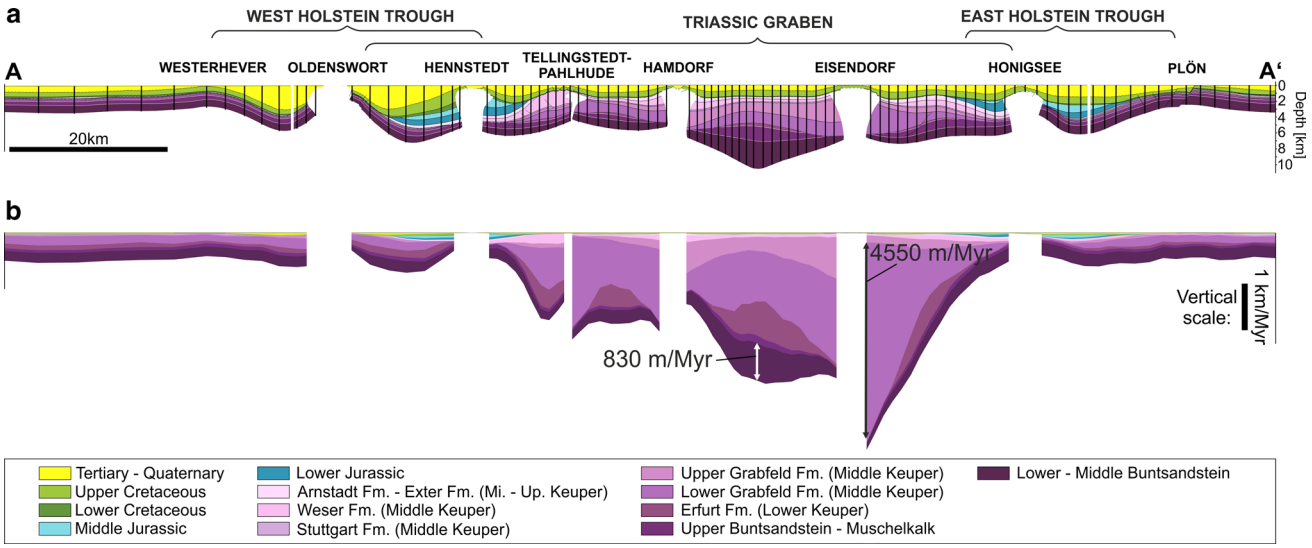

Fig. 8 Subsidence rates in the Glückstadt Graben. **a** Geological cross section including 1D profile used for deriving subsidence data. **b** Average subsidence rates calculated from decompacted layer thicknesses and plotted against x-values of the geological cross section. The 1D profiles are more closely spaced in the centre of the Glückstadt Graben to account for complex thickness variations. Fast regional subsidence occurred during Early–Middle Buntsandstein time. Subsidence was fastest in secondary peripheral sinks during Early–Middle Grabfeld Fm. time. In contrast, subsidence rates in the peripheral sinks of Jurassic, Cretaceous and Cenozoic ages were generally lower

1 created differential loading between regions of extended salt overburden and surrounding regions forcing the salt to flow towards the cover grabens. The innermost salt structures surrounding the CPS showed the highest uplift, as can be inferred from erosional truncation of Buntsandstein and Muschelkalk layers. This resulted from higher differential loading imposed by the CPS compared to relatively low differential loading imposed by the smaller peripheral sinks above the platforms.

Second phase: Middle Keuper time to Middle Jurassic

At the beginning of the Grabfeld Fm. time, the relatively abrupt change in depositional patterns—from the subsidence of PPSs to the formation of SPSs—and the strong increase in subsidence rates can mainly be explained by two processes: (1) Strong basement extension is observed within the entire CEBS during the Late Triassic (Frisch and Kockel 1999; Kockel 2002; Maystrenko et al. 2013). Similarly, enhanced crustal extension is suggested for the Glückstadt Graben (Maystrenko et al. 2005a). Subsidence curves presented here point out that increased tectonic subsidence occurred in particular from Early Keuper until Grabfeld Fm. time. Therefore, it can be suggested that regional extension beginning at the end of phase 1 led to widening of the graben structure (Maystrenko et al. 2005a) and to additional stretching of the cover grabens. (2) Consequently, the transition of the innermost salt structures (Tellingstedt-Pahlhude, Hamdorf and Eisendorf) from pillows or immature diapirs, respectively, into passively growing mature salt diapirs was initiated (Kockel and Krull 1995). Following this transition, flow rates in the salt commonly increased significantly (e.g. Seni and Jackson 1983; Sørensen 1998; Trusheim 1960; Zirngast 1996). Rapid evacuation of the salt beneath the primary sinks caused depletion of the salt layer, progressive rollover of the peripheral sink towards the rising salt diapirs, and eventually the formation of secondary peripheral sinks and turtleback structures. The absence of SPSs adjacent to the outer salt structures of Hennstedt and Honigsee during Grabfeld Fm. time indicates that these salt structures remained in the pillow or immature diapir stage (Fig. 9b).

The period from Stuttgart Fm. time until the Middle Jurassic is characterised by a lateral shift of the main depocentres from the central trough towards the graben flanks (Fig. 9c, d). However, this migration occurred over a much longer period of time (from 230–162 Myr) than the transition from primary to secondary peripheral sinks during deposition of the Grabfeld Fm. (238–232 Myr). This indicates that the long-lived migration was driven by slow salt expulsion from the basin centre towards the borders of the Glückstadt Graben. At the end of phase 2, the final structural fabric of the salt structures in the Glückstadt Graben was generally arranged (Frisch and Kockel 1999).

Third phase: Early Cretaceous to present

The burial of the inner salt structures by nearly isopachous Lower Cretaceous strata indicates that salt structure uplift over most of the Glückstadt Graben faded out after

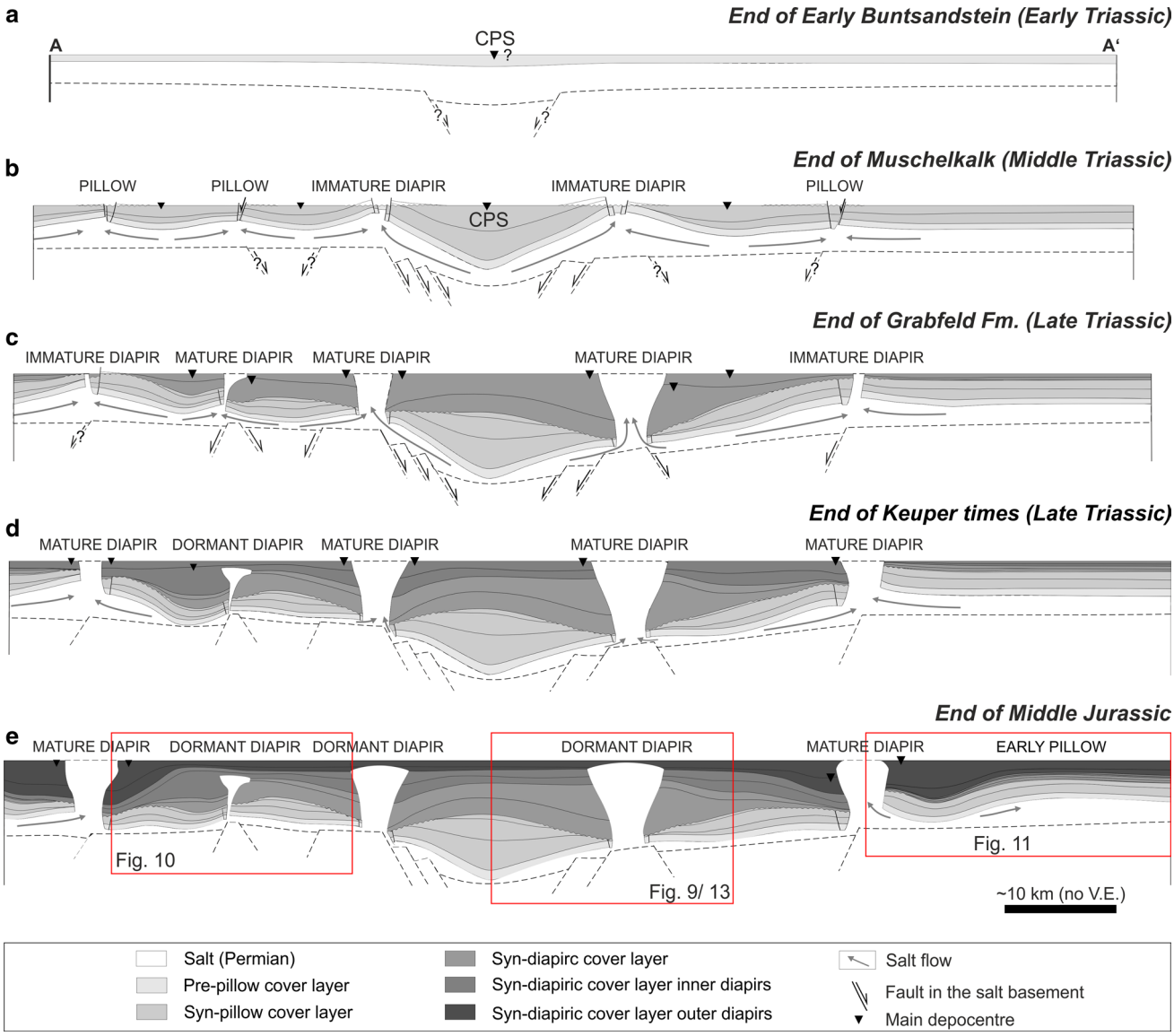

Fig. 9 Conceptual model of salt structure evolution in the Central Glückstadt Graben during phases 1 and 2. **a** Initial stage of the graben. **b** Pillow growth due to basement extension and cover faulting. **c** Phase of basement extension resulting in diapiric piercing of the innermost salt structures. **d** Ongoing basement extension and shifting of the depocentres towards the flanks of the Glückstadt Graben. **e** Main activity of the outer salt walls and decreased activity of the innermost salt walls followed by burial. *Triangles* denote locations of main depocentres. Note that the geometry of the basement and the amount of horizontal stretching of the cross section are speculative

the Middle Jurassic (Fig. 9d). This suggests that the salt layer in the centre of the Glückstadt Graben was already depleted at the end of the Jurassic preventing further salt expulsion. Meanwhile, minor SPSs of Cretaceous age close to the outer salt walls Hennstedt and Oldenswort and thinning of Cretaceous strata towards the Oldenswort salt structure (Maystrenko et al. 2006) implies that the shift of the main depocentres from the centre of the Glückstadt Graben towards its flanks slowly continued in the outer parts of the Glückstadt Graben, where relatively thick salt was left in the source layer.

During the Late Cretaceous and Early Tertiary, diapirs show upwarped and eroded layers as well as the formation of keystone grabens above their crests, which generally indicate squeezing of a salt structure due to lateral contraction (e.g. Dooley et al. 2009). In the Glückstadt Graben, this was interpreted to be due to thin-skinned shortening related to basement-involved shortening (Maystrenko et al. 2006), which affected regions further to the south, e.g. the Lower Saxony Basin (Betz et al. 1987; Baldschuhn et al. 1991) or the Allertal fault zone (Lohr et al. 2007). However, apart from rising diapirs, further indications for shortening of the

salt basement and the overburden are lacking in geological profiles (Baldschuhn et al. 2001) and seismic data of the Glückstadt Graben(Maystrenko et al. 2005a). Salt walls of the Glückstadt Graben are generally trending almost parallel to the contraction affecting Central Europe during Late Cretaceous to Early Tertiary time (N-S to NE-SW) (Scheck-Wenderoth and Lamarche 2005; Kley et al. 2008). Squeezing of the salt walls parallel to their long axes thus would also have to affect the surrounding post-salt strata. The link between the Late Cretaceous reactivation of salt movement in the Glückstadt Graben and regional contraction, however, needs further investigation.

During the Tertiary, revived growth of all diapirs can be inferred from layer thinning above the diapirs' crests. Particularly, diapiric piercing of the Oldenswort salt wall and increased uplift of the outermost salt pillows Westerhever and Plön (Kockel and Krull 1995) point to increased salt flowage in the marginal parts of the Glückstadt Graben. According to Maystrenko et al. (2006), this latest stage of growth took place during almost E-W-directed extension in Eocene to Miocene times.

Conceptual model for the migration of the main depocentres

In order to explain the temporal evolution of the salt structures in the Glückstadt Graben, multiple tectonic pulses that induced episodes of strong salt flow (e.g. Maystrenko et al. 2006) were proposed. These phases assumed to be interrupted by periods of arrested salt flow coinciding with tectonic quiescence. Our results confirm that the growth of salt pillows and adjoining PPS as well as pillow to diapir transition of the inner salt structures and subsidence of surrounding SPS were initiated by regional extension during Buntsandstein time or Early Keuper to Grabfeld FM. time, respectively.

However, the growth of salt pillows (from Late Buntsandstein to Early Keuper time) and the rise of passive diapirs (from Upper Grabfeld Fm. time to the end of the Jurassic or longer) further continued until the end of phase 1 or phase 2, respectively. During phase 1, ongoing salt flow can be inferred from the uninterrupted subsidence of peripheral sinks, even though rates of salt flow decreased during Muschelkalk time. During phase 2, subsidence of wedge-shaped secondary peripheral sinks next to the inner salt walls lasted throughout the entire Triassic until the salt layer beneath the peripheral sinks was depleted. Nevertheless, subsidence rates and, therefore, salt flow rates significantly decreased after Grabfeld Fm. time, which is likely because Arnstadt and Exter Fm. times are tectonically quiet periods (Kockel 2002).

The development of SPSs next to the outer salt walls Hennstedt and Honigsee began during Arnstadt Fm. time and continued until the Middle Jurassic (Fig. 4). In seismic data of the Glückstadt Graben, parallel reflections can be observed at the transition from the Triassic to the Jurassic (Maystrenko et al. 2005a, 2006; Baykulov et al. 2009). Only directly adjacent to salt structures, Triassic and Jurassic strata are separated by angular unconformities (Maystrenko et al. 2005a). In other regions of the CEBS, the beginning of Jurassic extension is dated to the Middle Jurassic, e.g. in the Central Graben (e.g. Duffy et al. 2013; Arfai et al. 2014) or in the Lower Saxony Basin (Betz et al. 1987), although some tectonic movements have been suggested for parts of the North German Basin during the Early Jurassic (e.g. Kockel 2002; Maystrenko et al. 2005a; Lohr et al. 2007). However, these tectonic events likely occurred later than the pillow–diapir transition of the outer salt walls Hennstedt and Honigsee. Therefore, we suggest that the structural patterns and the salt flow kinematics in the Glückstadt Graben were not significantly modified by additional tectonic pulses during Weser Fm. time (Frisch and Kockel 1999) or during the Jurassic (Maystrenko et al. 2006).

Our conceptual model proposes that salt flow and the migration of main depocentres during phase 2 and during the late stage of phase 3 were driven by differential loading after being triggered or reactivated by tectonic stresses. As it has been proposed by Sannemann (1968) and shown by analogue models (e.g. Warsitzka et al. 2013, 2015) as well as numerical models (e.g. Peel 2014), the formation of a diapir can lead to expulsion of the source layer towards neighbouring regions and force the formation of new salt structures. In the Glückstadt Graben, extensionally triggered peripheral sinks adjacent to the innermost salt structures might have also forced expulsion of salt towards the neighbouring salt structures. The latter pierced their overburden as soon as differential loading had increased sufficiently to overcome the strength of the overburden or when an additional tectonic pulse thins the cover of the salt pillows (cf. Hudec and Jackson 2007). Subsequent to piercing, additional SPSs formed adjacent to the younger salt diapirs.

The process of migration of the main depocentres and salt expulsion from beneath the SPS to the outer parts of the Glückstadt Graben significantly slowed after the Middle Jurassic. This can be attributed to three factors: (1) the initial thickness of the salt layer decreases towards the grabens flanks (Maystrenko et al. 2005a), which generally reduces flow velocities of the salt. (2) Due to the hiatus and erosion from the Late Jurassic to the Early Cretaceous, sediment accumulation in peripheral sinks ceased. Hence, the increase in load required for further salt expulsion was cut off. (3) Tectonic tranquillity was interpreted for the Glückstadt Graben during this time (Maystrenko et al. 2006), suggesting that fault-induced salt tectonics did not occur.

Major reactivation of salt flow and salt structure growth occurred not until the Late Cretaceous(?) and Cenozoic, when regional deformation again affected the Glückstadt Graben.

Structural characteristics of the peripheral sinks in the Glückstadt Graben

Typical structural features evolved in the peripheral sinks due to the expulsion of the salt layer will be discussed here.

1. Graben centre diapirs: The innermost diapirs (Hamdorf, Eisendorf) flank the CPS, which represents the main primary peripheral sinks of these salt walls (Fig. 10a). However, the deepest *secondary* peripheral sinks of these diapirs developed on their outer sides during deposition of the Lower Grabfeld Fm. (Fig. 10b). This switching of peripheral sinks from one side of the diapir to the other could either be explained by the activation of outward dipping normal faults beneath the SPSs of the diapirs, or by varying salt movement. The first option requires the formation of a fault underlying the outer SPS. However, there is no indication for basement normal faults with sufficiently large offsets (>1000 m) dipping away from the graben centre either in the original seismic profile used here (Baldschuhn 1996) or in other profiles (Baldschuhn et al. 2001) trending parallel to our cross section. The second option considers salt expulsion and salt extrusion close to the deep SPS as follows: At the beginning of the diapiric breakthrough (phase 1), salt was supplied to the innermost salt structures of the Glückstadt Graben mainly from beneath the CPS (Fig. 10a). This forced relative uplift of the inner flanks of these salt structures and probably salt extrusion on top of the outer flanks. These salt extrusions can produce topography above the general sedimentary surface (Fig. 10b), thus increasing the loading and the subsidence of the outer SPSs. This mechanism may also help to explain the enormous subsidence rates (>4000 m/Myr) characterising the SPSs of the innermost salt structures during Lower to Middle Grabfeld Fm. time. Salt extrusion as well as surficial dissolution and re-precipitation of Permian salt led to the accumulation of significant thicknesses of evaporites in the SPS (especially during Grabfeld and Weser Fm. time). Such surficial outflow of Permian salt in the North German Basin was proven by detecting Permian microfossils in younger evaporites of Triassic and Jurassic age (Trusheim 1960) and recognising buried salt extrusion (salt glaciers) in seismic profiles located south of the Glückstadt Graben (Mohr et al. 2007). Evaporites have relatively high densities (e.g. halite: 2.04 kg/m^3, anhydrite: 2.98 kg/m^3 (Urai et al. 2008)) compared to less compacted clastic sediments near the surface (1.5–1.8 kg/m^3) (Jackson and Talbot 1986). Consequently, the loading induced by evaporites in peripheral sinks is significantly higher than that of clastics, which accelerated subsidence of SPSs in Grabfeld Fm. time. Combined with a sudden acceleration of tectonic subsidence and isostatic response to the sediment load (Fig. 6), total subsidence rate can reach unusually high values.
2. Platform diapirs: Diapirs located at a distance from the CPS (Hennstedt, Tellingstedt-Pahlhude, Honigsee) are characterised by asymmetric peripheral sinks similar to the graben centre diapirs. However, the main peripheral

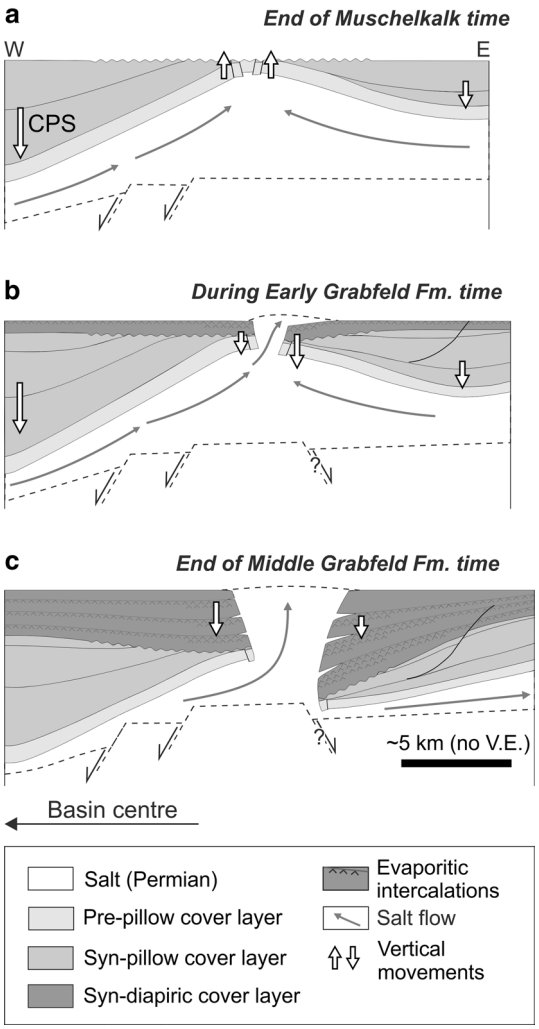

Fig. 10 Structural evolution of secondary peripheral sinks of a graben centre diapir in the Glückstadt Graben. **a** Strong subsidence of the central peripheral sink during phase 1 causes salt flow mainly from hanging wall side. **b** During and after piercing of the diapir in phase 2, salt upwelling forces slower subsidence of the inner flanks of the diapir compared to the outer flanks. **c** After depletion of the salt layer beneath the outer secondary peripheral sink, main depocentre switches back to the inner side of the downbuilding diapir

sinks of the platform diapirs switched multiple times from one side of the diapirs to the other (Fig. 4). This change in structural polarity of the peripheral sinks has been termed as "flip-flop salt tectonics" (Quirk and Pilcher 2012). Various mechanisms might be responsible for this behaviour: (1) During phase 1, differential subsidence of the overlying peripheral sinks can be caused by temporarily varying activity of oppositely dipping basement faults beneath the diapirs or by a succession of thin-skinned extension linked to the central graben and subsequently thick-skinned extension linked to basement faults beneath the salt structures (Fig. 11b). (2) During phase 2, a lateral shift of depocentres from the inner diapirs towards the outer diapirs can lead to asymmetric salt expulsion beginning at the inner side of the platform diapir (Fig. 11c) and later switching to the outer side of the diapir (Fig. 11d). (3) A further explanation could be the progradation of sedimentary wedges. As shown by analogue experiments (Ge et al. 1997), sediment propagation leads to asymmetric peripheral sinks next to squeezed out diapirs. However, the progradation of large sedimentary wedges in Keuper time is unlikely for the area of the Glückstadt Graben, since sedimentation at that time was dominated by evaporitic and playa lake facies (Barnasch 2010). These facies types are characterised by aggradation rather than progradation.

3. Basin-edge pillows: The Glückstadt Graben is bounded by elongated salt pillows, in regions showing no indications for cover faults of Triassic age (Fig. 12). These pillows formed at the outer edges of the West Holstein Trough and the East Holstein Trough as a consequence of the subsidence of peripheral sinks mainly during the Tertiary (Maystrenko et al. 2006). They remained in the pillow stage probably because the overburden of Triassic to Cretaceous age was too thick to allow diapiric breakthrough. However, geological cross sections south of the section presented here show that the salt intruded the cover layer through a normal fault formed during the Tertiary (Baldschuhn et al. 2001). This represents a possible example of a salt structure in the transition from pillow to diapir.

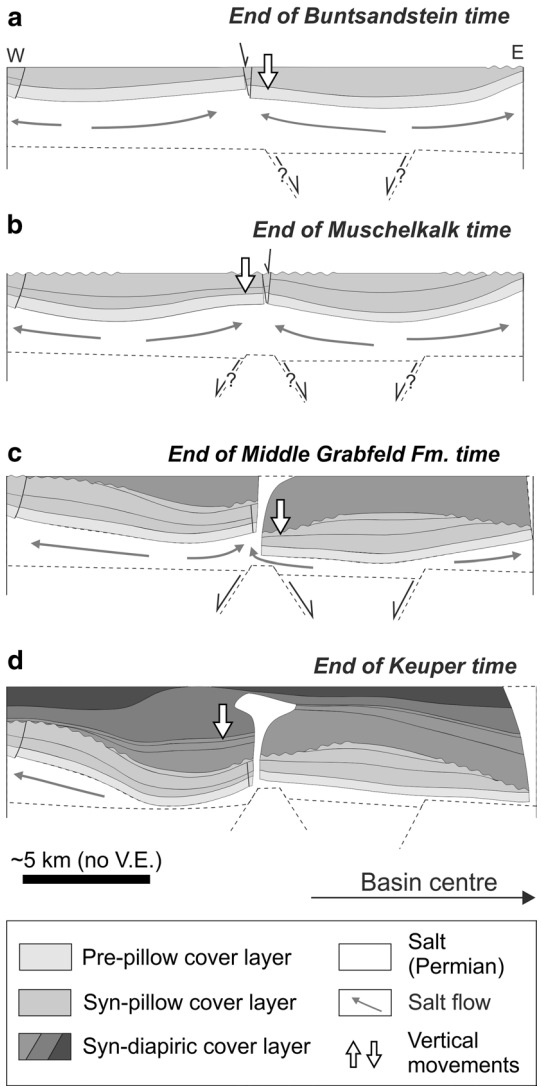

Fig. 11 Structural evolution of secondary peripheral sinks of a platform diapir in the Glückstadt Graben: Multiple switching of main depocentres adjacent to the diapir Tellingstedt-Pahlhude. **a** During Buntsandstein time, thin-skinned extension cause the initiation of PPSs. **b** Main depocentre shifts towards the outer side of the salt structure. **c** Further extension leads to piercing of the salt structure, whereas the deeper SPS develops at the inner side of the diapir. **d** During the Late Triassic, the main SPS shifts to the outer side possibly after salt welding beneath the inner side SPS

Limitations of the reconstruction

Technical uncertainties

The seismic interpretation of the geological cross section used here could have been affected by the following technical problems:

1. The correlation of stratigraphic horizons in the seismic data from outside the graben towards the graben centre basin may be partly inaccurate. This is because the quality of the data underlying the Geotectonic Atlas of Northern Germany (Baldschuhn 1996) is heterogeneous (Hese 2012), and seismic energy is lost with depth resulting in insufficient resolution especially of deeply buried (up to 11 km) Triassic strata in the basin centre that were never drilled (Maystrenko et al. 2005b). The corresponding lack of information about the petrophysical parameters of the rocks in the basin centre may have led to incorrect velocity models resulting in inaccurate depth migration of the seismic data.

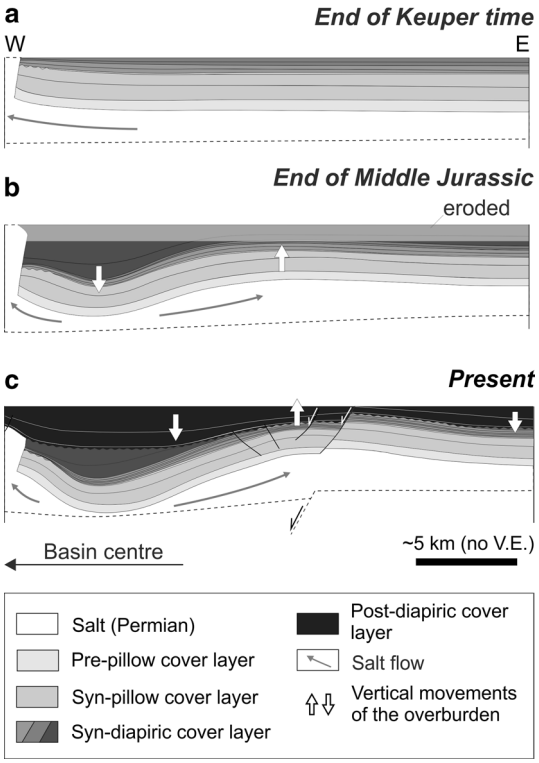

Fig. 12 Structural evolution of the basin-edge pillow Plön. **a** Pillow to diapir transition of the platform diapir (Honigsee). **b** Subsidence of the outer SPS of the downbuilding diapir cause salt expulsion towards the basin edges and the beginning of pillow uplift. **c** Slow growth continues during the Cretaceous. Tertiary extension leads to faulting of the pillow crest and increased growth of the pillow

2. The presence of salt structures and of salt layers in post-Permian successions (e.g. in the Middle Keuper) impairs seismic imaging beneath the salt bodies, since much of the seismic energy is lost at the boundary of the salt (Leveille et al. 2011; Jones and Davison 2014). Furthermore, seismic imaging in the vicinity of salt diapirs boundaries is poor, because of the steeply dipping and mostly irregular boundary of salt diapirs, salt overhangs at the heads of diapirs, or faults and folds in the post-salt strata around them. For instance, the Lower Buntsandstein to Middle Keuper succession may be dissected by normal faults as shown in Fig. 9. For these reasons, offsets of basement faults beneath salt diapirs as well as onlap geometries and thickness variation of post-salt layers in the vicinity of the salt walls are prone to high uncertainties. According to other interpretations of salt structures in Northern Germany (e.g. Baykulov et al. 2009; Mohr et al. 2005; Kukla et al. 2008), the shapes of the salt diapirs are usually much more irregular than the straight vertical salt wall boundaries interpreted in the cross section used here (Fig. 2). New techniques of stacking (e.g. common reflection surface stacking) applied to the seismic data of the Glückstadt Graben improved the seismic imaging of the layered sedimentary successions (Baykulov et al. 2009; Yoon et al. 2009). This revealed that the width of the diapirs in the Glückstadt Graben might be much smaller than interpreted in Baldschuhn (1996). Consequently, the salt volume and, thus, potential subsidence due to salt expulsion are overestimated. Furthermore, the widths of the peripheral sinks also carry errors of several hundreds of metres. However, seismic reflectors between the salt walls are relatively well imaged. Therefore, structural geometries in the centre of the peripheral sinks can be reconstructed reliably by the method applied here.
3. The stratigraphic resolution of the post-Triassic layers is low. Therefore, extensional phases, e.g. during the Jurassic or Cenozoic, might be levelled out in the subsidence data, which prevents a more detailed reconstruction of the post-Triassic subsidence history.

Overall, these technical issues point to the necessity of a new processing and interpretation of the seismic data, but this is beyond the scope of this study.

Uncertainties caused by geological processes

1. Erosional unconformities adjacent to or above salt structures (Fig. 2) may lead to underestimations of original layer thicknesses and, therefore, underestimations of compaction and decompacted thickness of the underlying layers. In particular, erosion of pillow crests during the transition from phase 1 to phase 2 (end of Early Keuper time) might amount to several hundreds of metres (Fig. 9). However, since the exact values are unknown, eroded parts of the layers were not reconstructed.
2. Mobile evaporitic rocks intercalated in the Triassic strata (Grabfeld Fm. and Weser Fm.) could be affected by post-depositional salt flow. In the southern part of the Glückstadt Graben, mobile halite layers in the Upper Triassic Weser Fm. can be as thick as 2400 m. A part of this thickness is attributed to the formation of salt pillows (Frisch and Kockel 1999). Unfortunately, there are no further quantifications of ductile deformations in the post-Permian salt layers.
3. The intrusion of Permian salt into younger evaporitic layers (e.g. Upper Buntsandstein or Middle Keuper) can increase the thickness of the peripheral sinks. Such intrusions with a maximum thickness of 700 m were interpreted in seismic profiles from the northern part of the Glückstadt Graben (Baldschuhn 1996). Salt intrusions are assumed to be caused by compres-

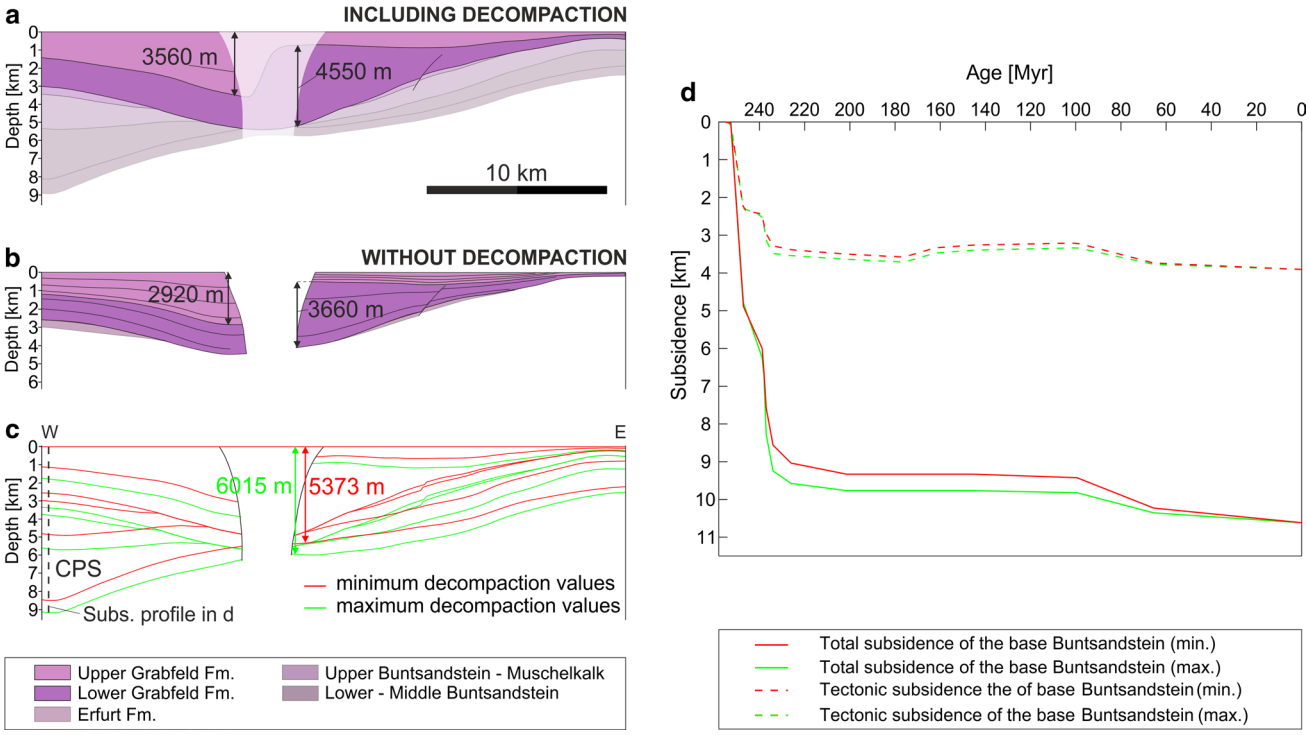

Fig. 13 Variations of decompacted layer thicknesses and subsidence curves depending on applied decompaction parameters (Table 1). **a** Structural reconstruction of the SPSs next to the Eisendorf salt wall (end of Grabfeld Fm. time) applying decompaction parameters according to the average lithological composition of the stratigraphic units. **b** Reconstruction of the Lower to Upper Grabfeld Fm. without applying decompaction (modified after Baldschuhn 1996). **c** Reconstruction showing differences in decompacted layer thicknesses related to minimum and maximum decompaction parameters in the sensitivity study. **d** Subsidence curves of the CPS (profile 8, Fig. 7) showing differences in the total subsidence and the tectonic subsidence of the base Buntsandstein

Table 2 Difference in total subsidence S_{totB}, tectonic subsidence S_{tecB} and subsidence rate of the base Buntsandstein using maximum or minimum decompaction parameters (Table 1)

Unit/formation	Age of top (Myr)	Difference in S_{totB} (m)	Difference in S_{tecB} (m)	Difference in subsidence rate (m/Myr)
Tertiary + Quatenary	0	0	0	0
Upper Cretaceous	65.5	127	35.6	3.7
Lower Cretaceous	99.5	398	125.8	8.7
Upper Jurassic	145.5	–	–	–
Middle Jurassic	162	–	–	–
Lower Jurassic	176	–	–	–
Arnstadt-Exter Fm. (Middle-Upper Keuper)	201.5	437	137.4	17.8
Weser Fm. Middle Keuper	226	540	154.0	67.5
Upper Grabfeld Fm. (Middle Keuper)	234	682	200.4	227.3
Lower–Middle Grabfeld Fm. (Middle Keuper)	237	698	195.6	698.0
Erfurt Fm. (Lower Keuper)	238	87	14.5	108.7
Upper Buntsandstein–Muschelkalk	238.8	256	37.0	30.8
Lower–Middle Buntsandstein	247.1	−94	−33.0	−16.8

Example is calculated for subsidence profile 8 (see Fig. 7 for location)

sion or transpression of a previously formed diapir (Baldschuhn et al. 1998). In the Glückstadt Graben, this requires a post-Triassic phase of compression or transpression—probably in the Late Cretaceous (Coniacian to Campanian; Baldschuhn et al. 1998).

4. Besides technical issues with defining the salt basement (see above), it is also problematic to sharply define the basement beneath the Permian salt in terms of mechanical behaviour. This is because Rotliegend (Permian) evaporites are involved in the salt diapirism in the centre of the Glückstadt Graben, whereas the Rotliegend strata in the outer parts of the Glückstadt Graben are undisturbed by salt movement (Maystrenko et al. 2005a). The lower mobility of the Upper Rotliegend succession away from the graben centre probably reflects a gradual increase in the proportion of shale.

Uncertainties of the decompaction procedure, in particular of the decompaction values (initial porosity data and depth coefficient) can result from the following factors:

1. The decompaction procedure applied does not include the effects of cementation of the pore space, which usually reduces mechanical compaction. This has to be considered especially for sandstones of the Buntsandstein and the Keuper (e.g. Stuttgart Fm.), which locally possess porosities of 25–35 % (including cemented pore space) in the CEBS (e.g. Purvis and Okkerman 1996; Wolfgramm et al. 2008). The state of compaction in the Glückstadt Graben, e.g. in the CPS, cannot be verified owing to the lack of well data.
2. Lateral and vertical lithological variations within a stratigraphic horizon cause uncertainties in the average decompaction values used here, e.g. the ratio between claystones and evaporites within the Grabfeld Fm. might change from the deep peripheral sinks in the basin centre to the platforms at the basin margin.

Sensitivity study

In order to test the influence of varying decompaction values, a sensitivity study was carried out setting minimum and maximum values for initial porosity and depth coefficient (Table 1). This yields a range of possible subsidence values exemplarily shown in Fig. 13 and Table 2. Variations of the total subsidence of as much as 30 to 130 m can be stated for the Lower to Middle Buntsandstein layer along the cross section (Table 2). Consequently, the error of subsidence rates during this interval is ~15–25 m/Myr. Larger differences in the total subsidence result for Middle and Upper Triassic strata, e.g. for the Lower to Upper Grabfeld Fm.. Differences range between 100 m in the outer parts of the Glückstadt Graben and up to 800 m in the deepest SPSs in the centre of the Glückstadt Graben. These large variations are due to the large absolute thickness of these layers and due to the large differences between the applied maximum and minimum values of the decompaction parameters (Table 1).

The abnormally high subsidence rates calculated for the Lower to Middle Grabfeld Fm. (>4000 m/Myr, Fig. 8) can be partly explained by poorly constrained decompaction parameters. However, palinspastic reconstructions (without applying decompaction) of the Keuper layers shown in the GTA (Baldschuhn 1996) yielded a maximum thickness of 3660 m for the Lower to Middle Grabfeld Fm. (Fig. 13b). This results in a similarly high subsidence rate (3660 m/Myr). Even when taking into account errors in the correlation of stratigraphic boundaries and the technical limitations discussed above (e.g. erroneous correlations of seismic reflectors), max. subsidence rates during Lower–Middle Grabfeld Fm. time remain significantly higher (~ 2000–3000 m/Myr) than in any other post-Permian phase in the Glückstadt Graben.

Conclusions

Based on a key geological cross section through the central Glückstadt Graben (Northern Germany), the growth of salt diapirs and subsidence of adjacent peripheral sinks were reconstructed using decompaction and backstripping. On the basis of these reconstructions, three phases of salt structure evolution can be distinguished:

1. Most salt structures were initiated by basement faulting in the period from Early to Middle Buntsandstein time (Early Triassic). Regional extension caused normal faulting in the centre of the Glückstadt Graben leading to thickness variations in the overburden of the Permian salt layer. From Late Buntsandstein to Early Keuper time, salt pillows or immature salt diapirs evolved accompanied by subsidence of primary peripheral sinks.
2. At the beginning of Keuper time, regional extension induced a major change in depositional patterns. An abrupt switch from primary to secondary peripheral sinks occurred adjacent to the innermost salt structures of the Glückstadt Graben. Extremely high subsidence rates in the time of the Grabfeld Formation (up to 4500 m/Myr) points to fast regional extension, strong salt flow and diapiric breakthrough in the centre of the Glückstadt Graben.

The interval from Late Grabfeld Fm. time to the Middle Jurassic was a long-lasting phase of salt flow and downbuilding of the diapirs. The main depocentres gradually migrated outwards from the graben centre towards the flanks. We suggest that this lateral shift was mainly caused by the expulsion of salt from salt diapirs towards their neighbouring salt structures, but was modulated and accelerated by phases of regional extension, e.g. during the Late Triassic (Weser Fm.) or the Jurassic.

3. After a phase of regional erosion (Late Jurassic–Early Cretaceous), salt movement and the growth of the inner salt walls ceased. Minor salt structure growth only continued at the margins of the Glückstadt Graben. The growth of the inner salt structures and especially of salt walls and salt pillows in the West Holstein Trough and in the East Holstein Trough was renewed during Late Cretaceous probably due to shortening and in particular during Tertiary due to regional extension.

Depending on their location, the peripheral sinks of the Glückstadt Graben exhibit characteristic structural features:

1. The innermost diapirs bounding the graben centre possess very deep secondary peripheral sinks filled by the Middle Keuper Grabfeld Formation. These peripheral sinks developed on the outer sides of the diapirs, facing away from the graben centre. This phenomenon can be explained by strong salt expulsion from beneath the central peripheral sinks, which caused relative uplift of the inner flanks of the innermost diapirs and salt expulsion onto the outer flanks.
2. The peripheral sinks of the outer diapirs located above the graben flanks switched multiple times from one side of a diapir to its other side. We suggest that this switching was related to variable basement faulting, changing directions of salt influx and the influence of salt expulsion from neighbouring salt walls.
3. The salt structures above the outer swells of the graben remained in the pillow stage and possess only one deep primary peripheral sink. The piercing of these pillows was probably prevented by the large thickness of the post-Permian sediments.

Acknowledgments Funding for Michael Warsitzka came from the Federal Ministry of Education and Research (BMBF) (Grant No. 03IS2091A INFLUINS) and the German Academic Exchange Service (DAAD). We gratefully acknowledge Midland Valley for providing free university licences of 2DMOVE™. We have benefited from helpful discussion with T. Voigt. Reviewers P. Kukla and Y. Maystrenko are thanked for valuable comments improving the contents and presentation of our paper.

References

Allen PA, Allen JR (2013) Basin analysis: principles and application to petroleum play assessment. Wiley, New York

Arfai J, Jähne F, Lutz R, Franke D, Gaedicke C, Kley J (2014) Late Palaeozoic to Early Cenozoic geological evolution of the northwestern German North Sea (Entenschnabel): new results and insights. Neth J Geosci 93(04):147–174

Athy LF (1930) Density, porosity, and compaction of sedimentary rocks. AAPG Bull 14(1):1–24

Bachmann GH, Grosse S (1989) Struktur und Entstehung des Norddeutschen Beckens - geologische und geophysikalische Interpretation einer verbesserten Bouguer-Schwerekarte. Nds Akad Geowiss Veröfftl 2:23–47

Baldschuhn R (1996) Geotektonischer Atlas von Nordwest-Deutschland und dem deutschen Nordsee-Sektor. Hannover

Baldschuhn R, Best G, Kockel F (1991) Inversion tectonics in the north-west German basin. Generation, accumulation, and production of Europes hydrocarbons. Spec Publ Eur Assoc Petroleum Geosci 1:149–159

Baldschuhn R, Frisch U, Kockel F (1998) Der Salzkeil, ein strukturelles Requisit der saxonischen Tektonik. Zeitschrift der deutschen geologischen Gesellschaft, pp 59–69

Baldschuhn R, Binot F, Fleig S, Kockel F (2001) Geotektonischer Atlas von Nordwest-Deutschland und dem deutschen Nordsee-Sektor. Hannover

Barnasch J (2010) Der Keuper im Westteil des Zentraleuropäischen Beckens (Deutschland, Niederlande, England, Dänemark): diskontinuierliche Sedimentation, Litho- , Zyklo- und Sequenzstratigraphie. Schriftenreihe der Deutschen Gesellschaft für Geowissenschaften, pp 7–169

Bayer U, Maystrenko Y, Hoffmann N, Scheck-Wenderoth M, Meyer H (2003) 3D structural modelling and basin analysis of the Central European Basin System (CEBS) between the North Sea and Poland. Terra Nostra 3:1–4

Baykulov M, Brink HJ, Gajewski D, Yoon MK (2009) Revisiting the structural setting of the Glueckstadt Graben salt stock family. North German basin. Tectonophysics 470(1):162–172

Best G, Kockel F, Schöneich H (1983) Geological history of the southern Horn Graben. In: Petroleum geology of the southeastern North Sea and the adjacent onshore areas. Springer, pp 25–33

Betz D, Führer F, Greiner G, Plein E (1987) Evolution of the Lower Saxony basin. Tectonophysics 137(1):127–170

Beutler G (2005) Stratigraphie von Deutschland, vol 4. E. Schweizerbart'sche, Verlagsbuchhandlung

Bishop DJ, Buchanan PG, Bishop CJ (1995) Gravity-driven thin-skinned extension above Zechstein Group evaporites in the western central North Sea: an application of computer-aided section restoration techniques. Mar Pet Geol 12(2):115–135

Brink H, Dürschner H, Trappe H (1992) Some aspects of the late and post-Variscan development of the Northwestern German Basin. Tectonophysics 207(1):65–95

Buchanan PG, Bishop DJ, Hood DN (1996) Development of salt-related structures in the Central North Sea: results from section balancing. Geol Soc Lond Spec Publ 100(1):111–128

Dooley TP, Jackson MPA, Hudec MR (2009) Inflation and deflation of deeply buried salt stocks during lateral shortening. J Struct Geol 31(6):582–600

Doornenbal JC, Stevenson AG (2010) Petroleum geological atlas of the Southern Permian basin area. Houten, Netherlands, European Association of Geoscientists & Engineers

Duffy OB, Gawthorpe RL, Docherty M, Brocklehurst SH (2013) Mobile evaporite controls on the structural style and evolution of rift basins: Danish Central Graben, North Sea. Basin Res 25(3):310–330

Frisch U, Kockel F (1999) Quantification of early Cimmerian movements in NW-Germany. Zentralblatt Geol Paläontol I 7:571–600
Gast R, Gundlach T (2006) Permian strike slip and extensional tectonics in Lower Saxony, Germany. Zeitschrift der deutschen Gesellschaft für Geowissenschaften 157(1):41–55
Ge H, Jackson MPA, Vendeville BC (1997) Kinematics and dynamics of salt tectonics driven by progradation. AAPG Bull 81(3):398–423
Haq BU, Hardenbol J, Vail PR (1987) Chronology of fluctuating sea levels since the Triassic. Science 235(4793):1156–1167
Hese F (2012) 3D-Modellierungen und Visualisierung von Untergrundstrukturen für die Nutzung des unterirdischen Raumes in Schleswig-Holstein. Christian-Albrechts-Universitat, Kiel
Hossack J (1995) Salt tectonics: a global perspective: based on the Hedberg international research conference, Bath, UK, September 1993. In: Jackson M, Roberts D, Snelson S (eds) Salt tectonics: a global perspective, AAPG memoir, vol 65, American Association of Petroleum Geologists, pp 29–40
Hudec MR, Jackson MPA (2007) Terra infirma: understanding salt tectonics. Earth Sci Rev 82(1):1–28
Hudec MR, Jackson MPA (2011) The salt mine: a digital atlas of salt tectonics, vol 99. Bureau of Economic Geology Udden Book Series No. 5
Jackson MPA, Talbot CJ (1986) External shapes, strain rates, and dynamics of salt structures. Geol Soc Am Bull 97(3):305–323
Jackson MPA, Vendeville BC (1994) Regional extension as a geologic trigger for diapirism. Geol Soc Am Bull 106(1):57–73
Jaritz W (1987) The origin and development of salt structures in Northwest Germany. In: O'Brien I, Lerche J (eds) Dynamical geology of salt and related structures. Academic Press, Cambridge, pp 479–493
Jaritz W, Best G, Hildebrand G, J U (1991) Regionale Analyse der seismischen Geschwindigkeiten in Nordwestdeutschland. Geologisches Jahrbuch E 45:23–57
Jones IF, Davison I (2014) Seismic imaging in and around salt bodies. Interpretation 2(4):SL1–SL20
Kley J, Franzke HJ, Jähne F, Krawczyk C, Lohr T, Reicherter K, Scheck-Wenderoth M, Sippel J, Tanner D, van Gent H, the SPP Structural Geology Group (2008) Strain and stress. In: Littke R, Bayer U, Gajewski D, Nelskamp S (eds) Dynamics of complex intracontinental basins: the Central European Basin System, Springer, Berlin, pp 97–124
Kockel F (2002) Rifting processes in NW-Germany and the German North Sea sector. Neth J Geosci 81:149–158
Kockel F, Krull P (1995) Endlagerung stark wärmeentwickelnder radioaktiver Abfalle in tiefen geologischen Formationen Deutschlands: Untersuchung und Bewertung von Salzformationen. Bundesanstalt für Geowissenschaften und Rohstoffe
Kozur H, Bachmann G (2008) Updated correlation of the Germanic Triassic with the Tethyan scale and assigned numeric ages. In: Krystyn L, Mandl GW (eds) Upper Triassic subdivisions, zonations and events, vol 76, Ber d Geol Bundesanst, pp 53–58
Kukla PA, Urai JL, Mohr M (2008) Dynamics of salt structures. In: Littke R, Bayer U, Gajewski D, Nelskamp S (eds) Dynamics of complex intracontinental basins: the Central European Basin System. Springer, Berlin, pp 291–306
Lepper J, Röhling H, der DSK SPT (2013) Stratigraphie von Deutschland XI: Buntsandstein. No. Bd. 11 in Schriftenreihe der Deutschen Gesellschaft für Geowissenschaften, Schweizerbart'sche, E
Leveille JP, Jones IF, Zhou ZZ, Wang B, Liu F (2011) Subsalt imaging for exploration, production, and development: a review. Geophysics 76(5):WB3–WB20
Littke R, Scheck-Wenderoth M, Brix MR, Nelskamp S (2008) Subsidence, inversion and evolution of the thermal field. In: Littke R, Bayer U, Gajewski D, Nelskamp S (eds) Dynamics of complex intracontinental basins: the Central European Basin System. Springer, Berlin, pp 125–153
Lohr T, Krawczyk C, Tanner D, Samiee R, Endres H, Oncken O, Trappe H, Kukla P (2007) Strain partitioning due to salt: insights from interpretation of a 3D seismic data set in the NW German basin. Basin Res 19(4):579–597
Maystrenko Y, Bayer U, Scheck-Wenderoth M (2005a) Structure and evolution of the Glueckstadt Graben due to salt movements. Int J Earth Sci 94(5–6):799–814
Maystrenko Y, Bayer U, Scheck-Wenderoth M (2005b) The Glueckstadt Graben, a sedimentary record between the North and Baltic Sea in north Central Europe. Tectonophysics 397(1):113–126
Maystrenko Y, Bayer U, Scheck-Wenderoth M (2006) 3D reconstruction of salt movements within the deepest post-Permian structure of the Central European Basin System-the Glueckstadt Graben. Neth J Geosci 85(3):181
Maystrenko YP, Bayer U, Scheck-Wenderoth M (2013) Salt as a 3D element in structural modeling—example from the Central European Basin System. Tectonophysics 591:62–82
Mohr M, Kukla P, Urai J, Bresser G (2005) Multiphase salt tectonic evolution in NW Germany: seismic interpretation and retrodeformation. Int J Earth Sci 94(5–6):917–940
Mohr M, Warren JK, Kukla PA, Urai JL, Irmen A (2007) Subsurface seismic record of salt glaciers in an extensional intracontinental setting (Late Triassic of northwestern Germany). Geology 35(11):963–966
Nalpas T, Brun JP (1993) Salt flow and diapirism related to extension at crustal scale. Tectonophysics 228(3):349–362
Peel FJ (2014) How do salt withdrawal minibasins form? Insights from forward modelling, and implications for hydrocarbon migration. Tectonophysics 630:222–235
Purvis K, Okkerman JA (1996) Inversion of reservoir quality by early diagenesis: an example from the Triassic Buntsandstein, offshore the Netherlands. In: Geology of gas and oil under the Netherlands. Springer, pp 179–189
Quirk DG, Pilcher RS (2012) Flip–flop salt tectonics. Geol Soc Lond Spec Publ 363(1):245–264
Reinhold K, Krull P, Kockel F (2008) Salzstrukturen Norddeutschlands, Geologische Karte 1:500 000. Bundesanstalt für Geowissenschaften und Rohstoffe
Rodon S, Littke R (2005) Thermal maturity in the Central European Basin System (Schleswig-Holstein area): results of 1D basin modelling and new maturity maps. Int J Earth Sci 94(5–6):815–833
Röhling HG, Gast RE (1991) A lithostratigraphic subdivision of the Lower Triassic in the northwest German lowlands and the German sector of the North Sea, based on gamma-ray and sonic logs. The perennial Rotliegend saline lake in northwest Germany. Geologisches Jahrbuch A 119:3–24
Rowan MG (1993) A systematic technique for the sequential restoration of salt structures. Tectonophysics 228(3):331–348
Rowan MG, Ratliff RA (2012) Cross-section restoration of salt-related deformation: best practices and potential pitfalls. J Struct Geol 41:24–37
Sannemann D (1968) Salt-stock Families in Northwestern Germany. AAPG Mem. 8:261–270
Scheck-Wenderoth M, Lamarche J (2005) Crustal memory and basin evolution in the Central European Basin System—new insights from a 3D structural model. Tectonophysics 397(1):143–165
Scheck-Wenderoth M, Krzywiec P, Zühlke R, Maystrenko Y, Froitzheim N (2008a) Permian to Cretaceous tectonics. In: McCann T (ed) The geology of Central Europe. The Geological Society of London, pp 999–1030
Scheck-Wenderoth M, Maystrenko Y, Hbscher C, Hansen M, Mazur S (2008b) Dynamics of salt basin. In: Littke R, Bayer U, Gajewski

D, Nelskamp S (eds) Dynamics of complex intracontinental basins: the Central European Basin System. Springer, Berlin, pp 307–321

Schöner R (2006) Comparison of Rotliegend sandstone diagenesis from the northern and southern margin of the North German Basin, and implications for the importance of organic maturation and migration. Dissertation, Univ. Jena

Sclater JG, Christie PAF (1980) Continental stretching: an explanation of the post-mid-Cretaceous subsidence of the Central North Sea basin. J Geophys Res Solid Earth (1978–2012) 85(B7):3711–3739

Seni SJ, Jackson MPA (1983) Evolution of salt structures, East Texas diapir province, part 1: sedimentary record of halokinesis. AAPG Bull 67(8):1219–1244

Sørensen K (1998) The salt pillow to diapir transition: evidence from unroofing unconformities in the Norwegian-Danish Basin. Pet Geosci 4(3):193–202

Stewart SA (2007) Salt tectonics in the North Sea Basin: a structural style template for seismic interpreters. Spec Publ Geol Soc Lond 272:361

Stollhofen H, Bachmann GH, Barnasch J, Bayer U, Beutler G, Franz M, Kästner M, Legler B, Mutterlose J, Radies D (2008) Upper Rotliegend to Early Cretaceous basin development. In: Littke R, Bayer U, Gajewski D, Nelskamp S (eds) Dynamics of complex intracontinental basins: the Central European Basin System. Springer, Berlin, pp 181–207

Trusheim F (1960) Mechanism of salt migration in northern Germany. AAPG Bull 44(9):1519–1540

Urai JL, Schléder Z, Spiers CJ, Kukla PA (2008) Flow and transport properties of salt rocks. In: Littke R, Bayer U, Gajewski D, Nelskamp S (eds) Dynamics of complex intracontinental basins: the Central European Basin System. Springer, Berlin, pp 277–290

Van Wees JD, Stephenson RA, Ziegler PA, Bayer U, McCann T, Dadlez R, Gaupp R, Narkiewicz M, Bitzer F, Scheck M (2000) On the origin of the southern Permian Basin, Central Europe. Mar Pet Geol 17(1):43–59

Warsitzka M, Kley J, Kukowski N (2013) Salt diapirism driven by differential loading—some insights from analogue modelling. Tectonophysics 591:83–97

Warsitzka M, Kley J, Kukowski N (2015) Analogue experiments of salt flow and pillow growth due to basement faulting and differential loading. Solid Earth 6(1):9–31

Wolfgramm M, Rauppach K, Seibt P (2008) Reservoir—geological characterization of Mesozoic sandstones in the North German Basin by petrophysical and petrographical data. Zeitschrift für geologische Wissenschaften 36:249–265

Yegorova T, Maystrenko Y, Bayer U, Scheck-Wenderoth M (2008) The Glueckstadt Graben of the North-German Basin: new insights into the structure from 3D and 2D gravity analyses. Int J Earth Sci 97(5):915–930

Yoon MK, Baykulov M, Dümmong S, Brink HJ, Gajewski D (2009) Reprocessing of deep seismic reflection data from the North German Basin with the common reflection surface stack. Tectonophysics 472(1):273–283

Ziegler PA (1982) Triassic rifts and facies patterns in Western and Central Europe. Geologische Rundschau 71(3):747–772

Ziegler PA (1990) Geological Atlas of Western and Central Europe, 1990. Geological Atlas of Western and Central Europe, Shell Internationale Petroleum Maatschappij, B.V

Zirngast M (1996) The development of the Gorleben salt dome (northwest Germany) based on quantitative analysis of peripheral sinks. Geol Soc Lond Spec Publ 100(1):203–226

4. Analogue experiments of salt flow and pillow growth due basement faulting and differential loading

Manuscript #2

Authors
Michael Warsitzka[1], Jonas Kley[2], Nina Kukowski[1]

Affiliations
[1] Institute of Geosciences, Friedrich Schiller University Jena, Burgweg 11, 07749 Jena, Germany
[2] Geoscience Centre, Structural Geology and Geodynamics, Georg-August-University Göttingen, Goldschmidtstr. 3, 37077 Göttingen, Germany

This chapter is published by Copernicus Publications on behalf of the European Geosciences Union (EGU) in the journal *Solid Earth*:

Warsitzka, M., Kley, J., and Kukowski, N., 2015. Analogue experiments of salt flow and pillow growth due to basement faulting and differential loading, *Solid Earth*, 6: 9–31, doi:10.5194/se-6-9-2015.

This chapter is presented in the layout of the published article. It contains a separate reference list and appendices (Appendix A, Appendix B), which are not included at the end of this thesis. The digital supplement of this article (doi:10.5194/se-15-9-2015-supplement) as well as additional material (photos, cross sections, tables) related to the experiments are attached in the electronic supplement of this thesis (Appendix C.2).

Solid Earth, 6, 9–31, 2015
www.solid-earth.net/6/9/2015/
doi:10.5194/se-6-9-2015

Solid Earth Open Access

Analogue experiments of salt flow and pillow growth due to basement faulting and differential loading

M. Warsitzka[1], J. Kley[2], and N. Kukowski[1]

[1]Friedrich-Schiller-University Jena, Institute for Geosciences, Germany
[2]Georg-August-University Göttingen, Geoscience Centre, Structural Geology & Geodynamics, Germany

Correspondence to: M. Warsitzka (michael.warsitzka@uni-jena.de)

Received: 23 June 2014 – Published in Solid Earth Discuss.: 17 July 2014
Revised: 14 November 2014 – Accepted: 20 November 2014 – Published: 6 January 2015

Abstract. Salt flow in sedimentary basins is mainly driven by differential loading and can be described by the concept of hydraulic head. A hydraulic head in the salt layer can be imposed by vertically displacing the salt layer (elevation head) or the weight of overburden sediments (pressure head). Basement faulting in salt-bearing extensional basins is widely acknowledged as a potential trigger for hydraulic heads and the growth of salt structures. In this study, scaled analogue experiments were designed to examine the kinematics of salt flow during the early evolution of a salt structure triggered by basement extension. In order to distinguish flow patterns driven by elevation head or by pressure head, we applied a short pulse of basement extension, which was followed by a long-lasting phase of sedimentation. During the experiments viscous silicone putty simulated ductile rock salt, and a PVC-beads/quartz-sand mixture was used to simulate a brittle supra-salt layer. In order to derive 2-D incremental displacement and strain patterns, the analogue experiments were monitored using an optical image correlation system (particle imaging velocimetry). By varying layer thicknesses and extension rates, the influence of these parameters on the kinematics of salt flow were tested. Model results reveal that significant flow can be triggered in the viscous layer by small-offset basement faulting. During basement extension downward flow occurs in the viscous layer above the basement fault tip. In contrast, upward flow takes place during post-extensional sediment accumulation. Flow patterns in the viscous material are characterized by channelized Poiseuille-type flow, which is associated with subsidence in regions of "salt" expulsion and surface uplift in regions of inflation of the viscous material. Inflation of the viscous material eventually leads to the formation of pillow structures adjacent to the basement faults (primary pillows). The subsidence of peripheral sinks adjacent to the primary pillow causes the formation of additional pillow structures at large distance from the basement fault (secondary pillows). The experimentally obtained structures resemble those of some natural extensional basins, e.g. the North German Basin or the Mid-Polish Trough, and can aid understanding of the kinematics and structural evolution of sedimentary basins characterized by the presence of salt structures.

1 Introduction

Generally, rock salt buried in sedimentary basins behaves as a viscous fluid (Urai et al., 2008; van Keken et al., 1993) and flows according to a pressure gradient. Pressure gradients in a salt layer can be described by the concept of hydraulic head, which depends on the sum of elevation head and pressure head (Kehle, 1988; Hudec and Jackson, 2007). In the case of basement faulting (Fig. 1a), an elevation head can be imposed on the salt layer by vertical displacement of the salt layer itself. An additional pressure head is induced on the salt layer by differential loading due to lateral changes in thickness of the sediments accumulating on the irregular topography of the faulted surface (e.g. Geil, 1991; Hudec and Jackson, 2007; Jackson et al., 1994; Jackson and Vendeville, 1994; Koyi et al., 1993; Koyi and Petersen, 1993; Krzywiec, 2004b; Remmelts, 1995; Stewart et al., 1996; Vendeville et al., 1995).

Previous scaled analogue experiments investigating salt diapirism driven by thick-skinned extension demonstrated that at the beginning discrete basement faulting is balanced

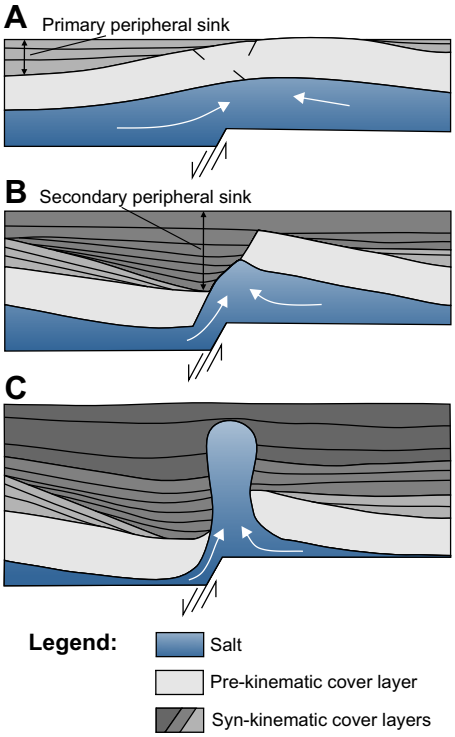

Figure 1. Conceptual model showing the evolution of a salt diapir induced by basement faulting: **(a)** due to sedimentary loading a salt pillow develops prior to diapiric piercing, **(b)** further basement extension leads to faulting of the overburden and **(c)** reactive diapirism. Salt flow is governed by vertical displacement of the salt layer (elevation head) and differential loading due to sediment accumulation in subsiding areas (modified after Koyi et al., 1993).

by flexural bending of the overburden and decoupled by diffuse faulting (Burliga et al., 2012; Dooley et al., 2003, 2005; Ge and Vendeville, 1997; Higgins and Harris, 1997; Jackson and Vendeville, 1994; Koyi et al., 1993; Nalpas and Brun, 1993; Oudmayer and de Jager, 1993; Richard, 1991; Soto et al., 2007; Stephansson, 1972; Vendeville, 1988; Vendeville et al., 1995; Vendeville and Jackson, 1992; Ventisette et al., 2005; Withjack and Callaway, 2000). Deformation within the viscous layer above an active basement normal fault is characterized by flow towards the hanging wall block under sediment-starved conditions. Reverse flow towards the footwall block occurs if sufficient sediment accumulates in the depocentre above the downthrown basement block (Jackson et al., 1994; Koyi et al., 1993; Nalpas and Brun, 1993; Ge and Vendeville, 1997). Furthermore, salt flow into a growing salt structure close to the basement fault can change through time from the footwall side during an early stage to the hanging wall side in a mature stage (Burliga et al., 2012; Koyi et al., 1993). However, in most of these experimental studies finite displacement of the basement faults was large compared to the thickness of the viscous layer. This obscures incremental flow patterns occurring during the early evolution of salt structures, when offsets of basement faults are still small (Fig. 1).

Therefore, our experimental study is designed to examine incremental strain patterns in a salt layer asserted by both components of the hydraulic head, elevation and pressure head during initiation of a salt structures triggered by basement normal faulting. We purposely divided the experimental procedure into a short pulse of basement faulting and a long phase of post-extensional sedimentation. Furthermore, a sensitivity study was carried out to test the role of characteristic parameters, namely salt thickness, cover thickness and extension rate, in affecting flow patterns and post-extensional structural evolution. A 2-D optical particle tracking system (PIV) was applied to observe incremental particle displacements and strain patterns in both the brittle and the ductile layer during the experiments.

2 Method and procedure

2.1 Scaling analogue experiments

The experiments presented here involve a two-layer ductile-brittle system covering a rigid basement. The viscous near-Newtonian behaviour of rock salt (Urai et al., 2008, van Keken et al., 1993) was simulated by using silicone putty (PDMS, polydimethylsiloxane; dynamic viscosity of 2.3×10^4 Pas at room temperature 20 °C and experimental strain rates of $< 10^{-1}\,s^{-1}$; see Appendix A for details). The silicone putty shows a power-law viscous rheology with a low power-law stress exponent ($n = 1.3$; Rosenau et al., 2009) so that it can be regarded as near-Newtonian. Frictional-plastic slip behaviour of overburden sediments is modelled by a granular mixture of quartz sand and PVC microspheres (1 : 1) (see Appendix A for details). This granulate deforms according to the Mohr–Coulomb criterion, a suitable rheology for the simulation of natural sedimentary rocks (e.g. Lohrmann et al., 2003).

For representative quantitative and qualitative information, analogue models have to be scaled geometrically, kinematically and dynamically (Hubbert, 1937; Ramberg, 1967). This requires dimensionless ratios relating the rheologies and stresses of nature to be similar to those for experiments. Referring to previous studies, we employ a geometric scaling factor $1 \times$ of about 10^{-5}, which means 1 cm in the model is equivalent to about 1 km in nature (Koyi et al., 1993; Nalpas and Brun, 1993; Ge and Vendeville, 1997; Withjack and Callaway 2000; Dooley et al. 2003). Dynamical scaling is ensured if force ratios and length ratios are similar (gravitational acceleration $= 9.81\,ms^{-2}$). The reliability of modelling results strongly depends on mechanical coupling between viscous layer and overburden and, therefore, on the ratio between brittle yield strength S_b and ductile strength S_d (see Appendix B for a detailed description of the scaling procedure). Calculation of this strength ratio results in the

following values (Table 1):

$$S_b / S_d \text{ (nature)} = \sim 100 - 1000 \quad (1)$$

and

$$S_b / S_d \text{ (model)} = 50 - 180. \quad (2)$$

The model ratio lies within the lower range of the natural ratio. Hence, the models can be considered as dynamically scaled. Scaling of time can be achieved by dividing the viscosity ratio η^* through the normal stress ratio σ_N^* (see Appendix B). The resulting time scaling factor $t^* = \sim 10^{-10}$ means that 1 h in the experiment equals ~ 1 Ma in nature.

Note that the applied scaling procedure is subject to high uncertainties, since especially salt viscosity and strain rate during salt flow are not well constrained and can vary over 2–3 orders of magnitude (Jackson and Talbot, 1986). Nevertheless, similar analogue materials and length ratios have been used for decades and found suitable for modelling of salt tectonic processes (see references above).

The mixture of quartz sand and PVC beads possesses slightly lower frictional properties ($\varphi \sim 27°$), but also a lower bulk density ($\rho_b = 1300\,\mathrm{kg\,m^{-3}}$) than pure quartz sand ($\rho_b = 1580$–$1710\,\mathrm{kg\,m^{-3}}$) (see Appendix A). By applying a low density contrast between cover and viscous layer in our experiments ($300\,\mathrm{kg\,cm^{-3}}$), buoyancy forces are not overestimated (Allen and Beaumont, 2012). Thus, we intend to ensure a more realistic stress relation during early stages of salt pillow development, and closer similarity to natural shallow (~ 1000 m), partly compacted sediments, which also possess densities lower or slightly higher than salt.

2.2 Experimental set-up

In this generic experimental study, we intend to simulate conditions of salt structure evolution during the onset of basement extension. In many rifts and intracontinental basins multiple extensional phases alternate with phases of tectonic quiescence as revealed by structural analysis or subsidence patterns (e.g. Alves et al., 2002; Jackson and Vendeville, 1994; Kockel, 2002; Mohr et al., 2005; van Wees et al., 2000). Therefore, the experimental procedure applied here assumes a relatively short extensional pulse followed by a longer phase of tectonic quiescence accompanied by sedimentation. In order to monitor the characteristic deformation patterns in both phases, we artificially separated basement extension and sedimentation in the experimental procedure. Furthermore, the salt layer in many extensional basins is overlain by more or less isopachous overburden before basement extension and salt movement begins (e.g. Alves et al., 2002; Baldschuhn et al., 2001; Duffy et al., 2013; Remmelts et al., 1995). Thus, we introduced an initial cover layer of uniform thickness in each experiment, which is here referred to as "pre-kinematic cover layer".

Appropriate experimental values for e.g. layer thicknesses, displacement of the basement faults or the duration of extension are adapted to the conditions of the Central European Basin system, which contains prominent extensional segments (e.g. Central Graben, Horn Graben, Mid-Polish Trough) (Ziegler, 1982) and numerous salt structures (Maystrenko et al., 2013). Here, the pre-extensional overburden thickness h_b varies from a few hundred metres (Mid-Polish Trough; Krzywiec, 2004a) to ~ 1000 m (North German Basin; Baldschuhn et al., 2001; Maystrenko et al., 2013; Scheck et al., 2003). The maximum original salt layer thickness h_d in the centre of extensional basins mainly lies between 1000 m (Northeast German Basin) and 1500 m (Mid-Polish Trough), but can attain 3500 m (Central North German Basin; Frisch and Kockel, 1999; Maystrenko et al., 2013). Hence, a ratio of overburden thickness to salt thickness of $H_r < 1$ is a reasonable assumption. Throughout this paper, we define small-offset displacement at the basement fault as being considerably smaller than the thickness of the salt layer. Thus, the ratio D_r of basement fault offset d to thickness of the salt layer h_d can also be assumed to be < 1.

Experiments were performed in a 90×20 cm wide glass-sided box (Fig. 2a). The rigid base is subdivided into three blocks by two opposite planes dipping 60°. The right block is fixed, the middle one subsides controlled by an engine and the left one is free to move horizontally. The left block is wider in order to investigate the post-extensional model evolution at distance from the basal faults. The initially planar

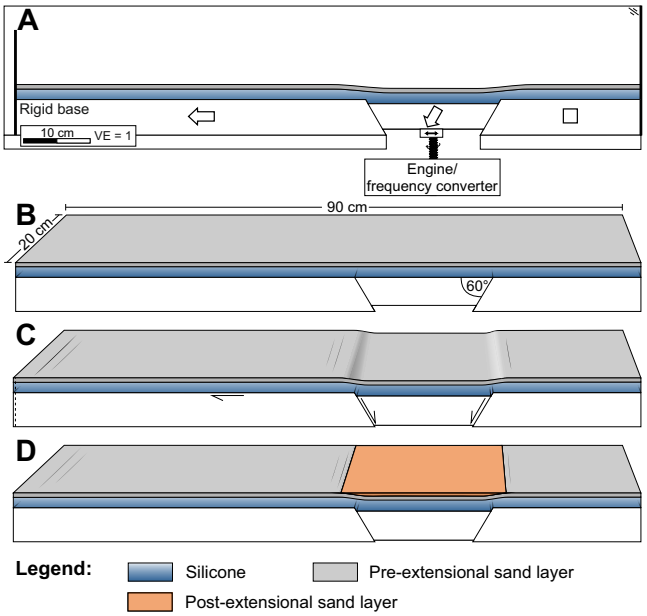

Figure 2. (a) Side view of experimental box comprising analogue materials silicone and granulate as well as subdivided rigid basement. Basal displacement is driven by a controlled engine. **(b)** In general the model procedure starts with a planar layer configuration. **(c)** Basal displacement is applied. **(d)** Surface depressions are filled with sifted granulate. Sieving procedure is repeated daily.

Table 1. Scaling parameters. Material properties (density, viscosity, friction and cohesion) are stated for analogue materials used in this experimental study (Appendix A).

Parameter	Sign	Dimension	Model	Nature	Scaling factor (model/nature)	Reference for natural values
Geometric	l^*	[m]	0.01	1000	$\sim 10^{-5}$	
Thickness (ductile layer)	h_d	[m]	0.01–0.02	1400–2500	10^{-5}	Kockel (2002); Maystrenko et al. (2013); Nalpas and Brun (1993); Scheck et al. (2003)
Thickness (brittle layer)	h_b	[m]	0.003–0.015	600–1200	10^{-5}	Nalpas and Brun (1993)
Kinematic						
Strain	ε	–			1	–
Time	t	[s]	$100\,\text{h} = 10^5\,\text{s}$	$\sim 30\,\text{Ma} = \sim 10^{15}$	10^{-10}	–
Extension rate	u	[m s^{-1}]	10^{-6}	$1\,\text{mm a}^{-1} = \sim 10^{-11}\,\text{m s}^{-1}$	$\sim 10^5$	Allen and Allen (2005)
Strain rate in viscous layer	ε'	[s^{-1}]	$\sim 10^{-5}$	10^{-11}–10^{-15}	10^{-6}–10^{-10}	Jackson and Talbot (1986); Nalpas and Brun (1993)
Dynamic						
Gravity acceleration	g	[m s^{-2}]	9.81	9.81	1	–
Density (ductile layer)	ρ_d	[kg m^{-3}]	970	2200	0.44	Jackson and Talbot (1986)
Density (brittle layer)	ρ_b	[kg m^{-3}]	1220	1800–2500	0.52–0.72	Jackson and Talbot (1986)
Dynamic viscosity (ductile layer)	η	[Pa s]	2.3×10^4	10^{17}–10^{19}	$\sim 10^{-14}$	Nalpas and Brun (1993)
Internal peak friction coefficient	μ	–	0.51 ($\pm$0.006)	0.5–0.6	1	Weijermars et al. (1993)
Internal friction angle	ϕ	[°]	27	~ 30		Weijermars et al. (1993)
Cohesion [Pa]	C_0	[Pa]	~ 100	5×10^6		Byerlee (1978)
Stress and pressure		[Pa]			$\sim 10^{-5}$	–
Brittle strength	S_b	[Pa]	60–160	$\sim 10^7$	$\sim 10^{-5}$	–
Ductile strength	S_d	[Pa]	0.5–2	$\sim 10^5$	$\sim 10^{-5}$	–
Brittle strength/ductile strength	S_b/S_d	–	50–180	$\sim$100–1000	~ 1	–

base is covered with a flat layer of silicone putty as well as a pre-kinematic granular layer (Fig. 2b).

Each experiment starts with a displacement of the basal plate (extensional phase), whereby the middle block is pulled down $d = \sim$6–7 mm (Fig. 2c), which causes $\sim$7 mm lateral stretching of the whole model ($\sim$0.8 %). The displacement rate e on the normal faults of the basal plate ranges from 0.6, 4 to 20 mm h^{-1}, which represents a natural extension rate of 0.05 to 2 mm a^{-1} (50 to 2000 m Ma^{-1}). According to our scaling, the duration of the extensional phase (0.3 to 10 h) is about 0.3 to 11 Ma, which are reasonable values for a short extensional pulse, as occurred e.g. in the North German Basin (e.g. Kockel, 2002). After termination of basal displacement, accumulation of additional sand was delayed another 15 min in order to record the post-extensional strain patterns. After this interim period additional sand (post-extensional layers) was sieved into topographic depressions to apply a pressure head on the viscous layer (Fig. 2d) (syn-sedimentary phase). The sieving procedure was repeated every day. The average sedimentation rate was $\sim$5 mm d^{-1} depending on the depth of the depressions. This rate represents a natural sedimentation rate of $\sim$0.002 mm a^{-1} ($\sim$20 m Ma^{-1}), which is 1 order of magnitude lower than the average extension rate. Since we intended to investigate post-extensional structural evolution with realistic initial density contrasts, the syn-sedimentary phase lasted much longer than the extensional phase (> 5 days equivalent up to > 100 million years in nature). In nature, sediment compaction would lead to an increase of the cover density and, therefore, to a faster growth of the salt structures during (see discussion).

In total, 12 experiments were carried out (Table 2). In order to examine sensitivity on the boundary conditions and reproducibility of the experiments, a reference experiment with equal initial conditions was repeated four times (Exp. 1a–c). The early phase was identical for these three experiments, although some variations were introduced at a later stage. In Exp. 1b, an additional phase of basal displacement was applied after 10 days. Exp. 1c was terminated earlier to observe intermediate structures. In additional experiments (Exp. 2–8) initial parameters (layer thicknesses and displacement rates) were changed systematically to test their influence on structural evolution and kinematics (Table 2). In Exp. 4b, sand accumulation was applied simultaneously with displacement of the basal plate.

We used coloured sand layers to track the structural evolution. On the basis of digitized photographs of cross-sections, the final structures were sequentially restored using a vertical-simple shear restoration algorithm (Rowan and Ratliff, 2012) in 2-D Move (Midland Valley). Furthermore, 3-D models were constructed in 3-D Move (Midland Valley).

A computer-based displacement data analysis (particle imaging velocimetry, PIV) tool provided by StrainMaster© (La Vision GmbH, 2002) was used to monitor incremental

Table 2. Experiments and key parameters, where h_d is the thickness of the ductile silicone and h_b the thickness of the brittle sand cover.

Experiment	h_d [cm]	h_b [cm]	Extension rate e [mm h^{-1}]	Subsidence d [mm]	Total duration [days]	PIV monitoring	Comment
1a	1.5	0.6	4	6	12	side view	–
1b	1.5	0.6	4	6 + 6	18	side view	two phases of extension
1c	1.5	0.6	4	6	18	side view	
1d	1.5	0.6	4	6	4	side view + top view	–
2	1.5	0.6	20	6	4	side view	–
3	1.5	0.6	0.6	6	4	side view	–
4a	1	0.6	4	6	8	side view	–
4b	1	0.6	4	6	8	side view	sand accumulation during basement extension
5	2	0.6	4	6	9	side view	–
6	1.5	0.4	4	6	9	side view	–
7	1.5	1	4	6	5	side view	–
8	1.5	1.5	4	6	6	side view	–

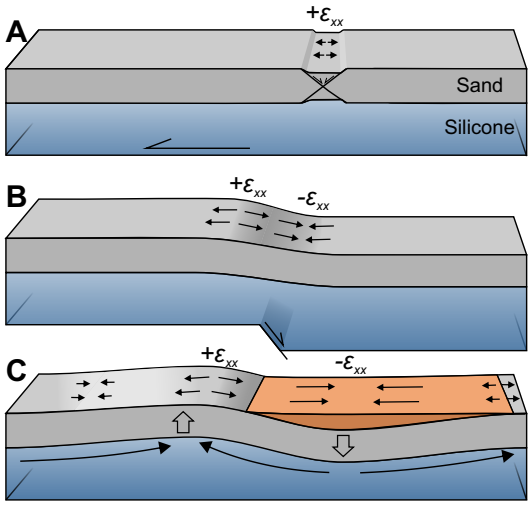

Figure 3. Explanation of lateral strain observed with PIV in top view (see results). **(a)** Cover extension, which is due to displacement of the basement, is measured as positive lateral strain ($+\varepsilon_{xx}$). **(b)** Layer bending due to extensional forced folding is accompanied by extension ($+\varepsilon_{xx}$) and compression ($-\varepsilon_{xx}$) of the sand surface. **(c)** Similarly, surface uplift due to silicone inflation leads to crestal extension ($+\varepsilon_{xx}$). Surface subsidence due to silicone deflation causes compression ($-\varepsilon_{xx}$).

strain in the granular and viscous layers, respectively, during the experiment. PIV is an optical, non-intrusive method for particle tracking consisting of digital 12-bit monochrome CCD (charge-coupled device) cameras (4 Mega Pixel; ~ 20 pixels cm^{-1}) and analysis software (LaVision 7.0). Images were taken every minute during the extensional phase and every 3 minutes during the syn-sedimentary phase. This is sufficient to follow deformation under low experimental strain rates. The images were processed with a cross-correlation algorithm calculating translation and distortion of textural differences (i.e. grey values) between two sequential images with a predefined time difference (Adam et al. 2005). Depending on the optical resolution of the cameras and the precision of the cross-correlation algorithm used, a spatial resolution < 0.1 pixels can be achieved (Adam et al., 2005). The resulting accuracy of the displacement vector is $\delta d = \sim 0.05$ mm for an assumed box width of 90 cm. On the basis of the calculated incremental vector displacement field, cumulative displacement, x- and y-component of displacement or strain tensor components (e.g. normal strain ε_{xx} and shear strain ε_{xy}) as well as long-term average flow velocities u can be calculated. To achieve a textural pattern in the transparent silicone, it was blended with a small amount of sand particles (~ 10 g sand per 1 kg silicone). The effect of this impurity on density or viscosity of the silicone is negligible (Boutelier et al., 2008; Warsitzka et al., 2013).

All experiments were monitored in 2-D side view, which provides strain patterns in the viscous layer close to the glass wall. This monitored strain can be assumed to be representative for strain occurring in the centre of the box at least during early stages of the experiment when deformation of the cover is similar between the centre and the edges of the box. During later stages of the experiment, flow patterns in the centre of the box are no longer parallel to the glass walls. Thus, strain patterns observed at the glass wall can merely provide rough estimations of strain occurring in the interior of the box. The Exp. 1c was additionally recorded in 2-D top view to observe lateral deformation on the sand surface. For analysis of flow kinematics, the horizontal displacement d_x in side view or normal strain ε_{xx} in top view was used. The 2-D top view shows lateral extensional ($+\varepsilon_{xx}$) or compressional strain ($-\varepsilon_{xx}$). This strain can be initiated for instance by thin-skinned extension of the sand cover (Fig. 3a). Furthermore, flexural bending of the sand produces extensional, as well as compressional domains at the sand surface (Fig. 3b). Similarly, it is possible to identify uplifting and subsiding areas in the sand layer due to silicone flow (Fig. 3c). Strain distribution in a folded layer is characterized

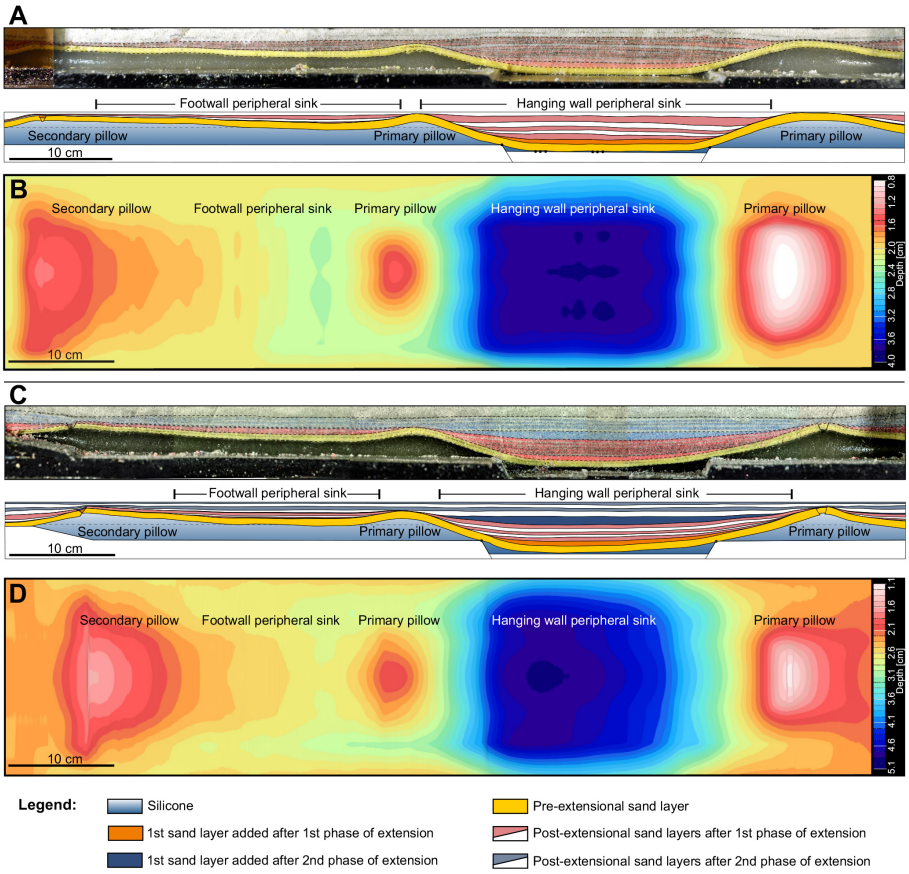

Figure 4. (a) Cross-section of reference Exp. 1a after 12 days. Post-extensional strata reveal the hanging wall peripheral sink (HPS) enclosed by two pillow-like silicone elevations. Additional sinks as well as an additional secondary pillow occur on the left side of the box. **(b)** Colour map displaying the depth of the top of the silicone layer related to the final surface from Exp. 1a. The diameters of the pillows are smaller than the diameter of the HPS. **(c)** Cross-section of reference Exp. 1b after 18 days, in which an additional phase of extension was applied after 10 days. The crests of the pillows are slightly faulted. **(d)** Depth map of the top of the silicone layer from Exp. 1b showing that the pillow structures are asymmetric.

by crestal stretching ($+\varepsilon_{xx}$) of the sand surface in anticlines, whereas synclinal bending is associated with compressional strain ($-\varepsilon_{xx}$) (Schultz-Ela and Jackson, 1996).

Strain monitoring with PIV is non-intrusive (Adam et al., 2005), i.e. only the strain at the model surface can be observed. This restricts monitoring of movement in the silicone, which is constrained by friction on the glass wall boundaries and, therefore, not plane-strain. Thus, displacement observed at the glass wall is merely a fractional amount of displacement, which takes place in the middle of the box (Warsitzka et al., 2013). We reduced the effect of lateral friction of viscous material on the glass walls by lubricating the glass with a thin film of glycerine. Due to this the silicone is able to easily slide along the side walls during the experiment, which improves strain monitoring by PIV. Without such lubrication, strain in the silicone layer would only take place at some distance from the glass walls.

3 Experimental results

3.1 Experimental structures

Cross-sections through the centre of the box of reference experiments 1a and 1b (Fig. 4a, c) show the final structures obtained after 12 days or 18 days, respectively. A peripheral sink with thickened sand layers developed above the downthrown hanging wall basement block. This sink is here called the hanging wall peripheral sink (HPS). It is bounded by two pillows at several centimetres distance from the basement faults. The post-extensional sand layers (red/white; blue/white) pinch out towards the crests of the two pillows causing a bowl-shaped structure of the HPS. The width of the HPS is larger than the width of the underlying basement graben. The silicone beneath the HPS is depleted, which eventually brings the base of the sand in contact with the edges of the basement footwall blocks.

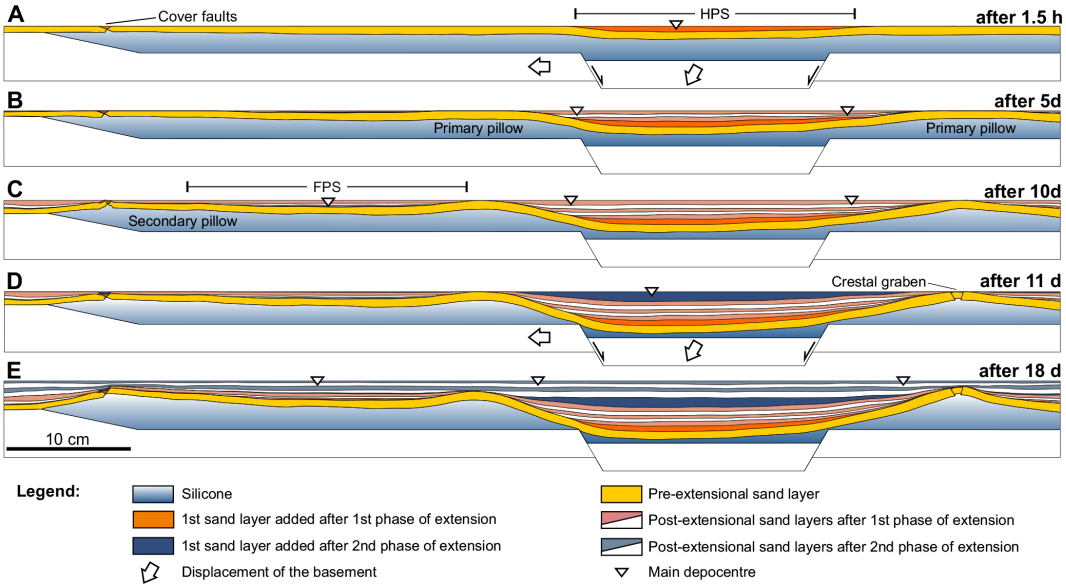

Figure 5. Restoration of final cross-section of Exp. 1b. **(a)** At the end of basement extension the hanging wall peripheral sink (HPS) begins to subside. **(b)** Additional sand accumulated causes the formation of pillow structures close to downthrown basement block as well as above the platform at the left side of the box (secondary pillow). **(c)** The subsidence during the second phase of basement extension is marked by the dark blue layer. **(d)** Further post-extensional sand accumulation (blue/white) increases the elevation of the pillow-like structures.

Two types of pillow-like structures can be distinguished in the experiments. The first (primary pillows) are situated adjacent to the basement fault above the footwall block. The second type (secondary pillow) is located on the footwall platform near the left-hand end of the experimental box. Depth maps of the top of the viscous layer (Fig. 4b, d) reveal that the pillows are elongated and their long axes trend parallel to the basement offset. An additional peripheral sink (footwall peripheral sink) containing thickened post-extensional layers is located between the left-hand primary pillow and the secondary pillow.

In Exp. 1b the basement was displaced a second time, which is marked by the blue/white layers. Here, the pre-kinematic sand layer (yellow) displays minor faulting at the crest of the pillows. Post-extensional layers of the first phase (red/white) are bent upward. Different from Exp. 1a, the silicone layer beneath the HPS is not completely depleted.

3.2 Evolution of experimental salt structures

The structural evolution of Exp. 1b is illustrated by means of restorations of the central cross-section shown in Fig. 4. During the first syn-extensional stage, a small depression (HPS) forms due to subsidence of the central basement block (Fig. 5a). The cover layer above each fault tip is bent into a monocline roughly 5 cm wide above a ductile layer that began 1.5 cm thick. Lateral extension in the cover layer is mainly balanced by peripheral cover grabens near the left edge of the box. These cover grabens are located close to the region where the silicone pinches out due to a basement wedge, and can be regarded as an edge effect. During the syn-sedimentary stage, surface depressions were filled by adding sand. The first post-extensional sand layer (orange) represents the surface subsidence due to basement displacement. Successive growth beds (red–white) reflect downwarping due to flow of the viscous material. After several phases of sand accumulation and accompanying expulsion of the silicone, the HPS widens significantly (Fig. 5b). Areas of maximum sand accumulation gradually move from the centre of the HPS towards the rising pillow crests. On the outer side of the left-hand primary pillow, an additional peripheral sink (FPS) develops. Eventually, a secondary pillow evolves above the left footwall block (Fig. 5c).

During the second pulse of rapid extension with additional 6 mm of displacement along the basement faults (displacement rate $= 4\,\mathrm{mm\,h^{-1}}$) (Fig. 5d), the subsidence of HPS increased. This leads to a contact of the base of the HPS with the edges of the footwall blocks. Consequently, no additional silicone is expelled from the hanging wall side and the depocentres move closer to the crests of the pillows (Fig. 5e). During successive post-extensional sand accumulation (blue–white), the primary pillow structures become more pronounced and elevated (Fig. 5e). The growth of the secondary pillow accelerates with increased subsidence of the footwall peripheral sink.

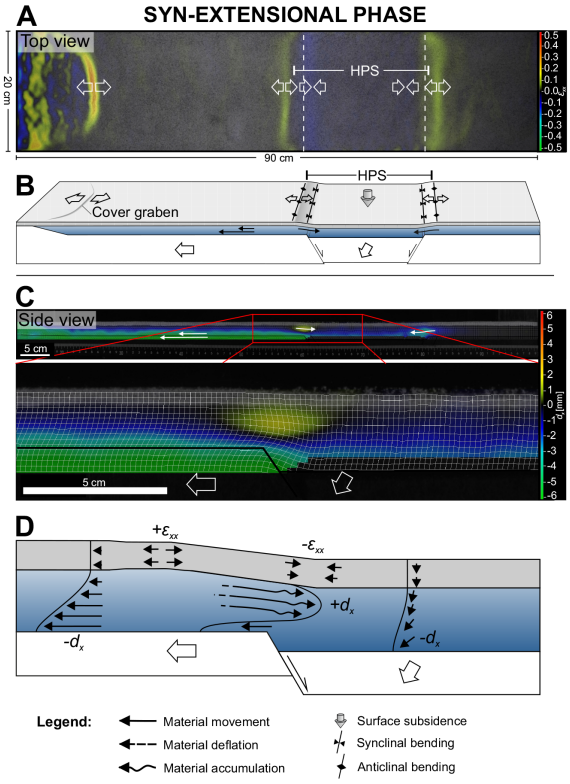

Figure 6. Results of PIV monitoring during syn-extensional phase of the reference experiments 1b and Exp. 1c. **(a)** Top view of Exp. 1c: lateral strain ε_{xx} observed with PIV displaying zones of extension (yellow) and zones of compression (blue). Dashed lines indicate location of basal faults. HPS = hanging wall peripheral sink. **(b)** Sketch showing the interpretation of the PIV strain patterns. **(c)** Side view of Exp. 1b: horizontal displacement d_x observed with PIV including a detailed view of the left basement fault. Coloured areas display rightward (yellow–red) and leftward (green–blue) movement of the analogue material. **(d)** Conceptual sketch (arrows are not to scale) summarizing the interpreted displacement patterns and showing vector profiles representing the material movement. The viscous material above the fault tip flows towards the hanging wall side opposed to the shearing along the basement.

4 Displacement and strain patterns

Displacements and strain patterns are visualized using PIV monitoring for the phases during basement extension, after termination of basement extension and during accumulation of post-extensional sand layers.

4.1 Syn-extensional phase

Figure 6 shows the displacement and strain patterns of Exp. 1b after 6 mm of vertical basal displacement or 1.5 h, respectively. Patterns of lateral strain (ε_{xx}) observed in top view of the sand surface (Fig. 6a) reveal zones of compression ($-\varepsilon_{xx}$, blue) and zones of extension ($+\varepsilon_{xx}$, red). Highest amounts of ε_{xx} are accommodated at a cover graben at the left side of the box in an extensional zone. Less pronounced zones of extensional strain occur adjacent to the basement faults. These zones are surrounded by two compressional zones above the edges of the hanging wall basement block. The extensional domains bordering the basement faults above the footwall blocks are the combined effect of bending of the cover (see explanation in Fig. 3) and lateral stretching due to opposite movement in the silicone (Fig. 6b). Similarly, the less pronounced compressional domains above the hanging wall block result from layer bending.

In the side view of Exp. 1b, horizontal displacement d_x illustrates the lateral movement of the left basement block (Fig. 6c). The amount of d_x decreases vertically within the viscous silicone layer and virtually drops to zero in the sand layer. Hence, shearing at the base is not transmitted into the cover. As indicated by the vector grid these strain patterns in the viscous layer can be described as shear flow (Couette flow). Additionally, significant horizontal movement in the silicone can be recognized directly above the fault tip in a 3–4 cm wide, elliptical zone. Although the silicone layer is sheared in the opposite direction by the leftward moving basement block, silicone flows towards the subsiding basement block (Fig. 6c). The vector grid in this elliptical zone shows a vertically parabolic shape, which is characteristic for channelized Poiseuille-type flow.

4.2 Post-extensional phase

After basement extension had been stopped, deformation was monitored for approximately 15 min, before the first post-extensional sand layer was added. During this interim period, patterns of the lateral strain ε_{xx} observed in top view of Exp. 1b (Fig. 7a, b) show extensional domains (yellow) at the edges of the central hanging wall block and at the peripheral cover graben. Zones of compressional strain (blue) are identified at the edges of the footwall blocks, in the centre of the hanging wall block and adjacent to the peripheral cover graben. As explained by means of Fig. 3, extensional strains can be attributed to uplift and anticlinal bending of the thinned cover, whereas areas of compressional strain indicate subsidence and synclinal bending of the cover. Hence, the surface subsides at the edges of the footwall blocks, whereas it is uplifted at the edges of the hanging wall block. Meanwhile the peripheral cover graben is uplifted, whereas adjacent areas subside. Complex strain patterns above the centre of the left footwall block are a result of slightly irregular thicknesses of the sand layer. The amount of strain (max. 0.025 %) is one order of magnitude lower than strain during the syn-extensional phase (max. 0.5 %).

The side view of Exp. 1b (Fig. 7c) reveals flow of the viscous material towards the subsided basement block. The zones of downward flow are roughly 6 cm wide, as identified through the coloured area. Therefore, this zone is twice as wide as in the syn-extensional stage. The vector grid allows

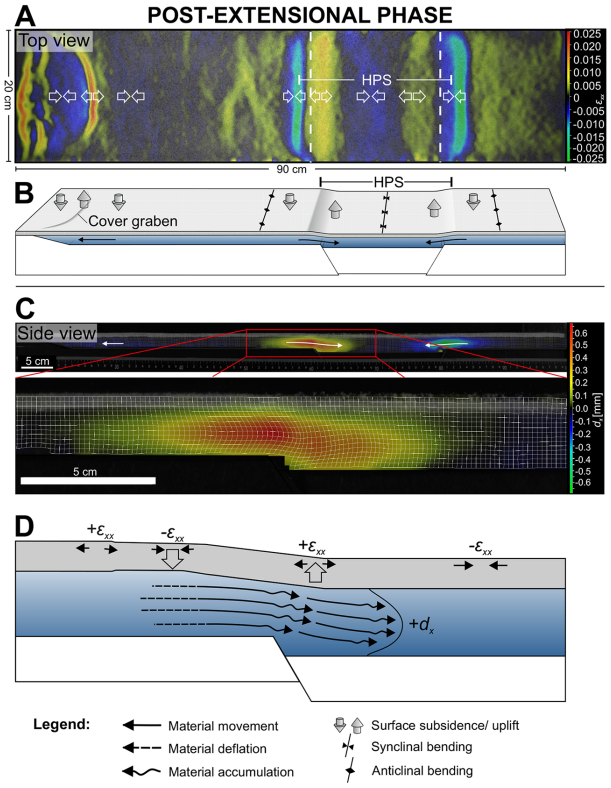

Figure 7. Results of PIV monitoring during the post-extensional phase of the reference experiments 1b and Exp. 1c 15 min after basement extension had ceased. **(a)** Top view of Exp. 1c: lateral strain ε_{xx} observed with PIV displaying zones of extension (yellow) and zones of compression (blue). Dashed lines indicate location of basal faults. HPS = hanging wall peripheral sink. **(b)** Sketch showing the interpretation of the PIV strain patterns. **(c)** Side view of Exp. 1b: horizontal displacement d_x observed with PIV including a detailed view of the left basement fault. Coloured areas display rightward (yellow–red) and leftward (green–blue) movement of the analogue material. **(d)** Conceptual sketch (arrows are not to scale) summarizing the interpreted displacement patterns and showing representative vector profiles of the material movement.

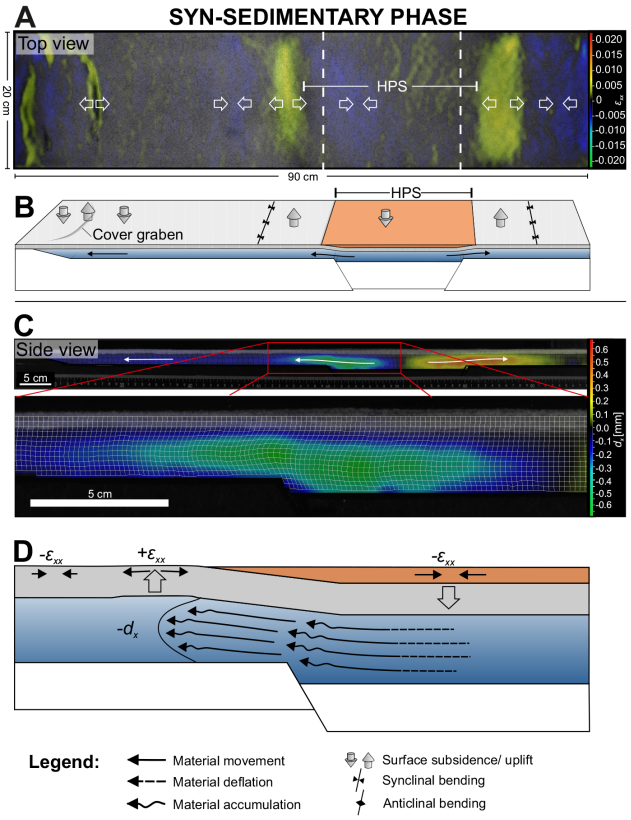

Figure 8. Results of PIV monitoring during syn-sedimentary phase of the reference experiments 1b and Exp. 1c 1h after addition of the first post-extensional sand layer. **(a)** Top view of Exp. 1c: lateral strain ε_{xx} observed with PIV displaying zones of extension (yellow) and zones of compression (blue). Dashed lines indicate location of basal faults. HPS = hanging wall peripheral sink. **(b)** Sketch showing the interpretation of the PIV strain patterns. **(c)** Side view of Exp. 1b: horizontal displacement d_x observed with PIV including a detailed view of the left basement fault. Coloured areas display rightward (yellow–red) and leftward (green–blue) movement of the analogue material. **(d)** Conceptual sketch (arrows are not to scale) summarizing the interpreted displacement patterns and showing representative vector profiles of the material movement.

identification of a vertically parabolic shape of the vector profile occurring in the region of active flow. The viscous material is mainly accumulated directly above the fault step and above the hanging wall block, which can be inferred by the horizontally compressed vector grid. Maximum displacement d_{xmax} in the silicone ranges between 0.6 and 0.7 mm in the 15 min of this interim period. Hence, maximum displacement rates u achieved by viscous flow are 2.4 to 2.8 mm h^{-1}, which is nearly twice as high as during the syn-extensional phase ($u = \sim 1.5$ mm h^{-1}).

The summarizing sketch (Fig. 7d) explains how the zones of silicone expulsion correspond to areas of lateral cover compression ($-\varepsilon_{xx}$) in the cover layer. The zone where silicone is accumulated is related to surface extension ($+\varepsilon_{xx}$) (Fig. 7d). This indicates that down-slope silicone flux above the fault tip entails uplift above the hanging wall block and subsidence above footwall blocks. In the same way, extensional strain observed at the peripheral cover graben denotes uplift. This suggests flow of viscous material towards the thinned cover.

4.3 Syn-sedimentary stage

One hour after filling the surface depressions, zones of extension ($+\varepsilon_{xx}$) and compression ($-\varepsilon_{xx}$) have developed (Fig. 8a). These zones are wider and the lateral strain (ε_{xx}) is more diffuse than in the post-extensional phase. In contrast to the post-extensional phase, slight compression occurs directly above the downthrown basement block. Meanwhile, areas adjacent to the basement fault on the footwall block are

characterized by extension, surrounded by additional zones of compression further outboard. The region around the peripheral cover graben at the left edge of the box displays slight extensional strain. As in the post-extensional stage, these zones of extensional strain and compressional strain can be related to surface uplift or subsidence, respectively, as illustrated in the interpretive sketch (Fig. 8b).

The displacement pattern revealed in side view (Fig. 8c) indicates that the viscous material flows from the downthrown block towards the footwall blocks. Hence, silicone is expelled from the lowered basement compartment to the higher basement compartments on both sides. The regions in the viscous layer affected by horizontal displacement are wider than in the previous phases. Furthermore, these regions are roughly twice as wide ($\sim$ 11 to 13 cm) as the monocline in the cover layer ($\sim$ 6 cm). A parabolic-shaped vector grid denotes Poiseuille-type flow within this zone. A horizontally compressed vector grid indicates that viscous material accumulates close to the edge of the basement fault and above the footwall block. The maximal horizontal displacement d_{xmax} in the viscous layer was approximately 0.6 to 0.7 mm during one hour of recording. Thus, displacement rates ($u = 0.6$ to $0.7\,\mathrm{mm\,h^{-1}}$) were significantly lower than during the post-extensional phase ($u = 2.4$ to $2.8\,\mathrm{mm\,h^{-1}}$).

Combining the observations from top view and side view, it can again be shown that the zones of silicone expulsion and silicone inflation fit with areas of surface compression or surface extension (Fig. 8d). Hence, horizontal flow in the viscous layer is predominantly compensated by vertical movement in the cover layer. Subsidence of the cover layer on the hanging wall block expels silicone up the basement fault. Consequently, silicone inflation onto the footwall block induces surface uplift adjacent to the basement step. Anticlinal uplift above the footwall blocks (yellow areas) eventually results in the formation of the primary pillow structures (Fig. 4). Furthermore, uplift of the peripheral cover graben continues. Nevertheless, the amount of uplift is less than during the post-extensional phase, which is a result of burial under sand in the centre of the cover graben.

4.4 Subsequent sedimentation phases

During ongoing accumulation of sand, the horizontal flow pattern in the silicone layer changes gradually (Fig. 9). Initially, horizontal flow is restricted to the region above the fault tip (Fig. 9a), while only minor displacement occurs away from the basement fault above the footwall block. Due to subsequent sand accumulation in the HPS, the zone affected by viscous flow above the fault tip widens and migrates away from the basement step along the footwall block (Fig. 9b). After 10 days significant viscous deformation is induced away from the initial basement fault (Fig. 9c). Although the primary pillows are mainly supplied from the area above the hanging wall block, a zone of rightward (yellow) directed flow can be observed. This indicates material influx from the footwall side into the primary pillows, which is driven by the subsidence of an additional peripheral sink (footwall peripheral sink, Fig. 5c). Furthermore, leftward directed displacement (blue) at the left edge of the box increases. This reflects material flow during increased growth of the secondary pillow. At this stage intense flow is active within the entire box. Note that at late stages, silicone flow is no longer parallel to the glass walls. The pillow-like structures developed only in the centre of the experimental box resulting in circular inflow from all sides. Only a part of this flow can be observed at the glass wall boundary.

4.5 Second phase of extension

After 11 days, a second phase of rapid extension with 6 mm of displacement was applied in reference experiment 1b (displacement rate $= 4\,\mathrm{mm\,h^{-1}}$). In general, displacement patterns during this second extensional phase are similar to those observed in the first extensional phase (Fig. 10). Nevertheless, absolute displacement in the silicone layer above the fault tip is larger in the second phase than in the first phase. During the post-extensional and the syn-sedimentary phase, the lateral extent of viscous flow is smaller after the second extensional phase. Furthermore, accumulation of the viscous material predominantly takes place above the footwall side. This indicates that the drainage channel in the silicone layer above the fault tip is reduced due to subsidence of the HPS.

5 Sensitivity study

The structural development and flow kinematics are basically similar in all experiments presented above. However, systematic variations depending on the thickness of the viscous layer h_{d}, the thickness of the cover layer h_{b} and the basement displacement rate e can be perceived. A comparison of all experimental cross-sections and displacement patterns occurring in the specific experiments can be found in the Supplement. A summary of these flow patterns for the syn-sedimentary stage, and the maximum flow velocities in the centre of the silicone layer is presented in Fig. 11a–c. Flow velocities u were calculated for the end of the extensional stage (after 1.5 h), the end of the post-extensional stage (after 15 min), and for each syn-sedimentary phase (1 h after accumulation of sand) by dividing the maximum displacement in the centre of the viscous layer by the total time (Fig. 11a–c). In general, displacement rates u are highest during the post-extensional phase ($u = 1$ to $5\,\mathrm{mm\,h^{-1}}$). Displacement rates during the syn-sedimentary phases are notably lower ($u = < 1\,\mathrm{mm\,h^{-1}}$). In most experiments, displacement rates increase gradually with each syn-sedimentary phase.

5.1 Effect of basement extension rate *e*

Slower basement extension causes a wider and smoother bending of the monoclines above the fault tips (Exp. 3;

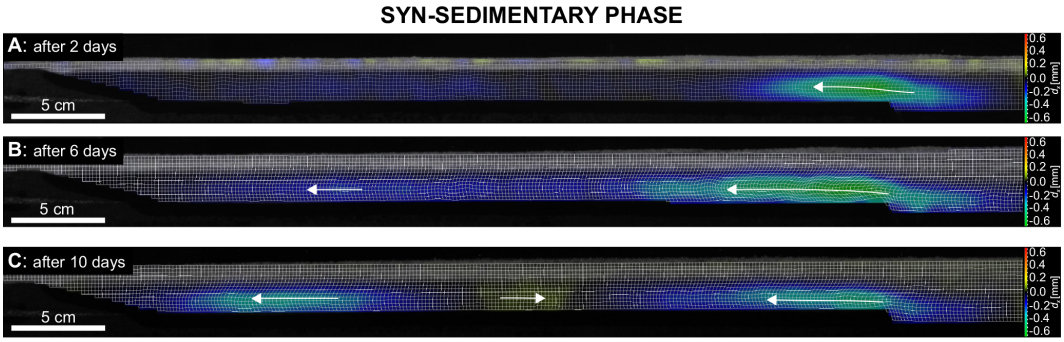

Figure 9. Time series of PIV displacement patterns of the reference experiment Exp. 1b during syn-sedimentary phase. **(a)** After 2 days, pronounced leftward (blue) directed movement occurs close to the basement fault tip. **(b)** After 6 days, the zone of leftward movement increases in width and additional flow appears away from the basement fault. **(c)** After 10 days, significant displacement can still be observed above the basement fault and away from it.

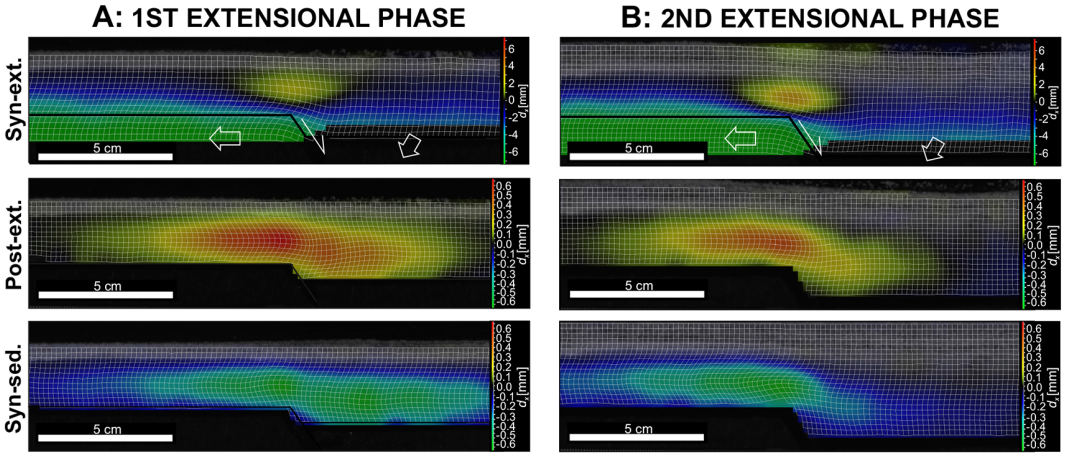

Figure 10. Comparison of horizontal displacement d_x in side view above the tip of the basement fault during **(a)** first and **(b)** second phase of basement extension of the reference experiment 1b after 11 days of experimental duration. Coloured areas denote rightward (yellow–red) and leftward (green–blue) movement of the analogue material.

Fig. 11a). Furthermore, the position of the cover graben is located in a greater distance from the basement fault. If e is large (Exp. 2), a comparably narrow monocline and a small cover graben develops adjacent to the basement fault.

During the syn-extensional phase, the zone above the fault tip, which is affected by downward flow, increases in width, if e is small (Fig. 11a). Maximum displacement d_{xmax} in the silicone layer is significantly higher at slow basement extension (Exp. 3: $d_{\mathrm{xmax}} = \sim 5$ mm in 495 min) than for rapid basement extension (Exp. 2: $d_{\mathrm{xmax}} = \sim 0.5$ mm in 16 min). However, the average flow velocity u in the viscous layer is lower in Exp. 3 ($u = \sim 0.6\,\mathrm{mm\,h^{-1}}$) than in Exp. 2 ($u = \sim 1.8\,\mathrm{mm\,h^{-1}}$; Fig. 11a).

During the post-extensional phase and during the syn-sedimentary phase, viscous flow above the fault tip spreads over a wider zone, if basement extension was slow (Fig. 11a). By contrast, maximum displacement d_{xmax} and flow velocity u in the viscous layer are higher, when basement extension was rapid (Exp. 2; Fig. 11a) compared to slow basement extension (Exp. 3).

In summary, decreasing the displacement rate of the basement fault e leads to an increased width of the monocline in the cover, a wider zone affected by flow in the viscous layer, but a lower flow velocity in the viscous layer (Fig. 11a).

5.2 Effect of the thickness of the viscous layer h_{d}

A thicker viscous layer h_{d} causes a wider and smoother bending of the monoclines above the fault tips (Exp. 5, Fig. 11b). At small h_{d} (Exp. 4) a cover graben develops adjacent to the basement fault. In Exp. 4, the mature pillow structures are comparatively narrow (~ 6 cm) and are located close to the basement faults. In experiments with larger h_{d} (Exp. 1a, 5), pillows are wider, their elevation is higher, and the distance to the basement graben is larger (see the Supplement).

The zone affected by viscous flow increases in width in all phases of the experiment, if the thickness of the silicone

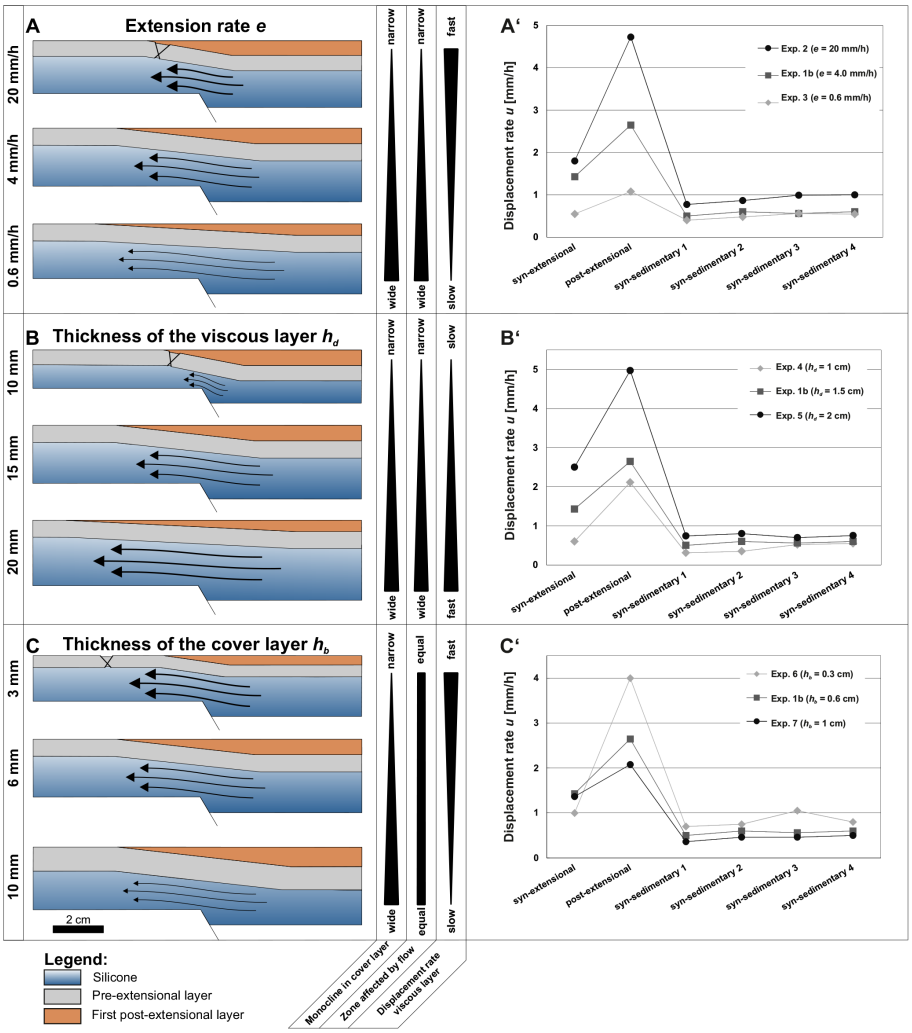

Figure 11. Summarized results of the structures, the kinematics, and the displacement rates u depending on **(a/a')** extension rate at the basement fault e, **(b/b')** thickness of the viscous layer h_{d}, and **(c/c')** thickness of the cover layer h_{b}. Black arrows indicate extent of flow in the silicone layer, whereas the thickness of the arrows represents the displacement rates. Triangles and bars in the centre column reflect increasing or decreasing effect on structures and kinematics. The displacement rates are generally highest during the post-extensional phase. During the syn-sedimentary phases, the displacement rates are notably lower. Note that only the values of the first four syn-sedimentary phases are displayed while most experiments last longer.

layer is larger (Exp. 5; Fig. 11b). During basement extension, flow velocities are higher for a thick viscous layer (Exp. 5: $u = \sim 2.5\,\mathrm{mm\,h^{-1}}$) than for a thin viscous layer (Exp. 4: $u = \sim 0.7\,\mathrm{mm\,h^{-1}}$) applying an equal amount of basement extension (Fig. 11b). A similar dependence can be observed for the post-extensional and the syn-sedimentary phase (Exp. 4: $u = \sim 0.4\,\mathrm{mm\,h^{-1}}$; Exp. 1b: $u = \sim 0.5\,\mathrm{mm\,h^{-1}}$; Exp. 5: $u = \sim 0.8\,\mathrm{mm\,h^{-1}}$). Exp. 5 ($h_{\mathrm{b}} = 20\,\mathrm{mm}$; Fig. 11b) shows the highest post-extensional flow velocities of all experiments ($u = \sim 5\,\mathrm{mm\,h^{-1}}$), which even exceeds the actual basement extension rate ($e = 4\,\mathrm{mm\,h^{-1}}$). Eventually, fast silicone flux leads to an initial active piercing of the silicone through the crest of the pillow structures in this experiment.

5.3 Effect of the thickness of the cover layer h_{d}

A thicker cover layer h_{b} (Exp. 1b, 8; Fig. 11c) causes a wider and smoother bending of the monoclines above the fault tips. Compared to this, a narrow monocline occurs if h_{b} is small (Exp. 6; Fig. 11c). With increasing h_{b} the pillows become wider and located in a larger distance from the basement graben (see the Supplement). Only if the thickness of the cover is very large ($h_{\mathrm{b}} = 15\,\mathrm{mm}$, Exp. 8), do no distinct pillow structures evolve. In this case, the silicone layer above the footwall block is thickened over a broad area and the sinking of the HPS merely lasts a few syn-sedimentary phases.

Varying h_b has relatively minor effects on flow patterns. In each phase of the experiments, the lateral extent of silicone flow is only slightly wider for larger cover thicknesses (e.g. Exp. 7) compared to experiments with smaller cover thicknesses. Flow velocities u in the viscous layer are roughly similar during the syn-extensional phase, independent of h_b ($u = 1$ to $1.5\,mm\,h^{-1}$; Fig. 11c). During the post-extensional and syn-sedimentary phases, respectively, flow velocities are higher in the experiment with a thinner pre-extensional cover layer (Exp. 6) compared to experiments using a thicker cover layer (Exp. 7, 1a; Fig. 11c).

6 Discussion

6.1 Structural evolution

Our experimental procedure involved a short pulse of basement extension followed by a long-lasting phase of post-extensional sedimentation, which is different from most previous experimental studies (Nalpas and Brun, 1993; Koyi et al., 1993; Dooley et al., 2005). As in experiments by Nalpas and Brun (1993) and Dooley et al. (2005), we can distinguish (1) basement fault-related salt structures and (2) platform salt structures.

1. The basement fault-related salt structures, here referred to as primary pillows, are located close to the basement faults, but entirely on the footwall block. In Fig. 5 we showed that the main depocentres in the HPS gradually migrate from the centre of the sink towards the crests of the rising pillows. This indicates that the viscous material is squeezed beyond the basement fault and that the primary pillows develop further away from the basement fault. This observation is in agreement with most of the previous experimental studies mentioned above, which showed that early stage salt structures or cover grabens are laterally offset from the basement fault tip if a viscous detachment is present (e.g. Withjack and Callaway, 2000).

2. The pillows of the second type (secondary pillows) are located further on the footwall block. In our experiments, decoupled cover faults developed close to the edge of the experimental box, which is likely an effect of the side wall (see below). Secondary pillows mainly grew during later syn-sedimentary phases, when the footwall peripheral sink (FPS) formed. This suggests that the formation of secondary pillows does not depend on layer thinning above the footwall platform. This type of pillow is rather forced by differential loading produced by the peripheral sink of the neighbouring primary pillow. This process is similar to the development of "secondary diapirs" (Warsitzka et al., 2013), which are generated by the subsidence of minibasins adjacent to diapirs (Cobbold et al., 1989; Goteti et al., 2012; Peel, 2014) and which have been exemplarily shown to occur in nature, e.g. in the North German Basin (Strunck et al., 1998).

6.2 Kinematics

Two end member types of flow patterns were observed in our experiments: (1) downward flow above the basement fault tip occurs during the initial phase of extension and the post-extensional phase; (2) subsequently, upward flow occurs during (post-extensional) sediment accumulation in the HPS. We interpret this reversal of flow direction in our experiment as a result of the prevailing gradient of the hydraulic head (e.g. Kehle, 1988; Koyi et al., 1993). Downward flow is driven by elevation head as soon as the viscous layer is vertically displaced. Sand accumulation in the hanging wall peripheral sink creates differential loading. Due to this, a pressure head in the viscous layer induces a reversal of the flow direction. Flow velocities during syn-sedimentary upward flow are small compared to those during downward flow (Fig. 11). Hence, we infer that the pressure head is only slightly higher than the elevation head. During subsequent phases of sedimentation, flow velocities in the viscous layer above the basement fault increase (Fig. 11) denoting a gradually increasing pressure head. During later stages of the experiments, lateral spreading of regions affected by viscous flow across the footwall platform (Fig. 9) suggests that an additional pressure head is imposed above the footwall block. This is due to the subsidence of the FPS. However, the more deeply subsided HPS and the strain patterns (Fig. 9) suggest that the supply of the primary pillow from the footwall side remains minor throughout the experimental evolution. The main portion of viscous material within the primary pillow flows in from the footwall side.

Deformation visualized through vector grids (Figs. 7, 8) suggests that lateral flow of the viscous material equilibrates the vertical movement of the overburden and viscous material is expelled from subsiding towards uplifting regions. Therefore, the flow regime within the viscous layer can be described as squeezed channel flow (e.g. Fuchs et al., 2014), i.e. the idealized parabolic vector profiles (Poiseuille flow) are vertically compressed beneath subsiding areas and vertically extended in regions of material accumulation. Such channel flow occurs in opposite direction to shearing at the basement during the syn-extensional phase (Fig. 6). This indicates that stresses applied by the hydraulic head can exceed shear stress caused by lateral strain. During post-extensional and syn-sedimentary phases, broad regions affected by channel flow were observed above the basement step. This demonstrates that small displacements of the basement ($D_r < 1$) can cause widespread stresses in the viscous layer.

6.3 Sensitivity study

Varying the layer thicknesses and extension rates provides insights into the reliability of the observed material flow patterns and conditions for pillow formation. By increasing the thickness of the viscous layer h_d, a wider region is affected by faster viscous flow. This indicates that frictional forces at the top and the bottom of the viscous layer are less significant in a thick viscous layer than in a thin viscous layer assuming the same hydraulic head. Therefore, the growth of pillows is facilitated if the salt layer is thicker.

In experiments with a thicker cover layer, flow velocities were generally lower and the formation of pronounced pillow structures was suppressed. This results from enhanced normal stresses at the top of the viscous layer, if the overburden is thick. Thus, the resistance against uplift above the footwall block increases and inflow of viscous material from the hanging wall block during the syn-sedimentary phase is impeded. Nevertheless, significant parts of the viscous layer are affected by horizontal material flow during the syn-sedimentary phase, even if the thickness of the cover layer is large (Exp. 8; see the Supplement). This indicates that viscous material accumulated over a larger region leading to subtle, but broad uplifts.

The basement extension rate e affects flow patterns and displacement rates u in the viscous layer during the post-extensional and syn-sedimentary phases. Post-extensional and syn-sedimentary flow velocities were lower after slow basement extension (Exp. 3; Fig. 11), because viscous flow was able to keep pace with the subsidence of the downthrown basement block. Hence, the space created by basement subsidence was partly equilibrated by increasing the thickness of the viscous layer (Jackson et al., 1994; Higgins and Harris, 1997). Fewer syn-kinematic sediment could be added to the hanging wall peripheral sink, which reduced the effect of differential loading. In experiments applying fast basement extension (Exp. 2) high syn-sedimentary flow velocities were observed above the basement fault. This is because the subsidence of the HPS was similar to basement subsidence. Hence, syn-kinematic layers in the HPS are thicker leading to a higher pressure head. Therefore, it can be assumed that fast basement extension promotes post-extensional pillow growth, at least when the displacement of the basement fault was small.

6.4 Limitations of the experimental procedure

All experiments have been set up with a pre-kinematic overburden layer before the onset of basement extension. However, the sensitivity study revealed that flow velocities are higher and pillow structures are larger in experiments with a thinner cover layer. Thus, it can be inferred that without a pre-kinematic cover layer, sand accumulation in the HPS would trigger the formation of a minibasin and nearby downbuilt diapirs (e.g. Burliga et al., 2012; Goteti et al., 2012).

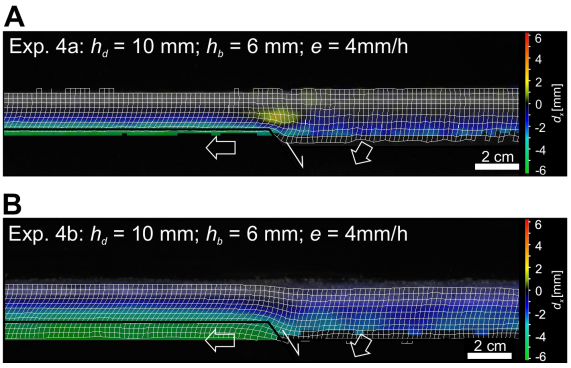

Figure 12. Comparison of two experiments with equal initial conditions, but **(a)** without syn-extensional sand accumulation and **(b)** with syn-extensional sand accumulation in the hanging wall peripheral sink. Downward flow is prevented in **(b)**. However, no upward flow can be recognized in **(b)**, although differential loading between the hanging wall side and the footwall side is present. Coloured areas display rightward (yellow–red) and leftward (green–blue) movement of the analogue material.

Decoupled cover grabens and secondary pillows developed close to the edge of the experimental box, where the silicone layer pinches out. In nature there is no comparable lateral confinement of the salt layer. However, irregularities of the basement, above which the thickness of the viscous layer changes, can also determine the location of decoupled thin-skinned extension (e.g. Gaullier et al., 1993). Similarly, secondary pillows can also be caused by a subsiding minibasin in a laterally extended salt layer (e.g. Peel et al., 2014).

Basement displacement and syn-kinematic sediment accumulation were artificially separated in our experiments, although these processes are contemporaneous in nature. In some preliminary experiments, e.g. Exp. 4b, additional sand was sieved into the subsiding HPS during basement extension. In these experiments downward flow above the basement fault was non-existent, but no upward flow was induced during the syn-extensional phase (Fig. 12). This might be due to shearing in the viscous layer above the basement fault, and due to the low density contrast between the viscous material and the cover layer. In other experimental studies simulating salt diapirism due to basement extension (e.g. Burliga et al., 2012; Dooley et al., 2005) syn-extensional sedimentation was applied and no phase of downward flow was described. However, the density of the sand cover in those experiments was $\Delta\rho = 500$–$700\,\mathrm{kg\,m^{-3}}$ higher than the density of the viscous layer. This exaggerates the effect of buoyancy and differential loading (Allen and Beaumont, 2012) compared to natural systems – at least for the initial stage of salt structure development.

In nature, overburden density increases due to compaction and exceeds that of salt at depths of 600–1500 m (Jackson and Talbot, 1986). This compaction process is difficult to simulate in analogue models. Assuming a relatively thin

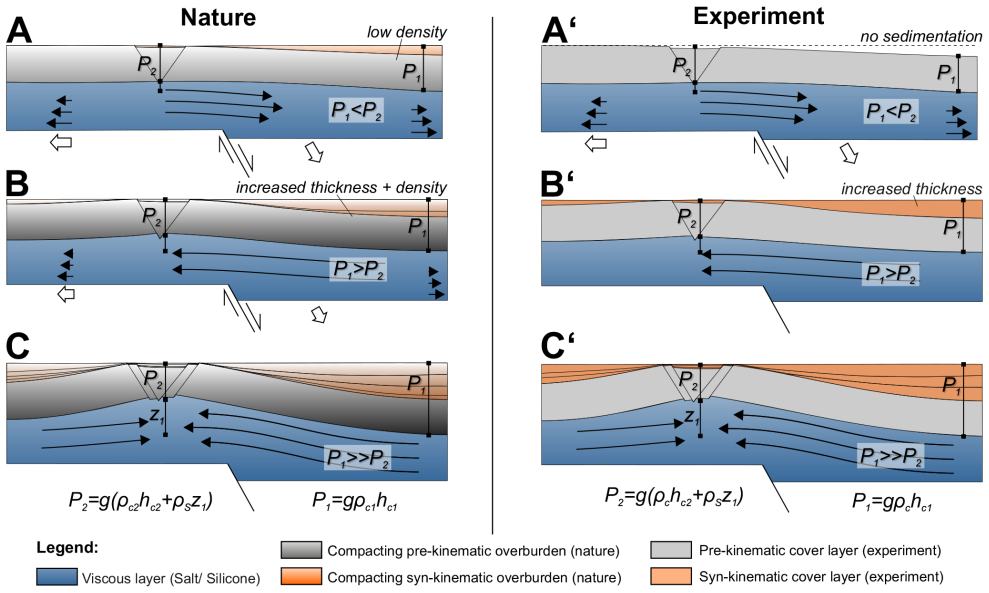

Figure 13. Conceptual model of the formation of a pillow and corresponding flow patterns in nature and experiment. **(a)** During initiation of basement faulting average density of the overburden in the HPS is still lower than that of salt causing only a low amount of differential loading. **(a')** This is similar to the lack of sedimentation in the experimental peripheral sinks. In both cases downward flow occurs above the fault tip since the pressure head is smaller than the elevation head. **(b)** Due to further basement extension, thickness and density of the overburden above hanging wall side increase. **(b')** Additional cover material is filled into the HPS. In both cases, upward flow above the basement fault is initiated by an increasing pressure head. **(c/c')** During decreased or stopped extension, the viscous material can continuously flow upward causing the formation of a pillow structure.

pre-kinematic overburden layer (< 1000 m), the average density of the natural overburden is lower than that of salt. However, density increases with burial especially in the hanging wall peripheral sink, where thick sediments are deposited. Therefore, differential loading between a peripheral sink and a nearby salt structure becomes more effective with increasing subsidence of the HPS. For comparison of our experimental results with natural salt tectonics, filling the HPS with additional sand slightly denser than the viscous material is similar to the gradual compaction process in nature during continuous syn-extensional sedimentation (see below). In both cases, the pressure head exceeds the elevation head at a certain amount of subsidence of the HPS (Fig. 13).

6.5 Inferences concerning pillow growth and salt flow in extensional basins

Both components of the hydraulic head (elevation head and pressure head), modelled separately in our experiments, temporally and spatially overlap in natural salt-bearing extensional basins. However, we suggest that as in our models, the elevation head can dominate during early growth stages of natural salt pillows according to the following conceptual model (Fig. 13): at the beginning a viscous layer and its overburden are gradually displaced by basement faulting. As long as the average density of the overburden is smaller than that of salt, differential loading is also small, even if sediment supply is high enough to keep pace with basement subsidence (Fig. 13a). Hence, early downward flow is driven by elevation head. If basement displacement continues, density of the overburden in the HPS increases due to compaction and, therefore, differential loading becomes more effective. At a certain depth of the HPS, pressure head increases sufficiently to exceed the elevation head and upward flow is induced (Fig. 13b). When this stage is reached, progressive subsidence of the HPS drives further expulsion of the viscous material even if basement extension terminates (Fig. 13c, c'). Consequently, the viscous material accumulates above the higher basement compartment, where the overburden is uplifted. Overall, this is a feasible mechanism explaining salt pillow formation and corresponding peripheral sinks in extensional settings. Other processes may modify the evolution described here, e.g. the accumulation of dense sediment (such as carbonates) in the HPS or erosion of the graben flanks.

Based on our experimental results, we propose the following hypotheses for salt structure evolution in extensional settings:

1. In contrast with previous analogue models (e.g. Dooley et al., 2005; Ge and Vendeville, 1997; Koyi et al., 1993; Nalpas and Brun, 1993), no diapirs evolved in our experiments. Therefore, we suggest that small-offset basement faults ($D_r < 1$) are generally insufficient to trigger reactive piercing of the salt.

2. Furthermore, we suggest that the successful formation of a salt pillow due to basement displacement requires a phase of tectonic quiescence, in which the salt is able to flow upwards and accumulate on the footwall side. As demonstrated by other analogue model studies (e.g. Burliga et al., 2012; Dooley et al., 2005) uninterrupted basement extension leads to enhanced cover faulting and shearing of the viscous material above the basement step. This reduces material supply from the hanging wall side (Burliga et al., 2012), but promotes reactive diapirism above the basement fault tip without the occurrence of a pillow stage.

3. In experiments involving large initial overburden thicknesses (> 1 cm), no distinct pillow structure evolved. Scaled to nature, this implies that pillows are suppressed when the overburden is thicker than ∼ 1000–1500 m. This value is only a rough quantitative estimation, since rock properties in nature (e.g. salt viscosity, strength of the overburden) are more variable than in analogue models. Salt pillows showing a particularly thick pre-kinematic overburden layer, e.g. in some parts of the North German Basin (Baldschuhn et al., 2001), were possibly generated by another mechanism than the one simulated in our experiments. Other viable mechanisms include regional tectonic contraction (Kossow and Krawczyk, 2002), the progradation of sedimentary wedges (Ge and Vendeville, 1997) or the formation of a residual elevation between two growing salt structures (Vendeville, 2002).

6.6 Comparison with natural examples

The structural development and kinematics derived from our experiments can be compared to natural examples of salt structures in extensional basins such as the North Sea Basin (Duffy et al., 2013; Korstgård et al., 1993), the Dniepr-Donets Basin (Stovba and Stephenson, 2003), the Lusitanian Basin (Alves et al., 2002), the Mid-Polish Trough (Krzywiec, 2004a; Wagner et al., 2002) or the North German Basin (Baldschuhn et al., 2001; Jaritz, 1987; Kockel, 1998). Cross-sections displayed in Fig. 14 show some examples of these basins. The overburden layers of the peripheral sinks have been reconstructed using vertical simple shear (Rowan and Ratliff, 2012) and line length unfolding in 2-DMove (Midland Valley). Different from our simplified experimental set-up, the present-day basement of the salt layer exhibits a complex fault pattern. Nevertheless, differentially subsided basement compartments can be distinguished, which we attribute to differential loading on the salt layer.

The salt pillow exhibited in Fig. 14a developed above a slightly deformed basement. The pillow bears a close resemblance to the experimental pillow structures observed in our analogue models (Fig. 4). Hence, we suggest that such salt pillows were initiated by differential basement subsidence and continued to grow due to differential loading applied by nearby peripheral sinks.

In cross-section C of the Weser Trough (North German Basin) (Fig. 14c), local thickness variations in the post-salt Middle Buntsandstein (Early Triassic) layer provide evidence for the onset of basement faulting. During a phase of intensified extension in Middle Keuper time (Late Triassic) in the North German Basin (Kockel, 2002; Mohr et al., 2005; Scheck-Wenderoth et al., 2008), the HPS in the Weser Trough had increased in depth and salt pillows evolved. Based on our modelling results, we suggest that the main driving forces for salt flow and pillow formation were differences in loading between the HPS and the locally faulted overburden above the footwall compartments. Small offset basement faults induced widespread expulsion of the salt into relatively broad pillow structures. Due to renewed extension during Late Keuper (Late Triassic) and Early to Middle Jurassic times reactive diapirism took place.

Extension in the Mid-Polish Trough (Fig. 14d) had already begun during Early Triassic or might have continued since Late Permian (Krzywiec, 2004b). For this reason, the pre-kinematic (pre-extensional) overburden above the Upper Permian (Zechstein) salt layer was probably very thin or completely absent. Nevertheless, the reconstruction of cross-section C suggests that no significant pillow formed before the Middle Triassic. According to our conceptual model, the density of the Lower Triassic layers was insufficient to generate significant differential loading and to support an upward directed salt flow at the beginning (Early Triassic). During the Middle Triassic, a second phase of basement extension and compaction of the sediments in the HPS created a pressure head, which was high enough to drive upward flow and pillow uplift. Syn-kinematic sediments in the HPS reveal that the main depocentre migrated towards the left-hand salt structure during the Middle Late Triassic. According to our experimental results this indicates that the salt was progressively expelled towards the footwall block, where it accumulated in the rising Klodawa salt structure. During the Late Triassic, the Klodawa salt structure began to pierce as a diapir due to further basement extension.

Early flow patterns within evolving salt structures cannot be retrieved from seismic interpretations, but can be proposed on the basis of our experimental results and from rare outcrop studies in salt mines. Burliga (1996) interpreted folded salt layers in a salt mine in the Klodawa salt diapir (Mid-Polish Trough) to be a result of different phases of salt flow. During an early stage (Early Triassic) salt flowed downwards towards the basin axis. During the mature stage of the Klodawa diapir, salt moved from the downthrown basement block towards the rising salt structure due to differential loading between the basin centre and the crest of the salt structure (Burliga, 1996). This interpretation is supported by our experimental results and shows how experiments can help to understand the evolution of salt structures and their reconstructions. Furthermore, examples from salt mines in the

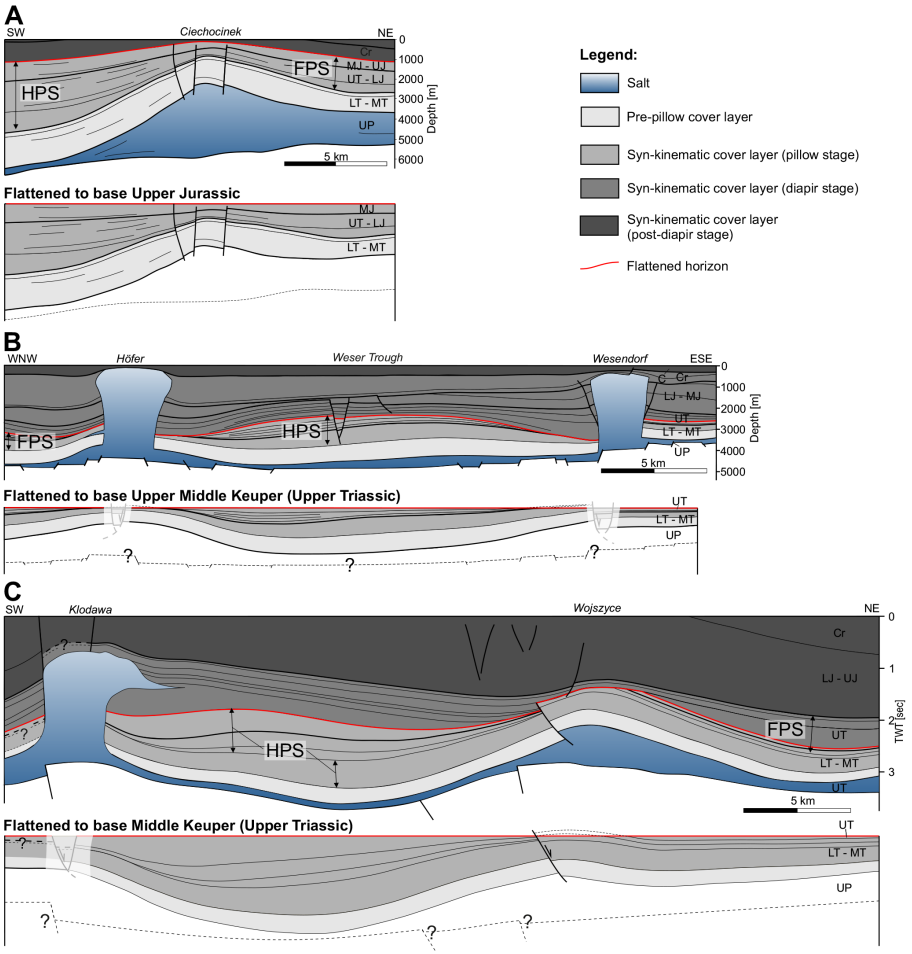

Figure 14. Interpreted seismic profiles of salt structures including reconstruction of the hanging wall peripheral sink (HPS) and the footwall peripheral sink (FPS). The sub-salt basement has not been restored, but its assumed geometry is schematically denoted. **(a)** The cross-section of the Mid-Polish Basin (modified after Dadlez, 2003) shows a typical salt pillow that was probably initiated by differentially subsided basement. In cross-sections **b–c**, the main depocentres overlie the downthrown basement part and salt structures are located above basement highs. **(b)** The Weser Trough (Central North German Basin) experienced several extensional phases during the Mesozoic, which led to the formation of salt pillows during Early Triassic and to diapiric piercing during the Late Triassic (modified from Baldschuhn et al., 2001). **(c)** The salt structures Klodawa and Wojszyce in the Mid-Polish Trough were initiated during the Middle to Late Triassic above a half graben (modified from Krzywiec, 2004b). Late Cretaceous inversion caused strong uplift of the sub-salt basement. UP – Upper Permian; LT – Lower Triassic; MT – Middle Triassic; UT – Upper Triassic, LJ – Lower Jurassic; MJ – Middle Jurassic; UJ – Upper Jurassic, Cr – Cretaceous; C – Cenozoic. For locations of the profiles see references.

North German Basin disclose complex internal folding of the evaporite succession even in regions of less external tectonic imprinting in the basement or the overburden (e.g. Bornemann, 1979; Richter-Bernburg, 1980; Strozyk et al., 2013; van Gent et al., 2010). Flow kinematics in our experiments demonstrate that significant strain in the viscous layer can occur despite only slight deformation of the basement and overburden.

7 Conclusions

Our experimental study simulated flow patterns in a salt layer during a short phase of basement normal faulting followed by a long period of sedimentation and the growth of post-extensional salt pillows.

1. Cross-sections of the final stages of our experiments demonstrate that two types of pillow structure can be distinguished. Primary pillows are located adjacent to basement faults and are mainly driven by differential loading induced by thicker sedimentary layers above the downthrown basement block (hanging wall peripheral

sink). Secondary pillows develop above the footwall block at considerable distance from the basement fault. These pillows are predominantly caused by the subsidence of the peripheral sink flanking the primary pillow on the side facing away from the basement fault (footwall peripheral sink). The sensitivity study revealed that the growth of salt pillows is facilitated by a large thickness of the viscous layer, a small thickness of the overburden and fast basement extension with a small offset of the basement fault.

2. Monitoring the deformation patterns within the analogue materials using PIV reveals that during basement extension, viscous material above the basement fault tip moves downward driven by elevation head. During the syn-sedimentary stage, the pressure head due to differential sedimentary loading forces upward flow. We propose that the downward and subsequent upward flow also occur successively in nature. At the beginning, average density of the overburden is lower than that of salt. Consequently, differential loading is low and the elevation head dominates. During further basement subsidence, syn-kinematic sedimentation and compaction in the hanging wall peripheral sink lead to an increased overburden density. Differential loading increases until the pressure head exceeds the elevation head and upward flow is induced. Viscous material is now squeezed out from beneath the hanging wall peripheral sink to form pillow-like structures on the footwall side. During further post-extensional phases, an additional pressure head is applied due to the development of a peripheral sink above the footwall block. This initiates the growth of the secondary pillow.

3. The flow regime in the viscous material can be mainly characterized as squeezed channel flow. Subsidence and uplift of the overburden are spatially correlated with expulsion or inflation of the viscous material. Compared to focused, small displacements at the basement faults, the region affected by viscous flow is widespread and widens further during post-extensional sedimentation. As shown by the sensitivity study, strain patterns in the viscous layer are basically independent of layer thicknesses or displacement rates. However, the zone affected by viscous flow above the fault tip is wider if the ductile layer is thicker, or if the basement displacement rate is smaller. Flow velocities in the viscous layer above the basement fault tip are higher if the ductile layer is thicker, if the overburden layer is thinner, or if the basement displacement rate is higher.

4. The comparison of our experimental results with natural salt-bearing extensional basins demonstrates the similarity of structural geometries, e.g. hanging wall peripheral sinks surrounded by pre-diapiric salt pillows. Despite the limitations of the experimental set-up, e.g. simple basement geometry or the temporal separation between extension and sedimentation, our experimental procedure provides a generic model for the early evolution of salt structures in basins that experienced multiple extensional phases followed by post-extensional thermal subsidence.

Appendix A

A1 Frictional-plastic material behaviour

The mechanical behaviour of granular material like sand is described by the coefficient of internal friction μ and the cohesion C (Lohrmann et al., 2003). These material properties were measured in two-cycle dynamic friction tests at variable normal loads and variable shear rates with the ring-shear tester RST-01.pc (Schulze, 1994). During a first shear load cycle, peak friction was determined. This defines the strength during material failure and shear zone formation. In a second shear load cycle, the static stable frictional strength was measured. This represents the strength during reactivation of shear zones within the material. Following material failure after exceeding peak strength or static stable strength, respectively, a constant dynamic-stable strength in a stage of ongoing fault activity is reached (Panien et al., 2006).

The values of average frictional properties and bulk density of the materials used in our experiments are listed in Table A1. Similar to our experimental procedure sand was sifted in the measurements of the ring shear tests to achieve optimal grain package (Lohrmann et al., 2003). The variability of densities of the sifted granular materials is of the order of $\Delta\rho = 30\,\mathrm{kg\,m^{-3}}$. Accuracy of the estimation of cohesion is quite low ($\sim 50\,\%$). Due to electrostatic forces, the cohesions between PVC beads might be significantly higher, especially under tension. Nevertheless, the mixture of PVC beads and quartz sand visibly reduces electrostatic accumulation of the particles.

A2 Viscoelastic material behaviour

The silicone oil (Polydimethylsiloxane; Momentive Performance Materials Baysilone® SE30) used in our experiments is characterized by a power-law viscous rheology. In creep and relaxation tests a low power-law stress exponent of $n = 1.3$ had been determined by Rosenau et al. (2009) for the same silicone material used in our study. Additionally, we measured the viscosity with a cone-plate rheometer RC20.1-CPS-P1 with C25-2 measurement system (RheoTec). During measurement a thin film of silicone is sheared between the plates of the rheometer at controlled shear rates and room temperature (20 °C). The viscosity is calculated as the ratio of measured shear stress and strain rate. The thickness of the silicone film was increased stepwise from 1 to 3 mm. Measurements were repeated three times for each thickness. Average values for viscosity are listed in Table A2.

In order to record material movement with PIV, the transparent silicone was mixed with PVC beads. The viscosity of the mixed silicone is only slightly higher ($\Delta\eta = 240\,\mathrm{Pas}$) than that of pure silicone (Table A2). The bulk density of the mixed silicone remains unaffected since the PVC beads possess a similar grain density compared to the density of pure silicone.

Appendix B

To ensure the significance of experimental results, experiments have to be properly scaled geometrically, kinematically and dynamically. Models are considered as geometrically scaled if ratios of linear dimensions in the model are proportionally similar to length ratios in nature (Hubbert, 1937). We used a length ratio l^* between model and nature of 10^{-5} (1 cm in the model corresponds to 1 km in nature), which is derived from the ratio of cohesion of the brittle cover (e.g. Koyi et al., 1993; Nalpas and Brun, 1993; Vendeville et al., 1995; Weijermars et al., 1993):

$$l^* = (C_0/g\rho)^* \tag{B1}$$

in which C_0 is the cohesion, g the gravitational acceleration, ρ the density and * represents the ratio between model and nature. Kinematic scaling is achieved if the ratios between strain and time are similar for model and nature (Hubbert, 1937). The time ratio considers the viscosity ratio η^* between the silicone and the rock salt and the stress ratio σ^* (Table 1):

$$t^* = (\eta^*/\sigma^*). \tag{B2}$$

Since we simulate a tensile stress regime, lithostatic pressure is the main principal stress (Twiss and Moores, 1992):

$$\sigma_\mathrm{N} = g \cdot \rho_\mathrm{b} \cdot h_\mathrm{b}, \tag{B3}$$

where g is the gravitational acceleration, ρ_b the bulk density and h_b the thickness of the salt cover layer. Implying values for viscosities, length and density of Table 1, the time ratio becomes $t^* = \sim 1.3 \times 10^{-9}$. Consequently, 1 h in experiments equals approximately 1 Ma. The strain rate ratio ε^* ($\varepsilon_\mathrm{m}\,/\,\varepsilon_\mathrm{n}$) is the inverse of time ratio $1\,/\,t^*$.

In order to fulfil dynamic scaling, the strength ratio between brittle cover S_b and ductile layer S_d has to be equal for nature and experiment (Weijermars et al., 1993). S_b equals the differential stress between maximum and minimum principal stresses:

$$S_\mathrm{b} = \sigma_1 - \sigma_3. \tag{B4}$$

As mentioned above, the maximal principal stress σ_1 equals the overburden pressure due to gravity σ_N, whereas the minimal principal stress σ_3 is horizontal and in direction of extension. Both natural sediment and granular analogue material are supposed to deform according to the Mohr–Coulomb failure criterion which is given by (Byerlee, 1978; Dahlen, 1990)

$$\tau_\mathrm{m} = \sigma_\mathrm{m} \sin\phi + C_0 \cos\phi \tag{B5}$$

in which σ_m = normal stress, τ_m = shear stress, φ is the angle of internal friction and C_0 the cohesion. Translating to an expression of maximum and minimum stresses gives

$$\frac{\sigma_1 - \sigma_3}{2} = \frac{\sigma_1 + \sigma_3}{2} \sin\phi + C_0 \cos\phi. \tag{B6}$$

Table A1. Material parameters (density ρ, coefficient of internal friction μ and the cohesion C) of used granular material measured with ring shear tester RST-01.pc.

Material	Grain size [mm]	Preparation	peak ρ [kg m^{-3}]	Peak μ	Peak C [Pa]	Stable static μ	Stable Static C [Pa]	Stable dynamic μ	Stable dynamic C [Pa]
PVC beads	0.36–0.5	sifted	750 ± 10	0.33 ± 0.006	109 ± 44	0.32 ± 0.003	119 ± 25	0.34 ± 0.030	121 ± 196
Quartz sand G23	0.02–0.63	sifted	1740 ± 17	0.70 ± 0.008	88 ± 45	0.61 ± 0.005	92 ± 36	0.55 ± 0.002	103 ± 10
Mixture PVC : quartz sand 1 : 1	0.02–0.63	sifted	1250 ± 10	0.51 ± 0.006	107 ± 44	0.50 ± 0.003	72 ± 25	0.45 ± 0.030	72 ± 196

Table A2. Physical properties of silicone putty used in the study presented here.

Material	Weight of sand added to silicone [kg]	Density ρ [kg m^{-3}]	Strain rate ε [s^{-1}]	Shear stresses τ [Pa]	Viscosity η [Pa s]
Silicone PDMS	0	970	0.01–0.08	< 2000	$23\,000 \pm 1000$
Silicone PDMS mixed with sand	0.01–0.03	970	0.01–0.08	< 2000	$23\,240 \pm 1000$

With separation of σ_3, one obtains

$$\sigma_3 = -\sigma_1 \frac{(1-\sin\phi)}{(1+\sin\phi)} + 2C_0 \sqrt{\frac{(1-\sin\phi)}{(1+\sin\phi)}}. \quad \text{(B7)}$$

Finally, brittle strength S_b can be expressed by

$$S_\mathrm{b} = \sigma_1 + \sigma_1 \frac{(1-\sin\phi)}{(1+\sin\phi)} - 2C_0 \sqrt{\frac{(1-\sin\phi)}{(1+\sin\phi)}}. \quad \text{(B8)}$$

For upper crustal rocks, a suitable value for angle of internal friction is $\varphi = 30°$ and for cohesion is $C_0 = 5 \times 10^6$ Pa (Byerlee, 1978). Generally, density of clastic sediments usually exceeds the density of rock salt (of $\rho_\mathrm{Salt} = 2200\,\mathrm{kg\,m^{-3}}$) at depths of 650 to 1500 m (Baldwin and Butler, 1985). Assuming a pre-kinematic cover thickness of $h_\mathrm{b} = 1000$ m we applied a cover density of $\rho_\mathrm{b} = 2300\,\mathrm{kg\,m^{-3}}$ for the calculation (Baldwin and Butler, 1985). Therefore, $\sigma_\mathrm{N} = \sigma_1 = 2.26 \times 10^7$ Pa and $\sigma_3 = 0.297 \times 10^7$ Pa. Hence, the brittle yield strength at the base is S_b (nature) $= 1.96 \times 10^7$ Pa.

The mixture of quartz sand and PVC beads possesses a slightly lower angle of internal friction ($\varphi = \sim 27°$). The density contrast between granulate and silicone ($\Delta\rho = 300\,\mathrm{kg\,m^{-3}}$) is only slightly higher than the natural salt-cover density contrast, which is an advance compared to previous analogue models using pure quartz sand ($\Delta\rho = 500$–$700\,\mathrm{kg\,m^{-3}}$). Using values of Table 1 S_b (model) $= 60$–160 Pa.

Shear stresses in a Newtonian fluid can be calculated by (Turcotte and Schubert, 2014)

$$S_\mathrm{d} = \eta \left(u \Big/ \frac{1}{2} h_\mathrm{d} \right) \quad \text{(B9)}$$

in which η is dynamic viscosity, u the displacement rate and h_d the thickness of the viscous layer. The extension rate for continental rifting varies between 0.1 and 1 mm a^{-1} (Allen and Allen, 2005), which gives strain rates in the viscous layer of $\varepsilon = 10^{-14}$ to $10^{-15}\,\mathrm{s^{-1}}$ for a salt thickness of 2000 m. Assuming an average viscosity for natural rock salt of $\eta = 10^{18}$ Pa s (Nalpas and Brun, 1993; van Keken et al., 1993) and a salt thickness of 2000 m, S_d (nature)$= 10^4$–10^5 Pa.

In our experiments, the displacement rate of the simulated basement extension is $e = 4\,\mathrm{mm\,h^{-1}}$ (except for one experiment with $e = 0.6\,\mathrm{mm\,h^{-1}}$ and another experiment with $e = 20\,\mathrm{mm\,h^{-1}}$, Table 2). Consequently, strain rates in the viscous layer reach values of $\varepsilon = \sim 10^{-5}\,\mathrm{s^{-1}}$. Incorporating a silicone layer of a thickness of $h_\mathrm{d} = 1.5$ cm and a viscosity of $\eta = 2.3 \times 10^4$ Pas, S_d (model) $= \sim 1$ Pa.

The dimensionless strength ratios are calculated by

$$S_\mathrm{b}/S_\mathrm{d}(\mathrm{nature}) = \sim 100\text{–}1000 \quad \text{(B10)}$$

and

$$S_\mathrm{b}/S_\mathrm{d}(\mathrm{model}) = 50\text{–}180. \quad \text{(B11)}$$

The model ratio lies within the lower range of the natural ratio. Hence, the models can be taken as dynamically scaled.

The Supplement related to this article is available online at doi:10.5194/se-15-9-2015-supplement.

Acknowledgements. This experimental study was funded by the German Research Foundation (DFG). Additional funding for Michael Warsitzka came from the Federal Ministry of Education and Research (BMBF) (grant Nr. 03IS2091A INFLUINS). Experiments and measurements of material properties were carried out at the Helmholtz Centre Potsdam GFZ German Research Centre for Geosciences. We thank the GFZ technicians for assistance in the laboratory as well as M. Rosenau, M. Scheck-Wenderoth, C. von Nicolai and F. Jähne for constructive discussions. The authors gratefully acknowledge the critical reviews by C. J. Talbot, P. Krzywiec and an anonymous reviewer that significantly improved this paper.

Edited by: F. Rossetti

References

Adam, J., Urai, J. L., Wieneke, B., Oncken, O., Pfeiffer, K., Kukowski, N., Lohrmann, J., Hoth, S., van der Zee, W., and Schmatz, J.: Shear localisation and strain distribution during tectonic faulting – new insights from granular-flow experiments and high-resolution optical image correlation techniques, J. Struct. Geol., 27, 283–301, doi:10.1016/j.jsg.2004.08.008, 2005.

Allen, P. A. and Allen, J. R.: Basin Analysis Principles & Applications, (Blackwell Science), 2nd edition, pp. 451, 2005.

Allen, J. and Beaumont, C.: Impact of inconsistent density scaling on physical analogue models of continental margin scale salt tectonics, J. Geophys. Res., 17, 1–22, doi:10.1029/2012JB009227, 2012.

Alves, T. M., Gawthorpe, R. L., Hunt, D. W., and Monteiro, J. H.: Jurassic tectono-sedimentary evolution of the Northern Lusitanian Basin (offshore Portugal), Mar. Petrol. Geol., 19, 727–754, doi:10.1046/j.1365-2117.2003.00202.x, 2002.

Baldschuhn, R., Binot, F., Frisch, U., and Kockel, F.: Geotektonischer Atlas von Nordwest-Deutschland und dem deutschen Nordsee-Sektor - Strukturen, Strukturentwicklung, Paläogeographie (Tectonic Atlas of Northwest Germany and the German North Sea Sector): Geologisches Jahrbuch A 153, 3 CD-ROM, 88 pp., 2001

Baldwin, B. and Butler, C. O.: Compaction curves: AAPG Bull., 69, 622–626, 1985.

Bornemann O.: Das Gefügeinventar nordwestdeutscher Salzstrukturen in Abhängigkeit von ihrer halokinetischen Stellung, Universitaet Braunschweig, Dissertationen, Braunschweig, 1–119, 1979.

Boutelier, D., Schrank, C., and Cruden, A.: Power-law viscous materials for analogue experiments: New data on the rheology of highly-filled silicone polymers, J. Struct. Geol., 30, 341–353, doi:10.1016/j.jsg.2007.10.009, 2008.

Burliga, S.: Implications for early basin dynamics of the Mid-Polish Trough from deformational structures within salt deposits in central Poland, Geol. Quart., 40, 185–202, 1996.

Burliga, S., Koyi, H. A., and Chemia, Z.: Analogue and numerical modelling of salt supply to a diapiric structure rising above an active basement fault, edited by: Alsop, G. I., Archer, S. G., Hartley, A. J., Grant, N. T., and Hodgkinson, R.: Salt Tectonics, Sediments and Prospectivity, Geol. Soc. Spec. Publ., 363, 395–408, doi:10.1144/SP363.18, 2012.

Byerlee, J. D.: Friction of Rocks, edited by: Byerlee, J. D. and Wyss, M., in: Pure and Applied Geophysics, Contribution to Current Research in Geophysics, 116, 615–626, 1978.

Cobbold, P., Rossello, E., and Vendeville, B.: Some experiments on interacting sedimentation and deformation above salt horizons, B Soc. Bull. Fr., 3, 453–460, doi:10.2113/gssgfbull.V.3.453, 1989.

Dadlez, R.: Mesozoic thickness pattern in the Mid-Polish Trough, Geol. Q., 47, 223–240, 2003.

Dahlen, F. A.: Critical Taper Model of Fold-and-Thrust Belts and Accretionary Wedges, Ann. Rev. Earth Pl. Sc., 18, 55–99, doi:10.1146/annurev.ea.18.050190.000415, 1990.

Dooley, T. P., McClay P. R., and Pascoe, R.: 3-D analogue models of variable displacement extensional faults: applications to the Revfallet Fault system, offshore mid-Norway, Geol. Soc. Spec. Publ., 212, 151–167, doi:10.1144/GSL.SP.2003.212.01.10, 2003.

Dooley, T. P., McClay, K. R., Hempton, M., and Smit, D.: Salt tectonics above complex basement extensional fault systems: results from analogue modeling, edited by: Doré, A. G. and Vining, B. A., Petroleum Geology: North-West Europe and Global Perspectives, Proceedings of the 6th Petroleum Geology Conference, Geological Society, London, 1631–1648, doi:10.1144/0061631, 2005.

Duffy, O. B., Gawthorpe, R. L., Docherty, M., and Brocklehurst, S. H.: Mobile evaporite controls on the structural style and evolution of rift basins: Danish Central Graben, North Sea, Basin Res., 25, 310–330, doi:10.1111/bre.12000, 2013.

Frisch, U. and Kockel, F.: Quantification of Early Cimmerian movements in NW-Germany, Zbl. Geo. Pal., 7–8, 571–600, 1999.

Fuchs, L., Koyi, H., and Schmeling, H.: Numerical modeling on progressive internal deformation in down-built diapirs, Tectonophysics, 632, 111–122, doi:10.1016/j.tecto.2014.06.005, 2014.

Gaullier, V., Brun, J. P., and Lecanu, H.: Raft tectonics: the effects of residual topography below a salt décollement, Tectonophysics, 228, 363–381, doi:10.1016/0040-1951(93)90349-O, 1993.

Ge, H. and Vendeville, B. C.: Influence of active subsalt normal faults on the growth and location of suprasalt structures, Gulf Coast Association of Geological Societies Transactions, XLVII, 169–176, 1997.

Geil, K.: The development of salt structures in Denmark and adjacent areas: the role of basin floor dip and differential pressure, First Break, 9, 467–483, doi:10.3997/1365-2397.1991022, 1991.

Goteti, R., Ings, S. J., and Beaumont, C.: Development of salt minibasins initiated by sedimentary topographic relief, Earth Plant. Sc. Lett., 339, 103–116, doi:10.1016/j.epsl.2012.04.045, 2012.

Higgins, R. I. and Harris, L. B.: The effect of cover composition on extensional faulting above re-activated basement faults: results from analogue modelling, J. Struct. Geol., 19, 89–98, doi:10.1016/S0191-8141(96)00083-1, 1997.

Hubbert, M. K.: Theory of scale models as applied to the study of geologic structures, Geol. Soc. Am. Bull., 48, 1459–1520, 1937.

Hudec, M. R. and Jackson, M. P. A.: Terra infirma: Understanding salt tectonics, Earth Sc. Reviews, 82, 1–27, doi:10.1016/j.earscirev.2007.01.001, 2007.

Jackson, M. P. A. and Talbot, C. J.: External shapes, strain rates, and dynamics of salt structures, Geol. Soc. Am. Bull., 97, 305–323, doi:10.1130/0016-7606(1986)97<305:ESSRAD>2.0.CO;2, 1986.

Jackson, M. P. A. and Vendeville B. C.: Regional extension as a geologic trigger for diapirism, Geol. Soc. Am. Bull., 94, 57–73, doi:10.1130/0016-7606(1994)106<0057:REAAGT>2.3.CO;2, 1994.

Jackson, M. P. A., Vendeville, B. C., and Schultz-Ela, D. D.: Structural Dynamics of Salt Systems, Ann. Rev. Earth Pl. Sc., 22, 93–117, doi:10.1146/annurev.ea.22.050194.000521, 1994.

Jaritz, W.: The origin and development of salt structures in Northwest Germany, eidted by: Lerche, I. and O'Brian, J. J., Dynamical Geology of Salt and Related Structures: Academic Press, Orlando, FL, 479–493, 1987.

Kehle, R. O.: The origin of salt structures, eidted by: Schreiber, B. C., in: Evaporites and Hydrocarbons, Columbia University Press, New York, 345–404, 1988.

Kockel, F.: Salt problems in NW-Germany and the German North Sea Sector, J. Seism. Explor., 7, 219–235, 1998.

Kockel, F.: Rifting processes in NW-Germany and the German North Sea Sector, Neth. J. Geosci.-Geol. Mijnbouw, 81, 149–158, 2002.

Korstgård, J. A., Lerche, I., Mogensen, T. E., and Thomsen, R. O.: Salt and fault interactions in the northeastern Danish Central Graben: observations and inferences, Bull. Geol. Soc. Den, 40, 197–255, 1993.

Kossow, D. and Krawczyk, C. M.: Structure and quantification of processes controlling the evolution of the inverted NE-German Basin, Mar. Petrol. Geol., 19, 601–618, doi:10.1016/S0264-8172(02)00032-6, 2002.

Koyi, H. A. and Petersen, K.: Influence of basement faults on the development of salt structures in the Danish Basin, Mar. Petrol. Geol., 10, 82–94, doi:10.1016/0264-8172(93)90015-K, 1993.

Koyi, H. A., Jenyon, M. K., and Petersen, K.: The effect of basement faulting on diapirism, J. Petrol. Geol., 163, 285–311, doi:10.1111/j.1747-5457.1993.tb00339.x, 1993.

Krzywiec, P.: Basement vs. salt tectonics and salt-sediment Interaction – case study of the Mesozoic evolution of the Intracontinental Mid-Polish Trough, In 24th Annual GCSSEPM Foundation Bob F. Perkins Research Conference Salt-Sediment Interactions and Hydrocarbon Prospectivity: Concepts, Applications and Case Studies for the 21st Century, Houston, Texas, 343–370, 2004a.

Krzywiec, P.: Triassic evolution of the Klodawa salt structure: basement-controlled salt tectonics within the Mid-Polish Trough (Central Poland), Geol. Quart., 48, 123–134, 2004b.

LaVision, Anon.: StrainMaster Manual for DaVis 6.2. LaVision GmbH, Goettingen, 154 pp., 2002.

Lohrmann, J., Kukowski, N., Adam, J., and Oncken, O.: The impact of analogue material parameters on the geometry, kinematics, and dynamics of convergent sand wedges, J. Struct. Geol., 25, 1691–1711, doi:10.1016/S0191-8141(03)00005-1, 2003.

Maystrenko, Y. P., Bayer, U., and Scheck-Wenderoth, M.: Salt as a 3-D element in structural modeling – Example from the Central European Basin System, Tectonophysics, 591, 62–82, doi:10.1016/j.tecto.2012.06.030, 2013.

Mohr, M., Kukla, P. A., Urai, J. L., and Bresser, G.: Multiphase salt tectonic evolution in NW Germany: seismic interpretation and retro-deformation, Int. J. Earth Sci., 94, 917–940, doi:10.1007/s00531-005-0498-8, 2005.

Nalpas, T. and Brun, J. P.: Salt flow and diapirism related to extension at crustal scale, Tectonophysics, 228, 349–362, doi:10.1016/0040-1951(93)90348-N, 1993.

Oudmayer, B. C. and de Jager, J.: Fault reactivation and oblique-slip in the Southern North Sea, eidted by: Parker, J. R., in: Petroleum Geology of Northwest Europe: Proceedings of the 4th Conference, Petroleum Geology '86 Ltd., Published by The Geological Society, London, 1281–1290, doi:10.1144/0041281, 1993.

Panien, M., Schreurs, G., and Pfiffner, A.: Mechanical behaviour of granular materials used in analogue modelling: insights from grain characterisation, ring-shear tests and analogue experiments, J. Struct. Geol., 28, 1710–1724, doi:10.1016/j.jsg.2006.05.004, 2006.

Peel, F. J.: How do salt withdrawal minibasins form?, Insights from forward modelling, and implications for hydrocarbon migration, Tectonophysics, 630, 222–235, doi:10.1016/j.tecto.2014.05.027, 2014.

Ramberg, H.: Gravity Deformation and the Earth's Crust, 1st Ed., Academic Press, London, 452 pp., 1967.

Remmelts, G.: Fault-related tectonics in the Southern North Sea, The Netherlands, edited by: Jackson, M. P. A., Roberts, D. G., and Snelson, S., in: Salt Tectonics: A Global Perspective, AAPG Memoir, 65, 261–272, 1995.

Richard, P.: Experiments on faulting in a two-layer cover sequence overlying a reactivated basement fault with oblique-slip, J. Struct. Geol., 13, 459–469, doi:10.1016/0191-8141(91)90018-E, 1991.

Richter-Bernburg, G.: Salt tectonics, interior structures of salt bodies, Bull. Cent. Rech. Explor.-Prod. Elf-Aquitaine, 4, 373–393, 1980.

Rosenau, M., Lohrmann, J., and Oncken, O.: Shocks in a box: An analog model of subduction earthquake cycles with application to seismotectonic forearc evolution, J. Geophys. Res., 114, 1978–2012, doi:10.1029/2008JB005665, 2009.

Rowan, M. G. and Ratliff, R. A.: Cross-section restoration of salt-related deformation: Best practices and potential pitfalls, J. Strut. Geol., 41, 24–37, doi:10.1016/j.jsg.2011.12.012, 2012.

Scheck, M., Bayer, U., and Lewerenz, B.: Salt movements in the Northeast German Basin and its relation to major post-Permian tectonic phases – results from 3-D structural modelling, backstripping and reflection seismic data, Tectonophysics, 361, 277–299, doi:10.1016/S0040-1951(02)00650-9, 2003.

Scheck-Wenderoth, M., Maystrenko, Y. P., Hübscher, C., Hansen, M., and Mazur, S.: Dynamics of salt basins, edied by: Littke, R., Bayer, U., and Gajewski, D. in: Dynamics of complex intracontinental basins: The Central European Basin System, Frontiers in Earth Science, Springer, Berlin, 307–322, 2008.

Schultz-Ela, D. D. and Jackson, M. P. A.: Relation of subsalt structures to suprasalt structures during extension, AAPG Bull., 80, 1896–1923, 1996.

Schulze, D.: Entwicklung und Anwendung eines neuartigen Ringschergerätes, Aufbereitungstechnik, 35, 524–535, 1994.

Soto, R., Casas-Sainz, A., and Del Río, P.: Geometry of half-grabens containing a mid-level viscous décollement, Basin Research, 19, 437–450, doi:10.1111/j.1365-2117.2007.00328.x, 2007.

Stephansson, O.: Theoretical and experimental studies of diapiric structures on Öland, Geol. Inst. Bull. Univ. Uppsala N. S., 3, 163–200, 1972.

Stewart, S. A., Harvey, M. J., Otto S. C., and Weston, P. J.: Influence of salt on fault geometry: examples from the UK salt basins, Geol. Soc. Spec. Publ., 100, 175–202, doi:10.1144/GSL.SP.1996.100.01.12, 1996.

Stovba, S. M. and Stephenson, R. A.: Style and timing of salt tectonics in the Dniepr-Donets Basin (Ukraine): implications for triggering and driving mechanisms of salt movement in sedimentary basins, Mar. Petrol. Geol., 19, 1169–1189, doi:10.1016/S0264-8172(03)00023-0, 2003.

Strozyk, F., van Gent, H., Urai, J. L., and Kukla, P. A.: 3-D seismic study of complex intra-salt deformation: an example from the Upper Permian Zechstein 3 stringer in the western Dutch offshore, Geol. Soc. Spec. Publ., 363, 489–501, doi:10.1144/SP363.23, 2013.

Strunck, P., Gaupp, R., and Steffan, M.: Early Triassic movement of Upper Permian (Zechstein) salt in Northwest Germany, Z Geol Paläont Teil, 1, Heft 7–8, 679–699, 1998.

Turcotte, D. L. and Schubert, G.: Geodynamics, Cambridge University Press, Cambridge, United Kingdom, 3rd edition, 636 pp., 2014.

Twiss, R. J. and Moores, E. M.: Structural Geology, W. H. Freeman and Company, Oxford, 532 pp., 1992.

Urai, J., Schléder, Z., Spiers, C., and Kukla, P.: Flow and transport properties of salt rocks, in: Dynamics of Complex Intracontinental Basins: The Central European Basin System, edied by: R. Littke, U. Bayer, D. Gajewski, S., and Nelskamp, 291–304, Springer, Berlin Heidelberg, 2008.

Van Gent, H., Urai, J. L., and de Keijzer, M.: The internal geometry of salt structures – A first look using 3-D seismic data from the Zechstein of the Netherlands, J. Struct. Geol., 33, 1–20, doi:10.1016/j.jsg.2010.07.005, 2010.

Van Keken, P. E., Spiers, C. J., van den Berg, A. P., and Muyzert, E. J.: The effective viscosity of rock salt: implementation of steady-state creep laws in numerical models of salt diapirism, Tectonophysics, 225, 457–476, doi:10.1016/0040-1951(93)90310-G, 1993.

van Wees, J.-D., Stephenson, R. A., Ziegler, P. A., Bayer, U., McCann, T., Dadlez, R., Gaupp, R., Narkiewicz, M., Bitzer, F., and Scheck, M.: On the origin of the Southern Permian Basin, Central Europe, Mar. Petrol. Geol., 17, 43–59, doi:10.1016/S0264-8172(99)00052-5, 2000.

Vendeville, B. C.: Scale models of basement-induced extension: Comptes Rendus de l'Academie des Sciences de Paris 307, 2, 1013–1019, 1988.

Vendeville, B. C.: A new Interpretation of Trusheim's classic Model of Salt-Diapir-Growth, Gulf Coast Association of Geological Societies Transactions, 52, 953–952, 2002.

Vendeville, B. C. and Jackson, M. P. A.: The rise of diapirs during thin-skinned extension, Mar. Petrol. Geol., 9, 331–353, doi:10.1016/0264-8172(92)90047-I, 1992.

Vendeville, B. C., Ge, H., and Jackson, M. P. A.: Scale models of salt tectonics during basement-involved extension, Petrol. Geosci., 1, 179–183, doi:10.1144/petgeo.1.2.179, 1995.

Ventisette, C. D., Montanari, D., Bonini, M., and Sani, F.: Positive fault inversion triggering "intrusive diapirism": an analogue modelling perspective, Terra Nova, 17, 478–485, doi:10.1111/j.1365-3121.2005.00637.x, 2005.

Wagner, R., Leszczyński, K., Pokorski, J., and Gumulak, K.: Palaeotectonic cross-sections through the Mid-Polish Trough, Geol. Q., 46, 293–306, 2002.

Warsitzka, M., Kley, J., and Kukowski, N.: Salt diapirism driven by differential loading – Some insights from analogue modelling, Tectonophysics, 591, 83–97, doi:10.1016/j.tecto.2011.11.018, 2013.

Weijermars, R., Jackson, M. P. A., and Vendeville, B. C.: Rheological and tectonic modeling of salt provinces, Tectonophysics, 217, 143–174, doi:10.1016/0040-1951(93)90208-2, 1993.

Withjack, M. O. and Callaway, S.: Active normal faulting beneath a salt layer: an experimental study of deformation patterns in the cover sequence, AAPG Bull., 84, 627–651, 2000.

Ziegler, P. A.: Triassic Rifts and Facies Patterns in Western and Central Europe, Geol. Rundsch., 71, 747–772, doi:10.1007/BF01821101, 1982.

5. Salt flow direction and velocity during sub-salt normal faulting and syn-kinematic sedimentation – implications from analytical calculations

Manuscript #3

Authors
Michael Warsitzka[1], Nina Kukowski[1], Jonas Kley[2]

Affiliations
[1] Institute of Geosciences, Friedrich Schiller University Jena, Burgweg 11, 07749 Jena, Germany
[2] Geoscience Centre, Structural Geology and Geodynamics, Georg-August-University Göttingen, Goldschmidtstr. 3, 37077 Göttingen, Germany

This article has been accepted for publication in *Geophysical Journal International* published by Oxford University Press on behalf of the Royal Astronomical Society:

Warsitzka, M., Kukowski, N., Kley, J. (submitted). Salt flow direction and velocity during sub-salt normal faulting and syn-kinematic sedimentation – implications from analytical calculations. Submitted to *Geophysical Journal International*, Oxford University Press. Date of submission: 11.02.2017.

A revised version of this manuscript (Date of submission: 12.07.2017) can be found in the digital attachments of this thesis (Appendix C.2).

---

submitted to *Geophys. J. Int.*

Salt flow direction and velocity during sub-salt normal faulting and syn-kinematic sedimentation – implications from analytical calculations

M. Warsitzka[1], N. Kukowski[1], J. Kley[2]

[1] *Institute of Geosciences, Friedrich Schiller University Jena, Burgweg 11, 07749 Jena, Germany*

[2] *Geoscience Centre, Structural Geology and Geodynamics, Georg-August-University Göttingen, Goldschmidtstr. 3, 37077 Göttingen, Germany*

SUMMARY

Salt flow induced by sub-salt normal faulting is mainly controlled by tilting of the salt layer, the amount of differential loading due to syn-kinematic deposition, and tectonic shearing at the top or the base of the salt layer. Our study addresses the first two mechanisms and aims to examine salt flow patterns above a continuously moving sub-salt normal fault and beneath a syn-kinematic minibasin. In such a setting, salt either tends to flow down towards the basin centre driven by its own weight or is squeezed up towards the footwall side owing to loading differences between the minibasin and the region above the footwall block.

Applying isostatic balancing in analytical models, we calculated the steady-state flow velocity in a salt layer. This procedure gives insights into (1) the minimum vertical offset required for upward flow to occur, (2) the magnitude of the flow velocity, and (3) the average density of the supra-salt cover layer at the point at which upward flow starts. In a sensitivity study, we examined how the point of flow reversal and the velocity patterns are influenced by changes of the salt and cover layer thickness, the geometry of the cover

flexure, the dip of the sub-salt fault, compaction parameters of the supra-salt cover, the salt viscosity and the salt density.

Our model results reveal that in most geological scenarios, salt flow above a continuously displacing sub-salt normal fault goes through an early phase of downward flow. At sufficiently high fault offset in the range of 700 – 2600 m, salt is later squeezed upward towards the footwall side. This flow reversal occurs at smaller vertical fault displacement, if the thickness of the pre-kinematic layer is larger, the sedimentation rate of the syn-kinematic cover is higher, the compaction coefficient of cover sediments (i.e. the density increase with depth) is larger or the average density of the salt is lower. Other geometrical parameters such as the width of the cover monocline, the dip of the basement fault or the thickness of the salt layer have no significant influence on the point of reversal, but modify the velocity of the salt flow.

Key words: Salt flow, salt tectonics, hydraulic head gradient, normal faulting, analytical model

1 INTRODUCTION

Many salt-bearing sedimentary basins experienced one or multiple phases of regional extension during or after the deposition of the salt layer (Jackson & Vendeville 1994; Hudec & Jackson 2007). In such basins, normal faulting in the sub-salt basement and resulting deformation in the supra-salt cover are prime mechanisms inducing and localizing flow of the ductile salt layer (e.g. Vendeville & Jackson 1992; Koyi 1993; Nalpas & Brun 1993; Jackson & Vendeville 1994; Vendeville et al. 1995). Salt flow dynamics can generally be described through the hydraulic-head gradient, because rock salt deforms as a fluid over geological time scales (Kehle 1988; Hudec & Jackson 2007). Considering a salt layer displaced by sub-salt normal faults, the hydraulic-head gradient is primarily governed by the (1) vertical offset of the salt layer and (2) differential loading due to sediment accumulation in syn-kinematic depocentres. A vertical offset imposes an elevation-head gradient (EHG) in the salt layer due to gravitational body forces (Fig. 1b) (Hudec & Jackson 2007). Differential loading causes a pressure-head gradient (PHG) because of lateral changes of thickness and density of the overburden between depocentres and elevated regions (Fig. 1c) (Kehle 1988; Cohen & Hardy 1996; Hudec & Jackson 2007). The direction and velocity of salt flow depend on the sum of the oppositely acting EHG and PHG, i.e.

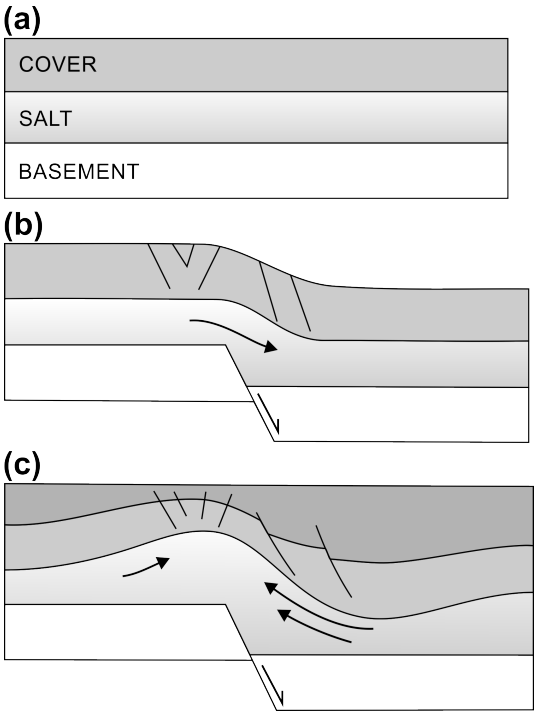

Figure 1. Conceptual model of salt flow above an active sub-salt fault. (a) The salt layer is overlain by a pre-kinematic cove layer. (b) Resulting from fault displacement, salt begins to flow toward the down-thrown basement block. (c) Syn-kinematic sedimentation leads to higher loading above the hanging wall block forcing the salt to flow upwards (modified from Remmelts 1995)

.

on the throw of the sub-salt fault and the sediment load of the minibasin above the hanging wall block (Ge et al. 1997; Warsitzka et al. 2015).

Numerous studies employing analogue or numerical modelling led to the suggestion that downward salt flow occurs if the basin above the hanging wall block remains underfilled so that some topographic relief persists. In contrast, upward flow takes place if sufficient sediment accumulates in the basin centre and if the average density of the cover becomes larger than salt density (density inversion) (e.g. Kehle 1988; Geil 1991; Koyi 1993; Nalpas & Brun 1993; Jackson & Vendeville 1994; Vendeville et al. 1995; Ge et al. 1997; Waltham 1997; Burliga et al. 2012; Warsitzka et al. 2015). Depending on the lithology and the compaction behaviour of the supra-salt cover sediments, density inversion usually occurs at depths larger than ~ 2000 m (Jackson & Talbot 1986; Hudec et al. 2009). However, reconstructions of extensional, salt bearing basins, e.g. the North Sea Central Graben (Duffy et al. 2013; Ge et al. 2016), the Braunschweig-Gifhorn fault zone (Northern Germany) (Vackiner et al. 2013)), or the Mid-Polish Trough (Wagner et al. 2002)) (Tab. 1) suggest that upwards directed salt flow from the centre of the basin towards salt structures (diapirs, domes) at the basin flanks was initiated be-

neath a cover thinner than 2000 m. Analytical models demonstrated that initiation of salt domes from a flat-lying salt layer requires only the density at the bottom of the minibasin to exceed salt density (Hudec et al. 2009; Goteti et al. 2012; Heidari et al. 2016). Further rise of the salt structure necessitates the average density of the neighbouring sediments to be higher than that of the salt. The critical depths for minibasins at which their density would become high enough to subside into a salt layer were calculated as 1900 to 2600 m (Goteti et al. 2012). Overall, the questions arise at which depth supra-salt minibasins filled with gradually compacting sediments are able to expel salt into neighbouring salt structures and which parameters mainly affect this onset of upward flow. These questions are addressed in the study presented here in which we used idealised analytical models to compute direction and intensity of lateral salt redistribution during the early stage of salt structure evolution as a function of the interplay between sub-salt faulting and supra-salt sediment compaction. The method calculates the steady-state velocity field in a salt layer according to a prevailing hydraulic-head gradient. We applied well-known compaction laws (e.g Hudec et al. 2009) for the supra-salt cover, a geometry that includes a normal fault in the sub-salt basement and a continuously filled-up supra-salt minibasin above the hanging wall block. In a sensitivity study, specific geometrical and lithological parameters (e.g. layer thicknesses or compaction coefficient) are systematically varied to identify the main influencing parameters.

Our study suggests that in most salt-bearing extensional basins (see Table 1), salt flows towards the downthrown block at the beginning of extensional basin formation, before thickness and density of the cover layer are large enough to induce upward flow. The threshold at which upward flow occurs, depends on the compaction behaviour (i.e. depth-related porosity decrease) and the pre-kinematic thickness of the overburden as well as on the average density of the salt layer. Furthermore, the mean density of sediments in the hanging wall minibasin exceeds salt density at larger vertical displacements than the turn to upward flow takes place.

2 METHOD

Salt flow according to gravitational loading can be calculated through an approximation of the three-dimensional Navier-Stokes equation (Mandl 1988) for an incompressible Newtonian fluid (Weijermars et al. 1993; Lehner 2000; Wagner & Jackson 2011; Turcotte & Schubert 2014):

$$\rho_S \frac{d\overrightarrow{V}}{dt} = -\rho_S \overrightarrow{g} + \overrightarrow{\nabla} P + \eta \overrightarrow{\nabla}^2 V \tag{1}$$

Here, $\overrightarrow{V}$ is the velocity field and the term on the left side describes the inertial acceleration. The first term on the right side describes the elevation-head gradient defined by the gravitational acceler-

Table 1. Compilation of data on extensional, salt-bearing basins including age and thickness of the main evaporitic layer, lithology and thickness of the salt cover layer, and maximum displacements of faults in the sub-salt basement. Average values of the original salt layer thickness and the pre-kinematic layer thickness are ∼1500 m and ∼800 m. The maximal fault offset is ∼3000 m on average. The average time elapsed between end of salt deposition and onset of extensional tectonics is ∼15 Myr.

Basin	**Region**	**Age of main salt layer**	**Period of initiation**	**Original salt layer thickness [m]**	**Thickness of pre-kinematic cover [m]**	**Max. offset of basement fault [m]**	**Lithology of pre-kinematic cover**	**References**
Atlas Basin	Tunesia	Late Triassic	Early Jurassic	1500 – 2500	0	?	Limestones, Shales	Hlaiem (1999), Masrouhi et al. (2014)
Braunschweig-Gifhorn fault zone	Northern Germany	Late Permian	Early Triassic	750 – 1000	∼ 1000	∼ 600	Sandstones, Mudstones	Vackiner et al. (2013)
Central Graben	Northern North Sea	Late Permian	Late Triassic	950 – 1000	< 1000	> 1000	Mudstones, sandstones	Buchanan et al. (1996), Duffy et al. (2013), Ge et al. (2016)
Central Graben	Southern North Sea	Late Permian	Early Triassic	1000 – 1500	300 – 400	> 3000	Mudstones, sandstones	Geluk (2005), Wong et al. (2007)
Dniepr-Donets Basin	Ukriane	Devonian	Late Devonian	3500	300 – 400	> 5000	Carbonates	Stovba & Stephenson (2003)
Feda Graben	Southern North Sea	Late Permian	Late Triassic	1000 – 1500	∼ 1000	> 1000	Shales, sandstones	Tanveer & Korstgård (2009)
Glückstadt Graben	North Germany	Early - Late Permian	Middle Early Triassic	2500 – 3000	800 – 1000	∼ 4000	Shales, sandstones	Maystrenko et al. (2005)
Horn Graben	Southern North Sea	Early - Late Permian	Middle Early Triassic	1000 – 1500	400 – 500	∼ 4000	Shales, sandstones	Best et al. (1983), Maystrenko et al. (2013)
Jeanne dArc Basin	Offshore Newfoundland	Late Triassic - Early Jurassic	Early Jurassic	∼ 2000	0	> 5000	Limestones, shales	Tankard et al. (1989); Withjack & Callaway (2000)
Mid Polish Trough	Poland	Late Permian	Middle Triassic	1000 – 1500	0 – 1000	∼ 3500	Shales, sandstone	Wagner et al. (2002); Krzywiec (2004),
Nordkapp Basin	Barents Sea	Late Carboniferous - Early Permian	Early Triassic	1400 – 3100	1500 – 2200	∼ 2000	Carbonates, shales	Jensen & Sørensen (1992); Koyi et al. (1995); Nilsen et al. (1996)
Lusitanian Basin	Offshore Portugal	Late Triassic - Early Jurassic	Early Jurassic	50 – 500	100 – 800	1000 – 2000	Limestones, dolomites	Rasmussen et al. (1998); Alves et al. (2002)
Parentis Trough	Bay of Biscay	Late Triassic	Early Cretaceous	500 – 1000	> 2000	4000	Limestones, dolomites	Ferrer et al. (2012)
Revfallet Fault System	Offshore mid-Norway	Late Triassic	Middle Jurassic	∼ 800	?	∼ 5000	Shales, sandstones	Pascoe et al. (1999); Dooley et al. (2003)
Viking Graben	Northern North Sea	Late Permian	Late Triassic	500	250 – 300	<1000	Sandstones	Kane et al. (2010)

ation g and the density of the salt layer ρ_S. $\overrightarrow{\nabla} P$ is the pressure-head gradient. The third term on the right-hand side defines the shear stress by means of the fluid viscosity η and the velocity field.

The simplest way to describe the direction of salt flow and the resulting velocity field in the salt layer is by assuming a 1D Poiseuille channel flow driven by a hydraulic-head gradient (Kehle 1988; Hudec & Jackson 2007). The hydraulic-head gradient consists of the pressure-head gradient and the

elevation-head gradient. The first is caused by lateral differences in loading on top of the salt layer, e.g. because of density or thickness variations of the overburden. The second is due to the gravity potential of a tilted salt layer or lateral differences in the height of the salt layer top above a defined datum. Since the pressure-head gradient only acts in horizontal x-direction, the Navier-Stokes equation (Eq. 1) can be simplified by considering only the horizontal (x) relationship:

$$\rho_S \frac{\partial u}{\partial t} = -\rho_S g + \frac{\partial P}{\partial x} + \eta \frac{\partial^2 u}{\partial z^2} \tag{2}$$

Here, u is the horizontal velocity component and $\frac{\partial P}{\partial x}$ the horizontal pressure-head gradient. Since inertial forces (Stokes flow) are insignificant compared to viscous forces, inertial acceleration (term on the left side of Eq. 2) can be neglected (Wagner & Jackson 2011). Consequently, Eq. 2 becomes:

$$\eta \frac{\partial^2 u}{\partial z^2} = \rho_S g - \frac{\partial P}{\partial x} \tag{3}$$

The term of the pressure-head gradient and the elevation-head gradient can be combined to a hydraulic-head gradient $\frac{\Delta H}{\Delta x}$:

$$\frac{\partial^2 u}{\partial z^2} = \frac{1}{\eta} \frac{\partial H}{\partial x} \tag{4}$$

Integrating Eq. 3 twice over the vertical axis z provides a linear equation for the steady-state flow velocity in terms of salt viscosity η, the depth z and the hydraulic-head gradient $\frac{\Delta H}{\Delta x}$ (Wagner & Jackson 2011; Turcotte & Schubert 2014):

$$u = \frac{1}{2\eta} \frac{\partial H}{\partial x} z^2 + C_1 z + C_2 \tag{5}$$

The integration constants C_1 and C_2 define the boundary conditions at the edges of the salt layer. We assumed that no-slip conditions at the salt layer boundaries (White 2011; Turcotte & Schubert 2014). For simplicity, only the Poiseuille flow component in horizontal x-direction is considered and shearing (u_C) at the upper or the lower salt boundary (White 2011) is omitted. Thus, C_1 = 0 and

$$C_2 = -\frac{1}{\eta} \frac{dH}{dx} h_S^2 \tag{6}$$

where h_S is the thickness of the salt layer. Inserting Eq. 6 into Eq. 5, the equation for the flow velocity becomes (White 2011):

$$u = -\frac{1}{2\eta} \frac{dH}{dx} (h_S^2 - z^2) \tag{7}$$

For convention, we define positive flow velocity for rightward movement and negative flow velocity for leftward movement, respectively.

2.1 Model set-up and procedure

We used Eq. 7 to calculate the steady-state velocity field in a three-layered configuration including a sub-salt basement, a salt layer and a cover layer (Fig. 1). In the geometrically simplified model set-up, we presumed that the cover monocline is a linear ramp (Fig. 2a). Height and width of the model are chosen to be $10 \times 5\,\mathrm{km}^2$, which is enough to simulate naturally occurring fault offsets and layer thickness (see Table 1). The sub-salt layer is displaced by a normal fault of defined offset (dip: β = 60 in the reference model). The salt layer is assumed to be an incompressible, viscous Newtonian fluid, which can be regarded as first-order simplification (see model limitations). The cover layer consists of an initial pre-kinematic layer with a constant thickness h_C and a minibasin on the hanging wall side, which is here called "hanging wall peripheral sink" (HPS). The cover layer is assumed to compact according to the chosen compaction law (see below), which results in a cover density increasing with depth (Fig. 2b). Three important density terms are used to quantify model results: 1. the maximum cover density at the bottom of the hanging wall peripheral sink ρ_{Cmax}, 2. the average density of the entire cover above the hanging wall block $\bar{\rho}_C$, and 3. the average effective density above the hanging wall block $\bar{\rho}_{Ceff}$ involving only parts of the hanging wall peripheral sink below the highest elevation of the salt layer. The vertical displacement of the cover layer, i.e. the depth of the HPS h_B (Fig. 2), is usually assumed to be equal to that of the down-thrown basement block except in one series of computations of the sensitivity study (see below). The cover above the basement fault forms a ramp to simulate a synclinally folded peripheral sink. The width of the ramp depends on the offset of the basement fault according to the following relationship:

$$w = Wlog(w_{coeff}d) \tag{8}$$

Here, W is a constant, w_{coeff} is a number (here called width coefficient) and d is the vertical displacement of the basement fault. W defines the initial width of the monocline at small d and is here defined to be 500. The relationship in Eq. 8 ensures that the width of the ramp increases fast at small basement offsets, but slow at larger offsets. Such a geometric evolution of the monocline detached from a basement fault by an incompetent layer was observed in analogue experimental studies (Dooley et al. 2003; Warsitzka et al. 2015) and nature (Withjack & Callaway 2000). We assume that the basement fault extends infinitesimally in the third y-dimension and hydraulic-head gradient only acts in the x-direction.

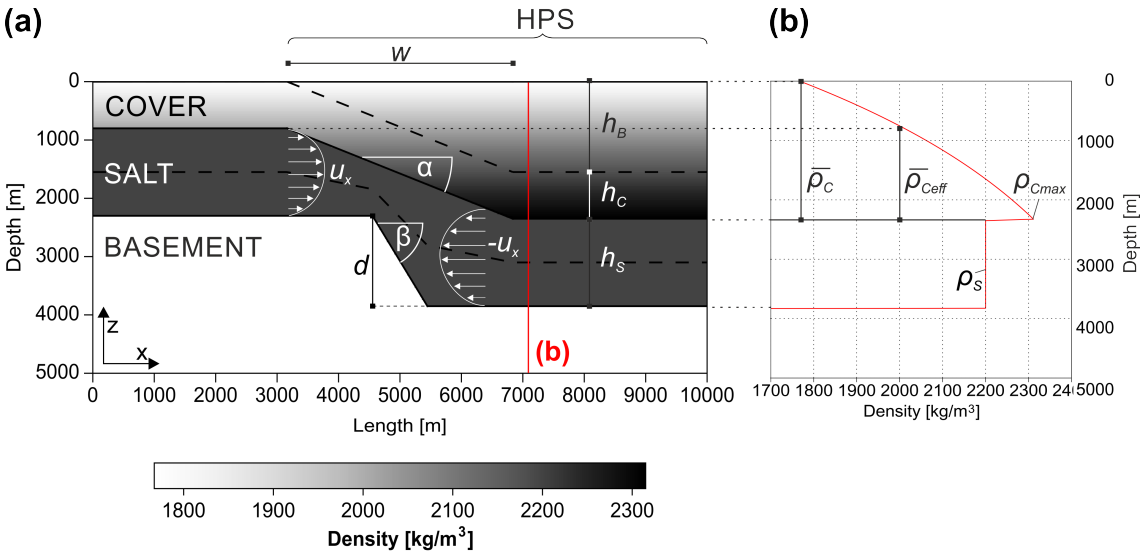

Figure 2. Sketches illustrating (a) set-up and (b) vertical density profile of the model. The set-up includes a sub-salt basement, the viscous salt layer and a supra-salt cover layer. The density of the cover layer increases exponentially with depth. The density of the salt layer is constant. The density of the basement is excluded, because it is irrelevant for the velocity calculation. The dashed lines denote the top of the pre-kinematic cover layer and the midline of the salt layer, respectively. α - dip of the cover monocline, β - dip of the basement fault, d - displacement of the basement fault, HPS - Hanging wall peripheral sink, h_C - thickness of the pre-kinematic cover layer, h_B - thickness of the basin fill, h_S - thickness of the salt layer, ρ_{Cmax} - maximal cover density in the HPS, $\bar{\rho}_C$ - average cover density in the HPS, $\bar{\rho}_{Ceff}$ - average effective cover density in the HPS, ρ_S - salt density, u_x - horizontal flow velocity, w - width of the cover monocline.

The computation of the velocity field first involves assigning the grid nodes and the layer boundaries, i.e. the sedimentary surface as well as the top and the base of the salt layer including the fault offset d in the base and cover monocline (Fig. 3). The spatial resolution of the set-up is arbitrary and the distance between each grid point in x- and z-direction was set to be 50 m. The average density of the cover is calculated at each grid point according to the prescribed compaction law (see below) and related to the depth. The resulting lithostatic pressure σ_N of the cover equals the depth independent pressure head (PH) in the salt layer. The elevation head (EH) within the salt layer is the weight of the salt layer above each node. The hydraulic-head gradient is then calculated by the difference of PH+EH between two horizontal nodes in x-direction divided by the distance between the grid points (Δx). The steady-state flow velocity at each grid point $u_{i,j}$ is determined by:

$$u_{i,j} = \frac{1}{2\eta} \frac{H_{i,j} - H_{i+1,j}}{x_{i,j} - x_{i+1,j}} (h_{Sj}^2 - z_{i,j}^2) \tag{9}$$

In order to mimic a temporally evolving fault displacement and coinciding salt flow, the vertical

offset of the sub-salt fault and the base of the cover above the hanging wall side is incrementally increased (e.g. Δd = 1 m). Then, the procedure of computing the velocity field is repeated (Fig. 3). In order to estimate, whether elevation-head gradient or pressure-head gradient dominates, we used the mean hydraulic-head gradient and mean flow velocity along the mid line of the salt layer (Fig. 2). The vertical offset d at which the PHG becomes larger than the EHG on average defines the here called "Point of reversal" (POR). Additionally, the d at which ρ_{Cmax}, $\bar{\rho}_C$ or $\bar{\rho}_{Ceff}$ exceeds the salt density ρ_S is called "Point of density inversion" (PDI) for each specific density term.

2.2 Sensitivity study

In order to quantify geometrical and rheological parameters for the model set-up and for a sensitivity study, we compiled published ranges of layer thicknesses, fault offsets, lithological units and ages of 15 different salt-bearing extensional basins (Table 1). In a reference model, mean geometric and rheologic parameters are chosen according to average values of this compilation. In the sensitivity study, the model procedure described above repeatedly applies iterations in which one parameter is changed stepwise (Fig. 3) to assert its effect on the velocity field and the POR. The following parameters are varied (Table 2): thickness of the salt layer, thickness of the pre-kinematic cover layer, width of the supra-salt monocline, thickness of the basin fill, salt density, salt viscosity, and cover lithology (i.e. compaction parameters according to Athy's law (1930). The thickness of the basin fill is defined as multiplier (basin fill coefficient h_{Bcoeff}) of the basement fault offset, e.g. h_{Bcoeff} = 0.5 means that the thickness of the basin fill is half the displacement of the basement fault d. Assuming fault displacement increasing with time, the thickness of the basin fill represents a sedimentation rate resulting in either underfilled or overfilled basins. In most models, we assume that the hanging wall peripheral sink (HPS) is always filled up with sediments or, in other words, the accumulation rate is equal to the displacement rate of the basement fault. This represents an idealised case in nature, but it is the most simple case applicable for modelling purposes. The width of the monocline is varied by applying different values for w_{coeff} in equation Eq. 8. Analogue models have shown that the monocline above a displaced salt layer may increase with larger salt layer thickness or with slower displacement rate of the basement fault (Withjack & Callaway 2000; Warsitzka et al. 2015).

Additional to the compaction law used in the reference model (Athy's law), 3 other compaction laws presented by Sclater & Christie (1980); Baldwin & Butler (1985) and Hudec et al. (2009) are applied in the analytical procedure and compared to each other.

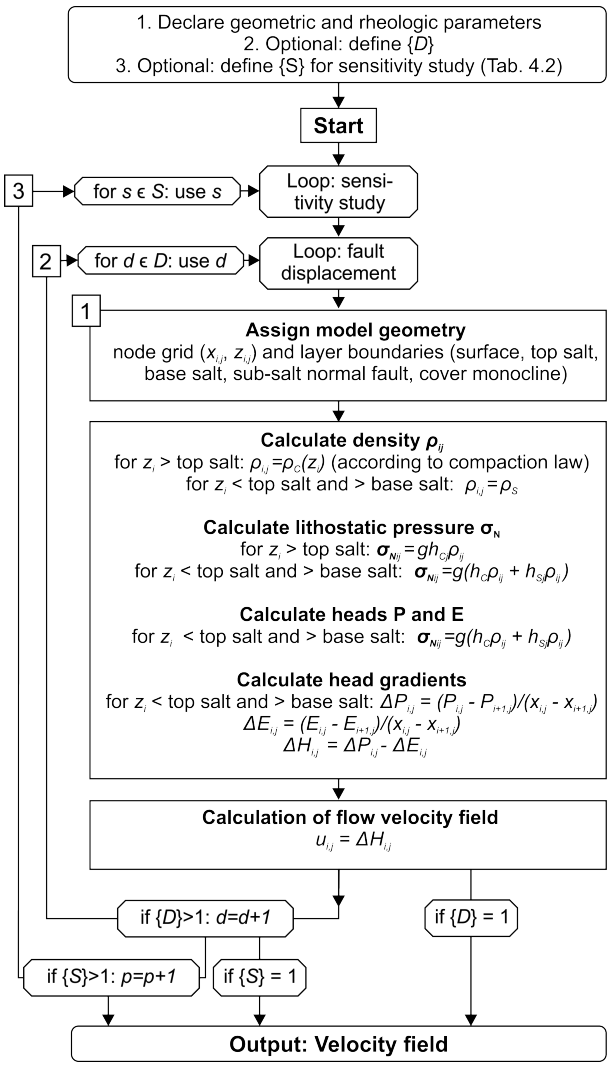

Figure 3. Illustration of the computation procedure conducted in the analytical models. Initial parameters involve height and length of the model, amount of grid nodes as well as geometric and rheologic parameters as listed in Table 2. $\{D\}$ defines a range of offsets of the sub-salt fault d for which the velocity field is incrementally calculated. $\{S\}$ defines the range of one of the parameters listed in Table 2 that is applied for the sensitivity study. E - elevation head, H - hydraulic head, g - gravitational acceleration, P - pressure head, ρ_C - density of the cover layer, ρ_S - density of the salt layer, σ_N - vertical normal stress.

2.3 Cover density and compaction

Generally, the density of the cover sediments exceeds the density of the salt (2200 kg m^{-3}) at a depth between 600 to 3000 m (e.g. Hudec et al. 2009; Goteti et al. 2012). The variability of the cover density is related to complex processes of sediment compaction depending on factors like lithology, pore pressure, depositional environment and diagenetic processes (Allen & Allen 2013). We assume only physical compaction and an exponential or power-law relationship between density and depth (Athy

1930). This most commonly used compaction law describes a depth-dependent decrease of porosity according to:

$$\phi(z) = \phi_0 e^{-cz} \tag{10}$$

$\phi(z)$ is the porosity in a certain depth. ϕ_0 and c stand for the initial porosity and the depth coefficient, both characteristic for specific lithologies (Table 2). The corresponding density ρ_C at each depth is given by:

$$\rho_C(z) = \phi(z)\rho_W + (1 - \phi(z))\rho_G \tag{11}$$

Here, ρ_G is the grain density (Table 2) and ρ_W the density of water. Integrating over the entire thickness of the cover h_C gives the average density $\bar{\rho_C}$ of the cover:

$$\bar{\rho_C} = \rho_G + \frac{(\rho_G - \rho_W)\phi_0}{c}\frac{(e^{-ch_C} - 1)}{h_C} \tag{12}$$

There are various other relationships purposing to fit porosity-depth relationships of compacting sediments. Baldwin & Butler (1985) provided empirical equations for the depth dependent solidity fraction S (= 1 - ϕ) to fit published compaction curves. Substituting S with the bulk density of the sediment gives an equation for the depth dependent density e.g. of compaction curves for sandstones as presented by Sclater & Christie (1980) :

$$\rho_C = (\rho_G - \rho_W)(1 - 0.49e^{\frac{-d}{3700}}) + \rho_W \tag{13}$$

Integrated over the thickness of the sediment layer, the average density can be calculated as (Hudec et al. 2009):

$$\bar{\rho_C} = \frac{1}{h_C}(\rho_G h_C + 1813(\rho_G - \rho_W)(e^{\frac{-d}{3700}} - 1) \tag{14}$$

Additionally, Baldwin & Butler (1985) provided a power-law equation for the solidity of normally compacted shales. The resulting equation for bulk density versus depth is (Hudec et al. 2009):

$$\rho_C = (\rho_G - \rho_W)(\frac{d}{6020}^{\frac{1}{6.35}}) + \rho_W \tag{15}$$

Integrating over the sediment thickness gives the average density:

$$\bar{\rho_C} = \frac{1}{h_C}(5201(\rho_G - \rho_W)(\frac{d}{6020})^{\frac{7.35}{6.35}} + \rho_W h_C) \tag{16}$$

Hudec et al. (2009) provided a best fit equation for a depth-dependent average density of sediment in the Gulf of Mexico basin:

$$\bar{\rho_C} = 1400 + 142d^{0.21} \tag{17}$$

2.4 Model limitations

The deformation of natural rock salt is mostly characterised by a combination of dislocation creep and pressure solution creep. Hence, rock salt exhibits a non-Newtonian rheology with a shear-thinning behaviour. The effective viscosity of rock salt is temperature and strain-rate dependent and ranges between 10^{16} and 10^{21} Pa s (e.g. Urai et al. 1986; Carter et al. 1993; Van Keken et al. 1993; Ter Heege et al. 2005; Li et al. 2012). However, in most studies, it is convenient to assume linear, Newtonian salt viscosity when approximating first-order kinematics of salt flow (e.g. Gemmer et al. 2004; Chemia et al. 2008; Peel 2014). Thus, we assumed Newtonian-viscous behaviour of the salt layer possessing a viscosity of 10^{18} Pa s.

The composition of a natural evaporitic succession can be highly variable because of intercalations of less dense and less viscous evaporite minerals, e.g. carnallite or sylvite, or denser and more competent rocks, e.g. gypsum or carbonate (e.g Jackson et al. 1990; Van Gent et al. 2011). Each of these intercalations might react differently to an imposed hydraulic-head gradient. In nature the actual velocity field should be much more complex than dealt here.

Lateral stretching, faulting of the cover and shear stresses are neglected in our velocity computation. Shearing at the boundaries of the salt layers may superimpose Poiseuille flow by a specific velocity competent of Couette flow (Weijermars & Jackson 2014). Besides, resisting forces against salt flow arising from the shear strength of the cover layer (Jackson & Vendeville 1994) were not included. Cover deformation is characterised by viscous or in most cases elasto-plastic rheology. Including this into the simplified model would be much too complex. The calculated velocity values can be regarded as upper limits, because no resisting forces other than shear resistance at the (no slip) salt layer boundaries are considered and the salt is treated as Newtonian fluid. The flow velocity field illustrated here can be regarded as initial velocity boundary condition for each period after the salt layer was displaced, whereas the complete time-dependent velocity field would have to be computed by solving the differential Navier-Stokes equation (Eq. 1) numerically.

3 RESULTS

3.1 Reference model

In the reference model, basically two stages of flow patterns can be distinguished, when the offset of the basement fault is stepwise increased and hydraulic-head gradient (HHG) and flow velocity is calculated.

Stage 1: The calculated HHG and the flow velocity in x-direction are positive (red) meaning the elevation-head gradient (EHG) is larger than the pressure-head gradient (PHG) (Fig. 4a). Thus, material in the viscous layer flows downward towards the hanging wall block. With increasing displacement along the basement fault, downward flow accelerates until achieving a "Point of maximum" (POM) at an offset of ~ 600 m for the flow velocity (Fig. 4e) and at ~ 850 m for the HHG (Fig. 4f). The POM of the HHG equals the "point of density inversion" (PDI) at the base of the cover ρ_{Cmax}. At larger fault offsets, the flow velocity and the HHG decrease. This implies that the effect of the PHG enhances because of increasing compaction of the cover. The PHG becomes larger than the EHG in the lower parts of the salt layer beneath the hanging wall peripheral sink, which would induce upward directed material flow (Fig. 4b). However, as the mean HHG of the entire salt layer is still positive, downward directed flow still dominates.

Stage 2: At a displacement of roughly 1800 m, the mean HHG is zero indicating that the mean total EHG is equal to the mean total PHG. Beyond this "Point of reversal" (POR) (Fig. 4f), the mean HHG becomes negative inferring that the differential loading between the hanging wall and the footwall side is sufficient to force upward flow of the salt (blue). The POR of the flow velocity occurs at a smaller vertical displacement (1550 m) than the POR of the HHG. This is caused by the geometry of the salt layer and dependence of flow velocity on the layer thickness. Such an effect diminishes, if the top and the base of the salt layer are exactly parallel (see below).

It is noteworthy that the PDI of the average effective cover density $\bar{\rho}_{Ceff}$ (Fig. 2) nearly coincides with the POR of the HHG (Fig. 4f). Apparently, $\bar{\rho}_{Ceff}$, i.e. the average density of the cover beneath the level of the salt layer top on the footwall side, determines the onset of upward flow. Meanwhile, the average density of the entire cover above the hanging wall block $\bar{\rho}_C$ remains less than salt density ($2200\,\mathrm{kg\,m^{-3}}$) (Figs 4e and f), even when the mean flow velocity and the mean HHG are already directed upwards.

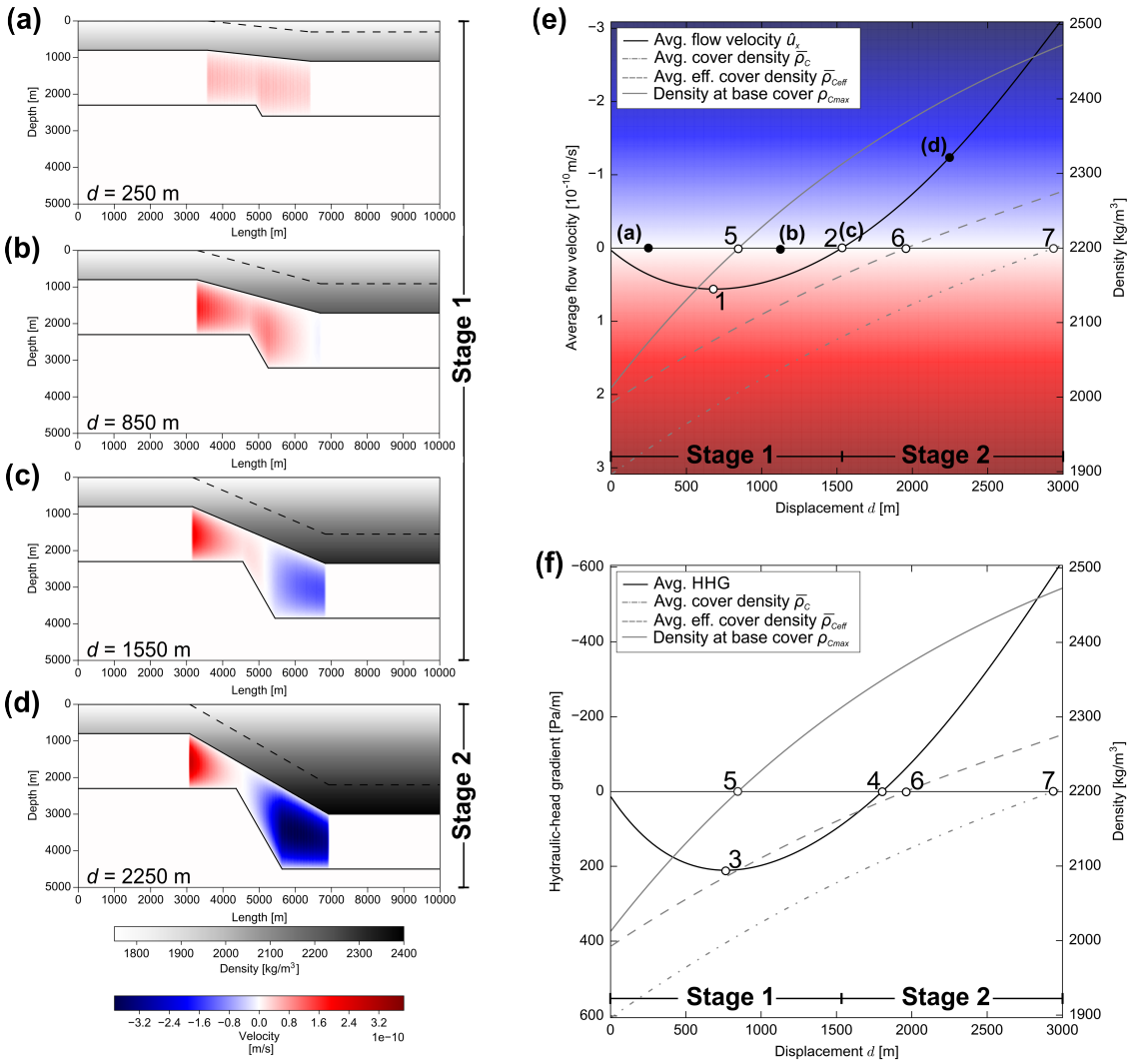

Figure 4. (a)-(d) Reference model illustrating the steady-state Poiseuille flow velocity distribution in a salt layer and depth dependent cover density exemplarily for four different offsets of the sub-salt normal fault: (a) 250 m, (b) 850 m, (c) 1550 m, (d) 2250 m (see Table 2 for applied geometrical and lithological values). (e)/(f) The curves show the mean flow velocity, the mean hydraulic-head gradient and characteristic density terms related to the vertical offset d. At first, increasing downward flow (red) occurs. With increasing d, reversal to upward flow (blue) takes place. $\bar{\rho}_C$ remains lower than the average salt density (2200 kg m^{-3}). 1 - Point of maximum (POM) of flow velocity, 2 - Point of reversal (POR) of flow velocity, 3 POM of HHG, 4 - POR of HHG, 5 - Point of density inversion (PDI) of ρ_{Cmax}, 6 - PDI of $\bar{\rho}_{Ceff}$, 7 - PDI of $\bar{\rho}_C$.

3.2 Sensitivity study

3.2.1 Thickness of the salt layer

The flow velocity is proportional to the second power of salt layer thickness h_S (Eq. 7). Hence, the maximum downward flow velocity at the POM ($\sim$700 m) increases from 0.2×10^{-10} m s^{-1} to

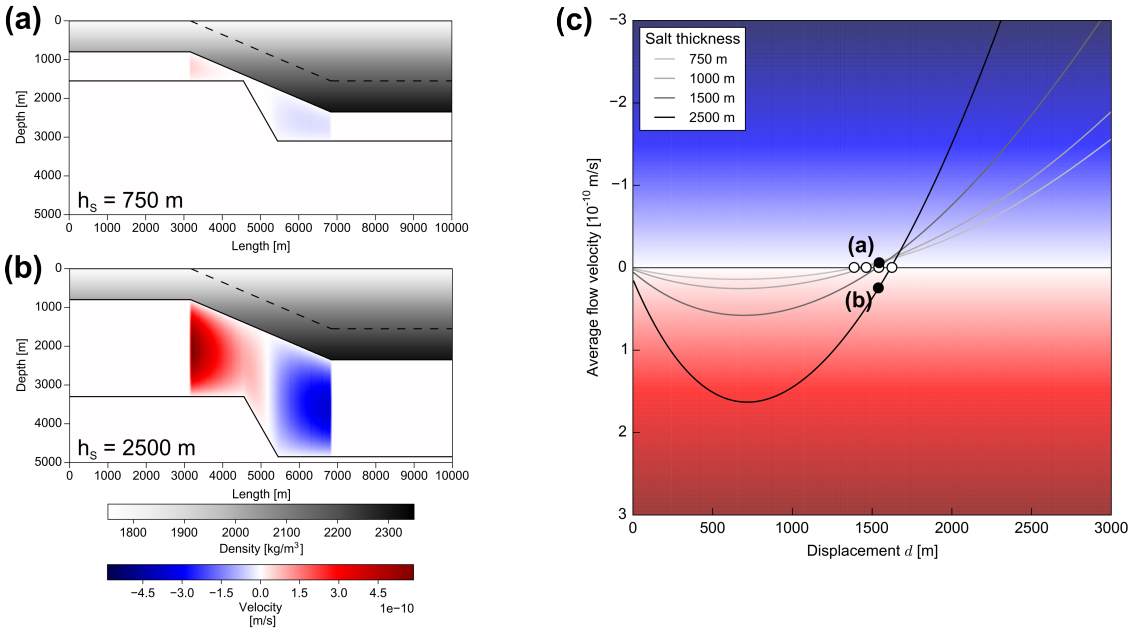

Figure 5. Sensitivity study comparing the influence of the salt layer thickness h_S on the flow velocity (d = 1550 m). The velocity field is illustrated for (a) h_S = 750 m, (b) h_S = 2500 m. (c) Curves of the mean flow velocity depending on 4 different h_S reveal that the Points of reversal (POR; white dots) are only affected to a small degree. The black dots depict fault displacements applied in (a) and (b).

1.8×10^{-10} m s^{-1} when increasing h_S from 750 m to 2500 m (Figs 5a and b). Nevertheless, the amount of HHG and, therefore, the POR of the HHG (Table 2) are not affected by h_S. This is because PHG depends on the weight of the cover and the EHG only depends on the tilting of the top of the salt layer. Similarly, the POR for the flow velocity only slightly varies (Fig. 5c). Differences between both PORs result from the geometric configuration of the salt layer (see below).

3.2.2 Thickness of the pre-kinematic cover

The thickness of the pre-kinematic cover layer h_C significantly affects direction and magnitude of flow in the salt layer. In case of no pre-kinematic cover layer (Fig. 6a), the transition from downward to upward flow occurs at a comparatively large fault offset (POR = $\sim$ 2900 m). The density at the base of the hanging wall peripheral sink surpasses the salt density first at a vertical displacement of PDI = $\sim$ 1650 m and, therefore, much later than the PDI of the reference model ($\sim$ 600 m). Applying larger h_C leads to a highly compacted and dense cover layer. Therefore, the POM and the POR occur at smaller fault offsets (Fig. 6e). With h_C increasing by 400 m, the fault displacement required to induce upward flow is reduced by $\sim$ 650 m.

Fig. 6(f) displays the dependence of the PORs and the PDIs on the amount of h_C. It demonstrates

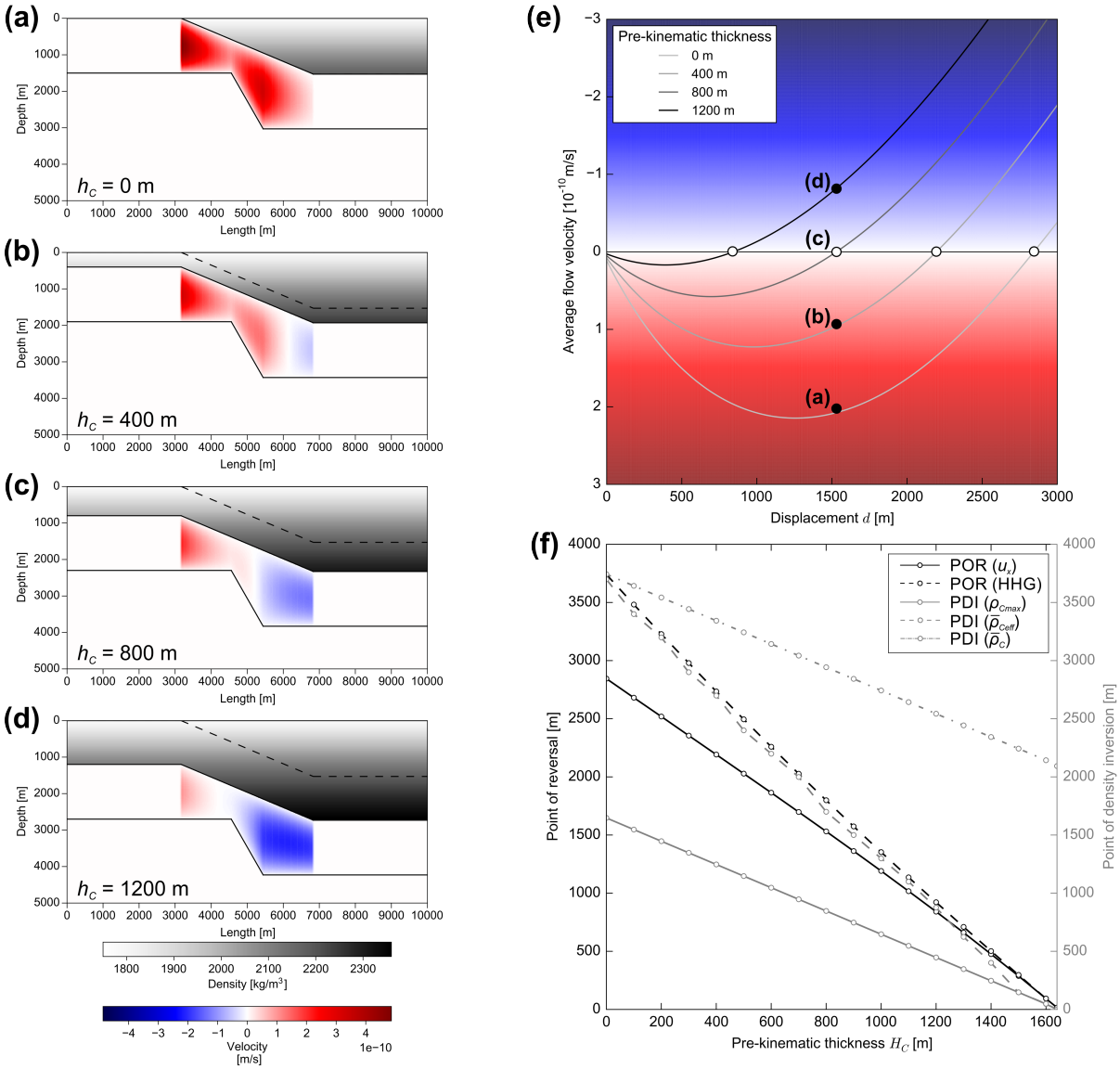

Figure 6. Sensitivity study comparing the influence of the pre-kinematic layer thickness h_C on the flow velocity. The velocity field is illustrated for (a) h_C = 0 m, (b) h_C = 400 m, (c) h_C = 800 m and (d) h_C = 1200 m (d = 1550 m). The graph of (e) relates the mean flow velocity to the vertical offset d. White dots denote the POR and black dots the fault displacements applied in (a) to (d). **F.** shows Points of reversal (POR) and Points of density inversion (PDI) depending on h_C.

that a larger pre-kinematic thickness h_C leads to smaller POR and PDI. For h_C larger than $\sim$ 1650 m, the POR is 0. This means that PHG is larger than EHG already at the beginning of fault displacement and the salt is immediately expelled upwards.

3.2.3 Thickness of syn-kinematic basin fill

The top of the cover layer in the hanging wall peripheral sink represents the "syn-kinematic" sediment accumulation with regard to the displacement of the basement fault. In the models with an underfilled hanging wall peripheral sink (HPS) ($h_{Bcoeff} < 1$), the space is assumed to be filled with water and the pre-kinematic layer is assumed to compact in the same manner as under sedimentary loading of a filled-up HPS. In models without syn-kinematic basin fill (h_{Bcoeff} = 0; Fig. 7a), the average density of the entire hanging wall peripheral sink is much lower compared to models with complete sedimentary fill. Consequently, $\bar{\rho}_{Ceff}$ is not sufficient for the PHG to exceed the EHG and downward flow dominates even at very large fault displacements. In the model in which the thickness in the HPS is half the vertical displacement (h_{Bcoeff} = 0.5; Fig. 7b), differential loading is still lower and the POR of the flow velocity occurs at a fault displacement larger than 5000 m. In the case of an overfilled basin (h_{Bcoeff} = 1.5; Fig. 7d), the turn of the flow direction occurs earlier (POR = $\sim$820 m) compared to the reference model. This results from a stronger sediment compaction in the lower parts of the cover layer.

Fig. 7(f) reveals that the PORs and PDIs decrease in a non-linear relationship when h_{Bcoeff} becomes larger. It can be deduced from the calculations that a minimum thickness of the basin fill of approximately h_{Bcoeff} = $\sim$0.6 is necessary to achieve a POR at fault offsets smaller than 5000 m. This value means that the thickness of the basin fill has to be at least $\sim$60 % of the fault displacement to induce upward flow at all. In cases of an overfilled hanging wall peripheral sink ($h_{Bcoeff} > 1$), the PORs decrease with increasing h_{Bcoeff} and approximate a constant level of $\sim$400 m (Fig. 7f).

3.2.4 Width of the cover monocline

The monocline above the basement fault grows wider with increasing displacement of the basement fault according to Eq. 8. If the width coefficient w_{coeff} is larger, i.e. the width of the monocline increases faster, the region in which the hydraulic-head gradient acts is wider, whereas the dip of the cover monocline flattens (Figs 8a and b). Since the PHG is defined as pressure differences per distance, and the EHG depends on the dip of the top of the salt layer, the resulting HHG is lower when the cover monocline is wider. Hence, flow velocity also decreases, but the POR is not affected (Fig. 8c). The latter observation implies that the PHG and the EHG change equally when varying the width of the monocline.

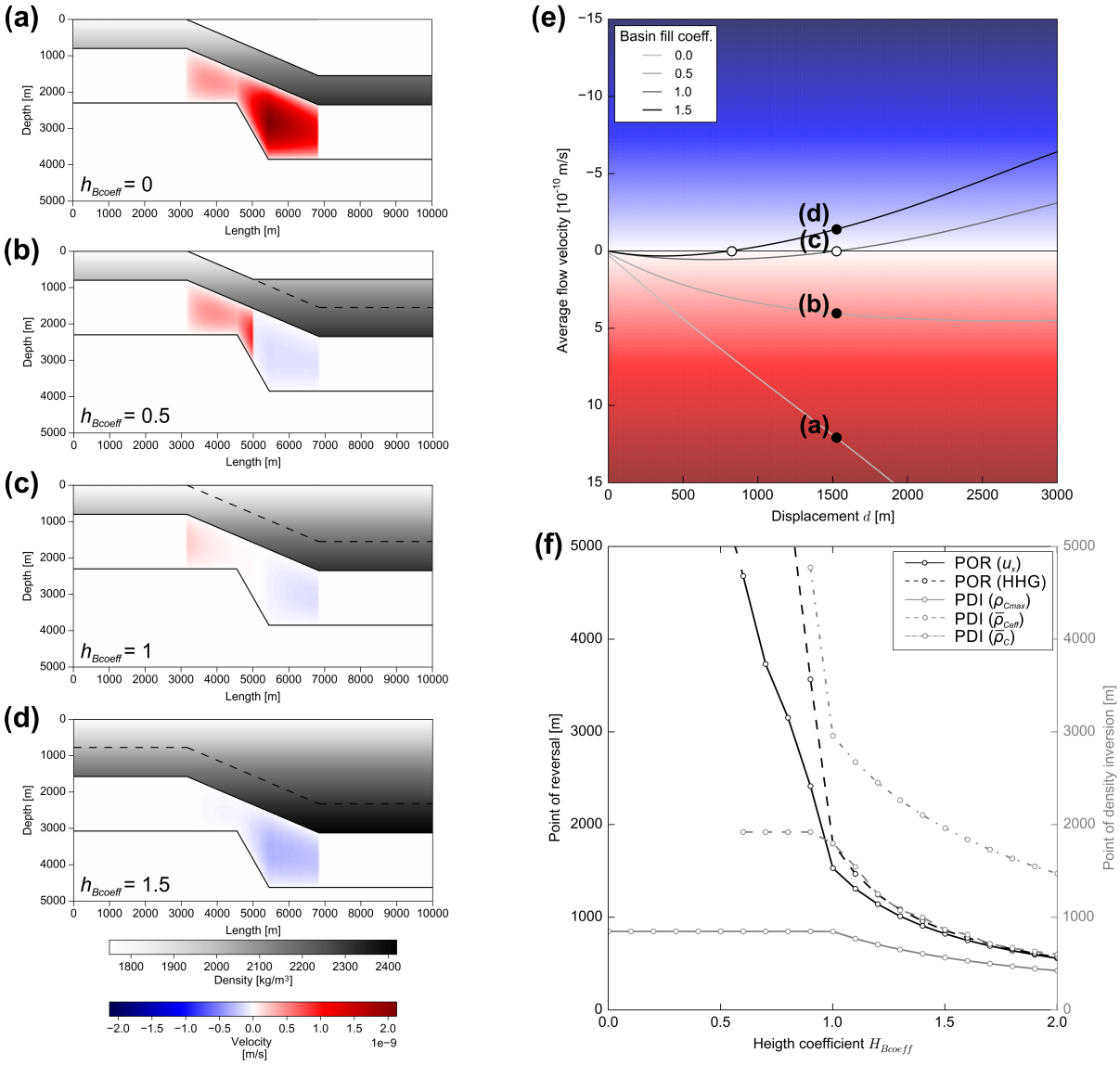

Figure 7. Sensitivity study comparing 4 different scenarios of fill the hanging wall peripheral sink defined by a factor (h_{Bcoeff}) multiplied with the vertical displacement d: (a) $h_{Bcoeff} = 0$, (b) $h_{Bcoeff} = 0.5$, (c) $h_{Bcoeff} = 1$, (d) $h_{Bcoeff} = 1.5$ (d = 1550 m). (e) Curves of the mean flow velocity versus offset at the basement fault. White dots denote the POR and black dots the fault displacement applied in (a) to (d). (f) The graphs show Points of reversal (POR) and Points of density inversion (PDI) depending on h_{Bcoeff}.

3.2.5 Dip of the basement fault

The dip of the basement fault β locally modifies the thickness of the salt layer and, thus, the velocity according to Eq. 7. The thickness of the salt layer in downthrown parts of the salt layer above the kink of the basement is larger than the thickness above the fault tip. Therefore, flow velocities in the downthrown parts, where the PHG exceeds the EHG earlier, become slightly larger applying an equal

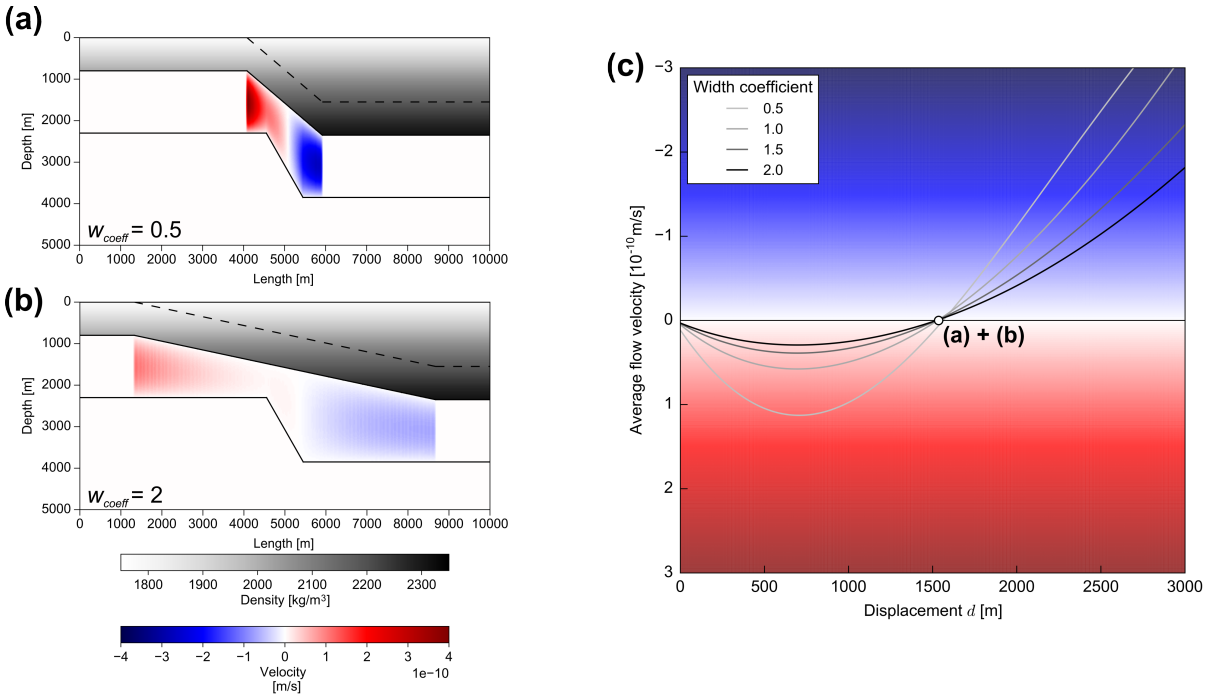

Figure 8. Sensitivity study comparing the flow velocity depending on the width of the cover monocline (w_{coeff}). (a) illustrates the velocity field for w_{coeff} = 0.5 and (b) for w_{coeff} = 2 (d = 1550 m). (c) displays trends of flow velocity related to increasing fault displacement. The Point of reversal (white dot) is not affected by the width of the cover monocline.

amount for the HHG. This effect is stronger, if the basement fault dips steeper (Fig. 9a). Nevertheless, the PORs only slightly vary, if β increases (Fig. 9c). If β is equal to the dip of the cover monocline α (Fig. 9b), the geometrical influence on the POR completely vanishes. Then, the POR of the flow velocity matches the POR of the HHG (Table 2).

3.2.6 Lithology of the cover layer

Considering Athy's law (1930), different lithologies and their specific compaction parameters (c, ϕ_0, ρ_G; Table 2) can be taken into account. The compaction behaviour determines the average density of the cover layer and, therefore, the amount of the PHG. Sandstone has a comparatively low initial porosity (ϕ_0 = 0.49), which results in a relatively high surface density. Nevertheless, its compaction coefficient (c = 0.27 km^{-1}) is also small causing a minor physical compaction during increasing burial. Hence, the PHG increases also slightly and the tendency for upward flow occurs at larger fault displacements (POR = $\sim$ 2150 m) compared to models with other lithologies (Fig. 10a). Shales and carbonates typically possess a relatively large initial porosity (ϕ_0 = 0.63, 0.7) (Sclater & Christie 1980), but compact faster than sandstone (c = 0.51 km^{-1}, 0.71 km^{-1}). Hence, the transition from downward

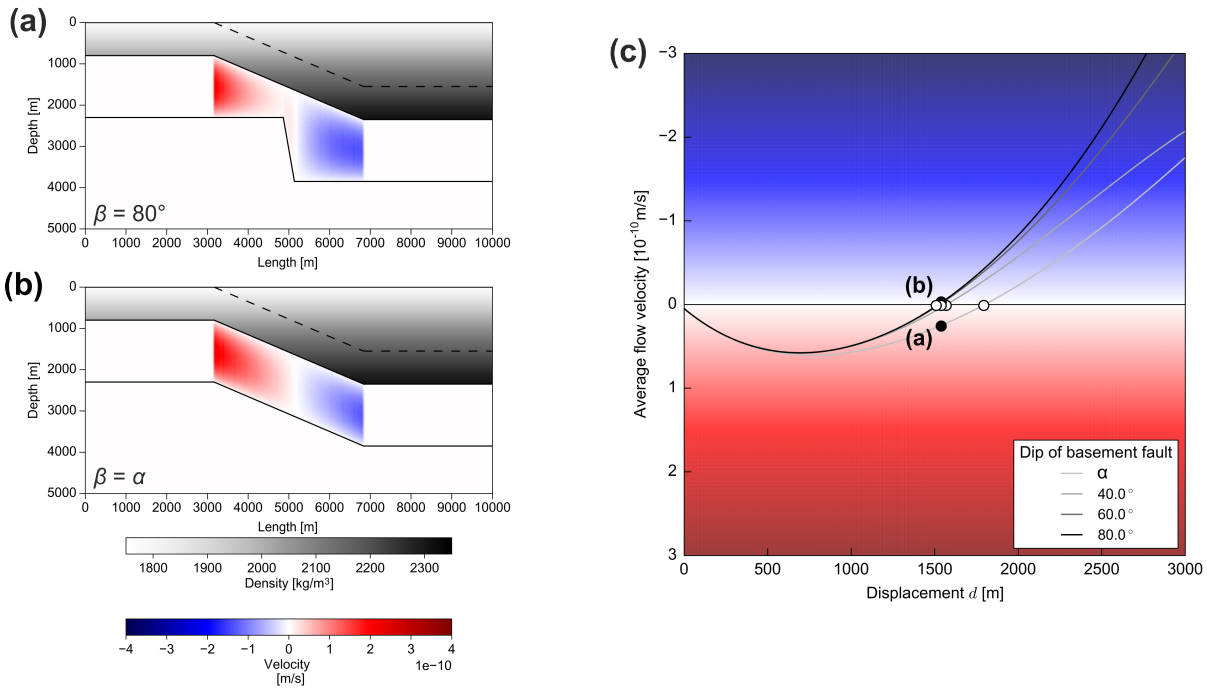

Figure 9. Sensitivity study comparing the flow velocity depending on the dip of the basement fault β. (a) illustrates the velocity field for β = 80 and (b) for $\beta = \alpha$ (d = 1550 m). (c) The trend of the flow velocity demonstrates that the Point of reversal (white dots) is slightly larger, if the dip of the basement fault is smaller.

to upward flow takes place at a smaller vertical offsets of POR = $\sim$ 1100 m or $\sim$ 700 m, respectively (Figs 10e and f). Assuming a mixture of sandy shale (reference model) with average amounts of compaction parameters, the switch of flow direction is moderate compared to assuming either pure sand or pure shale, respectively.

Fig. 10(f) displays PORs and PDIs related to a faster compacting cover layer, i.e. an increasing compaction coefficient c, but an equal initial porosity of ϕ_0 = 0.55 and grain density of ρ_G = 2680 kg m^{-3}. Applying larger values of c, the POR and PDI decrease in a non-linear relationship. With a $c > 0.75$, upward flow is already initiated at small fault displacements.

3.2.7 Density and viscosity of the salt layer

The EHG directly depends on the salt density (Eq. 7). A lower salt density, i.e. a higher positive buoyancy, promotes the ability for upward flow, because the PHG counterbalances the EHG at smaller vertical displacements (Figs 11a - d). Small changes in salt density (e.g. $\Delta\ \rho_S$ = 50 kg m^{-3}) lead to significant changes of the POM and the POR (ΔPOM/POR = $\sim$ 400 m) (Fig. 11E).

Fig. 11(f) displays that with a larger density of the salt layer ρ_S, the POR and the PDI increase nearly linearly. If ρ_S is smaller than $\sim$ 2050 kg m^{-3}, the salt would immediately flow upwards.

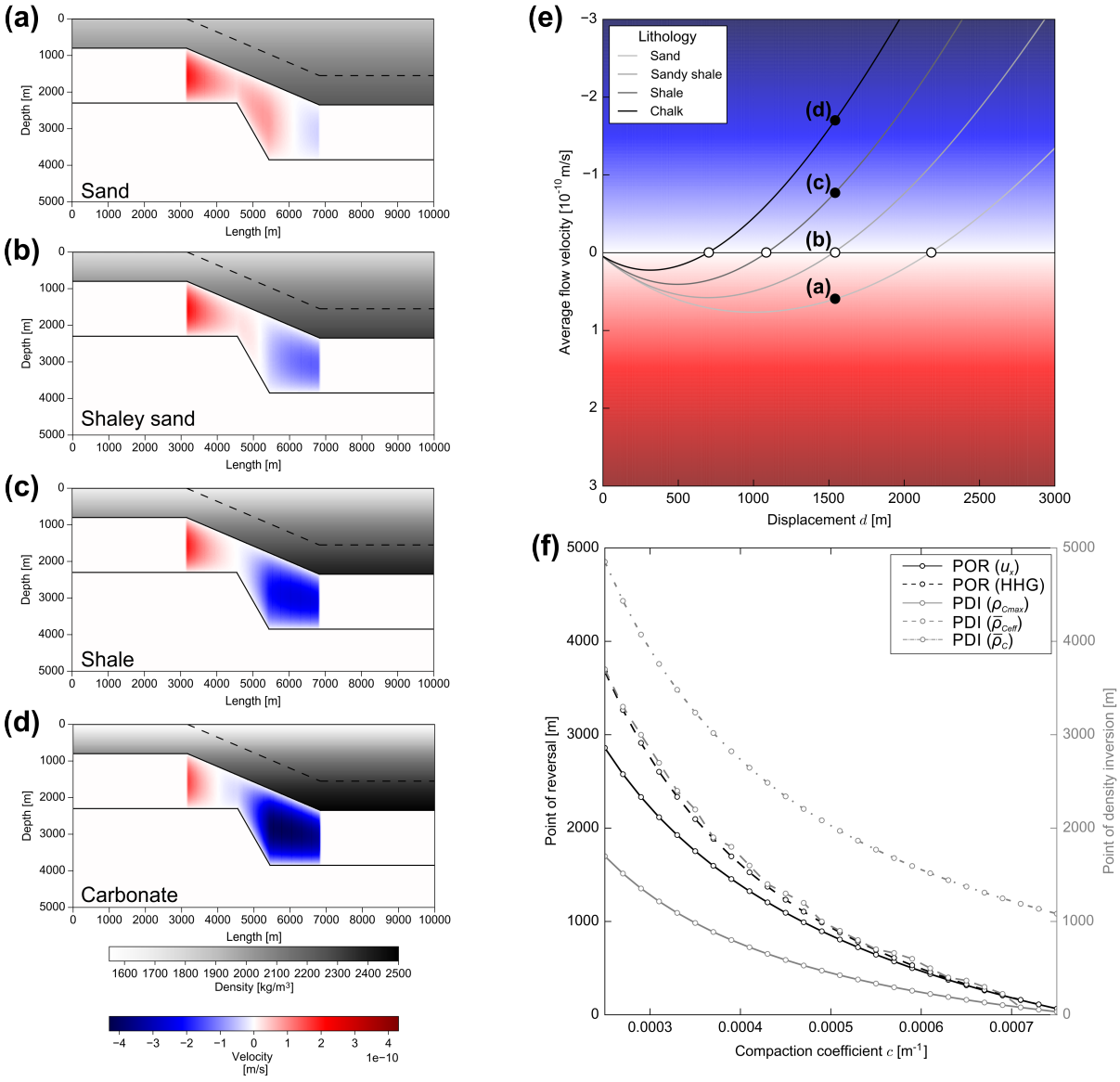

Figure 10. Sensitivity study comparing 4 different lithologies: (a) Sand, (b) shaley sand, (c) shale, (d) carbonate (d = 1550 m). (e) Curves of the mean flow velocity versus offset at the sub-salt normal fault d. White dots denote the POR and black dots the fault displacement applied in (a) to (d). (f) The graphs show Points of reversal (POR) and Points of density inversion (PDI) depending on the compaction coefficient c.

The mean viscosity of a salt layer can vary over several orders of magnitudes from 10^{16} to 10^{21} Pa s (e.g. Van Keken et al. 1993). Accordingly, flow velocities change in the same range (Eq. 7). In the same way as the thickness of the salt layer, the viscosity of the salt layer only affects the flow velocity, but not the direction of the material movement.

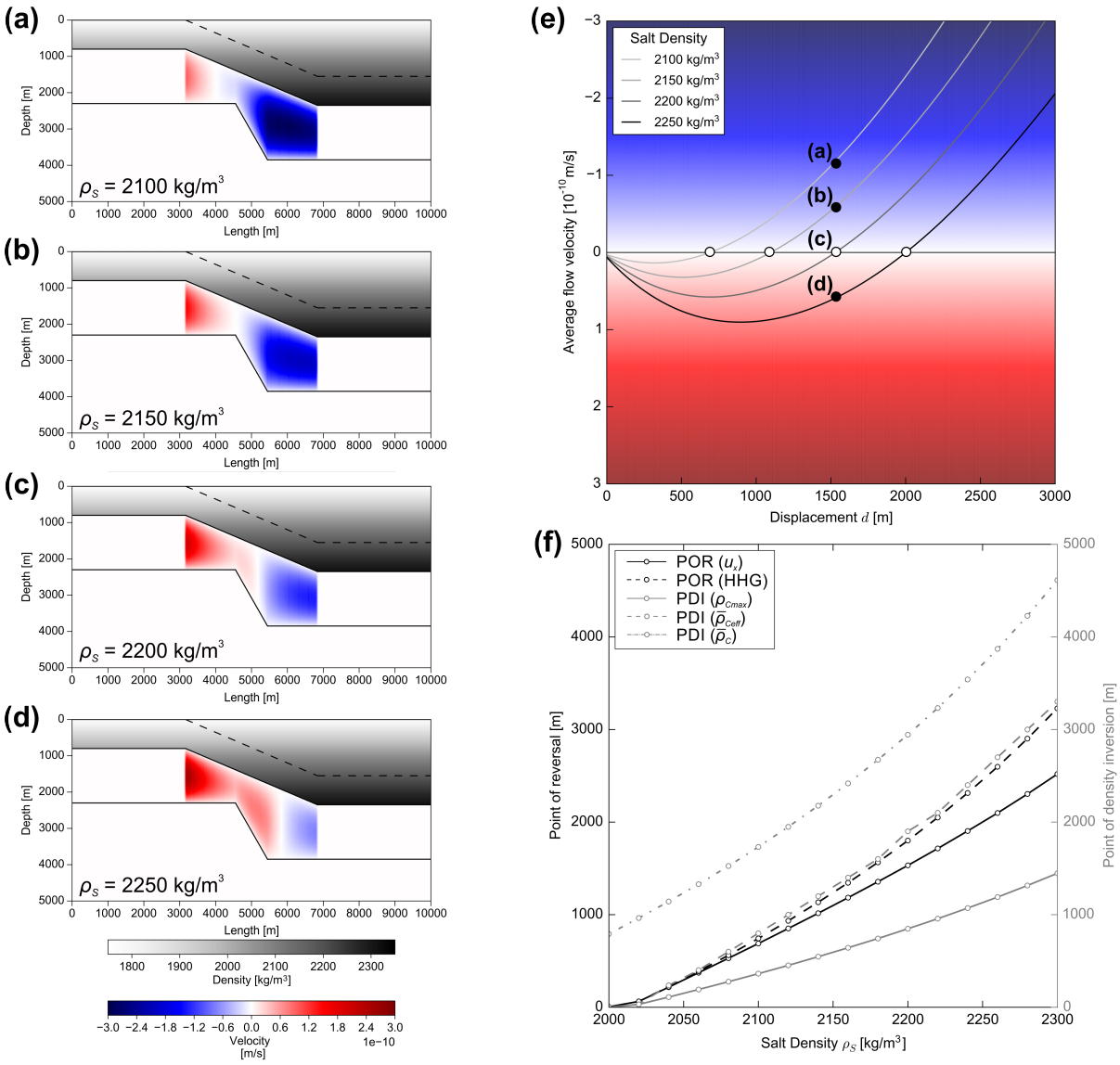

Figure 11. Sensitivity study comparing the influence of the salt density ρ_S on the flow velocity. (a) illustrates the velocity field for ρ_S = 2100 kg m^{-3}, (b) for ρ_S =2150 kg m^{-3}, (c) for ρ_S = 2200 kg m^{-3}, and (d) for ρ_S = 2250 kg m^{-3} (d = 1550 m). (e) Curves of the mean flow velocity versus offset at the basement fault. White dots denote the POR and black dots the fault displacement applied in (a) to (d). (f) The graphs show PORs and PDIs depending on ρ_S.

4 DISCUSSION

The analytical computations presented here imply that a significant vertical displacement of the salt layer is required to initiate upward directed flow. Under most geological conditions, salt flow during basement faulting and simultaneous differential loading first tends to be directed downward towards

Table 2. Summary of initial geometric and petrophysical model parameters as well as outcomes of the sensitivity study (POR, POM, PDI). Values applied in the standard model are bold. The thickness of the basin filling is defined as percentage of displacement of the basement fault. The width coefficient defines the width of the cover monocline as factor in Eq. 8. The lithology of the cover determines the compaction parameters assuming the law by Athy (1930). For sand, these are: ρ_G = 2650 kg m^{-3}, ϕ_0 =0.49 and c = 0.27 km^{-1}. For shaley sand: ρ_G = 2680 kg m^{-3}, ϕ_0 = 0.56 and c = 0.39 km^{-1}. For shale: ρ_G = 2720 kg m^{-3}, ϕ_0 = 0.63 and c = 0.51 km^{-1}. For limestone: ρ_G = 2710 kg m^{-3}, ϕ_0 = 0.7 and c = 0.71 km^{-1}.

	Salt thickness h_S **[m]**	**Pre-kinematic thickness** h_C **[m]**	**Basin fill coefficient** h_{Bcoeff}	**Width coefficient** w_{coeff}	**Dip of the basement fault** β [°]	**Lithology of the cover**	**Compaction law**	**Salt density** ρ_S **[kg m^{-3}]**	**Salt viscosity** η **[Pa s]**
P1	750	0	0	0.5	α	Sand	Sclater & Christie (1980)	2100	10^{16}
P2	1000	400	0.5	**1**	40	**Shaley sand**	**Athy (1930)**	2150	10^{17}
P3	**1500**	**800**	**1**	1.5	**60**	Shale	Hudec et al. (2009)	**2200**	$\mathbf{10}^{18}$
P4	2500	1200	1.5	2	80	Limestone	Baldwin & Butler (1985)	2250	10^{19}
P1	1766	3742	>5000	1801	1801	2671	2284	743	1801
P2	1795	2737	>5000	1801	1801	1801	1800	1237	1801
P3	1801	1801	1801	1801	1801	1227	1538	1801	1801
P4	1801	924	860	1801	1801	753	0	2454	1801
					Point of reversal (for Vel.) [m]				
P1	1385	2845	-	1571	1801	2171	1896	689	1532
P2	1452	2193	>5000	1533	1574	1533	1532	1099	1532
P3	1533	1532	1533	1527	1533	1088	1332	1533	1532
P4	1619	843	822	1526	1522	696	0	2001	1532
					Point of Maximum (for HHG) [m]				
P1	849	1649	5360	849	849	1256	900	362	849
P2	849	1248	4240	849	849	848	849	593	849
P3	849	848	712	849	849	581	606	848	849
P4	849	407	566	849	849	275	0	1129	849
					Point of Maximum (for Vel.) [m]				
P1	712	1339	-	765	851	975	958	275	712
P2	712	900	1341	712	760	712	712	518	712
P3	712	607	607	674	754	518	518	712	712
P4	712	408	398	657	760	275	0	975	712
					Point of density inversion (for density at base of the cover) [m]				
P1	849	1648	849	849	849	1257	1084	363	849
P2	849	1249	849	849	849	849	849	594	849
P3	849	849	849	849	849	582	720	849	849
P4	849	449	566	849	849	360	0	1131	849
					Point of density inversion (for avg. cover density) [m]				
P1	2943	3744	327	2944	2944	3778	3352	1733	2944
P2	2943	3343	653	2944	2944	2943	2943	2295	2944
P3	2943	2943	2943	2944	2944	2385	2960	2943	2944
P4	2943	2544	1963	2944	2944	1956	871	3703	2944
					Point of density inversion (for avg. effective cover density) [m]				
P1	1841	3700	1278	1841	1841	2701	2300	801	1841
P2	1841	2800	1701	1841	1841	1901	1840	1281	1841
P3	1841	1900	1901	1841	1841	1300	1601	1841	1841
P4	1841	1000	852	1841	1841	800	0	2480	1841

basement lows. At a certain "point of reversal" (POR), the cover is sufficiently compacted to produce a pressure head gradient that is able to squeeze salt uphill.

Assuming parameter values typical for salt-bearing extensional basins (Table 1), the POR of the flow velocity occurs at vertical offsets between 700 and 2200 m (Table 2). The PDI (point of density

inversion) of the density at the base of the cover ρ_{Cmax} is usually located at smaller fault displacements than the PORs. This suggests that at least the deeper parts of the cover layer are significantly compacted at fault offsets smaller then that at the POR.

The PDI of the average cover density $\bar{\rho}_C$ requires significantly larger vertical displacements d than the PORs implying that a density inversion of the entire cover layer is not necessary to force upward flow. In contrast, the PDI of the average effective cover density $\bar{\rho}_{Ceff}$, roughly occurs at the same d as the POR of the HHG ($\Delta\ d = \sim 40$ m; Table 2). This implies that the effective cover density is the parameter crucially controlling the onset of upward directed flow.

4.1 Factors promoting differential loading and upward flow

Our sensitivity study illustrates the high variability of salt flow direction and intensity when changing geometrical and lithological parameters (Table 2). The ratio between cover density and salt density is the most crucial parameter determining the point at which upward flow occurs. Increasing cover density provoked by a larger thickness (high sedimentation rate, large h_C) or a faster compaction promotes a stronger increase of the PHG with increasing fault displacement. A further mechanism changing the cover density is chemical compaction (cementation), which might significantly enhance the density of the cover sediment. For instance, cementation of sandstones due to mineralisation from carbonate-rich fluids during early diagensis replaces pore water (density = 1050 kg m^{-3}) with e.g. calcite (density = 2715 kg m^{-3}) in the pore space. Assuming an initial porosity of 40 %, a sediment grain density of 2650 kg m^{-3} and a cemented portion of the pore space of 50 %, the bulk density of the sandstone increases from 2010 kg m^{-3} (only water filled pores) to 2343 kg m^{-3}. Consequently, the density of the cover exceeds salt density at small thicknesses leading to early stage upward flow. A similar effect results from the accumulation of usually heavier evaporites (gypsum, carbonates) in the hanging wall peripheral sink instead of high porous and initially lighter siliciclastics or limestones.

The density of the salt layer or parts of the salt layer can be reduced by intercalations of bittern salt minerals, e.g. carnallite ($\sim$ 1600 kg m^{-3}) or sylvite ($\sim$ 1900 kg m^{-3}) or even when considering pure halite rocks (2163 kg m^{-3}). If the volumetric portion of these less dense salt minerals is large compared to heavier minerals such as anhydrites or carbonates, the bulk density of the salt layer is reduced and upward flow is initiated at smaller vertical offsets (Fig. 11). Furthermore, it can be deduced from analogue experiments (e.g. Cartwright et al. 2012) and analytical calculations (e.g. Wagner & Jackson 2011) that less competent components of a salt layer deform in channel flow between competent layers at small differential stresses. Evaporite minerals with lower density usually also possess a lower viscosity. Therefore, in intercalations with a low density and a low viscosity, material flow might be faster and pushed upwards earlier then in the rest of the salt layer.

4.2 Factors resisting hydraulic-head gradient and flow velocity

The principal factor resisting salt flow in general and upward flow in particular is the strength of the cover layer (Hudec & Jackson 2007), which is usually characterised by a brittle-plastic behaviour and depends on the thickness and the state of compaction of the sedimentary rock (Jackson & Vendeville 1994). A large thickness of the cover layer enhances the amount of the PHG and the tendency for upward directed flow. Nevertheless, it also results in high strength of the cover layer. Pressures in the viscous layer calculated in our models are relatively low 0.1 – 1 MPa compared to pressures necessary to overcome the shear strength of compacted sediments >10 MPa (Schultz-Ela et al. 1993; Jackson & Vendeville 1994). Nevertheless, partly compacted sediments above the footwall block should be weaker. Furthermore, extension of the basement fault is accommodated by grabens or listric faults in the cover layer. This additionally reduces the strength of and loading through the cover above the footwall block. A combination of weakening the cover above the footwall block and a large PHG due ot a deeply subsided HPS should be most effective in forcing upward flow.

Assuming a scenario, in which sediments in the hanging wall peripheral sink remain undercompacted during burial - e.g. because they are sealed by low-permeable clays - physical compaction is reduced. Thus, the effectiveness of differential loading decreases and downward flow should dominate even at large basement offsets. Similarly, hydrocarbon-rich pore fluids with a density lower than that of water reduce the bulk density of the cover and, therefore, the PHG.

4.3 Comparison with previous studies

The initiation of autonomous subsidence of minibasins into a salt layer was considered by Hudec et al. (2009). They compiled several published compaction models applied for sediments of the Gulf of Mexico (e.g. Sclater & Christie 1980; Baldwin & Butler 1985) and calculated at which depth the density at the bottom of the minibasin surpasses the salt density. Their results imply that minibasins become negatively buoyant with thicknesses of 2300 m to 4000 m.

We implemented some compaction models compiled by Hudec et al. (2009) in the reference model of our calculations. The evolution of the velocity field, the density distribution in the cover layer and trends of flow direction related to the fault offset are relatively similar when juxtaposing the compaction laws by Sclater & Christie (1980) (for sandstones, Eq. 14), Hudec et al. (2009) (Fig. 12; Eq. 17) and the reference model using Athy's law (1930) (for shaley sand, Eq. 12) (Figs 12a - c). The PORs of the flow velocity are achieved at displacements of $\sim$ 1900 m, 1300 m, and 1550 m, respectively (Fig. 12e). Indeed, the POR in the model using the compaction model by Sclater & Christie (1980) for sandstone is almost equal to the POR in the model using Athy's law (1930) for sandstone (Table 2). In contrast, the compaction law by Baldwin & Butler (1985) (for normally compacted shale)

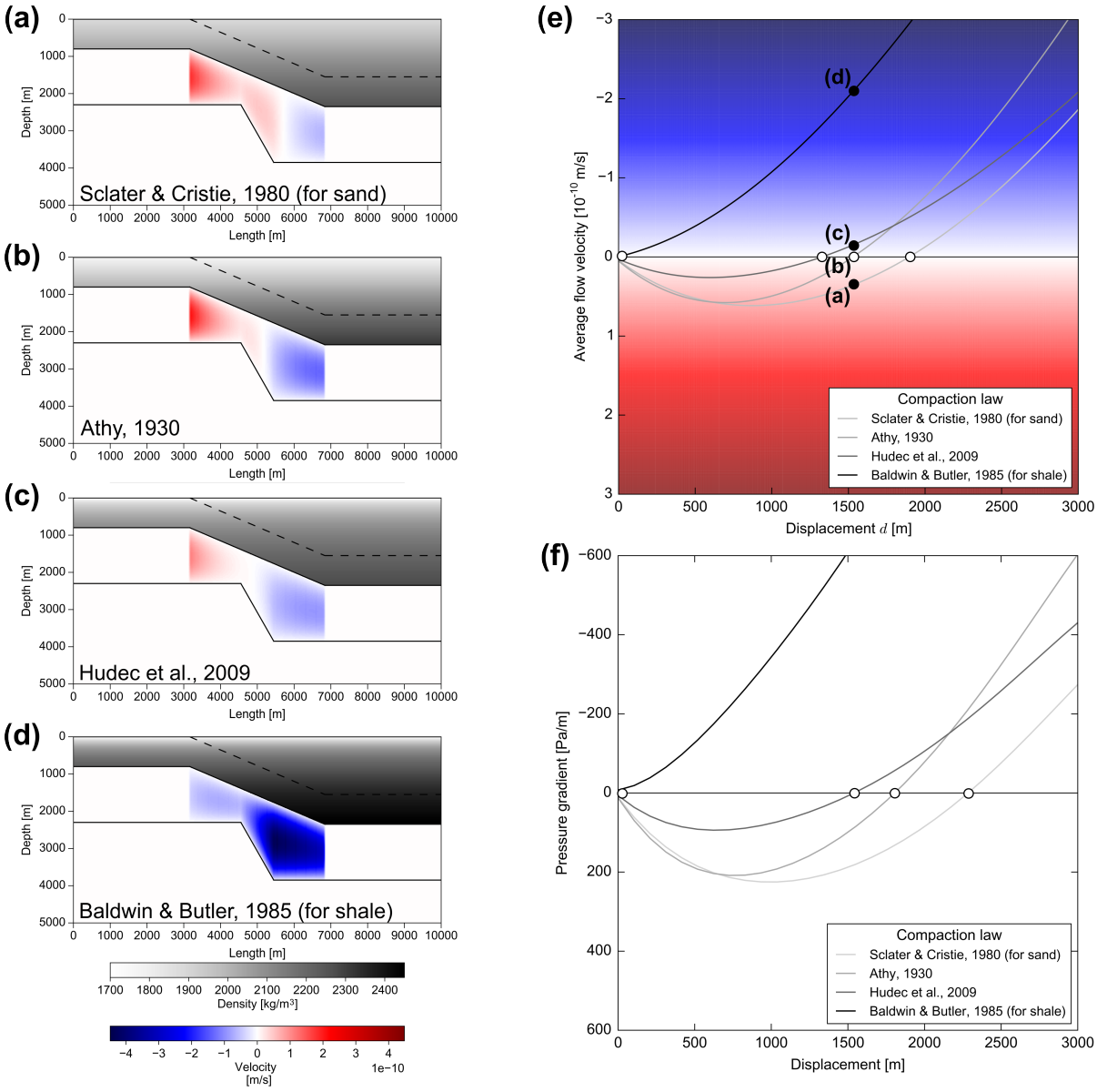

Figure 12. Comparison of the reference model with 3 models applying different compaction laws. The velocity field is illustrated for (a) Sclater & Christie (1980), (b) Athy (1930) (Reference model), (c) Hudec et al. (2009) and (d) Baldwin & Butler (1985). Curves of (e) illustrate the mean flow velocity and (f) the HHG versus offset at the basement fault for the applied compaction laws. White dots denote the Points of reversal (POR) and block dots the faults displacement applied in (a) to (d).

(Eq. 15) assumes an initial surface porosity of hundred percent and a porosity decline to zero at a depth of ~ 6000 m. This mimics very fast depth-related compaction in comparison with the other compaction laws, and causes an upwards directed material flow already at small vertical displacements (Fig. 12e).

PORs in our models occur much earlier than points at which minibasins subside buoyantly as proposed by Hudec et al. (2009). This is because Hudec et al. (2009) did not include pre-kinematic

layers on top of the salt. As we pointed out, a pre-kinematic layer contributes to the effective density of the cover layer, which is most important for triggering salt expulsion from beneath the minibasin.

Analytical calculations by Heidari et al. (2016) addressed the stress distribution and evolution in and around a rising salt dome. Stresses in the vertical salt dome column are balanced by the weight of the neighbouring minibasin. The latter is filled with sediments compacting according to Eq. 17. Their analytical solution demonstrated that (1) initiation of a dome structure from a flat lying salt layer and, therefore, upward salt flow from beneath a minibasin towards the crest of the dome requires only the density at the bottom of the minibasin (ρ_{Cmax}) to exceed the salt density, and (2) the salt dome is only able to reach the sedimentary surface if the average density of the neighbouring sediments ($\bar{\rho}_C$) are denser than salt on average.

Goteti et al. (2012) determined critical thicknesses of minibasins at which their density would be high enough to subside into a salt layer. In analytical models, isostatic equilibrium of an uneven sediment lens floating on a salt layer was calculated applying Athy's law (1930) with typical compaction parameters for sediments in the Gulf of Mexico region. The critical depths – these are equivalent to points of density inversion in our study – were calculated as 1900 m for carbonates (South Florida Basin), 2300 m for non-overpressured shale (Gulf of Mexico) and 2600 m for siliciclastics (Louisiana Upper Slope, Gulf of Mexico) presuming no pre-kinematic cover layer. These values are similar to PDIs of average cover densities in our models (mostly 1000 m to 3000 m; Table 2).

Based on numerical models, Goteti et al. (2012) concluded that no inversion of the average cover density is required to sustain autonomous minibasin subsidence, if sediments on top of the salt layer are unevenly distributed. Moreover, they found that even if cover sediment possesses a finite strength, uneven sedimentation can be sufficient to initiate minibasin subsidence and, therefore, salt flow upward into a neighbouring diapir.

The outcomes of these studies are supported by our models in which formation of a minibasin and initiation of salt flow are provoked by basement displacement instead of uneven sedimentation, but salt upward flow is induced before the average cover density surpasses the density of salt.

4.4 Applications

The variability of geometrical and rheological parameters is manifold in natural extensional salt basins, but in all basins listed in Table 1, post-salt normal faulting started under a relatively thin pre-kinematic cover layer of 0 to 1000 m. Our model results indicate that in all these basins, salt first flowed towards downthrown basin parts and subsequently upwards into evolving salt structures. The simplified models as outlined here can help to understand the timing at which salt tectonics started, i.e. when an extensionally induced minibasin was deep enough to drive uprise of salt structures. Furthermore, the

restoration of halokinetic sequences in such extensional basins can be improved, if cover lithology, state of compaction and composition of the salt layer are well known. During sequential restoration of the basin evolution, our models can estimate whether extensionally induced supra-salt minibasins are able to autonomously drive salt expulsion from underneath them towards elevated regions or still float on top of the salt layer because of insufficient compaction. One well-studied natural example is the Kłodawa salt diapir in the Mid-Polish Trough. Here, salt is suggested to have flown downward towards the subsiding basement block at the beginning of graben formation (Burliga 1996). Hence, subsidence in the graben centre was probably reduced, since salt partly filled the space created by fault displacement. Later, during increased fault displacement, salt flowed back into the evolving diapir (Burliga 1996). At this stage, the effective density of cover sediments in the basin centre was apparently high enough to drive upward flow increasing the amount of subsidence in the basin centre. Similar considerations should be taken into account in restorations of other salt-bearing extensional basins.

5 CONCLUSION

In the light of the presented models, we concluded that salt flow above an evolving normal fault and below a subsiding minibasin undergoes two stages under most geological conditions. First, salt moves downwards to the hanging wall side as long as vertical offset and compaction of the cover layer are small. As soon as the effective average density of the cover is exceeded, the direction of the hydraulic-head gradient reverses (point of reversal) and causes upward flow towards the footwall side. The point of reversal of the flow occurs earlier because of the geometry of the basement and related thickness of the salt layer. Our analytical model implies that upward flow can occur even if the average density of the overburden does not exceed the density of salt.

By testing several different geometrical and lithological parameters, our models suggest that the POR usually requires a cover thicknesses in the hanging wall minibasin between 700 and 2200 m. When the POR takes place, primarily depends on the thickness of the supra-salt cover layer and the density contrast between the salt and the cover. If the pre-kinematic overburden is thicker, the compaction of the cover increases faster with depth or the average salt density is smaller, the transition from downward to upward flow occurs at smaller fault displacements. Furthermore, the basin created by basement subsidence has to be continuously filled up with sediments for upward flow to be initiated. If the basin remains underfilled, i.e. the sedimentation rate is lower than the displacement rate, downward flow persists, because the pressure-head gradient cannot sufficiently increase to drive upward flow. Variations of the layer geometries, i.e. the width of the cover monocline, the dip of the basement fault and the thickness of the salt layer have no influence on the POR, but affect flow velocities.

Our simple analytical approach based on solving the Navier-Stokes equation provides a straightforward prediction for salt flow directions and maximum flow velocity. However, more advanced numerical models would be required to better understand the complex deformation mechanisms in a flowing salt layer by including e.g. elastic bending, brittle faulting, non-linear viscous flow of the salt, or variable sediment accumulation.

ACKNOWLEDGMENTS

We thank P. Methe, T. Jahr and A. Teixell for their ideas and comments on earlies versions of the manuscript.

REFERENCES

Allen, P. A. & Allen, J. R., 2013. *Basin analysis: principles and application to petroleum play assessment*, Wiley, New York, 642 pp, 3rd edn.

Alves, T. M., Gawthorpe, R. L., Hunt, D. W., & Monteiro, J. H., 2002. Jurassic tectono-sedimentary evolution of the Northern Lusitanian Basin (offshore Portugal), *Marine and Petroleum Geology*, **19**(6), 727–754.

Athy, L. F., 1930. Density, porosity, and compaction of sedimentary rocks, *AAPG Bulletin*, **14**(1), 1–24.

Baldwin, B. & Butler, C. O., 1985. Compaction curves, *AAPG bulletin*, **69**(4), 622–626.

Best, G., Kockel, F., & Schöneich, H., 1983. Geological history of the southern Horn Graben, in *Petroleum geology of the southeastern North Sea and the adjacent onshore areas (The Hague, 1982)*, vol. 62, pp. 25–33, eds Kaasschieter, J. P. H. & Reijers, T. J. A., Geol. Mijnbouw.

Buchanan, P. G., Bishop, D. J., & Hood, D. N., 1996. Development of salt-related structures in the central north sea: results from section balancing, *Geological Society, London, Special Publications*, **100**(1), 111–128.

Burliga, S., 1996. Kinematics within the Kłodawa salt diapir, central Poland, *Geological Society, London, Special Publications*, **100**(1), 11–21.

Burliga, S., Koyi, H. A., & Chemia, Z., 2012. Analogue and numerical modelling of salt supply to a diapiric structure rising above an active basement fault, *Geological Society, London, Special Publications*, **363**(1), 395–408.

Carter, N. L., Horseman, S. T., Russell, J. E., & Handin, J., 1993. Rheology of rocksalt, *Journal of Structural Geology*, **15**(9–10), 1257–1271.

Cartwright, J., Jackson, M., Dooley, T., & Higgins, S., 2012. Strain partitioning in gravity-driven shortening of a thick, multilayered evaporite sequence, in *Salt Tectonics, Sediments and Prospectivity*, vol. 363, pp. 449–470, eds Alsop, G. I., Archer, S. G., Hartley, A. J., Grant, N. T., & Hodgkinson, R., Geological Society of London.

Chemia, Z., Koyi, H., & Schmeling, H., 2008. Numerical modelling of rise and fall of a dense layer in salt diapirs, *Geophysical Journal International*, **172**(2), 798–816.

Cohen, H. A. & Hardy, S., 1996. Numerical modelling of stratal architectures resulting from differential loading of a mobile substrate, *Geological Society, London, Special Publications*, **100**(1), 265–273.

Dooley, T. P., McClay, K. R., & Pascoe, R., 2003. 3D analogue models of variable displacement extensional faults: applications to the Revfallet Fault system, offshore mid-Norway, *Geological Society, London, Special Publications*, **212**(1), 151–167.

Duffy, O. B., Gawthorpe, R. L., Docherty, M., & Brocklehurst, S. H., 2013. Mobile evaporite controls on the structural style and evolution of rift basins: Danish Central Graben, North Sea, *Basin Research*, **25**(3), 310–330.

Ferrer, O., Jackson, M., Roca, E., & Rubinat, M., 2012. Evolution of salt structures during extension and inversion of the Offshore Parentis Basin (Eastern Bay of Biscay), *Geological Society, London, Special Publications*, **363**(1), 361–380.

Ge, H., Jackson, M. P. A., & Vendeville, B. C., 1997. Kinematics and dynamics of salt tectonics driven by progradation, *AAPG Bulletin*, **81**(3), 398–423.

Ge, Z., Gawthorpe, R. L., Rotevatn, A., & Thomas, M. B., 2016. Impact of normal faulting and pre-rift salt tectonics on the structural style of salt-influenced rifts: The Late Jurassic Norwegian Central Graben, North Sea, *Basin Research*, pp. 1–5.

Geil, K., 1991. The development of salt structures in Denmark and adjacent areas: the role of basin floor dip and differential pressure, *First Break*, **9**(10), 467–483.

Geluk, M. C., 2005. *Stratigraphy and tectonics of Permo-Triassic basins in the Netherlands and surrounding areas*, Ph.D. thesis, Utrecht University, 171 pp.

Gemmer, L., Ings, S. J., Medvedev, S., & Beaumont, C., 2004. Salt tectonics driven by differential sediment loading: stability analysis and finite-element experiments, *Basin Research*, **16**(2), 199–218.

Goteti, R., Ings, S. J., & Beaumont, C., 2012. Development of salt minibasins initiated by sedimentary topographic relief, *Earth and Planetary Science Letters*, **339**, 103–116.

Heidari, M., Nikolinakou, M. A., Flemings, P. B., & Hudec, M. R., 2016. A simplified stress analysis of rising salt domes, *Basin Research*, pp. 1–14.

Hlaiem, A., 1999. Halokinesis and structural evolution of the major features in eastern and southern Tunisian Atlas, *Tectonophysics*, **306**(1), 79–95.

Hudec, M. R. & Jackson, M. P. A., 2007. Terra infirma: Understanding salt tectonics, *Earth-Science Reviews*, **82**(1), 1–28.

Hudec, M. R., Jackson, M. P. A., & Schultz-Ela, D. D., 2009. The Paradox of Minibasin Subsidence into Salt, *Geological Society of America Bulletin*, **121**(1/2), 201–221.

Jackson, M. P. A. & Talbot, C. J., 1986. External shapes, strain rates, and dynamics of salt structures, *Geological Society of America Bulletin*, **97**(3), 305–323.

Jackson, M. P. A. & Vendeville, B. C., 1994. Regional extension as a geologic trigger for diapirism, *Geological society of America bulletin*, **106**(1), 57–73.

Jackson, M. P. A., Cornelius, R. R., Craig, C. H., Gansser, A., Stöcklin, J., & Talbot, C. J., 1990. Salt diapirs

of the Great Kavir, central Iran, *Geological Society of America Memoirs*, **177**, 1–150.

Jensen, L. N. & Sørensen, K., 1992. Tectonic framework and halokinesis of the Nordkapp Basin, Barents Sea, *Structural and tectonic modelling and its application to petroleum geology. Norwegian Petroleum Society (NPF) Special Publication*, **1**, 109–120.

Kane, K. E., Jackson, C. A.-L., & Larsen, E., 2010. Normal fault growth and fault-related folding in a salt-influenced rift basin: South viking graben, offshore norway, *Journal of Structural Geology*, **32**(4), 490–506.

Kehle, R. O., 1988. The origin of salt structures, in *Evaporites and Hydrocarbons*, pp. 345–404, ed. Schreiber, B. C., Columbia University Press, New York.

Koyi, H., 1993. The effect of basement faulting on diapirism, *Journal of Petroleum Geology*, **16**(3), 285–312.

Koyi, H., Talbot, C. J., & Torudbakken, B. O., 1995. Salt tectonics in the northeastern Nordkapp Basin, southwestern Barents Sea, in *Salt tectonics: a global perspective*, vol. 65, pp. 437–447, eds Jackson, M. P. A., Roberts, D. G., & Snelson, S.

Krzywiec, P., 2004. Basement vs. salt tectonics and salt-sediment Interaction – case study of the Mesozoic evolution of the Intracontinental Mid-Polish Trough, in *GCSSEPM Foundation 24th Annual Research Conference: Salt-Sediment Interactions and Hydrocarbon Prospectivity: Concepts, Applications and Case Studies for the 21st Century*, pp. 5–8, SEPM.

Lehner, F. K., 2000. Approximate theory of substratum creep and associated overburden deformation in salt basins and deltas, in *Aspects of Tectonic Faulting*, pp. 21–47, Springer, Berlin, Heidelberg.

Li, S., Abe, S., Reuning, L., Becker, S., Urai, J. L., & Kukla, P. A., 2012. Numerical modelling of the displacement and deformation of embedded rock bodies during salt tectonics: A case study from the South Oman Salt Basin, *Geological Society, London, Special Publications*, **363**(1), 503–520.

Mandl, G., 1988. Mechanics of tectonic faulting: models and basic concepts, in *Developments in Structural Geology*, vol. 1, pp. 1–407, ed. Zwart, H. J.

Masrouhi, A., Bellier, O., & Koyi, H., 2014. Geometry and structural evolution of Lorbeus diapir, northwestern Tunisia: polyphase diapirism of the North African inverted passive margin, *International Journal of Earth Sciences*, **103**(3), 881–900.

Maystrenko, Y., Bayer, U., & Scheck-Wenderoth, M., 2005. Structure and evolution of the Glueckstadt Graben due to salt movements, *International Journal of Earth Sciences*, **94**(5-6), 799–814.

Maystrenko, Y. P., Bayer, U., & Scheck-Wenderoth, M., 2013. Salt as a 3D element in structural modeling – Example from the Central European Basin System, *Tectonophysics*, **591**, 62–82.

Nalpas, T. & Brun, J.-P., 1993. Salt flow and diapirism related to extension at crustal scale, *Tectonophysics*, **228**(3), 349–362.

Nilsen, K. T., Johansen, J. T., & Vendeville, B. C., 1996. Influence of regional tectonics on halokinesis in the Nordkapp Basin, Barents Sea, in *Salt tectonics: a global perspective*, vol. 65, pp. 413–436, eds Jackson, M. P. A., Roberts, D. G., & Snelson, S., AAPG Memoir.

Pascoe, R., Hooper, R., Storhaug, K., & Harper, H., 1999. Evolution of extensional styles at the southern termination of the Nordland Ridge, Mid-Norway: a response to variations in coupling above Triassic salt, in

Geological Society, London, Petroleum Geology Conference Series, vol. 5, pp. 83–90, Geological Society of London.

Peel, F. J., 2014. How do salt withdrawal minibasins form? Insights from forward modelling, and implications for hydrocarbon migration, *Tectonophysics*, **630**, 222–235.

Rasmussen, E. S., Lomholt, S., Andersen, C., & Vejbæk, O. V., 1998. Aspects of the structural evolution of the Lusitanian Basin in Portugal and the shelf and slope area offshore Portugal, *Tectonophysics*, **300**(1), 199–225.

Remmelts, G., 1995. Fault-related salt tectonics in the southern North Sea, the Netherlands, in *Salt tectonics: a global perspective*, vol. 65, pp. 261–272, eds Jackson, M. P. A., Roberts, D. G., & Snelson, S., AAPG Memoir.

Schultz-Ela, D. D., Jackson, M. P. A., & Vendeville, B. C., 1993. Mechanics of active salt diapirism, *Tectonophysics*, **228**(3), 275–312.

Sclater, J. G. & Christie, P. A. F., 1980. Continental stretching: An explanation of the post-mid-cretaceous subsidence of the central North Sea basin, *Journal of Geophysical Research: Solid Earth (1978–2012)*, **85**(B7), 3711–3739.

Stovba, S. M. & Stephenson, R. A., 2003. Style and timing of salt tectonics in the Dniepr-Donets Basin (Ukraine): implications for triggering and driving mechanisms of salt movement in sedimentary basins, *Marine and Petroleum Geology*, **19**(10), 1169–1189.

Tankard, A. J., Welsink, H. J., & Jenkins, W. A. M., 1989. Structural styles and stratigraphy of the Jeanne dArc Basin, Grand Banks of Newfoundland, *Extensional tectonics and stratigraphy of the North Atlantic margins: AAPG Memoir*, **46**, 265–282.

Tanveer, M. & Korstgård, J. A., 2009. Structural evolution of the Feda Graben area – A new model, *Marine and Petroleum Geology*, **26**(6), 990–999.

Ter Heege, J. H., De Bresser, J. H. P., & Spiers, C. J., 2005. Dynamic recrystallization of wet synthetic polycrystalline halite: dependence of grain size distribution on flow stress, temperature and strain, *Tectonophysics*, **396**(1), 35–57.

Turcotte, D. L. & Schubert, G., 2014. *Geodynamics*, Cambridge University Press, 623 pp, 3rd edn.

Urai, J. L., Spiers, C. J., Zwart, H. J., & Lister, G. S., 1986. Weakening of rock salt by water during long-term creep, *Nature*, **324**, 554–557.

Vackiner, A. A., Antrett, P., Strozyk, F., Back, S., Kukla, P., & Stollhofen, H., 2013. Salt kinematics and regional tectonics across a Permian gas field: a case study from East Frisia, NW Germany, *International Journal of Earth Sciences*, **102**(6), 1701–1716.

Van Gent, H., Urai, J. L., & De Keijzer, M., 2011. The internal geometry of salt structures – A first look using 3D seismic data from the Zechstein of the Netherlands, *Journal of Structural Geology*, **33**(3), 292–311.

Van Keken, P. E., Spiers, C. J., Van den Berg, A. P., & Muyzert, E. J., 1993. The effective viscosity of rocksalt: implementation of steady-state creep laws in numerical models of salt diapirism, *Tectonophysics*, **225**(4), 457–476.

Vendeville, B. C. & Jackson, M. P. A., 1992. The rise of diapirs during thin-skinned extension, *Marine and Petroleum Geology*, **9**(4), 331–354.

Vendeville, B. C., Ge, H., & Jackson, M. P. A., 1995. Scale models of salt tectonics during basement-involved extension, *Petroleum Geoscience*, **1**(2), 179–183.

Wagner, B. H. & Jackson, M. P. A., 2011. Viscous flow during salt welding, *Tectonophysics*, **510**(3), 309–326.

Wagner, R., Leszczyński, K., Pokorski, J., & Gumulak, K., 2002. Palaeotectonic cross-sections through the Mid-Polish Trough, *Geological Quarterly*, **46**(3), 293–306.

Waltham, D., 1997. Why does salt start to move?, *Tectonophysics*, **282**(1), 117–128.

Warsitzka, M., Kley, J., & Kukowski, N., 2015. Analogue experiments of salt flow and pillow growth due to basement faulting and differential loading, *Solid Earth*, **6**(1), 9–31.

Weijermars, R. & Jackson, M. P. A., 2014. Predicting the depth of viscous stress peaks in moving salt sheets: Conceptual framework and implications for drilling, *AAPG Bulletin*, **98**(5), 911–945.

Weijermars, R., Jackson, M. P. A., & Vendeville, B. C., 1993. Rheological and tectonic modeling of salt provinces, *Tectonophysics*, **217**(1), 143–174.

White, F. M., 2011. *Fluid Mechanics*, New York, McGraw Hill, 864 pp, 7th edn.

Withjack, M. O. & Callaway, S., 2000. Active normal faulting beneath a salt layer: an experimental study of deformation patterns in the cover sequence, *AAPG Bulletin*, **84**(5), 627–651.

Wong, T. E., Batjes, D. A., de Jager, J., & van Wetenschappen, K. N. A., 2007. *Geology of the Netherlands*, Amsterdam : Royal Netherlands Academy of Arts and Sciences, 354 pp.

6. Synthesis

In this thesis, kinematics and dynamics of extensionally driven salt flow and consequent syn-kinematic overburden structures have been investigated by means of 2D retro-deformation, analogue modelling and analytical computations. Main outcomes of the individual Chapters 2 – 5 are summarised and reflected in this synthesis. Then, the reliability and the scope of application of each method used in this thesis is tested by applying the analytical computation (see Chapter 5) to geological and experimental examples presented in Chapter 3 and Chapter 4. Scenarios of salt flow evolution in different types of extensional basins are ultimately described based on the main outcomes of this thesis and mostly oriented at geological conditions of the Central European Basins System. At the end, a perspective is given to point out future directions of investigating salt flow in an extensional tectonic setting.

6.1 Summary and main outcomes

Chapter 2: The literature-based age analysis of salt structures in the Southern Permian Basin (Central Europe) reveals that a significant amount of salt structures started to rise in extensional sub-basins and along sub-salt fault zones during the Early and Middle Triassic and, thus in the first $\sim$15 Myrs after deposition of the Upper Permian salt. During the Late Triassic and the Jurassic, many of these extant salt structures reached their phase of fastest growth coinciding with phases of extensional tectonics in the sub-basins. These relationships confirm that basement-involved extensional deformation was the dominant trigger and driver for salt movement in the Southern Permian Basin. Besides insights into the dynamics of salt structures, the temporal patterns of activated or reactivated salt structures highlight tectonically active basin parts and help to correlate salt structure activity to the potential tectonic stress field.

Chapter 3 (Manuscript #1): In this chapter, 2D retro-deformation was performed on a key geological cross section of the Glückstadt Graben (central Southern Permian Basin) in order to understand the geometry and spatial evolution of supra-salt peripheral sinks forming in extensional basins. The structural evolution can be broadly outlined as follows: (1) a symmetric minibasin (central hanging wall peripheral sink) formed in the graben centre in response to differential basement subsidence during the Early Triassic. Additionally, extension of the supra-salt cover above the platform regions led to thinning and weakening of the overburden. The central peripheral sink and the thinned cover induced differential loading on the salt layer causing the formation of reactive diapirs or salt pillows, respectively. (2) At the beginning of the Keuper time, strong diapirism and the structural change to secondary peripheral sinks adjacent to the innermost salt structures of the graben was initiated by another phase of regional extension. (3) Protracted downbuilding of diapirs took place during

different time periods of the graben evolution. Thereby, the age of the downbuilding phase became progressively younger from the graben centre towards its flanks, which can be deduced from a gradual shift of the depocentres in the secondary peripheral sinks. This shift was occasionally accelerated and reactivated by discrete tectonic events and completed with the formation of marginal salt pillows during the latest period from the Late Cretaceous throughout the Cenozoic.

Similar early-stage structures, such as the central hanging wall peripheral sink or detached peripheral sinks above the footwall sides, have been recognised in many other extensional basins, e.g. in the Central Graben (Korstgård et al., 1993; Stewart et al., 1996; Wong et al., 2007), in the Horn Graben (Best et al., 1983), in the Feda Graben (Tanveer and Korstgård, 2009), or in the Mid-Polish Trough (Krzywiec, 2004a). For this reason, these structures can be regarded as characteristic features of salt-bearing extensional basins. In contrast, such a long-lasting sequence of outward migrating depocentres in secondary peripheral sinks can hardly be found in other extensional basins. Probably, the exceptionally high original thickness of the salt layer and the almost continuous subsidence from the Triassic to the present are responsible for this evolution in the Glückstadt Graben.

Chapter 4 (Manuscript #2): In this study, flow patterns in a viscous layer and the development of syn-kinematic structures in the overburden occurring during basement normal faulting were simulated in scaled analogue experiments. Four evolutionary phases of the flow pattern are deduced from the experiments: (1) during basement displacement, viscous material is affected by Couette shear flow induced by laterally moving basement blocks. Additionally, Poiseuille-type flow from the footwall blocks downward to the downthrown block occurs directly above the tip of the basement fault. (2) After the end of extension, downward material flow continues in a wide region above the basement faults. (3) Due to accumulation of sandy material in the hanging wall peripheral sink, the direction of the Poiseuille-type flow returns, i.e. the ductile material is squeezed from the downthrown block to the footwall blocks. Consequently, viscous material accumulates on the platform leading to the formation of pillow-like structures (“primary pillows“). (4) After further phases of sediment accumulation, depocentres at the outer side of the pillow structures develop (away from the hanging wall peripheral sink) causing material expulsion away from the primary pillows and towards a second generation of pillow-like structures (“secondary pillows“).

In a series of experiments, the thickness of the cover layer, the thickness of the ductile layer and the displacement rate of the basement faults were systematically varied. This series reveals that the zone affected by viscous flow above the fault tip is wider when: the viscous layer is thicker, or if the basement displacement is slower. Flow velocities in the viscous layer above the basement fault tip are higher when: the viscous layer is thicker, the overburden layer is thinner, or the basement displacement is faster.

The systematic examination undertaken in the analogue modelling study provides fundamental understanding of flow patterns in a ductile layer above a basement normal fault, which can otherwise not be observed or retraced in nature. The particle imaging velocimetry technique applied in the experiments also improves the strain analysis in salt tectonic experiments by directly monitoring ductile flow patterns. In the future, this application might increase outcomes of experimental studies using

coloured silicone oil to visualise the finite stage of ductile deformation (e.g. Nalpas and Brun, 1993; Dooley et al., 2009; Burliga et al., 2012).

Chapter 5 (Manuscript #3): The analytical computations performed in this chapter are applied to determine direction and velocity of salt movement evolving above a sub-salt normal fault. The steady-state velocity field in the salt layer is incrementally calculated for a stepwise increasing displacement of the sub-salt fault. In a series of models, calculations were conducted for varying initial thicknesses of the salt layer and the cover layer, syn-kinematic filling of the depocentre above the downthrown block (hanging wall peripheral sink), fault and cover geometries, salt densities and viscosities as well as compaction parameters of the cover.

The model outcomes suggest that under most geological conditions, two stages of salt flow above an evolving basement normal fault occur: (1) salt moves downwards to the hanging wall side as long as compaction of the cover layer and, therefore, the pressure-head gradient is small. (2) As soon as an "effective density" of the cover is exceeded, the pressure-head gradient (due to differential loading) overcomes the elevation-head gradient (due to tilting of the salt layer) and the flow directions turns from downward to upward flow.

The results of the sensitivity study enable identifying specific geological thresholds at which salt flow above the sub-salt fault changes from downward to upward direction. They imply that upward flow occurs when: the fault displacement is large enough, the sedimentation rate can keep pace with fault displacement rate, the pre-extensional thickness of the cover is large or the cover sediments compact fast with depth. Overall, the analytical computation is a simple, but effective method to comprehend conditions under which salt structures close to a sub-salt normal fault are initiated. Furthermore, on the basis of the velocity field, a rough approximation of the magnitude and the location of stress peaks and shear zones in salt bodies can be deduced. Identifying such regions is important for assessing well bore stresses during drilling campaigns through salt bodies (Weijermars et al., 2014) or for the calculation of the in-situ stress field in geomechanical modelling of salt mines or intra-salt storage sites.

Main outcomes: In the light of the initially formulated aims addressing the intra-salt deformation and syn-kinematic sediment accumulation induced by basement faulting, the main outcomes of this thesis are:

1. Due to sub-salt normal faulting in a salt-bearing extensional basin, a deep primary peripheral sink develops directly above the downthrown basement block, which is bounded by primary salt pillows or reactive diapirs. Additionally, minor peripheral sinks and related salt pillows or reactive diapirs form above the platform coevally or delayed to the primary salt structures.
2. During initiation of an extensional basin, salt first flows downward because of an elevation-head gradient. During progressive fault displacement, salt flow changes to upward flow because of a now dominating pressure-head gradient. The flow patterns above the basement normal fault are characterised by a combination of channelised Poiseuille flow and Couette flow during basement extension and by pure Poiseuille flow after the end of extension.

3. A reversal of salt flow above a sub-salt normal fault can be suggested to occur in all salt-bearing extensional basins that subsided sufficiently deep. The timing of the reversal as well as the flow velocity in the salt layer are mainly governed by the compaction behaviour (average density), the thickness of the supra-salt cover above the downthrown side and the density of the salt.

6.2 Applicability of the model results

In this section, analytical computations of Chapter 5 are applied to structures observed in Chapter 3 and Chapter 4 in order to address the question how results found in this thesis can be validated and translated to nature? In Fig. 6.1, velocity distributions and shear strain patterns deduced from the PIV-analysis of an analogue experiment (Fig. 4.7 – Fig. 4.9) are compared to analytical models implementing reconstructed cross sections from the same experiment (Fig. 4.5) into the computation procedure. Both methods, the PIV-analysis (Fig. 6.1A) and the analytical calculations (Fig. 6.1B), reveal a similar distribution of the flow patterns. These include an early stage of downward flow (red) and a subsequent stage of upward flow (blue), whereby downward flow velocities are higher than upward flow velocities. The shear strain (rate) patterns consistently demonstrate that strongest shearing occurs at the upper and the lower boundaries of the viscous layer (Fig. 6.1B/C).

However, the regions in which the material movement act, are smaller and the absolute flow velocities are about one order of magnitude higher in the analytical calculations. The first phenomenon occurs because the hydraulic-head gradient only acts in regions in which the top of the salt layer and the thickness of the cover changes laterally. In contrast, the actual material flow observed in the analogue experiments reflects the dynamic material redistribution including deflation on the hanging wall side and inflation on the footwall side. Differences of the flow velocity result from two reasons: (1) the strength of the analogous cover layer is not included in the analytical calculations. (2) The PIV-technique detects material movement at the frontal glass wall, whereas the analytical calculations are undertaken for a cross section passing through the centre of the experimental box. Owing to boundary friction, flow velocities at the glass walls are smaller than those in the middle of the box.

The observed overburden structures in the final stage of the analogue experiments are comparable to the restored early minibasins in the Glückstadt Graben presented in Chapter 3 indicating the similarity of flow patterns between both examples. Fig. 6.2 illustrates analytical computations of the velocity field with implementing reconstructed overburden layers of an early-stage salt pillow of the Glückstadt Graben (Fig. 3.10). In stage I, the cover layer (Lower to lower Middle Buntsandstein, $\sim$800 to 1300 m) is insufficiently compacted resulting in downward flow (blue). In stage II, the pressure-head gradient induced by the central (hanging wall) peripheral sink (CPS) is large enough to trigger upward directed flow, i.e. the average between upward flow velocity (red, positive) and downward flow velocity (blue, negative) is positive. The oppositely directed flow beneath the crest of the pillow is because of the lower density of the overburden above the pillow top. In stage III, material influx from the outer side of the pillow starts. The amounts of the flow velocity differ by a factor of 20 with a maximum velocity of 20×10^{-10} m s^{-1} ($\sim$6 cm yr^{-1}) and a maximum strain rate of $\sim 2 \times 10^{-12}$ s^{-1}. Similarly high displacement rates of about 10 cm yr^{-1} are only recorded from passive

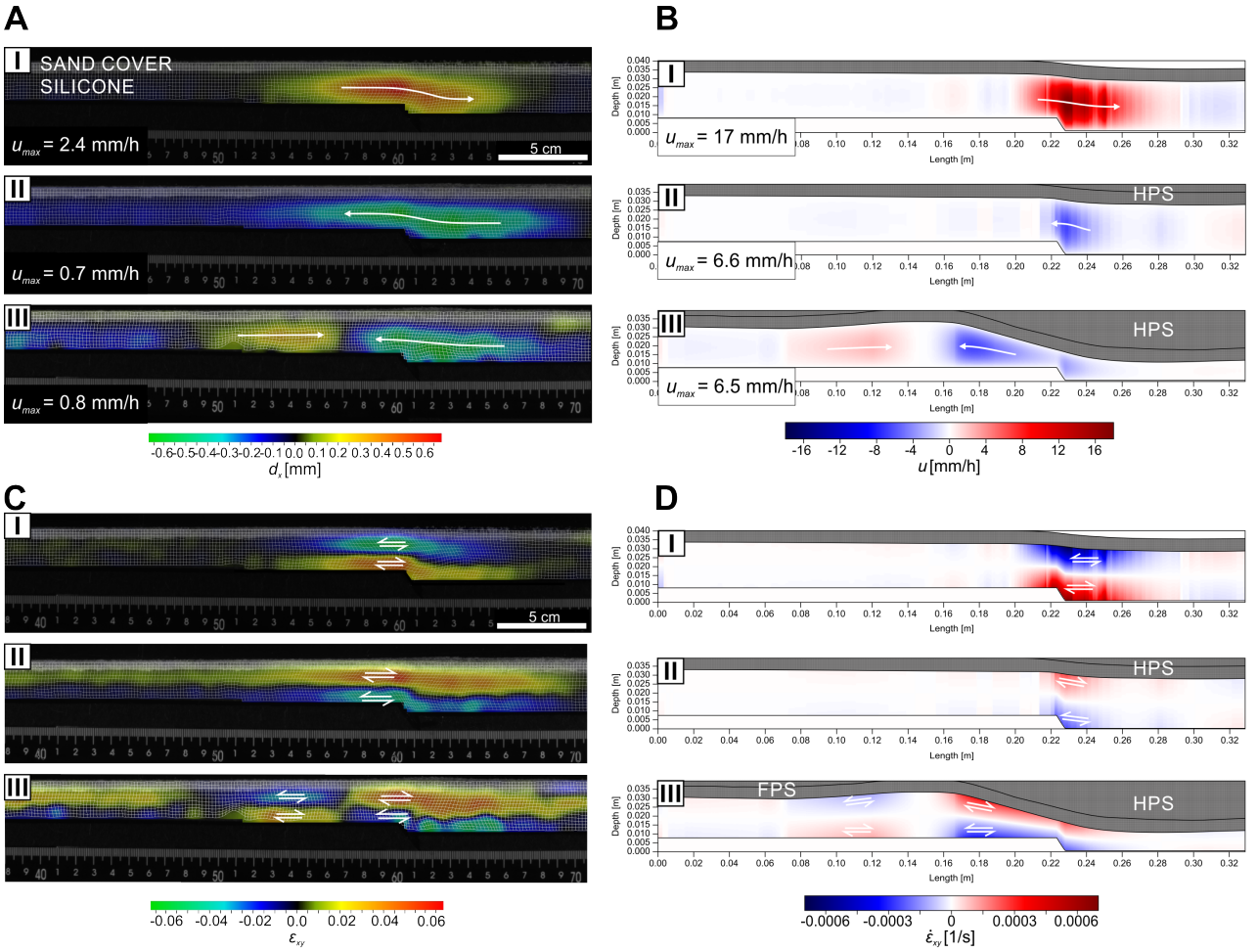

Figure 6.1: Comparison between flow patterns in a viscous layer in an analogue experiment (Fig. 4.7; Fig. 4.8; Fig. 4.9) and the analytical computation (Chapter 5) of the same configuration. **A** shows amounts of the horizontal displacement d_x and the deformation grid of the material flow in the analogue experiment Exp. 1b. **B** shows amounts of the horizontal velocity u of the analytical computations. **C** displays the shear strain ϵ_{xy} calculated by the derivation of the horizontal displacement over the vertical z-axis. **D** displays the shear strain rate $\dot{\epsilon}_{xy}$ calculated by the derivation of the horizontal velocity over the vertical z-axis. Physical properties of silicone putty (density = 970 kg m^{-3}, viscosity = 2.32 $\times$ 10^4 Pa s) and a granular mixture of 1:1 Quartz sand and PVC beads (density = 1330 kg m^{-3}) as well as the layer geometries of the analogue experiment Exp. 1b (Fig. 4.5) are implemented in the analytical model. During stage I, the minibasin above the downthrown block is unfilled resulting in downward (rightward) flow. After filling the hanging wall peripheral sink (HPS) with additional sand (stage II), the viscous material is pushed upward (leftward) towards the footwall block. After further phases of syn-kinematic sand accumulation (stage III), viscous material flows into a developed pillow structure from the HPS and the footwall peripheral sink (FPS). The maximal displacement rates u_{max} are roughly 10 times higher in the analytical calculations than in the analogue experiments. The arrows denote material movement and shearing in the viscous layer.

margin salt tectonics (Weijermars et al., 2014). These exceptionally high strain rates calculated here result from the large amount of differential loading imposed by the ~6000 m deep CPS and from not considering the strength of the overburden in the calculations.

Although the simplicity of the analytical computation presented here (e.g. homogeneous, simplified rheologies) limits its application to realistic geological scenarios, the two presented examples demonstrate acceptable estimations of material flow directions only by implementing salt layer boundaries and overburden lithology. Applying this procedure can help to deduce if and at which time tectonically induced depocentres were deep enough to drive the growth of adjacent salt structures.

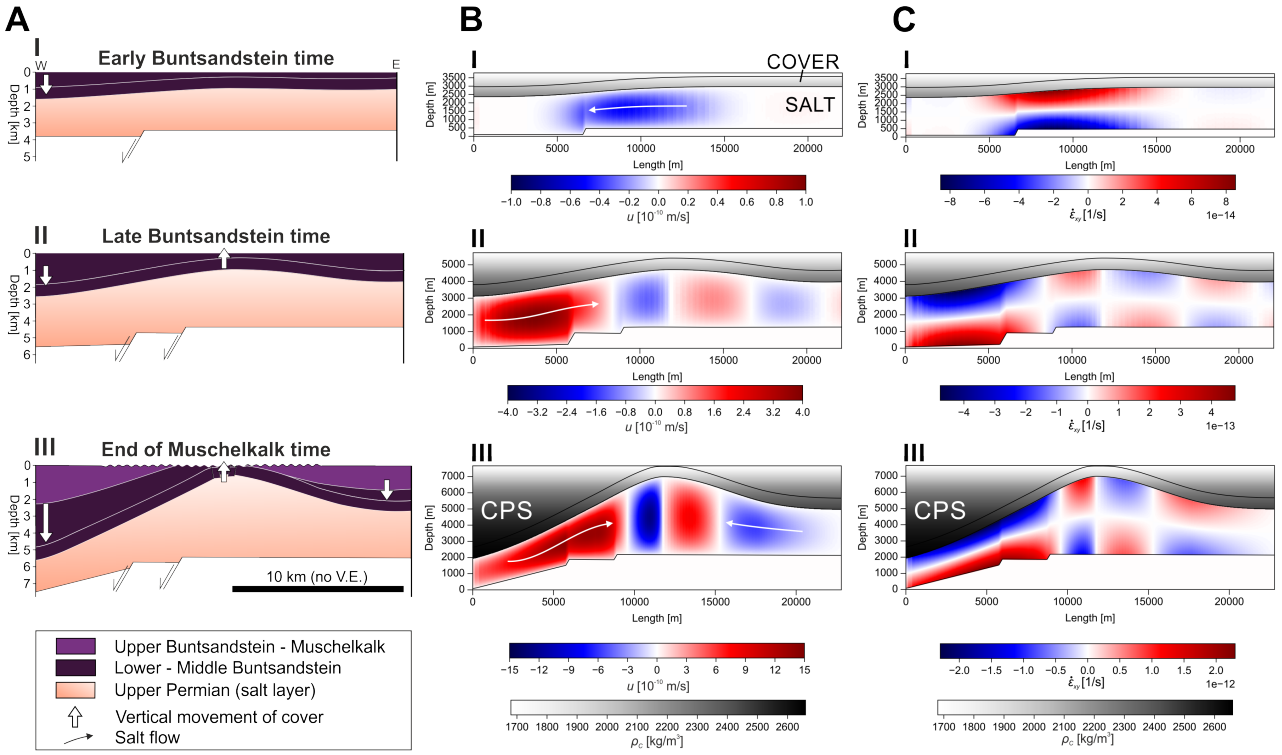

Figure 6.2: Application of the analytical computations (Chapter 5) to a reconstructed salt pillow of the Glückstadt Graben (Chapter 3). **A** The reconstruction was produced from a cross section shown in Fig. 3.10 applying decompaction and vertical simple shear restoration (2DMOVE^{TM}) of the supra-salt cover layers. It displays the initial stages of a salt pillow, which was triggered by sub-salt normal faulting. **B** shows the horizontal velocity u and the density of the overburden ρ_C calculated with the analytical computation by implementing the geological cross sections of A. In the computations, shale as cover lithology, a salt density of $\rho_S = 2200\,\mathrm{kg\,m^{-3}}$ and a salt viscosity of $\eta = 1 \times 10^{18}\,\mathrm{Pa\,s}$ was applied. **C** shows patterns of the shear strain rate $\dot{\epsilon}_{xy}$ calculated by the derivation of the horizontal velocity over the vertical z-axis. After the beginning (stage I), the salt moves down towards the basin centre. During further basement displacement and deeper subsidence of the central peripheral sink (stage II+III), salt is squeezed upward towards the pillow crest. Highest shear strain rates occur close to the top and the base of the salt layer. Note the different scales of the flow velocities.

6.3 Scenarios of early-stage salt flow in extensional basins

On the basis of the outcomes of this thesis, scenarios for the early-stage salt flow evolution in extensional basins are described for various examples of the Southern and the Northern Permian Basin; both basins are parts of the Central European Basin System (CEBS) (e.g. Maystrenko et al., 2013). Numerous phases of extensional tectonics took place in different basin parts and periods in the CEBS (Chapter 2). Hence, initial geological conditions during salt mobilisation were different in terms of original salt layer thickness, pre-kinematic overburden thickness, fault displacements and strain rates (see Table 5.1).

6.3.1 Early-stage downward flow

In most parts of the CEBS, pronounced rifting and salt movement commenced in the Early Triassic (∼Middle Buntsandstein) (see Chapter 2 and references therein). The pre-kinematic thickness (Lower Buntsandstein) varied between ∼200 m in marginal parts of the CEBS and up to 800 m in the

basin centre (Doornenbal and Stevenson, 2010). The analytical computation presented in Chapter 5 predict that the compaction of Lower Buntsandstein sediments, which are dominated by siliciclastics (sandstones, mudstones), was not sufficient to drive upward flow at this stage (see e.g. Fig. 6.2). Therefore, early-stage basin stretching was most likely accompanied by salt movement towards the centres of the sub-basins. Indications for early downward flow above an extensionally faulted basement are reported on the northern segment of the Central Graben (Northern Permian Basins) (Roberts et al., 1990; Erratt, 1993) and the Egersund Basin (Norwegian North Sea) (Tvedt et al., 2013) based on conceptual reconstructions, on the Kłodawa salt diapir in the central Mid-Polish Trough based on salt mine outcrop data (Burliga, 1996), and on fault zones in the Outer Moray Firth Basin (northern North Sea) based on 3D-seismic data of intra-salt structures (Clark et al., 1998). Such examples provide clues for the general occurrence of early-stage downward flow. Yet, indications for early-stage downward flow can hardly be found in most extensional basins, because: (1) intra-salt structures were mostly overprinted by subsequent phases of salt flow; (2) deformation in the cover is often only manifested in reduced subsidence in the basin centre due to salt redistribution (Chapter 4), which is also overprinted by following phase of salt flow; and (3) in many sub-basins, early-stage deformation structures are deeply subsided today impeding examinations by detailed seismic and well data (e.g. Glückstadt Graben, Horn Graben). Nevertheless, the process of early-stage downward flow has to be further studied in salt-bearing extensional basins because of its importance for the subsequent basin evolution. The analogue and analytical models presented in this thesis show that downward flow rates are generally higher then subsequent upward flow rates. At least during relatively slow basement extension, downward salt flow might buffer fault-related subsidence in the basin centre and probably hide or underestimate early phases of tectonic fault movements.

6.3.2 Upward flow dominated basins

The structural development subsequent to the Early Triassic initiation significantly differs between the sub-basins of the CEBS. With respect to initial geological conditions, the Glückstadt Graben, the Horn Graben and the Mid-Polish Trough represent sub-basins characterised by a very large original salt layer thickness (1500 – 3000 m), large fault offsets (2000 – 4000 m), a narrow and deep shape of the initial basin, and high strain rates of the Early Triassic faults (Vejbæk, 1990; Maystrenko et al., 2005a; Krzywiec, 2012). The latter can be inferred from deeply subsided hanging wall peripheral sinks containing thick successions of Early Triassic sediments accumulated in roughly 5 Myrs, precisely ∼3500 m in the Glückstadt Graben (see Fig. 3.5), ∼4000 m in the Horn Graben (Baldschuhn et al., 2001), and ∼2000 m in the Mid-Polish Trough (Dadlez, 2003)). It can be suggested that during this rapid basement faulting combined with syn-kinematic sediment accumulation, the period of downward Poiseuille-type flow was short or completely absent. In fact, sediment compaction in the hanging wall peripheral sinks and consequent differential loading were sufficient to induce upward flow throughout the Early Triassic, which is confirmed by the presence of salt pillows and reactive diapirs (Best et al., 1983; Krzywiec, 2004b; Warsitzka et al., 2017). The large thickness of the salt layer in these sub-basins facilitated high flow velocities (see Fig. 4.11) and, therefore, rapid growth of salt structures from the Early Triassic onward. Consequently, diapirs in these basins passed through

their phase of fastest growth already at the beginning of the middle Late Triassic (Fig. 2.2).

A similar structural development of fault-bounded salt structures is observed in other sub-basins of the CEBS, e.g. in the southern and central segment of the Central Graben (Baldschuhn et al., 2001; Wong et al., 2007; Duffy et al., 2013), in the Feda-Graben (Central North Sea) (Tanveer and Korstgård, 2009) and the Braunschweig-Gifhorn fault zone (Fig. C.2) (Baldschuhn et al., 2001; Vackiner et al., 2013). However, the phase of main salt structure growth in these sub-basins was significantly delayed from Early Triassic basin initiation. During the Triassic, only low-amplitude salt structures rose until strong salt structure growth started in the Jurassic (see Fig. 2.2). On the basis of the results of our analogue and analytical models, this evolution can be interpreted as follows: during Triassic basin initiation, relatively slow fault-related subsidence induced a shallow hanging wall peripheral sink (e.g. $\sim$1500 m in the Braunschweig-Gifhorn fault zone (Baldschuhn et al., 2001); $\sim$1000 m in the central Central Graben, (Duffy et al., 2013)) and, therefore, a pressure-head gradient that was only slightly larger than its opposing elevation-head gradient. Moreover, the original salt layer thickness in these sub-basins was comparatively small (750 – 1500 m; see Table 5.1 and references therein), which further limited flow velocities (see Fig. 4.11). For these reasons, slow, upward-directed salt flow and consequent slow rise of salt pillows occurred. Renewed extensional tectonics in Late Keuper – Jurassic times (e.g. Tanveer and Korstgård, 2009; Wong et al., 2007; Duffy et al., 2013; Vackiner et al., 2013) then caused an increased pressure-head gradient due to deepening of the central peripheral sinks and weakening of the supra-salt cover (see Fig. 4.5). Consequently, fast upward flow into emerging diapirs took place.

Outside the CEBS, other examples of salt structures potentially triggered by sub-salt normal faulting and the subsidence of a hanging wall peripheral sink are documented e.g. for the Atlas Basin (Tunisia) (Masrouhi et al., 2014), for the Dniepr-Donets Basin (Ukraine) (Stovba and Stephenson, 2003), or for the Sverdrup Basin (Northern Canada) (Stephenson et al., 1992). However, only few sufficiently detailed investigations of salt tectonics and published geological cross sections exist for these basins making it difficult to discuss the salt flow evolution for these cases.

6.3.3 Downward flow dominated basins

Different from the previous basin type, downward flow dominated basins in the CEBS are rather characterised by small initial fault displacements in combination with a relatively wide initial basin shape. Thicknesses of the original salt layer (1000 – 1500 m) and the pre-kinematic layer ($\sim$500 m) were similar compared to upward flow dominated sub-basins. Examples from the CEBS are the northern segment of the Central Graben (Stewart and Clark, 1999), the Egersund Basin (Tvedt et al., 2013), the Ems Trough (Mohr et al., 2005), the Norwegian-Danish Basin (Geil, 1991), and the Silver Pit Basin/ Sole Pit Trough (Griffiths et al., 1995). At the western edge of the Ems Trough, it is suggested that gravitational downward gliding of overburden sediments (termed "rafting") took place during Early – Middle Buntsandstein times coinciding with the growth of salt pillows in the basin centre (Thieme and Rockenbauch, 2001; Mohr et al., 2005; Vackiner et al., 2013). The Triassic evolution of the Silver Pit Basin/ Sole Pit Trough and the Egersund basin was characterised by the

formation of small grabens and listric growth faults in the supra-salt overburden at the basin edges and buckled salt pillows in the centre of these half-graben basins (Griffiths et al., 1995; Tvedt et al., 2013). On the tilted graben flanks of the northern Central Graben (UK North Sea), rollovers and salt rollers (sensu Hudec and Jackson, 2011) can be observed, which are suggested to have been formed by rafting and detached extension from basin-centre normal faults (Penge et al., 1999) coeval to the growth of large diapirs in the graben centre (Stewart and Clark, 1999). Similar structural features were identified in the Norwegian-Danish Basin. Furthermore, a similar structural development can be supposed for several other world-wide extensional basins based on geological cross sections and description in the literature, e.g. the East Texas Basin (Seni and Jackson, 1983), the Ghaba salt basin (Oman) (Peters et al., 2003), the Nordkapp Basin (Barents Sea) (Nilsen et al., 1996), and the Red Sea basin (Heaton et al., 1995).

In all these basins, the early-stage structural evolution can be attributed to the gravitational collapse of the supra-salt cover (e.g. Coward and Stewart, 1995; Tvedt et al., 2013) and, thus, to regional, basinward directed salt flow. At least in the sub-basins of the CEBS, the wide shape of the sub-basin and the relatively small initial, extensionally driven subsidence during the Early – Middle Triassic reduced the formation of a deeply subsided hanging wall peripheral sink and, therefore, the effectiveness of the pressure-head gradient (Chapter 5). Probably, sediment accumulation rates were low and centres of these basin remained underfilled. Both facts, the slope of the bowl-shaped basin floor and the underfilled basin centre potentially result in a widespread dominance of the elevation-head gradient superimposing local hydraulic-head gradients induced by basement faulting. When overburden thickness and density became larger during the following basin evolution (post-Middle Triassic), salt flow in these downward flow dominated basins was localised in pillows and diapirs emerged between the cover rafts or from the buckled salt pillows (e.g. Geil, 1991; Mohr et al., 2005).

In summary, the main differences between upward and downward flow dominated basins seem to be the basin shape, which is narrow and deep in the first case and wide and shallow in the second, as well as the early-stage extension rates and probably the sediment accumulation rates, which are high in the first case and relatively low in the second. A detailed explanation of the superimposing effects of regional and local scale hydraulic-head gradients on salt flow dynamics is beyond the scope of this thesis. However, since this potentially important effect has not been examined yet, it is a prime target for future research.

6.4 Perspectives

The simplified experiments and models presented in this thesis can coarsely approximate deformation patterns in natural salt successions. Nevertheless, to provide more sophisticated predictions of strain patterns and salt flow dynamics of complex layering and boundary conditions, future work should address the following subjects:

- The presented experimental and analytical model studies should be complemented by numerical modelling that simulates dynamic interactions between salt flow and the vertical adjustment of a

compacting cover layer. The models should include a more complex rheology of the cover (e.g. elasto-plastic behaviour) and the salt layer (e.g. Non-Newtonian viscosity, vertical stratification) as well as shear stresses imposed on the upper and the lower boundary of the salt layer.

- It should be investigated if the process of early downward flow and subsequent upward flow in salt layers above a differentially subsiding basement might also be relevant for salt flow in an entire intra-continental basin of >100 km in size. Depending on the basin shape, the ratio between subsidence rate of the rather symmetric basin floor and sediment aggradation rate, two scenarios are imaginable: (1) as described above, gravity gliding of the salt layer and its overburden towards the basin centre is initiated, a processes occurring in salt-bearing passive margin basins (e.g. Brun and Fort, 2011). (2) Similar to salt flow in smaller scale extensional basins, gravity spreading of salt from the basin centre towards the basin edges can be triggered by differential loading. Numerical simulations of 3D redistribution of Permian salt in the Northeast German Basin by Scheck et al. (2003a) allow the conclusion that such process took place there.

References

Al Hseinat, M., Hübscher, C., Lang, J., Lüdmann, T., Ott, I., and Polom, U., 2016. Triassic to recent tectonic evolution of a crestal collapse graben above a salt-cored anticline in the Glückstadt Graben/North German Basin. *Tectonophysics*, 680:50–66. doi:http://dx.doi.org/10.1016/j.tecto.2016.05.008.

Allen, J. and Beaumont, C., 2012. Impact of inconsistent density scaling on physical analogue models of continental margin scale salt tectonics. *Journal of Geophysical Research: Solid Earth*, 117(B8). doi:http://dx.doi.org/10.1029/2012JB009227.

Allen, M. R., Griffiths, P. A., Craig, J., Fitches, W. R., and Whittington, R. J., 1994. Halokinetic initiation of Mesozoic tectonics in the southern North Sea: a regional model. *Geological Magazine*, 131(04):559–561. doi:https://doi.org/10.1017/S0016756800012164.

Arfai, J., Jähne, F., Lutz, R., Franke, D., Gaedicke, C., and Kley, J., 2014. Late palaeozoic to early cenozoic geological evolution of the northwestern german north sea (Entenschnabel): new results and insights. *Netherlands Journal of Geosciences-Geologie en Mijnbouw*, 93(04):147–174. doi:https://doi.org/10.1017/njg.2014.22.

Arrhenius, S. and Lachmann, R., 1912. Die physikalisch-chemischen Bedingungen bei der Bildung der Salzlagerstätten und ihre Anwendung auf geologische Probleme. *Geologische Rundschau*, 3(3):139–157. doi:http://dx.doi.org/10.1007/BF0180198.

Baldschuhn, R. and Kockel, F., 1998. Der Untergrund von Hannover und seiner Umgebung. *Berichte der Naturhistorischen Gesellschaft*, 140:5–98.

Baldschuhn, R., Best, G., and Kockel, F., 1991. Inversion tectonics in the north-west German basin. In: Spencer, A. M., editor, *Generation, accumulation, and production of Europe's hydrocarbons*, Spec. Publ. Eur. Assoc. Petroleum Geosci., 1:149–159.

Baldschuhn, R., Binot, F., Fleig, S., and Kockel, F., 1996. *Geotektonischer Atlas von Nordwest-Deutschland und dem deutschen Nordsee-Sektor*. 1:300 000, Teile 1–17, Hannover (Bundesanstalt für Geowissenschaften und Rohstoffe), Stuttgart, Germany.

Baldschuhn, R. and Kockel, F., 1999. Das Osning-Lineament am Südrand des Niedersachsen-Beckens. *Zeitschrift der Deutschen Geologischen Gesellschaft*, 150(4):673–695.

Baldschuhn, R., Frisch, U., and Kockel, F., 1985. Inversionsstrukturen in NW-Deutschland und ihre Genese. *Zeitschrift der Deutschen Geologischen Gesellschaft*, 136:129–139.

Baldschuhn, R., Frisch, U., and Kockel, F., 1998. Der Salzkeil, ein strukturelles Requisit der saxonischen Tektonik. *Zeitschrift der deutschen geologischen Gesellschaft*, 149(1):59–69.

Baldschuhn, R., Binot, F., Fleig, S., and Kockel, F., 2001. Geotektonischer Atlas von Nordwest-Deutschland und dem deutschen Nordsee-Sektor. Strukturen, Strukturentwicklung, Paläogeographie. *Geol. Jb. Reihe A*, A 153:1–88.

Barnasch, J., Franz, M., and Beutler, G., 2005. Hochauflösende Gliederung des Keupers der Eichsfeld-Altmark-Schwelle zur Präzisierung der Diskordanzen. *Hallesches Jb Geowiss B*, 19:153–160.

Barnasch, J., 2010. Der Keuper im Westteil des Zentraleuropäischen Beckens (Deutschland, Niederlande, England, Dänemark): diskontinuierliche Sedimentation, Litho- , Zyklo- und Sequenzstratigraphie. *Schriftenreihe der Deutschen Gesellschaft für Geowissenschaften*, pages 7–169. doi:10.1127/sdgg/71/2010/7.

Barton, D. C., 1933. Mechanics of formation of salt domes with special reference to Gulf Coast salt domes of Texas and Louisiana. *AAPG Bulletin*, 17(9):1025–1083.

Bayer, U., Scheck, M., and Koehler, M., 1997. Modeling of the 3D thermal field in the Northeast German Basin. *Geologische Rundschau*, 86(2):241–251. doi:10.1007/s005310050137.

Behlau, J. and Mingerzahn, G., 2001. Geological and tectonic investigations in the former Morsleben salt mine (Germany) as a basis for the safety assessment of a radioactive waste repository. *Engineering Geology*, 61(2):83–97. doi:http://dx.doi.org/10.1016/S0013-7952(01)00038-2.

Benox, D., Ludwig, A. O., Schulze, W., Schwab, G., Hartmann, H., Knebel, G., and Januszewski, I., 1997. Struktur und Entwicklung mesozoischer Störungszonen in der Südwest-Altmark. *Hallesches Jb Geowiss B*, 19:83–114.

Best, G., Kockel, F., and Schöneich, H., 1983. Geological history of the southern Horn Graben. In: *Petroleum geology of the southeastern North Sea and the adjacent onshore areas*, Springer, pages 25–33. doi:10.1007/978-94-009-5532-5_2.

Best, G. and Zirngast, M., 2000. Die strukturelle Entwicklung der exhumierten Salzstruktur "Oberes Allertal". *Geologisches Jahrbuch, Sonderheft, Reihe A*, 1:1–518.

Beutler, G. and Schüler, F., 1978. Über altkimmerische Bewegungen im Norden der DDR und ihre regionale Bedeutung (Fortschrittsbericht). *Zeitschrift für Geologische Wissenschaften*, 6:403–420.

Beutler, G., Hauschke, N., Nitsch, E., and Vath, U., 2005. *Stratigraphie von Deutschland IV Keuper*, volume 4. E. Schweizerbart'sche Verlagsbuchhandlung.

Beutler, G., Junker, R., Niediek, S., and Rößler, D., 2012. Tektonische Diskordanzen und tektonische Zyklen im Mesozoikum Nordostdeutschlands. *Zeitschrift der Deutschen Gesellschaft für Geowissenschaften*, 163(4):447–468. doi:https://doi.org/10.1127/1860-1804/2012/0163-0447.

Binot, F., 1988. Strukturentwicklung des Salzkissens Helgoland. *Zeitschrift der Deutschen Geologischen Gesellschaft*, 139:51–62.

Bornemann, O., 1979. *Das Gefügeinventar nordwestdeutscher Salzstrukturen in Abhängigkeit von ihrer halokinetischen Stellung*. PhD thesis, Technische Universität Braunschweig.

Bornemann, O., 1991. *Zur geologie des salzstocks Gorleben nach den Bohrergebnissen*. Bundesamt für Strahlenschutz.

Brandes, C., 2012. Reactivation of basement faults in NW Germany: interplay of ice-sheet dynamics and crustal structure. *Quaternary International*, 279:64. doi:10.1016/j.quaint.2012.07.283.

Brandes, C., Schmidt, C., Tanner, D. C., and Winsemann, J., 2013. Paleostress pattern and salt tectonics within a developing foreland basin (north-western Subhercynian Basin, northern Germany). *International Journal of Earth Sciences*, 102(8):2239–2254. doi:10.1007/s00531-013-0911-7.

Brink, H., Dürschner, H., and Trappe, H., 1992. Some aspects of the late and post-Variscan development of the Northwestern German Basin. *Tectonophysics*, 207(1):65–95. doi:http://dx.doi.org/10.1016/0040-1951(92)90472-I.

Brückner-Röhling, S., Fleig, S., Forsbach, H., Kockel, F., Krull, P., and Wirth, H., 2004. Die Bewegungsphasen tektonischer Störungen im Tertiär Norddeutschlands – Ergebnisse strukturgeologischer Untersuchungen). *Z. Geol. Wiss*, 5(6):295–231.

Brun, J.-P. and Fort, X., 2011. Salt tectonics at passive margins: Geology versus models. *Marine and Petroleum Geology*, 28(6): 1123–1145. doi:http://dx.doi.org/10.1016/j.marpetgeo.2011.03.004.

Burchardt, I., 1990. Salzer Dislokationszone und Eggersdorfer Keuper Mulde – Gleitschollen im postsalinaren Deckgebirge der Subherzynen Senke. *Z. geol. Wiss. Berlin*, 18(1):837–848.

Burchardt, S., Koyi, H., and Schmeling, H., 2011. Strain pattern within and around denser blocks sinking within Newtonian salt structures. *Journal of Structural Geology*, 33(2):145–153. doi:http://dx.doi.org/10.1016/j.jsg.2010.11.007.

Burliga, S., 1996. Kinematics within the Kłodawa salt diapir, central Poland. *Geological Society, London, Special Publications*, 100 (1):11–21. doi:10.1144/GSL.SP.1996.100.01.02.

Burliga, S., Koyi, H. A., and Chemia, Z., 2012. Analogue and numerical modelling of salt supply to a diapiric structure rising above an active basement fault. *Geological Society, London, Special Publications*, 363(1):395–408. doi:10.1144/SP363.18.

Carter, N. L., Horseman, S. T., Russell, J. E., and Handin, J., 1993. Rheology of rocksalt. *Journal of Structural Geology*, 15(9-10): 1257–1271. doi:http://dx.doi.org/10.1016/0191-8141(93)90168-A.

Cartwright, J., Stewart, S., and Clark, J., 2001. Salt dissolution and salt-related deformation of the Forth Approaches Basin, UK North Sea. *Marine and Petroleum Geology*, 18(6):757–778. doi:http://dx.doi.org/10.1016/S0264-8172(01)00019-8.

Chemia, Z., Koyi, H., and Schmeling, H., 2008. Numerical modelling of rise and fall of a dense layer in salt diapirs. *Geophysical Journal International*, 172(2):798–816. doi:https://doi.org/10.1111/j.1365-246X.2007.03661.x.

Clark, J. A., Stewart, S. A., and Cartwright, J. A., 1998. Evolution of the NW margin of the North Permian Basin, UK North Sea. *Journal of the Geological Society*, 155(4):663–676. doi:10.1144/gsjgs.155.4.0663.

Costa, E. and Vendeville, B. C., 2002. Experimental insights on the geometry and kinematics of fold-and-thrust belts above weak, viscous evaporitic décollement. *Journal of Structural Geology*, 24(11):1729–1739. doi:http://dx.doi.org/10.1016/S0191-8141(01)00169-9.

Coward, M. and Stewart, S., 1995. Salt-influenced structures in the Mesozoic-Tertiary cover of the southern North Sea, UK. In: Jackson, M., Roberts, D., and Snelson, S., editors, *Salt tectonics; a global perspective*, American Association of Petroleum Geologists, 65:229–250.

Dadlez, R., Narkiewicz, M., Stephenson, R. A., Visser, M. T. M., and Van Wees, J. D., 1995. Tectonic evolution of the Mid-Polish Trough: modelling implications and significance for central European geology. *Tectonophysics*, 252(1):179–195. doi:http://dx.doi.org/10.1016/0040-1951(95)00104-2.

Dadlez, R., 2003. Mesozoic thickness pattern in the Mid-Polish Trough. *Geological Quarterly*, 47(3):223–240.

Daudré, B. and Cloetingh, S. A. P. L., 1994. Numerical modelling of salt diapirism: influence of the tectonic regime. *Tectonophysics*, 240(1-4):59–79.

Davison, I., Alsop, I., and Blundell, D., 1996. Salt tectonics: some aspects of deformation mechanics. *Geological Society, London, Special Publications*, 100(1):1–10.

Dèzes, P., Schmid, S. M., and Ziegler, P. A., 2004. Evolution of the European Cenozoic Rift System: interaction of the Alpine and Pyrenean orogens with their foreland lithosphere. *Tectonophysics*, 389(1):1–33. doi:http://dx.doi.org/10.1016/j.tecto.2004.06.011.

Dickinson, G., 1953. Geological aspects of abnormal reservoir pressures in Gulf Coast Louisiana. *AAPG Bulletin*, 37(2):410–432.

Dooley, T. P., McClay, K. R., and Pascoe, R., 2003. 3D analogue models of variable displacement extensional faults: applications to the Revfallet Fault system, offshore mid-Norway. *Geological Society, London, Special Publications*, 212(1):151–167. doi:10.1144/GSL.SP.2003.212.01.10.

Dooley, T. P., McClay, K. R., Hempton, M., and Smit, D., 2005. Salt tectonics above complex basement extensional fault systems: results from analogue modelling. In: *Geological Society, London, Petroleum Geology Conference series*, 6:1631–1648. Geological Society of London. doi:10.1144/0061631.

Dooley, T. P., Jackson, M. P. A., and Hudec, M. R., 2007. Initiation and growth of salt-based thrust belts on passive margins: results from physical models. *Basin Research*, 19(1):165–177. doi:10.1111/j.1365-2117.2007.00317.x.

Dooley, T. P., Jackson, M. P. A., and Hudec, M. R., 2009. Inflation and deflation of deeply buried salt stocks during lateral shortening. *Journal of Structural Geology*, 31(6):582–600. doi:http://dx.doi.org/10.1016/j.jsg.2009.03.013.

Dooley, T. P., Jackson, M. P. A., Jackson, C. A.-L., Hudec, M. R., and Rodriguez, C. R., 2015. Enigmatic structures within salt walls of the Santos Basin—Part 2: Mechanical explanation from physical modelling. *Journal of Structural Geology*, 75:163–187. doi:http://dx.doi.org/10.1016/j.jsg.2015.01.009.

Doornenbal, J. C. and Stevenson, A. G., 2010. Petroleum Geological Atlas of the Southern Permian Basin Area. *Houten, Netherlands, European Association of Geoscientists & Engineers*.

Dronkers, A. J. and Mrozek, F. J., 1991. Inverted basins of the Netherlands. *First Break*, 9(9):409–425.

Duffy, O. B., Gawthorpe, R. L., Docherty, M., and Brocklehurst, S. H., 2013. Mobile evaporite controls on the structural style and evolution of rift basins: Danish Central Graben, North Sea. *Basin Research*, 25(3):310–330. doi:10.1111/bre.12000.

Duin, E. J. T., Doornenbal, J. C., Rijkers, R. H. B., Verbeek, J. W., and Wong, T. E., 2006. Subsurface structure of the Netherlands-results of recent onshore and offshore mapping. *Netherlands Journal of Geosciences*, 85(4):245.

Erratt, D., 1993. Relationships between basement faulting, salt withdrawal and Late Jurassic rifting, UK Central North Sea. In: Parker, J. R., editor, *Petroleum Geology of Northwest Europe: Proceedings of the 4th Conference*, Geological Society of London, 4:1211–1219. doi:10.1144/0041211.

Fahrion, H., 1953. Die Struktur Calberlah und ihre regionale Stellung. *N. Jb. Geol. Paläontol. Abh*, 97:57.

Ferrer, O., Roca, E., and Vendeville, B., 2014. The role of salt layers in the hangingwall deformation of kinked-planar extensional faults: Insights from 3D analogue models and comparison with the Parentis Basin. *Tectonophysics*, 636:338–350. doi:http://dx.doi.org/10.1016/j.tecto.2014.09.013.

Fort, X., Brun, J.-P., and Chauvel, F., 2004. Salt tectonics on the Angolan margin, synsedimentary deformation processes. *AAPG bulletin*, 88(11):1523–1544.

Franke, D. and Hoffmann, N., 1999. Das Elbe-Lineament-bedeutende Geofraktur oder Phantomgebilde? – Teil 1: Die Referenzgebiete. *Zeitschrift fur Geologische Wissenschaften*, 27(3/4):279–318.

Franz, M., 2008. *Litho-und Leitflächenstratigraphie, Chronostratigraphie, Zyklo-und Sequenzstratigraphie des Keupers im östlichen Zentraleuropäischen Becken (Deutschland, Polen) und Dänischen Becken (Dänemark, Schweden)*. PhD thesis, Naturwissenschaftliche Fakultät III der Martin-Luther-Universität Halle-Wittenberg.

Franzke, H. J., Heise, G., and Rauche, H., 1986. Analyse der strukturellen entwicklung der finne-störung und der naumburger mulde. *Hall Jahrbuch Geowiss*, 11:77–94.

Franzke, H. J., Voigt, T., von Eynatten, H., Brix, M. R., and Burmester, G., 2004. Geometrie und Kinematik der Harznordrandstörung, erläutert an Profilen aus dem Gebiet von Blankenburg. *Geowiss Mitt Thüringen*, 11:39–62.

Frisch, U. and Kockel, F., 1999. Quantification of early Cimmerian movements in NW-Germany. In: Bachmann, G. H. and Lerche, I., editors, *Epicontinental Triassic*, Zbl. Geol. Paläontol. Teil 1, 7-8:571–600.

Frisch, U. and Kockel, F., 2004. *Der Bremen-Knoten im Strukturnetz Nordwest-Deutschlands: Stratigraphie, Paläogeographie, Strukturgeologie*. Forschungszentrum Ozeanränder, RCOM, Univ.

Fuchs, L., Koyi, H., and Schmeling, H., 2014. Numerical modeling on progressive internal deformation in down-built diapirs. *Tectonophysics*, 632:111–122.

Gast, S., Pollok, L., von Goerne, G., and Simon, A., 2014. Structural Evolution of the Salt Domes Blankensee, Sperenberg and Paplitz – Based on a Detailed Part of the 3D-Model of Brandenburg. *Conference abstract – GeoFrankfurt 2014 Earth System Dynamics*.

Ge, H., Jackson, M. P. A., and Vendeville, B. C., 1997. Kinematics and dynamics of salt tectonics driven by progradation. *AAPG bulletin*, 81(3):398–423.

Geil, K., 1991. The development of salt structures in Denmark and adjacent areas: the role of basin floor dip and differential pressure. *First Break*, 9(10). doi:10.3997/1365-2397.1991022.

Geluk, M. C. and Röhling, H.-G., 1997. High-resolution sequence stratigraphy of the Lower Triassic 'Buntsandstein' in the Netherlands and northwestern Germany. *Geologie en Mijnbouw*, 76(3):227–246. doi:10.1023/A:1003062521373.

Geluk, M. C., 2005. *Stratigraphy and tectonics of Permo-Triassic basins in the Netherlands and surrounding areas*. PhD thesis, Utrecht University.

Gemmer, L., Ings, S. J., Medvedev, S., and Beaumont, C., 2004. Salt tectonics driven by differential sediment loading: stability analysis and finite-element experiments. *Basin Research*, 16(2):199–218. doi:10.1111/j.1365-2117.2004.00229.x.

Glennie, K. W., 1986. Development of NW Europe's Southern Permian gas basin. *Geological Society, London, Special Publications*, 23(1):3–22.

Goteti, R., Ings, S. J., and Beaumont, C., 2012. Development of salt minibasins initiated by sedimentary topographic relief. *Earth and Planetary Science Letters*, 339:103–116. doi:http://dx.doi.org/10.1016/j.epsl.2012.04.045.

Griffiths, P. A., Allen, M. R., Craig, J., Fitches, W. R., and Whittington, R. J., 1995. Distinction between fault and salt control of Mesozoic sedimentation on the southern margin of the Mid-North Sea High. *Geological Society, London, Special Publications*, 91 (1):145–159.

Hansen, M. B., Lykke-Andersen, H., Dehghani, A., Gajewski, D., Hübscher, C., Olesen, M., and Reicherter, K., 2005. The Mesozoic–Cenozoic structural framework of the Bay of Kiel area, western Baltic Sea. *International Journal of Earth Sciences*, 94(5-6): 1070–1082.

Hansen, M. B., Scheck-Wenderoth, M., Hübscher, C., Lykke-Andersen, H., Dehghani, A., Hell, B., and Gajewski, D., 2007. Basin evolution of the northern part of the Northeast German Basin—Insights from a 3D structural model. *Tectonophysics*, 437(1):1–16.

Harding, R. and Huuse, M., 2015. Salt on the move: Multi stage evolution of salt diapirs in the Netherlands North Sea. *Marine and Petroleum Geology*, 61:39–55.

Heaton, R. C., Jackson, M. P. A., Bamahmoud, M., and Nani, A. S. O., 1995. Superposed Neogene extension, contraction, and salt canopy emplacement in the Yemeni Red Sea. In: Jackson, M. P. A., Roberts, D. G., and Snelson, S., editors, *Salt tectonics: a global perspective*, AAPG Memoir, 65:333–351.

Hiller, K., 1971. Über dem Werdegang des Salzstock Mellum-Eversand-Scharhörn. *Erdöl und Kohle - Erdgas – Petrochemie vereinigt mit Brennstoff-Chemie,*, 24(2):137–141.

Hübscher, C., Hansen, M. B., Trinanes, S. P., Lykke-Andersen, H., and Gajewski, D., 2010. Structure and evolution of the Northeastern German Basin and its transition onto the Baltic Shield. *Marine and Petroleum Geology*, 27(4):923–938.

Hudec, M. R. and Jackson, M. P. A., 2007. Terra infirma: understanding salt tectonics. *Earth-Science Reviews*, 82(1):1–28. doi:http://dx.doi.org/10.1016/j.earscirev.2007.01.001.

Hudec, M. R. and Jackson, M. P. A., 2011. *The salt mine: a digital atlas of salt tectonics*, volume 99. Bureau of Economic Geology Udden Book Series No. 5.

Hudec, M. R., Jackson, M. P. A., and Schultz-Ela, D. D., 2009. The Paradox of Minibasin Subsidence into Salt. *Geological Society of America Bulletin*, 121(1/2):201–221. doi:10.1130/B26275.1.

Hughes, M. and Davison, I., 1993. Geometry and growth kinematics of salt pillows in the southern North Sea. *Tectonophysics*, 228 (3):239–254.

Hunsche, U., 1978. Modellrechnungen zur Entstehung von Salzstockfamilien. *Geol. Jb., E*, 12:53–107.

Hunsche, U. and Hampel, A., 1999. Rock salt – the mechanical properties of the host rock material for a radioactive waste repository. *Engineering geology*, 52(3):271–291.

Ings, S. J. and Beaumont, C., 2010. Shortening viscous pressure ridges, a solution to the enigma of initiating salt 'withdrawal' minibasins. *Geology*, 38(4):339–342.

Jackson, M. P. A., 1995. Retrospective salt tectonics. In: Jackson, M. P. A., Roberts, D. G., and Snelson, S., editors, *Salt tectonics: a global perspective*, AAPG Memoir, 65:1–28.

Jackson, M. P. A. and Talbot, C. J., 1986. External shapes, strain rates, and dynamics of salt structures. *Geological Society of America Bulletin*, 97(3):305–323. doi:10.1130/0016-7606(1986)97<305:ESSRAD>2.0.CO;2.

Jackson, M. P. A. and Talbot, C. J., 1991. A glossary of salt tectonics. *Geological Circular - Bureau of Economic Geology, University of Texas at Austin*, 91(4):1–44.

Jackson, M. P. A. and Vendeville, B. C., 1994. Regional extension as a geologic trigger for diapirism. *Geological society of America bulletin*, 106(1):57–73. doi:10.1130/0016-7606(1994)106<0057:REAAGT>2.3.CO;2.

Jackson, M. P. A., Cornelius, R. R., Craig, C. H., Gansser, A., Stöcklin, J., and Talbot, C. J., 1990. Salt diapirs of the Great Kavir, central Iran. *Geological Society of America Memoirs*, 177:1–150. doi:10.1130/MEM177-p1.

Jackson, M. P. A., Vendeville, B. C., and Schultz-Ela, D. D., 1994. Structural dynamics of salt systems. *Annual Review of Earth and Planetary Sciences*, 22:93–117. doi:10.1146/annurev.ea.22.050194.000521.

Jähne-Klingberg, F., 2016. Geological cross section of the altmark-fläming low, unpublished. unpublished.

Jähne-Klingberg, F., Wolf, M., Steuer, S., Bense, F., Kaufmann, D., and Weitkamp, A., 2014. Speicherpotenziale im zentralen deutschen Nordsee-Sektor. In: *Speicherpotenziale im zentralen deutschen Nordsee-Sektor*, Bundesanstalt für Geowissenschaften und Rohstoffe, Hannover, page 96.

Jaritz, W., 1973. Zur Entstehung der Salzstrukturen Nordwestdeutschlands. *Geologisches Jahrbuch, A10*, pages 3–77.

Jordan, H. and Kockel, F., 1991. Die Leinetal-Struktur und ihr Umfeld. Ein tektonisches Konzept für Südniedersachsen. *Geologisches Jahrbuch, Reihe A*, 126:171–196.

Jubitz, K.-E., editor, 1964. *Führer zu den Exkursionen anlässlich der 11. Jahrestagung der Geologischen Gesellschaft in der Deutschen Demokratischen Republik*, volume 11. Geologischen Gesellschaft in der Deutschen Demokratischen Republik.

Karlo, J. F., van Buchem, F. S. P., Moen, J., and Milroy, K., 2014. Triassic-age salt tectonics of the Central North Sea. *Interpretation*, 2(4):SM19–SM28.

Kastner, O., Sippel, J., Scheck-Wenderoth, M., and Huenges, E., 2013. The deep geothermal potential of the Berlin area. *Environmental earth sciences*, 70(8):3567–3584.

Kehle, R. O., 1988. The origin of salt structures. In: Schreiber, B. C., editor, *Evaporites and Hydrocarbons*, Columbia University Press, New York, pages 345–404.

Kley, J., Franzke, H.-J., Jähne, F., Krawczyk, C., Lohr, T., Reicherter, K., Scheck-Wenderoth, M., Sippel, J., Tanner, D., van Gent, H., and the SPP Structural Geology Group, 2008. Strain and stress. In: Littke, R., Bayer, U., Gajewski, D., and Nelskamp, S., editors, *Dynamics of Complex Intracontinental Basins: The Central European Basin System*, Springer Science & Business Media, Berlin, pages 97–124.

Kley, J. and Voigt, T., 2008. Late Cretaceous intraplate thrusting in central Europe: Effect of Africa-Iberia-Europe convergence, not Alpine collision. *Geology*, 36(11):839–842.

Knape, H., 1963. Tektonischer Bau und Strukturgenese im nordwestlichen Vorland des Flechtinger Höhenzuges. *Geologie*, 12:509.

Kockel, F., 2003. Inversion structures in Central Europe-Expressions and reasons, an open discussion. *Netherlands Journal of Geosciences*, 82(04):351–366.

Kockel, F. and Krull, P., 1995. *Endlagerung stark wärmeentwickelnder radioaktiver Abfalle in tiefen geologischen Formationen Deutschlands: Untersuchung und Bewertung von Salzformationen*. Bundesanstalt für Geowissenschaften und Rohstoffe.

Kockel, F., 1991. Die Strukturen im Untergrund des Braunschweiger Landes. *Geol. Jb., A*, 127:391–404.

Kockel, F., 04 1995. *Structural and Palaeogeographical Development of the German North Sea Sector*. Schweizerbart Science Publishers, Stuttgart, Germany.

Kockel, F., 1998. Salt problems in NW-Germany and the German North Sea Sector. *Journal Seismic Exploration*, 7:219–235.

Kockel, F., 2002. Rifting processes in NW-Germany and the German North Sea Sector. *Netherlands Journal of Geosciences: Geologie en Mijnbouw*, 81:149–158.

Korstgård, J. A., Lerche, I., Mogensen, T. E., and Thomsen, R. O., 1993. Salt and fault interactions in the northeastern Danish Central Graben: observations and inferences. *Bulletin of the Geological Society of Denmark*, 40:197–255.

Kossow, D., 2001. *Die kinematische Entwicklung des invertierten, intrakontinentalen Nordostdeutschen Beckens*. PhD thesis, University of Potsdam.

Kossow, D. and Krawczyk, C. M., 2002. Structure and quantification of processes controlling the evolution of the inverted NE-German Basin. *Marine and Petroleum Geology*, 19(5):601–618.

Kossow, D., Krawczyk, C., McCann, T., Strecker, M., and Negendank, J. F., 2000. Style and evolution of salt pillows and related structures in the northern part of the Northeast German Basin. *International Journal of earth sciences*, 89(3):652–664.

Köthe, A., Hoffmann, N., and Krull, P., editors, 06 2007. *Standortbeschreibung Gorleben Teil 2*. Schweizerbart Science Publishers, Stuttgart, Germany.

Koyi, H., Jenyon, M. K., and Petersen, K., 1993. The effect of basement faulting on diapirism. *Journal of Petroleum Geology*, 16(3): 285–312. doi:10.1111/j.1747-5457.1993.tb00339.x.

Koyi, H. A., 2001. Modeling the influence of sinking anhydrite blocks on salt diapirs targeted for hazardous waste disposal. *Geology*, 29(5):387–390.

Krauss, M. and Mayer, P., 2004. Das Vorpommern-Störungssystem und seine regionale Einordnung zur Transeuropaischen Störung. *Zeitschrift fürgeologische Wissenschaften*, 32(2/4):227–246.

Krzywiec, P., 2002. The Owino structure (NW Mid-Polish Trough) – salt diapir or inversion-related compressional structure? *Geological Quarterly*, 46(3):337–346.

Krzywiec, P., 2004a. Basement vs. salt tectonics and salt-sediment Interaction—case study of the Mesozoic evolution of the Intracontinental Mid-Polish Trough. In: *GCSSEPM Foundation 24th Annual Research Conference: Salt—Sediment Interactions and Hydrocarbon Prospectivity: Concepts, Applications and Case Studies for the 21st Century*, pages 5–8. SEPM.

Krzywiec, P., 2004b. Triassic evolution of the Kłodawa salt structure: basement-controlled salt tectonics within the Mid-Polish Trough (Central Poland). *Geological Quarterly*, 48(2):123–134.

Krzywiec, P., 2006. Triassic-Jurassic evolution of the Pomeranian segment of the Mid-Polish Trough–basement tectonics and subsidence patterns. *Geological Quarterly*, 50(1):139–150.

Krzywiec, P., 2012. Mesozoic and Cenozoic evolution of salt structures within the Polish basin: An overview. *Geological Society, London, Special Publications*, 363(1):381–394. doi:10.1144/SP363.17.

Kukla, P. A., Urai, J. L., and Mohr, M., 2008. Dynamics of salt structures. In: Littke, R., Bayer, U., Gajewski, D., and Nelskamp, S., editors, *Dynamics of Complex Intracontinental Basins: The Central European Basin System*, Springer Science & Business Media, Berlin, pages 291–306.

Lachmann, R., 1911. Der Salzauftrieb. *Kali*, 4:130.

Lamarche, J. and Scheck-Wenderoth, M., 2005. 3D structural model of the Polish Basin. *Tectonophysics*, 397(1):73–91.

Li, S., Abe, S., Urai, J. L., Strozyk, F., Kukla, P. A., and van Gent, H., 2012a. A method to evaluate long-term rheology of Zechstein salt in the Tertiary. In: Berest, P., Ghoreychi, M., Hadj-Hassen, F., and Tijani, M., editors, *Mechanical Behaviour of Salt VII*, CRC Press, pages 215–220.

Li, S.-Y. and Urai, J. L., 2016. Rheology of rock salt for salt tectonics modeling. *Petroleum Science*.

Li, S., Abe, S., Reuning, L., Becker, S., Urai, J. L., and Kukla, P. A., 2012b. Numerical modelling of the displacement and deformation of embedded rock bodies during salt tectonics: A case study from the South Oman Salt Basin. *Geological Society, London, Special Publications*, 363(1):503–520. doi:10.1144/SP363.24.

Löffler, J., 1962. *Die Kali- und Steinsalzlagerstätten des Zechsteins in der DDR. Teil 3: Sachsen-Anhalt*. Freiberger Forschungshefte, C 97(3), Berlin.

Lohr, T., Krawczyk, C. M., Tanner, D. C., Samiee, R., Endres, H., Oncken, O., Trappe, H., and Kukla, P. A., 2007. Strain partitioning due to salt: insights from interpretation of a 3D seismic data set in the NW German Basin. *Basin Research*, 19(4):579–597.

Magri, F., Littke, R., Rodon, S., Bayer, U., and Urai, J. L., 2008. Temperature fields, petroleum maturation and fluid flow in the vicinity of salt domes. In: Littke, R., Bayer, U., Gajewski, D., and Nelskamp, S., editors, *Dynamics of Complex Intracontinental Basins: The Central European Basin System*, Springer Science & Business Media, Berlin, pages 323–330.

Malz, A. and Kley, J., 2012. The Finne fault zone (central Germany): structural analysis of a partially inverted extensional fault zone by balanced cross-sections. *International Journal of Earth Sciences*, 101(8):2167–2182.

Masrouhi, A., Bellier, O., and Koyi, H., 2014. Geometry and structural evolution of Lorbeus diapir, northwestern Tunisia: polyphase diapirism of the North African inverted passive margin. *International Journal of Earth Sciences*, 103(3):881–900. doi:10.1007/s00531-013-0992-3.

Massimi, P., Quarteroni, A., Saleri, F., and Scrofani, G., 2007. Modeling of salt tectonics. *Computer methods in applied mechanics and engineering*, 197(1):281–293.

Mayer, P., Krauss, M., and Vormbaum, M., 2000. Der Strukturbau des Vorpommern-Stförungssystems im Bereich der NE-Fortsetzung des DEKORP-Profils BASIN 9601 (DFG-Projekt VPSS I). *Zeitschrift für Geologische Wissenschaften*, 28(3/4):397–404.

Maystrenko, Y., Bayer, U., Brink, H.-J., and Littke, R., 2008. The Central European Basin System – an Overview. In: Littke, R., Bayer, U., Gajewski, D., and Nelskamp, S., editors, *Dynamics of Complex Intracontinental Basins: The Central European Basin System*, Springer Science & Business Media, Berlin, pages 17–34.

Maystrenko, Y., Bayer, U., and Scheck-Wenderoth, M., 2005a. Structure and evolution of the Glueckstadt Graben due to salt movements. *International Journal of Earth Sciences*, 94(5-6):799–814. doi:10.1007/s00531-005-0003-4.

Maystrenko, Y., Bayer, U., and Scheck-Wenderoth, M., 2005b. The Glueckstadt Graben, a sedimentary record between the North and Baltic Sea in north Central Europe. *Tectonophysics*, 397(1):113–126. doi:http://dx.doi.org/10.1016/j.tecto.2004.10.004.

Maystrenko, Y. P., Bayer, U., and Scheck-Wenderoth, M., 2013. Salt as a 3D element in structural modeling – Example from the Central European Basin System. *Tectonophysics*, 591:62–82. doi:http://dx.doi.org/10.1016/j.tecto.2012.06.030.

Mazur, S., Scheck-Wenderoth, M., and Krzywiec, P., 2005. Different modes of the Late Cretaceous–Early Tertiary inversion in the North German and Polish basins. *International Journal of Earth Sciences*, 94(5-6):782–798.

McBride, B. C., Weimer, P., and Rowan, M. G., 1998. The effect of allochthonous salt on the petroleum systems of northern Green Canyon and Ewing Bank (offshore Louisiana), northern Gulf of Mexico. *AAPG bulletin*, 82(5):1083–1112.

McCann, T., Pascal, C., Timmerman, M. J., Krzywiec, P., López-Gómez, J., Wetzel, L., Krawczyk, C. M., Rieke, H., and Lamarche, J., 2006. Post-variscan (end carboniferous-early permian) basin evolution in western and central europe. *Geological Society, London, Memoirs*, 32(1):355–388.

Meinhold, R., 1956. Bemerkung zur Frage des Salzstockaufstiegs. *Freiberger Forschungshefte*, C 22:65–77.

Meinhold, R., 1959. Salzbewegung und Tektonik in Norddeutschland. *Geol. Gessell. DDR Ber*, 4:157–168.

Meinhold, R. and Reinhardt, H. G., 1967. Halokinese im nordostdeutschen Tiefland. *Ber dt Ges geol Wiss, A, Geol Palaont*, 12: 329–353.

Mohr, M., Kukla, P. A., Urai, J., and Bresser, G., 2005. Multiphase salt tectonic evolution in NW Germany: seismic interpretation and retro-deformation. *International Journal of Earth Sciences*, 94(5-6):917–940.

Mohr, M., Warren, J. K., Kukla, P. A., Urai, J. L., and Irmen, A., 2007. Subsurface seismic record of salt glaciers in an extensional intracontinental setting (Late Triassic of northwestern Germany). *Geology*, 35(11):963–966.

Mukherjee, S., Talbot, C. J., and Koyi, H. A., 2010. Viscosity estimates of salt in the Hormuz and Namakdan salt diapirs, Persian Gulf. *Geological Magazine*, 147(04):497–507.

Nalpas, T. and Brun, J.-P., 1993. Salt flow and diapirism related to extension at crustal scale. *Tectonophysics*, 228(3):349–362. doi:http://dx.doi.org/10.1016/0040-1951(93)90348-N.

Nikolinakou, M. A., Hudec, M. R., and Flemings, P. B., 2014. Comparison of evolutionary and static modeling of stresses around a salt diapir. *Marine and Petroleum Geology*, 57:537–545.

Nilsen, K. T., Johansen, J. T., and Vendeville, B. C., 1996. Influence of regional tectonics on halokinesis in the Nordkapp Basin, Barents Sea. In: Jackson, M. P. A., Roberts, D. G., and Snelson, S., editors, *Salt tectonics: a global perspective*, AAPG Memoir, pages 413–436, 65.

Noack, V., Cherubini, Y., Scheck-Wenderoth, M., Lewerenz, B., Höding, T., Simon, A., and Moeck, I., 2010. Assessment of the present-day thermal field (NE German Basin)—inferences from 3D modelling. *Chemie Der Erde-Geochemistry*, 70:47–62.

Norden, B. and Förster, A., 2006. Thermal conductivity and radiogenic heat production of sedimentary and magmatic rocks in the Northeast German Basin. *AAPG Bulletin*, 90(6):939–962.

Osman, A., Pollok, L., Brandes, C., and Winsemann, J., 2013. Sequence stratigraphy of a Paleogene coal bearing rim syncline: interplay of salt dynamics and sea-level changes, Schöningen, Germany. *Basin Research*, 25(6):675–708.

Otto, V., 2003. Inversion-related features along the southeastern margin of the North German Basin (Elbe Fault System). *Tectonophysics*, 373(1):107–123.

Patzelt, G., 2003. *Nördliches Harzvorland*, volume 50. Berlin/Stuttgart, Gebrüder Bornraeger, Sammlung Geologischer Führer.

Pchalek, J., 1962. Beitrag zur Stratigraphie und Tektonik SW-Brandenburgs. *Berichte der Geologischen Gesellschaft der DDR*, 6 (2/3):204–209.

Peel, F. J., Travis, C. J., and Hossack, J. R., 1995. Genetic structural provinces and salt tectonics of the Cenozoic offshore U.S. Gulf of Mexico: A preliminary analysis. In: Jackson, M. P. A., Roberts, D. G., and Snelson, S., editors, *Salt tectonics: A global perspective*, AAPG Memoir, 65:153–175.

Peel, F. J., 2014. How do salt withdrawal minibasins form? insights from forward modelling, and implications for hydrocarbon migration. *Tectonophysics*, 630:222–235. doi:http://dx.doi.org/10.1016/j.tecto.2014.05.027.

Penge, J., Taylor, B., Huckerby, J. A., and Munns, J. W., 1993. Extension and salt tectonics in the East Central Graben. In: *Geological Society, London, Petroleum Geology Conference series*, 4:1197–1209. Geological Society of London. doi:10.1144/0041197.

Penge, J., Munns, J. W., Taylor, B., and Windle, T. M. F., 1999. Rift–raft tectonics: examples of gravitational tectonics from the Zechstein basins of northwest Europe. In: Fleet, A. J. and Boldy, S. A. R., editors, *Geological Society, London, Petroleum Geology Conference series*, 5:201–213. Geological Society of London.

Pennock, G. M., Drury, M. R., and Spiers, C. J., 2005. The development of subgrain misorientations with strain in dry synthetic NaCl measured using EBSD. *Journal of structural geology*, 27(12):2159–2170.

Perić, D. and Crook, A. J. L., 2004. Computational strategies for predictive geology with reference to salt tectonics. *Computer methods in applied mechanics and engineering*, 193(48):5195–5222.

Peters, J. M., Filbrandt, J., Grotzinger, J., Newall, M., Shuster, M., and Al-Siyabi, H., 2003. Surface-piercing Salt Domes of interior North Oman, and their significance of the Ara Carbonate" Stinger" hydrocarbon play. *GeoArabia*, 8:231–270.

Raith, A. F., Strozyk, F., Visser, J., and Urai, J. L., 2015. Evolution of rheologically heterogeneous salt structures: a case study from the northeast of the Netherlands. *Solid Earth Discussions*, 7(3):67–82.

Reinhardt, H.-G., 1993. Structure of northeast germany: Regional depth and thickness maps of permian to tertiary intervals compiled from seismic reflection data. In: Spencer, A. M., editor, *Generation, Accumulation and Production of Europe's Hydrocarbons III: Special Publication of the European Association of Petroleum Geoscientists No. 3*, Springer Berlin Heidelberg, pages 155–165. ISBN 978-3-642-77859-9. doi:10.1007/978-3-642-77859-9_13.

Reinhold, K. and Hammer, J., 2016. Steinsalzlager in den salinaren Formationen Deutschlands. *Zeitschrift der Deutschen Gesellschaft für Geowissenschaften*, 167(2-3):167–190.

Remmelts, G., 1995. Fault-related salt tectonics in the southern North Sea, the Netherlands. In: Jackson, M. P. A., Roberts, D. G., and Snelson, S., editors, *Salt tectonics: a global perspective*, AAPG Special Volumes, 65:261–272.

Richard, P., 1991. Experiments on faulting in a two-layer cover sequence overlying a reactivated basement fault with oblique-slip. *Journal of Structural Geology*, 13(4):459–469.

Richter-Bernburg, G., 1980. Salt tectonics, interior structures of salt bodies. *Bull. Cent. Rech. Explor.-Prod. Elf-Aquitaine*, 4(1): 373–393.

Riedel, L., 1944. Einige Fragen hinsichtlich des Alters und Aufdringes der Salzstöcke in Nordwestdeutschland, besonders auf der Pompeckj'schen Schwelle. *Geol. Jb.*, 63:39–81.

Roberts, A. M., Price, J. D., and Olsen, T. S., 1990. Late Jurassic half-graben control on the siting and structure of hydrocarbon accumulations: UK/Norwegian Central Graben. *Geological Society, London, Special Publications*, 55(1):229–257. doi:10.1144/GSL.SP.1990.055.01.11.

Röhling, H.-G., 1991. A lithostratigraphic subdivision of the Lower Triassic in the northwest German lowlands and the German sector of the North Sea, based on gamma-ray and sonic logs.- The perennial Rotliegend saline lake in northwest Germany. *Geologisches Jahrbuch A*, 119:3–24.

Rowan, M. G. and Ratliff, R. A., 2012. Cross-section restoration of salt-related deformation: Best practices and potential pitfalls. *Journal of Structural Geology*, 41:24–37.

Rudolf, M., Boutelier, D., Rosenau, M., Schreurs, G., and Oncken, O., 2016. Rheological benchmark of silicone oils used for analog modeling of short-and long-term lithospheric deformation. *Tectonophysics*, 684:12–22. doi:http://dx.doi.org/10.1016/j.tecto.2015.11.028.

Rühberg, N., 1976. Probleme der Zechsteinsalzbewegung. *Zeitschrift fü angewandte Geologie*, 22/9:413–420.

Sannemann, D., 1968. Salt-stock Families in Northwestern Germany. *AAPG Memoir*, 8:261–270.

Scheck, M. and Bayer, U., 1999. Evolution of the Northeast German Basin – inferences from a 3D structural model and subsidence analysis. *Tectonophysics*, 313(1):145–169.

Scheck, M., Bayer, U., Otto, V., Lamarche, J., Banka, D., and Pharaoh, T., 2002. The Elbe Fault System in North Central Europe—a basement controlled zone of crustal weakness. *Tectonophysics*, 360(1):281–299.

Scheck, M., Bayer, U., and Lewerenz, B., 2003a. Salt movements in the Northeast German Basin and its relation to major post-Permian tectonic phases—results from 3D structural modelling, backstripping and reflection seismic data. *Tectonophysics*, 361(3):277–299.

Scheck, M., Bayer, U., and Lewerenz, B., 2003b. Salt redistribution during extension and inversion inferred from 3D backstripping. *Tectonophysics*, 373(1):55–73.

Scheck-Wenderoth, M., Krzywiec, P., Zühlke, R., Maystrenko, Y., and Froitzheim, N., 2008a. Permian to cretaceous tectonics. In: McCann, editor, *The geology of central Europe*, The Geological Society of London London, pages 999–1030.

Scheck-Wenderoth, M., Maystrenko, Y., Hübscher, C., Hansen, M., and Mazur, S., 2008b. Dynamics of salt basin. In: Littke, R., Bayer, U., Gajewski, D., and Nelskamp, S., editors, *Dynamics of Complex Intracontinental Basins: The Central European Basin System*, Springer Science & Business Media, Berlin, pages 307–321.

Scheck-Wenderoth, M., Cacace, M., Maystrenko, Y. P., Cherubini, Y., Noack, V., Kaiser, B. O., Sippel, J., and Björn, L., 2014. Models of heat transport in the Central European Basin System: Effective mechanisms at different scales. *Marine and Petroleum Geology*, 55:315–331. doi:http://dx.doi.org/10.1016/j.marpetgeo.2014.03.009.

Schléder, Z., Urai, J. L., Nollet, S., and Hilgers, C., 2008. Solution-precipitation creep and fluid flow in halite: a case study of Zechstein (Z1) rocksalt from Neuhof salt mine (Germany). *International Journal of Earth Sciences*, 97(5):1045–1056.

Schoenherr, J., Schléder, Z., Urai, J. L., Fokker, P. A., and Schulze, O., 2007. Deformation mechanisms and rheology of Pre-cambrian rocksalt from the South Oman Salt Basin. *The mechanical behaviour of salt—understanding of THMC processes in salt. Taylor & Francis, London*, pages 167–173.

Schultz-Ela, D. D. and Jackson, M. P. A., 1996. Relation of subsalt structures to suprasalt structures during extension. *AAPG bulletin*, 80(12):1896–1923.

Schultz-Ela, D. D. and Walsh, P., 2002. Modeling of grabens extending above evaporites in Canyonlands National Park, Utah. *Journal of Structural Geology*, 24(2):247–275. doi:http://dx.doi.org/10.1016/S0191-8141(01)00066-9.

Schultz-Ela, D. D., Jackson, M. P. A., and Vendeville, B. C., 1993. Mechanics of active salt diapirism. *Tectonophysics*, 228(3): 275–312. doi:http://dx.doi.org/10.1016/0040-1951(93)90345-K.

Seni, S. J. and Jackson, M. P. A., 1983. Evolution of salt structures, East Texas diapir province, part 1: sedimentary record of halokinesis. *AAPG Bulletin*, 67(8):1219–1244.

Sirocko, F., Reicherter, K., Lehné, R., Hübscher, C., Winsemann, J., and Stackebrandt, W., 2008. Glaciation, salt and the present landscape. In: Littke, R., Bayer, U., Gajewski, D., and Nelskamp, S., editors, *Dynamics of Complex Intracontinental Basins: The Central European Basin System*, Springer Science & Business Media, Berlin, pages 233–245.

Sørensen, K., 1998. The salt pillow to diapir transition: evidence from unroofing unconformities in the Norwegian-Danish Basin. *Petroleum Geoscience*, 4(3):193–202.

Soto, R., Casas-Sainz, A. M., and Del Río, P., 2007. Geometry of half-grabens containing a mid-level viscous décollement. *Basin Research*, 19(3):437–450.

Spiers, C. J., Schutjens, P. M. T. M., Brzesowsky, R. H., Peach, C. J., Liezenberg, J. L., and Zwart, H. J., 1990. Experimental determination of constitutive parameters governing creep of rocksalt by pressure solution. *Geological Society, London, Special Publications*, 54(1):215–227.

Stackebrandt, W. and Franzke, H. J., 1989. Alpidic reactivation of the Variscan consolidated lithosphere – The activity of some fracture-zones in Central-Europe. *Zeitschrift fur Geologische Wissenschaften*, 17(7):699–712.

Stephenson, R. A., Berkel, J. T. v., and Cloetingh, S. A. P. L., 1992. Relation between salt diapirism and the tectonic history of the Sverdrup Basin, Arctic Canada. *Canadian Journal of Earth Sciences*, 29(12):2695–2705. doi:10.1139/e92-213.

Stewart, S. A., 2007. Salt tectonics in the North Sea Basin: a structural style template for seismic interpreters. *Special Publication - Geological Society of London*, 272:361.

Stewart, S. A. and Clark, J. A., 1999. Impact of salt on the structure of the Central North Sea hydrocarbon fairways. In: *Geological Society, London, Petroleum Geology Conference series*, 5:179–200. doi:10.1144/0050179.

Stewart, S. A., Harvey, M. J., Otto, S. C., and Weston, P. J., 1996. Influence of salt on fault geometry: examples from the uk salt basins. *Geological Society, London, Special Publications*, 100(1):175–202.

Stollhofen, H., Bachmann, G. H., Barnasch, J., Bayer, U., Beutler, G., Franz, M., Kästner, M., Legler, B., Mutterlose, J., and Radies, D., 2008. Upper Rotliegend to Early Cretaceous basin development. In: Littke, R., Bayer, U., Gajewski, D., and Nelskamp, S., editors, *Dynamics of Complex Intracontinental Basins: The Central European Basin System*, Springer Science & Business Media, Berlin, pages 181–207.

Stovba, S. M. and Stephenson, R. A., 2003. Style and timing of salt tectonics in the Dniepr-Donets Basin (Ukraine): implications for triggering and driving mechanisms of salt movement in sedimentary basins. *Marine and Petroleum Geology*, 19(10):1169–1189. doi:http://dx.doi.org/10.1016/S0264-8172(03)00023-0.

Strozyk, F., Van Gent, H., Urai, J., and Kukla, P., 2012. 3D seismic study of complex intra-salt deformation: An example from the Upper Permian Zechstein 3 stringer, western Dutch offshore. *Geological Society, London, Special Publications*, 363(1):489–501.

Strunck, P., Gaupp, R., and Stefan, M., 1998. Early Triassic movement of Upper Permian (Zechstein) salt in Northwest Germany. In: Ed.: Bachmann, G. H. and Lerche, I., editors, *Epicontinental Triassic, Volume 1*, Schweizerbart Science Publishers, Stuttgart. ISBN 9783510660117.

Talbot, C. J. and Jackson, M. P. A., 1987. Internal kinematics of salt diapirs. *AAPG Bulletin*, 71(9):1068–1093.

Talbot, C. J., Tully, C. P., and Woods, P. J. E., 1982. The structural geology of Boulby (potash) mine, Cleveland, United Kingdom. *Tectonophysics*, 85(3-4):167–204.

Tanveer, M. and Korstgård, J. A., 2009. Structural evolution of the Feda Graben area–A new model. *Marine and Petroleum Geology*, 26(6):990–999. doi:http://dx.doi.org/10.1016/j.marpetgeo.2008.04.010.

Ten Veen, J. H., Van Gessel, S. F., and Den Dulk, M., 2012. Thin-and thick-skinned salt tectonics in the Netherlands; a quantitative approach. *Netherlands Journal of Geosciences*, 91(04):447–464. doi:https://doi.org/10.1017/S0016774600000330.

Ter Heege, J. H., De Bresser, J. H. P., and Spiers, C. J., 2005. Dynamic recrystallization of wet synthetic polycrystalline halite: dependence of grain size distribution on flow stress, temperature and strain. *Tectonophysics*, 396(1):35–57. doi:http://dx.doi.org/10.1016/j.tecto.2004.10.002.

Thieme, B. and Rockenbauch, K., 2001. Flosstektonik in der Trias der deutschen südlichen Nordsee. *Erdöl, Erdgas, Kohle*, 117(12): 568–573.

Trudgill, B. D., 2011. Evolution of salt structures in the northern Paradox Basin: Controls on evaporite deposition, salt wall growth and supra-salt stratigraphic architecture. *Basin Research*, 23(2):208–238.

Trusheim, F., 1960. Mechanism of salt migration in northern Germany. *AAPG Bulletin*, 44(9):1519–1540.

Turcotte, D. L. and Schubert, G., 2014. *Geodynamics*, third edition. Cambridge University Press.

Tvedt, A. B. M., Rotevatn, A., Jackson, C. A.-L., Fossen, H., and Gawthorpe, R. L., 2013. Growth of normal faults in multilayer sequences: a 3D seismic case study from the Egersund Basin, Norwegian North Sea. *Journal of Structural Geology*, 55:1–20. doi:http://dx.doi.org/10.1016/j.jsg.2013.08.002.

Urai, J. L., Schléder, Z., Spiers, C. J., and Kukla, P. A., 2008. Flow and Transport Properties of Salt Rocks. In: Littke, R., Bayer, U., Gajewski, D., and Nelskamp, S., editors, *Dynamics of Complex Intracontinental Basins: The Central European Basin System*, Springer Science & Business Media, Berlin, pages 277–290.

Urai, J. L., Spiers, C. J., Zwart, H. J., and Lister, G. S., 1986. Weakening of rock salt by water during long-term creep. *Nature*, 324: 554–557. doi:10.1038/324554a0.

Vackiner, A. A., Antrett, P., Strozyk, F., Back, S., Kukla, P., and Stollhofen, H., 2013. Salt kinematics and regional tectonics across a Permian gas field: a case study from East Frisia, NW Germany. *International Journal of Earth Sciences*, 102(6):1701–1716. doi:10.1007/s00531-013-0887-3.

Van Gent, H., Urai, J. L., and De Keijzer, M., 2011. The internal geometry of salt structures – A first look using 3D seismic data from the Zechstein of the Netherlands. *Journal of Structural Geology*, 33(3):292–311. doi:http://dx.doi.org/10.1016/j.jsg.2010.07.005.

van Hoorn, B., 1987. Structural evolution, timing and tectonic style of the Sole Pit inversion. *Tectonophysics*, 137(1):239–284.

van Keken, P. E., Spiers, C. J., Van den Berg, A. P., and Muyzert, E. J., 1993. The effective viscosity of rocksalt: implementation of steady-state creep laws in numerical models of salt diapirism. *Tectonophysics*, 225(4):457–476. doi:http://dx.doi.org/10.1016/0040-1951(93)90310-G.

Van Wees, J.-D., Stephenson, R. A., Ziegler, P. A., Bayer, U., McCann, T., Dadlez, R., Gaupp, R., Narkiewicz, M., Bitzer, F., and Scheck, M., 2000. On the origin of the southern Permian Basin, Central Europe. *Marine and Petroleum Geology*, 17(1):43–59.

Van Wijhe, D. v., 1987. Structural evolution of inverted basins in the Dutch offshore. *Tectonophysics*, 137(1-4):171179185191213–175181187210219.

Vejbæk, O. V., 1990. The Horn Graben, and its relationship to the Oslo Graben and the Danish Basin. *Tectonophysics*, 178(1):29–49.

Vendeville, B. C. and Jackson, M. P. A., 1992a. The fall of diapirs during thin-skinned extension. *Marine and Petroleum Geology*, 9 (4):354–371. doi:http://dx.doi.org/10.1016/0264-8172(92)90048-J.

Vendeville, B. C. and Jackson, M. P. A., 1992b. The rise of diapirs during thin-skinned extension. *Marine and Petroleum Geology*, 9 (4):331–354. doi:http://dx.doi.org/10.1016/0264-8172(92)90047-I.

Vendeville, B. C. and Nilsen, K. T., 1995. Episodic growth of salt diapirs driven by horizontal shortening. In: Travis, C. J., Vendeville, B. C., Harrison, H., Peel, F. J., Hudec, M. R., and Perkins, B. F., editors, *Salt, Sediment, and Hydrocarbons*, Society of Economic Paleontologists and Mineralogists, Gulf Coast Section, 16th Annual Research Conference Program and Extended Abstracts, 16: 285–295.

Vendeville, B. C., Ge, H., and Jackson, M. P. A., 1995. Scale models of salt tectonics during basement-involved extension. *Petroleum Geoscience*, 1(2):179–183. doi:10.1144/petgeo.1.2.179.

Voigt, T., Reicherter, K., von Eynatten, H., Littke, R., Voigt, S., and Kley, J., 2008. Sedimentation during basin inversion. In: Littke, R., Bayer, U., Gajewski, D., and Nelskamp, S., editors, *Dynamics of Complex Intracontinental Basins: The Central European Basin System*, Springer Science & Business Media, Berlin, pages 211–232.

Voigt, T., von Eynatten, H., and Franzke, H.-J., 2004. Late Cretaceous unconformities in the Subhercynian Cretaceous Basin (Germany). *Acta Geologica Polonica*, 54(4):673–694.

Wagner, B. H. and Jackson, M. P. A., 2011. Viscous flow during salt welding. *Tectonophysics*, 510(3):309–326. doi:http://dx.doi.org/10.1016/j.tecto.2011.07.012.

Wagner, R., Leszczyński, K., Pokorski, J., and Gumulak, K., 2002. Palaeotectonic cross-sections through the Mid-Polish Trough. *Geological Quarterly*, 46(3):293–306.

Walker, D., Verma, P. K., Cranswick, L., Jones, R. L., Clark, S. M., and Buhre, S., 2004. Halite-sylvite thermoelasticity. *American Mineralogist*, 89(1):204–210.

Waltham, D., 1997. Why does salt start to move? . *Tectonophysics*, 282(1):117–128. doi:http://dx.doi.org/10.1016/S0040-1951(97)00215-1.

Warren, J. K., 2008. Salt as sediment in the Central European Basin system as seen from a deep time perspective. In: Littke, R., Bayer, U., Gajewski, D., and Nelskamp, S., editors, *Dynamics of Complex Intracontinental Basins: The Central European Basin System*, Springer Science & Business Media, Springer–Verlag, Berlin, pages 249–276.

Warsitzka, M., Kley, J., and Kukowski, N., 2015. Analogue experiments of salt flow and pillow growth due to basement faulting and differential loading. *Solid Earth*, 6(1):9–31. doi:10.5194/sed-6-1625-2014.

Warsitzka, M., Kley, J., and Kukowski, N., 2013. Salt diapirism driven by differential loading - Some insights from analogue modelling. *Tectonophysics*, 591:83–97. doi:http://dx.doi.org/10.1016/j.tecto.2011.11.018.

Warsitzka, M., Kley, J., Jähne-Klingberg, F., and Kukowski, N., 2017. Dynamics of prolonged salt movement in the Glückstadt Graben (NW Germany) driven by tectonic and sedimentary processes. *International Journal of Earth Sciences*, 106(1):131–155. ISSN 1437-3262. doi:10.1007/s00531-016-1306-3.

Weber, H., 1977. Salzstrukturen, Erdöl und Kreidebasis in Schleswig-Holstein, Übersichtskarten zur Geologie von Schleswig-Holstein 1:50000. Landesamt für Natur und Umwelt des Landes Schleswig-Holstein, Flintbek.

Weijermars, R., Jackson, M. P. A., and Dooley, T. P., 2014. Quantifying drag on wellbore casings in moving salt sheets. *Geophysical Journal International*, 198(2):965–977. doi:https://doi.org/10.1093/gji/ggu174.

Weijermars, R. and Jackson, M. P. A., 2014. Predicting the depth of viscous stress peaks in moving salt sheets: Conceptual framework and implications for drilling. *AAPG bulletin*, 98(5):911–945. doi:10.1306/09121313044.

Weinberger, R., Lyakhovsky, V., Baer, G., and Begin, Z. B., 2006. Mechanical modeling and InSAR measurements of Mount Sedom uplift, Dead Sea basin: Implications for effective viscosity of rock salt. *Geochemistry, Geophysics, Geosystems, AGU*, 7(5):20pp.

White, F. M., 2011. *Fluid Mechanics*, 7th edition. New York, McGraw Hill, 864 pp.

Withjack, M. O. and Callaway, S., 2000. Active normal faulting beneath a salt layer: an experimental study of deformation patterns in the cover sequence. *AAPG bulletin*, 84(5):627–651.

Wong, T. E., Batjes, D. A. J., de Jager, J., and van Wetenschappen, K. N. A., 2007. *Geology of the Netherlands*. Amsterdam : Royal Netherlands Academy of Arts and Sciences.

Wu, Z., Yin, H., Wang, X., Zhao, B., Zheng, J., Wang, X., and Wang, W., 2015. The structural styles and formation mechanism of salt structures in the Southern Precaspian Basin: Insights from seismic data and analog modeling. *Marine and Petroleum Geology*, 62: 58–76.

Yücel, K., 2010. *3D modelling of salt related structures in the Friesland Platform, the Netherlands*. PhD thesis, Middle East Technical University.

Zander-Schiebenhöfer, D., Donadei, S., Horvath, P. L., D, Z., Staudtmeister, K., Rokahr, R. B., Fleig, S., Pollok, L., Hölzner, M., Hammer, J., Gast, S., Riesenberg, C., and von Goerne, G., 2015. Bestimmung des Speicherpotenzials Erneuerbarer Energien in den Salzstrukturen Norddeutschlands: Projekt InSpEE. *Erdöl Erdgas Kohle*, 131(7-8):289–293.

Ziegler, P. A., 1987. Late Cretaceous and Cenozoic intra-plate compressional deformations in the Alpine foreland—a geodynamic model. *Tectonophysics*, 137(1-4):389–420.

Ziegler, P. A., 1990. *Geological Atlas of Western and Central Europe, 1990*. Geological Atlas of Western and Central Europe. Shell Internationale Petroleum Maatschappij, B.V. ISBN 9789066441255.

Zirngast, M., 1996. The development of the Gorleben salt dome (northwest Germany) based on quantitative analysis of peripheral sinks. *Geological Society, London, Special Publications*, 100(1):203–226.

Zöllner, H., Reicherter, K., and Schikowsky, P., 2008. High-resolution seismic analysis of the coastal Mecklenburg Bay (North German Basin): the pre-Alpine evolution. *International Journal of Earth Sciences*, 97(5):1013–1027.

Zulauf, G., Zulauf, J., Bornemann, O., Kihm, N., Peinl, M., and Zanella, F., 2009. Experimental deformation of a single-layer anhydrite in halite matrix under bulk constriction. Part 1: Geometric and kinematic aspects. *Journal of Structural Geology*, 31(4):460–474.

C. Appendix

C.1 Database for the age analysis of salt structures in the Southern Permian Basin

Salt structures of the Southern Permian Basin (SPB) were collected in a database (see electronic supplement on the CD; Appendix C.2) containing information on:

- the type of salt structure (pillow, diapir);
- location;
- age of the involved salt formation;
- age of initiation of the salt;
- age of diapiric breakthrough;
- age of main activity of the salt structure;
- age of the oldest overburden covering diapiric structures.

Terms and definitions concerning salt structures are adopted to Trusheim (1960), Jackson and Talbot (1991) and Hudec and Jackson (2011). Salt structure means salt pillow or salt-cored anticline (elongated pillow), which are still covered by an overburden (non-pierced), and salt diapir or wall (highly elongated diapir), which broke through the overburden (pierced). The terms are here used without any implications on the formation mechanism, but only in geometrical sense (e.g. salt-cored anticlines are not necessarily formed by lateral shortening). Other types of salt structures, e.g. salt intrusions, overhangs, salt sheets or salt rollers are excluded, since they are usually related to one of these salt structures mentioned first. All salt structures included in the database are displayed in the geological map in Fig. C.1B (salt structures named). For some salt structures, neither particular descriptions nor cross sections crossing these structures could be found in literature (white colour in Fig. C.1B). These structures are not listed in the database. Nevertheless, ages of these structures were estimated based on surrounding structures or based on the regional evolution of the specific part of the basin.

C.1.1 Determination of ages of initiation and main activity

Previous studies intending to date the ages of salt structures (e.g. Jaritz, 1973; Riedel, 1944; Trusheim, 1960) were only focussed on the western part of the North German Basin (here referred to as Northwest German Basin). Since then, widespread exploration and investigation of the SPB provide new geological and geophysical data and numerous publications concerning evolution of the basin or particular salt structures. Nevertheless, approaches of previous studies were adapted and used for dating salt structures in the entire SPB.

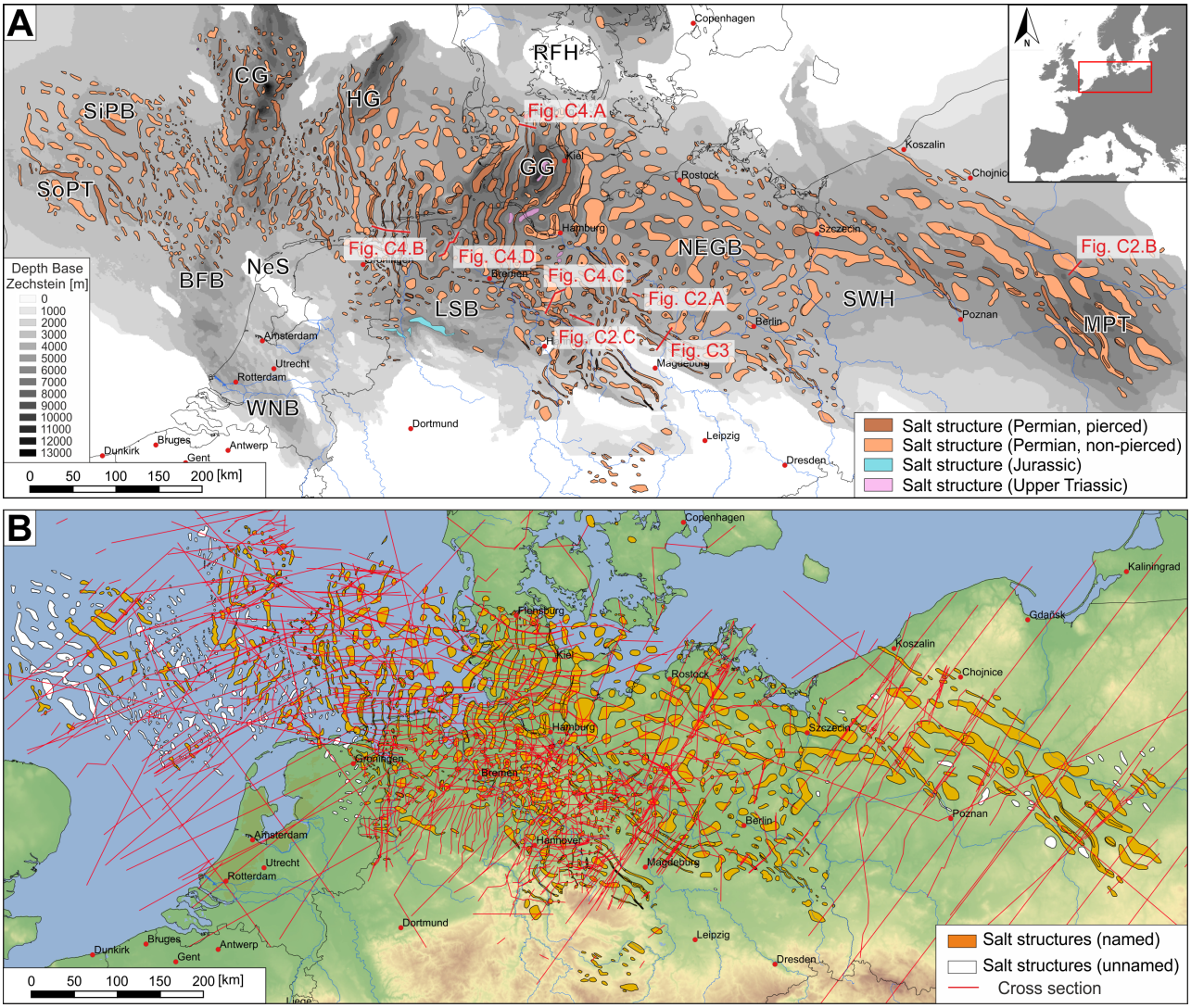

Figure C.1: **A** Map of central Europe illustrating salt structures included in the database (named salt structures). **B** Map of Central Europe illustrating pierced and non-pierced salt structures of Permian salt as well as salt structures of Upper Triassic salt and Jurassic salt. Note that salt structures without names (white) are not listed in the salt structure data base (Appendix C.2). BFB – Broad Fourteens Basin, CG – Central Graben, HG – Horn Graben, GG – Glückstadt Graben, LSB – Lower Saxony Basin, MPT – Mid Polish Trough, NEGB – Northeast German Basin, NeS – Netherland Swell, RFH – Ringkøbing-Fyn High, SiPB – Silver Pit Basin, SoPT – Sole Pit Trough, SWH – Szczecin-Wolsztyn High, WNB – West Netherlands Basin. (shapes of salt structures after Doornenbal and Stevenson (2010)).

The ages of salt structures are determined based on clues from local scale deformation or changes of sedimentary patterns of the post-Permian layers (Jaritz, 1973). These are:

- thickness variations across a diapir (Fig. C.2A) indicating normal faulting or differential subsidence;
- unconformities, thickness reduction and upturned beds along the flanks of salt structures indicating crestal uplift (Fig. C.2B; Fig. C.3);
- increased overburden thickness next to salt structures (peripheral sinks) indicating salt expulsion (Fig. C.2C);
- local scale facies changes (Strunck et al., 1998; Doornenbal and Stevenson, 2010; Beutler et al.,

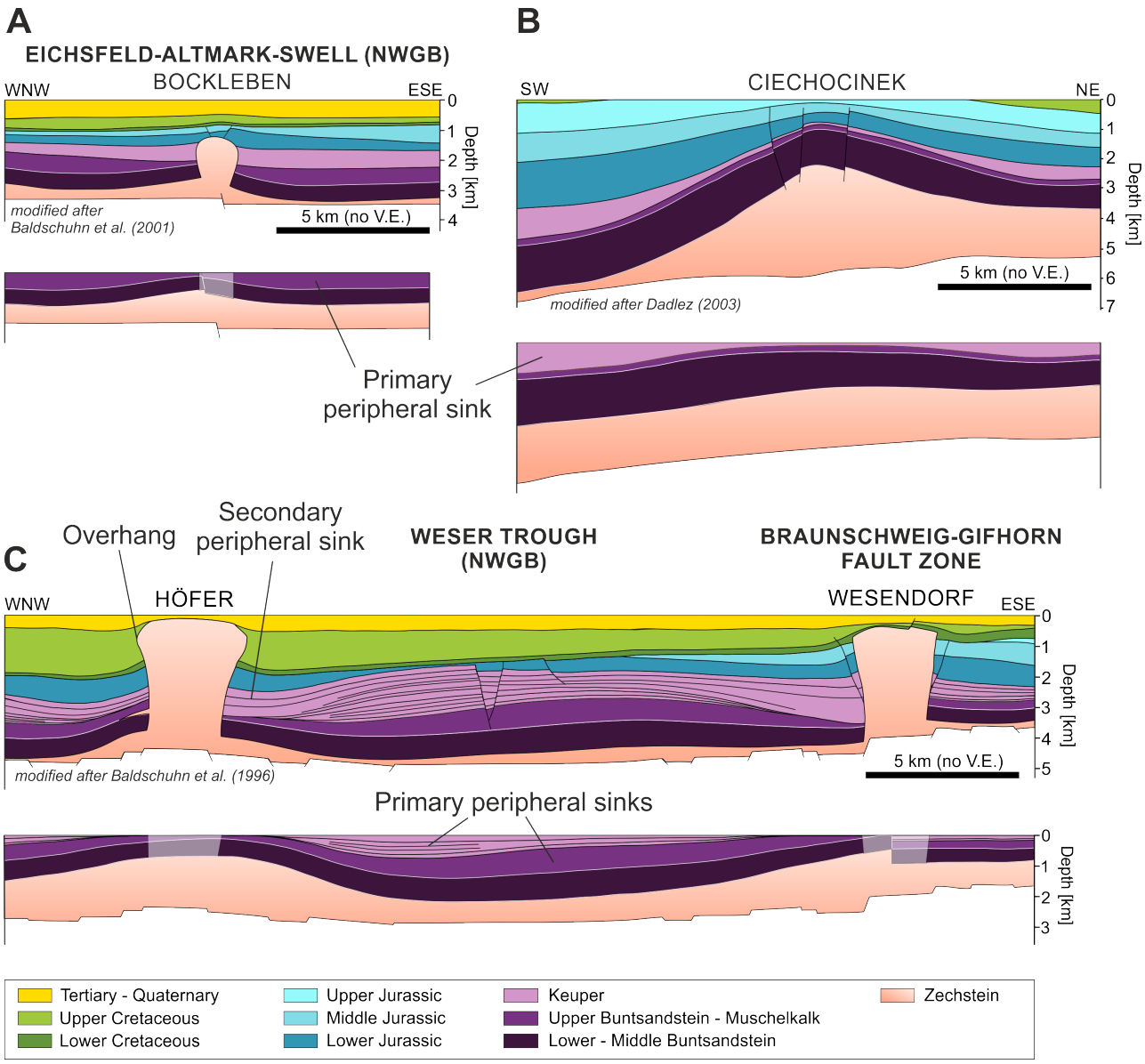

Figure C.2: Geological cross sections displaying different types of salt structures in the Southern Permian Basin. The reconstructions of the overburden strata demonstrates first occurrence of peripheral sinks or fault offsets as well as the deepest secondary peripheral sinks next to salt structures. **A** The normal fault in the overburden was probably initiated by a basement fault during Muschelkalk time. **B** A primary peripheral sink next to the pillow first developed during Keuper time. **C** Differential basement subsidence potentially led to the formation of a broad primary peripheral sink between both diapirs during Keuper time or earlier. The reconstructions of the geological cross sections were conducted by applying vertical shear restoration in 2DMOVE^{TM}. See Fig. C.1A for locations of the cross sections.

2012), e.g. expressed by grain size distribution in siliciclastic sediments, indicating a topographic relief due to salt structure growth.

Generally, the initiation of a salt structure (corresponding to the **age of first activity**) can be provoked by (1) any deformation or structural change of the overburden or the sub-salt basement or (2) by any laterally varying sedimentary thickness above or close to the present-day salt structure (see Section 1.2.3). The first mechanism involves normal or thrust faulting in the sub-salt basement or faults, roll-overs and folds in the supra-salt overburden (Fig. C.4A-C). The second mechanism

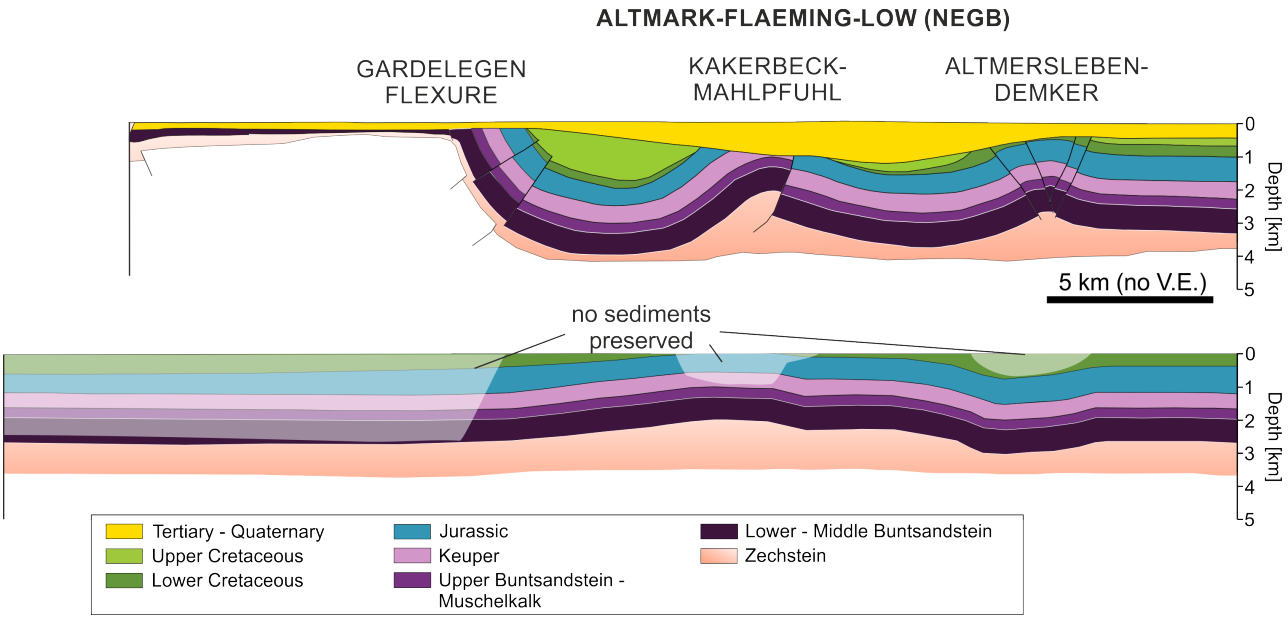

Figure C.3: Geological cross section from the southern edge of the Northeast German Basin (NEGB). During the Late Cretaceous, a pre-existing salt pillow (Kakerbeck-Mahlpfuhl) was overprinted by horizontal contraction concurrent to the formation of a new salt anticline (Altmersleben-Demker) next to it. The cross section and the restoration were modified from Jähne-Klingberg (2016). See Fig. C.1A for the location of the cross section.

is mainly created by uneven sedimentation, e.g. progradating sediment wedges, reefs or peripheral sinks of neighbouring salt structures (Fig. C.4D), but also by erosional incision.

It is here assumed that both mechanisms produce a hydraulic-head gradient in the salt layer causing local-scale salt flow (see Section 1.2.3). Therefore, the oldest, post-salt indication for deformation of the sub- and supra-salt or laterally differential sediment accumulation defines the age of initiation. The validity of this assumption is supported by numerous analogue (see Warsitzka et al., 2013, 2015; Wu et al., 2015, and references therein) and numerical modelling studies (e.g. Schultz-Ela and Jackson, 1996; Ings and Beaumont, 2010; Goteti et al., 2012; Peel, 2014).

The **age of main activity** is defined as the period in which growth of a salt structure was fastest. Actually, the fastest growth corresponds with the highest subsidence rates in the neighbouring peripheral sinks (Jaritz, 1973; Zirngast, 1996). Thus, to be accurate, subsidence rates in each peripheral sink have to be determined by measuring the exact thickness and the age of boundaries of each layer. This procedure has been conducted for salt structures in the central Glückstadt Graben (Chapter 3). However, applying this method to all salt structures in the SPB is beyond the scope of this study, because it requires acquisition and investigation of well data or depth-migrated seismic profiles of each salt structure. Therefore, the period of fastest growth of a salt structure (= main activity) is here assumed to be marked by the overburden layer possessing the largest thickness. Since nearly all authors use equal layer boundaries for post-Permian stratigraphy in the SPB (see Appendix C.1.3), this simplification is a suitable approximation.

For salt pillows or anticlines, the main depocentres are mostly primary peripheral sinks (PPS). For diapirs or walls, secondary peripheral sinks (SPS) are usually much thicker than PPS (Fig. C.2). An

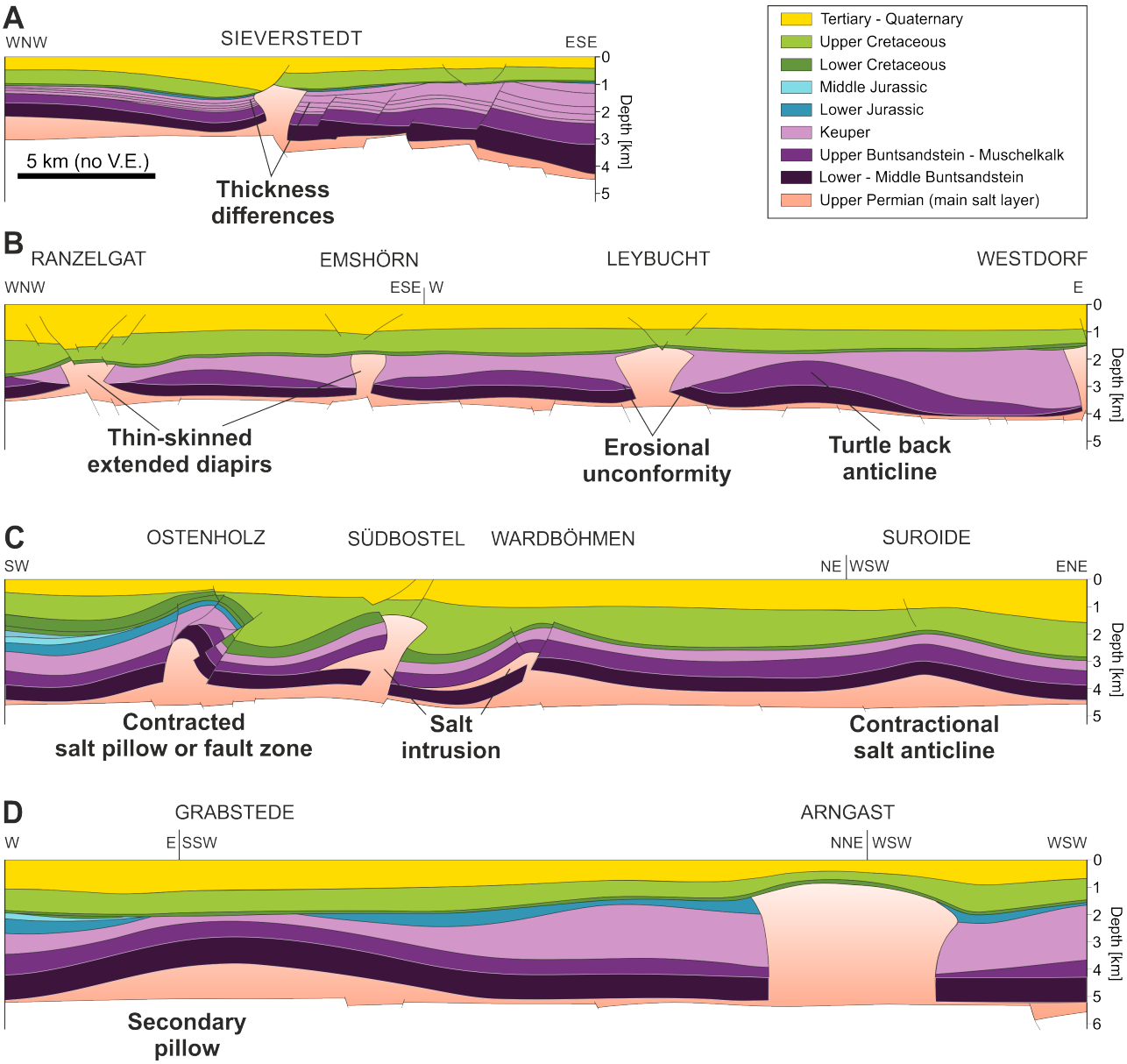

Figure C.4: Geological cross section of salt structures in the North German Basin (modified from Baldschuhn et al., 2001). **A** The diapir is encompassed by differently deep secondary peripheral sinks and underlain by basement faults. This indicates an initiation of salt flow due to thick-skinned extension during Buntsandstein time. **B** Diapirs are surrounded by turtle-back anticlines and roll-overs, which are envisage as indications for detached gravitational gliding of the supra-salt cover on a tilted salt layer. This process potentially started during Buntsandstein time. **C** Salt intrusions, thrust faults and anticlinal uplift suggest contractional overprinting of pre-existing diapirs or formation of new salt anticlines, respectively. The contraction took place during the Late Cretaceous phase of shortening that affected southern parts of the North German Basin. **D** Adjacent to the deep secondary peripheral sink of the Arngast diapir a salt pillow developed during Keuper time. Probably differential loading caused salt expulsion from beneath the SPS toward neighbouring regions. See Fig. C.1A for locations of the cross sections.

exception is made for salt structures affected by the Late Cretaceous – Tertiary contractional tectonics and possessing no adjacent peripheral sinks older than Late Cretaceous. These structures are assumed to pass the phase of main activity during the Late Cretaceous.

The **age of diapiric breakthrough** of a salt structure provides useful insights into salt dynamics of the basin. In this study, the age of diapiric breakthrough is defined by the first occurrence of secondary

peripheral sinks adjacent to diapirs. In contrast, studies e.g. by Sørensen (1998) demonstrated that piercing occurs earlier than the development of secondary peripheral sinks. Actually, some diapirs in the SPB are only surrounded by deep primary peripheral sinks. Because of these limitations, this age determination is prone to high uncertainties and, therefore, not visualised in a geological map.

The **age of overburden covering salt diapirs** gives hints to the termination of the growth of a salt structure. It is here defined by oldest strata completely covering the top of a pierced salt structures (diapir, walls). Both, the age of diapiric breakthrough and the age of termination of salt structure growth are included in the salt structure data base (Appendix C.2). In future work, it would be worthwhile to visualise these ages in geological maps and to examine salt structures in the SPB regarding to these criteria.

C.1.2 Data and certainty of age analysis

The data used for age determinations of the salt structures was entirely extracted from published sources. Categories characterizing the data consists of:

Descriptions and explanations of specific salt structures: This data is usually based on intense investigation of well data and seismic profiles and, therefore, the most reliable. Specific descriptions are particularly available for salt structures in the North German Basin and the German North Sea Sector in terms of detailed catalogues and publications (Fahrion, 1953; Hiller, 1971; Jaritz, 1973; Weber, 1977; Bornemann, 1979; Binot, 1988; Jordan and Kockel, 1991; Kockel, 1991; Kockel and Krull, 1995; Kockel, 1995; Zirngast, 1996; Baldschuhn and Kockel, 1998; Strunck et al., 1998; Baldschuhn and Kockel, 1999; Baldschuhn et al., 2001; Frisch and Kockel, 2004; Köthe et al., 2007; Al Hseinat et al., 2016), but also for some structures in the Northeast German Basin (e.g. Meinhold, 1956, 1959; Löffler, 1962; Pchalek, 1962; Meinhold and Reinhardt, 1967; Rühberg, 1976; Beutler and Schüler, 1978; Burchardt, 1990; Benox et al., 1997; Mayer et al., 2000; Kossow, 2001; Otto, 2003; Franzke et al., 2004; Gast et al., 2014), in the Netherlands (Yücel, 2010; Geluk, 2005; Harding and Huuse, 2015; Raith et al., 2015), or in the Mid-Polish Trough (e.g. Burliga, 1996; Krzywiec, 2002, 2004b).

Seismic cross sections (depth-converted or in Two way travel time) or geological cross sections interpreted from seismic data: These types of data can be found in numerous publications concerning almost all parts of the SPB. The complete coverage of cross sections used in the analysis presented here is shown in Fig. C.1B. Cross sections are relatively different in quality, spatial resolution, extent and quality of interpretation. Ideally, publications display depth-converted geological cross sections including reconstructions of the evolution of the presented structures (e.g. Knape, 1963; Benox et al., 1997; Wagner et al., 2002; Mohr et al., 2005; Tanveer and Korstgård, 2009; Ten Veen et al., 2012; Duffy et al., 2013; Vackiner et al., 2013). These reconstructions serve as primary indication for the age of initiation. At worst, only raw seismic time sections without much further description concerning the salt structures are presented in the publication (e.g. Van Wijhe, 1987; Dronkers and Mrozek, 1991) or cross sections extend across the entire basin preventing the recognition of smaller salt struc-

tures (e.g. Ziegler, 1990; Lamarche and Scheck-Wenderoth, 2005). Seismic time sections have to be treated with care when considering thickness variations in peripheral sinks. Apparent local thickening of cover layers might be caused by lateral or vertical variations of the seismic velocity and possibly disappear during depth conversion applying a proper velocity model of the underground. Thus, age interpretation of salt structures based on a seismic travel time cross section is generally regarded as uncertain.

2D cross sections bare the limitation that 3D variations of layer thicknesses probably remain unrecognised. Especially salt structures, which are roughly circular in map view sometimes possess peripheral sinks whose depocentres rotate around the vertical axis of the salt structure with time (e.g. Brink et al., 1992). Thus, the ages of circular or slight-elongated salt structures only crossed by one cross section have to be treated with care and validated by isopach maps.

Subcrop maps of regional unconformities: This data provides a proxy for topographic highs and lows at the specific time of the unconformity (e.g. Geluk and Röhling, 1997; Beutler et al., 2012) and, therefore, for uplifts of pillow crests or subsidence centres of peripheral sinks, if the resolution is sufficient (e.g. Voigt et al., 2004; Barnasch et al., 2005). However, published subcrop maps are mostly regional and cover wide parts of the SPB, e.g. the entire SPB (Stollhofen et al., 2008), the Netherlands and Northern Germany (Geluk and Röhling, 1997; Geluk, 2005), the Northwest German Basin (Baldschuhn et al., 1996), or the Northeast German Basin (Beutler et al., 2005; Barnasch, 2010; Beutler et al., 2012). This results in lack of detail considering small scale salt structure uplifts of a few kilometre width. Moreover, ages derived from subcrop maps only represent the latest age possible, whereas the true age of initiation might be older. For instance, the basin-wide unconformity of the base Lower Cretaceous (Stollhofen et al., 2008) can indicate the presence of pillow uplifts, which then should have initiated during Late Jurassic at the latest.

Isopach maps: Such data can display local scale layer thinning above crests of salt pillows or thickening of peripheral sinks (e.g. Meinhold and Reinhardt, 1967; Reinhardt, 1993; Frisch and Kockel, 1999; Dadlez, 2003; Scheck et al., 2003a,b; Brückner-Röhling et al., 2004; Beutler et al., 2005; Maystrenko et al., 2005b; Hansen et al., 2007; Franz, 2008; Noack et al., 2010; Kastner et al., 2013; Arfai et al., 2014). Isopach maps can indicate the age of first activity and the age of main activity of a salt structure. Similar to subcrop maps of unconformities, isopach maps are often basin scale and not sufficiently detailed. Furthermore, locally occurring thinning of a unit can be a misleading indicator for uplifted crests of salt pillows or normal faulting of the supra-salt cover, because the thickness of a unit can be altered subsequent to its deposition due to erosion or faulting (see e.g. Grabstede and Leybucht in Fig. C.4B and D). Most thickness maps display vertical thickness measurements. This might significantly differ from the true thickness, if layers are tilted. For these reasons, isopach maps are only reliable, if they are used in combination with cross sections.

Facies analysis based on well data or outcrops: Outcrop studies from other basins demonstrate that sedimentary facies distribution is sensitive to differential subsidence, in particular in the continental realm (Trudgill, 2011) as occurring for instance during Buntsandstein time. Therefore, facies changes are an accurate indicator for small scale surface movements as possibly resulting from the growth of

a salt structure. Unfortunately, there are only a few studies addressing facies distributions sufficiently detailed to reveal insights on the locations of salt structure uplifts (e.g. Strunck et al., 1998; Brandes, 2012; Osman et al., 2013).

Besides the quality and quantity of published data, the subjective interpretation and its underlying concepts of structural interpretation, e.g. of seismic data, differ from editor to editor. Consequently, interpreted geological cross sections of salt structures and adjacent sedimentary structures can be very heterogeneous between different basin parts and countries. Such differences can be neither evaluated nor avoided in this study.

Additionally, geological reasons can reduce the certainty of the age dating. In regions of the basin affected by uplift, parts of the supra-salt sediment have been eroded to varying degrees (e.g. southern parts of the North German Basin). In regions characterised by a long-lasting hiatus, peripheral sinks are not supplied by sediments (e.g. North Sea region during the Late Jurassic). In both cases, there can be a lack of peripheral sinks documenting salt movements and, thus, no indications for dating the ages.

On the basis of the available data and the sources of inaccuracies described above, the certainty of the ages of salt structures (age of first initiation and main activity; see Fig. 2.1 and Fig. 2.2) is divided into three groups:

1. **Age: well constrained** based on detailed geological cross section and/ or descriptions in literature (filled colour)
2. **Age: uncertain** based on regional geological cross sections, thickness maps of overburden layers, subcrop maps of regional unconformities (e.g. subcrop map of the base Solling unconformity) (horizontal stripes)
3. **Age: unknown** because no specific data could be found. Age was estimated either from ages of neighbouring salt structures or from broad scale structural development and tectonic setting of the region (vertical stripes). Ages are estimated based on the ages of neighbouring salt structures or on the broad-scale evolution of the basin part.

The author emphasizes that the database of salt structures ages does not claim to be complete or absolutely correct. There might be many additional sources of information (particularly local literature), unpublished or confidential data available, which therefore could not be included here. The database should rather provide an impression of regional differences of initiation and structural trends to give insight in the dynamics of salt structures and is open for discussion and improvements.

C.1.3 Periods of the age analysis

The subdivision of periods used in the age analysis (Table C.1) refers to the Geotectonic Atlas of Northern Germany (Baldschuhn et al., 1996, 2001) and the Petroleum Geological Atlas of the Southern Permian Basin Area (Doornenbal and Stevenson, 2010). The duration of the intervals is highly variable (5.6 to 65.5 Myr). This coarse division is generally used in most literature concerning the SPB for dividing seismic units or intervals for thickness maps (e.g. Jaritz, 1973; Baldschuhn et al.,

Table C.1: Periods applied for age analysis. The division refers to the Geotectonic Atlas of Northern Germany (GTA) (Baldschuhn et al., 2001) and the Petroleum Geological Atlas of the Southern Permian Basin Area (Doornenbal and Stevenson, 2010).

Era		Epoch	Age of Top [Myr]	Duration [Myr]
Cenozoic		Tertiary - Quartenary	0	65.5
Creatceous		Late	65.5	34
		Early	99.5	46
Jurassic		Late	145.5	16.5
		Middle	162	14
		Early	176	25.5
Triassic	Late	Keuper	201.5	37.3
	Middle	Late Buntsandstein - Muschelkalk	238.8	8.3
	Early	Early - Middle Buntsandstein	247.1	5.6

2001). Hence, sources from different regions in the SPB can be easily compared. In the study presented, Early and Middle Jurassic were combined. This is because, Middle Jurassic units are missing or are relatively thin in many parts of the basin (despite active rift basins, e.g. Lower Saxony Basin, Central Graben) due to erosion or non-deposition (Stollhofen et al., 2008).

For some regions, a finer stratigraphic resolution and, thus, a more precise determination of the ages might be possible, e.g. a detailed discrimination of main activities of salt diapirs in the Glückstadt Graben during Keuper time (Frisch and Kockel, 1999). Nevertheless, this impedes the comparability with regions lacking such detailed investigations.

The temporal division used here is favourable for analysing the first initiation of salt structures, because most salt structures were initiated during Triassic (Fig. 2.1), where the temporal resolution is comparatively high. In contrast, the analysis of periods of the main activity revealed that many salt structures reach their fastest growth during the Late Cretaceous (duration = 34 Myr) or Cenozoic (duration = 65.5 Myr) (Fig. 2.2). Hence, a finer stratigraphic resolution particularly of these periods would improve the significance especially concerning tectonic active regions in the SPB.

C.2 Digital supplement

The following data can be found on the attached DVD:

Chapter 2: In the folder *Chapter02*, the data base of the salt structure age analysis is attached as Excel sheet ("Database-AgeAnalysisSPB.xlsx"). Additionally, the geological maps presented in Chapter 2 are included.

Chapter 4/ Manuscript #2: In the folder *Chapter04*, the electronic supplement related to the publication Warsitzka et al. (2015) is attached (folder: "Warsitzka-2015-SolidEarthSupplement"). Additional data of the analogue experiments can be found in subfolder *DataExperiments* including a list of all experiments (*"List-Experiments.xlsx"*), photos made during the experiments and images of the vector analysis made with the particle imaging velocimetry technique.

Publications: In the the folder *Puplications*, the peer-reviewed articles (manuscript #1 and #2), the first submitted manuscript #3 and the revised version of manuscript #3 as well as all conference abstracts and posters related to this thesis are attached. A list of citations of all publications related to this thesis can be found in *"Publications.pdf"*.

The pdf-version of this thesis is attached as "Warsitzka-Diss-Characteristics of salt flow and syn-kinematic sedimentary structures in extensional basins.pdf".

Selbstständigkeitserklärung

Ich erkläre, dass ich die vorliegende Arbeit selbständig und unter Verwendung der angegebenen Hilfsmittel, persönlichen Mitteilungen und Quellen angefertigt habe.

Name	Datum	Unterschrift

Erklärung zu den Eigenanteilen des Promovenden/der Promovendin sowie der weiteren Doktoranden/Doktorandinnen als Koautoren an den Publikationen und Zweitpublikationsrechten bei einer kumulativen Dissertation

Für alle in dieser kumulativen Dissertation verwendeten Manuskripte liegen die notwendigen Genehmigungen der Verlage („Reprint permissions“) für die Zweitpublikation vor.

Die Co-Autoren der in dieser kumulativen Dissertation verwendeten Manuskripte sind sowohl über die Nutzung, als auch über die oben angegebenen Eigenanteile der weiteren Doktoranden/ Doktorandinnen als Koautoren an den Publikationen und Zweitpublikationsrechten bei einer kumulativen Dissertation informiert und stimmen dem zu.

Die Anteile des Promovenden/der Promovendin sowie der weiteren Doktoranden/Doktorandinnen als Koautoren an den Publikationen und Zweitpublikationsrechten bei einer kumulativen Dissertation sind in der Anlage aufgeführt.

Name des Promovenden/der Promovendin	Ort, Datum	Unterschrift

Ich bin mit der Abfassung der Dissertation als publikationsbasiert, d.h. kumulativ, einverstanden und bestätige die vorstehenden Angaben. Eine entsprechend begründete Befürwortung mit Angabe des wissenschaftlichen Anteils des Doktoranden/der Doktorandin an den verwendeten Publikationen werde ich parallel an den Rat der Fakultät der Chemisch-Geowissenschaftlichen Fakultät richten.

Name Erstbetreuer(in)	Ort, Datum	Unterschrift

Publikation: Warsitzka, M., Kley, J., and Kukowski, N., 2015. Analogue experiments of salt flow and pillow growth due to basement faulting and differential loading, *Solid Earth*, 6: 9-31, doi:10.5194/se-6-9-2015.			
Beteiligt an:			
	Autor 1: Michael Warsitzka	Autor 2: Jonas Kley	Autor 3: Nina Kukowski
Konzeption des Forschungsansatzes	×	×	×
Planung der Untersuchungen	×	×	×
Datenerhebung	×		
Datenanalyse und -interpretation	×		
Schreiben des Manuskripts	×	×	×
Vorschlag Anrechnung Publikationsäquivalente	1,0		

Publikation: Warsitzka, M., Kley, J., Jähne-Klingberg, F., and Kukowski, N., 2017. Dynamics of prolonged salt movement in the Glückstadt Graben (NW Germany) driven by tectonic and sedimentary processes. *Int J Earth Sci (Geol Rundsch)*, 106: 131-151, doi:10.1007/s00531-016-1306-3.				
Beteiligt an:				
	Autor 1: Michael Warsitzka	Autor 2: Jonas Kley	Autor 3: Fabian Jähne-Klingberg	Autor 4: Nina Kukowski
Konzeption des Forschungsansatzes	×	×		×
Planung der Untersuchungen	×	×		×
Datenerhebung	×		×	
Datenanalyse und -interpretation	×		×	
Schreiben des Manuskripts	×	×	×	×
Vorschlag Anrechnung Publikationsäquivalente	1,0			

Publikation: Warsitzka, M., Kukowski, N., Kley, J. Salt flow direction and velocity during sub-salt normal faulting and syn-kinematic sedimentation – implications from analytical calculations. submitted to *Geophysical Journal International*, Oxford University Press.			
Beteiligt an:			
	Autor 1: Michael Warsitzka	Autor 2: Nina Kukowski	Autor 3: Jonas Kley
Konzeption des Forschungsansatzes	×	×	×
Planung der Untersuchungen	×		
Datenerhebung	×		
Datenanalyse und -interpretation	×		
Schreiben des Manuskripts	×	×	×
Vorschlag Anrechnung Publikationsäquivalente	1,0		

Acknowledgments/ Danksagung

This PhD thesis benefited from funding by the German Research Foundation (DFG), the German Federal Ministry of Education and Research (BMBF) in the framework of the research project INFLUINS and the German Academic Exchange Service (DAAD) in the framework of a short term scholarship at the University of Texas at Austin (USA). Furthermore, the Federal Institute for Geosciences and Natural Resources (BGR) funded the project I am working on since 2012.

I would like to thank many people for their contribution on the scientific studies and for their personal support during the time of my PhD. The first and greatest gratitude is given to my supervisors Prof. Jonas Kley and Prof. Nina Kukowski for their inspirations and critical discussions on my scientific work, for encouraging me to follow my scientific career and for their patience during the long road to finish my PhD.

At the Institute of Geosciences, I want to thank my colleagues who helped to improve my work and accompanied me during the time of my PhD. I wish to acknowledge scientific advices by Prof. Kamil Ustaszewski, Prof. Reinhard Gaupp, Prof. Thomas Jahr, Prof. Ulrich Wegler and Thomas Voigt. My working group and further colleagues deserve special appreciation for sharing a fruitful time and helping me with any problem occurred during the work on my dissertation and other projects: Pascal Methe, Marco Paschke, Stephan Neugebauer-Semsch, Andreas Goepel, Matthias Queitsch, Daniel Beyer, Stephan Donndorf, Alexander Malz, Nadine John, Robert Lehmann, Andreas Hoffmann, Janet Kreßler, Gery Herbozo, Frank Buchwald and Volker Schwarz.

I would like to thank supervisors, scientists, technicians, who are or were working at the Helmholtz-Zentrum Potsdam - Deutsches GeoForschungsZentrum GFZ for their support in scientific issues, in conducting the analogue experiments and in organising my work at the GFZ and my life in Potsdam. In particular, I wish to thank Prof. Magdalena Scheck-Wenderoth, Prof. Onno Oncken, Christina von Nicolai, Matthias Rosenau, Judith Sippel, Karsten Reiter, Vera Noack, Katja Hirsch, Tasca Santimano, Björn Lewerenz, Yvonne Cherubini, Julia Autin, Franziska Alberg, Alexandra Wille, David Boutelier, Thomas Ziegenhagen, Frank Neumann, Michael Henze, Jannes Kinscher and Jens Strauß.

During my research exchange at the University of Texas at Austin, I received the great opportunity to learn scientific knowledge of various topics and to experience the cultural life of the USA. I am especially grateful to Prof. Brian K. Horton for integrating me in his working group and letting me join his lecture and his field trip. I would like to acknowledge scientific discussions on early outcomes of my thesis especially with Prof. Antonio Teixell, Martin P. A. Jackson, Tim P. Dooley, Maria A. Nikolinakou and Joel Saylor. Special thanks go to my friends in Austin, who made student life in Austin much more comfortable, most importantly Jahja Fongngern, Enri Quartini, Renas I. Koshnaw, Sebastian Ramirez and Marie Cavitte.

This thesis benefited from helpful discussions with colleagues from the Federal Institute for Geosciences and Natural Resources (BGR) especially concerning the geology of the North German Basin. With this regard, special thanks go to Fabian Jähne-Klingberg, who contributed to parts of this thesis as a co-author and was always open for discussion on salt tectonics, as well as Klaus Reinhold, Gesa Kuhlmann and Franz May.

For reviews and improvements on the manuscripts included in this thesis, I would like to thank Piotr Krzywiec, Peter Kukla, Yuriy P. Maystrenko and Christopher J. Talbot.

Meinen letzten, aber dafür wichtigsten Dank möchte ich meiner Familie und meine Freunden schenken, insbesondere Sabrina Apitz, Christina Warsitzka, Adrien Warsitzka, Michael Friedrich, Claudia Eisentraut und alle, die mich in dieser Lebensphase unterstützt haben. Meine Dissertation widme ich meinem Vater Rainer, der meinen Abschluss leider nicht mehr erleben konnte, es sich aber sehr gewünscht hätte.

,